Improving Magneto-Optical Filter Performance: Cascading and Oblique B-fields

FRASER DAVID LOGUE

Improving Magneto-Optical Filter Performance: Cascading and Oblique B-fields

Fraser D. Logue

A thesis presented for the degree of

Doctor of Philosophy

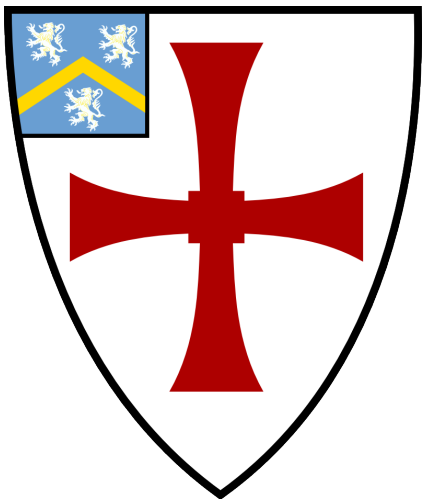

Quantum, Light and Matter Group

The University of Durham, UK, July 2023.

Improving Magneto-Optical Filter Performance: Cascading and Oblique B-fields

Fraser D. Logue

Abstract

Magneto-optical filters are ultra-narrow frequency selection devices that use atoms as the active medium. Frequency dependent dispersion, scattering and absorption make alkali atoms ideal for polarisation sensitive filtering, traditionally with equivalent noise bandwidths of several GHz and little control over the lineshape profile. Our investigations focus on two major improvements to magneto-optical filter performance: a) cascading two vapour cells with independent parameters and b) exerting magnetic fields at oblique angles to the light propagation direction. Optimised two-cell cascaded setups have a polarisation 'transformation' cell and a cell which 'extinguishes' unwanted features. Oblique magnetic fields result in frequency dependent non-orthogonal propagation eigenmodes which are directly responsible for narrower birefringent regions and better extinction of light outside these regions. We find very good agreement with theory and realise filters with equivalent noise bandwidths as low as $\sim$ 100 MHz with greater control of lineshape features. We consider theoretically further performance improvements which utilise exceptional points where the propagation eigenmodes coalesce completely.

Contents

Acknowledgements

Completing a PhD is no mean feat not least given the current times. Nonetheless a thesis lies before you because of the great support I have received. I'd like to thank my supervisors, Profs. Ifan Hughes and Steven Wrathmall, who have been very active in my development and have always been available for discussions despite their busy schedules. They have been forward thinking in mitigating problems which has led to our research output continuing through COVID and strike action. Most of all, they have valuably contributed to this research by helping me hone my ideas and by asking questions that got to the heart of the matter. My viva was hosted by examiners, Profs. Stuart Adams and Sonja Franke-Arnold, in the safe haven of Stuart's office whilst, from all four corners, we were surrounded by the raging Storm Babet! I thank them both for the concerted efforts they made to read the thesis in detail and I am glad the research inspired much conversation. Their suggested edits have made the thesis much clearer in its message and goals. It is also imperative I thank ESPRC for funding my PhD without which I would not have been able to undertake this work.

I would also like to thank my colleagues Francisco, Jack, Sharaa and Dani. Francisco ensured I hit the ground running offering me the breadth of his coding and experimental experience. It was great to see Francisco go through the thesis submission process and I'm glad to see his cold Yb work is already producing exciting results at FEMTO-ST. Jack has been a breath of fresh air to the group bringing new visualisation techniques and theoretical understanding. His thoughts and questions have challenged me and I wish him all the best in completing his PhD. Sharaa has always been a kind and courteous lab partner and her insights into the readability of our tutorial review were extremely valuable. Given the interest generated in her first year talk, her research will also be on my list to follow. Dani has played an integral role without whom no experiments would have taken place. She always has an idea up her sleeve and commits a great deal of time to helping me and others in their research goals. I have to offer Dani a special thanks for

setting up and managing a new lab space during COVID protocols without which it may have been impossible to complete my PhD.

The whole Quantum, Light and Matter group has been a warm and supportive environment. In particular, I'd like to thank Tom Cutler, Matt Jamieson, Luke Fernley, Albert Tao, Jack Segal, Matt Hill, Shuying Chen, Steph Foulds, Lucy Downes, and Clare Higgins for all their help and advice, and Alex Guttridge for our work together organising group meetings. My running and football friends have kept my heart racing. I trust matches will run much smoother now that there isn't someone having a chat in the middle of the pitch. Beyond recreation, we are a community that supports each other on key social issues. Many thanks to Puya Mirkarimi for inviting us to protests against the Iranian regime and to all those who educated me on the promotion of women and LGBT individuals in science.

My wider Durham life has brought me much needed respite from physics. My thanks to Principal Rob Lynes, Harriet Axbey and Josh Crawshaw at Stephenson College for helping me set up Rocket! theatre and inviting me to toast one of their wee haggises. St Chad's and St. Oswald's choirs have been delightful singing communities that have really stretched me musically. My thanks to the choir directors, Matthew Kelley and David Harris (*Morning Thoughts* and *Love Came Down at Christmas* still pop into my head...) Additionally, I thank Tony and John for dealing with my constant change of mood, a Bass one minute and a Tenor the next!

I'm indebted to the Methodist Church for giving me the space to develop as a preacher and leader. Whether it was working with Gwen, Mark and the Shell Group to plan the Bearpark Youth Service or meeting the locals at Sherburn Hill Community Centre, it has been a pleasure to serve in the circuit. I'd like to thank Revd. John Squares, Mary Tribe, Frances Proud, Elaine Goy, Penny and Steve Bissell, and Soo Illingworth alongside Elvet, North Road, Bowburn and Carrville Churches for their support and guidance. Equally, the whole cast of 'Save the Church!' deserve a round of applause. I doubt any of us will ever sing 'Holy Holy Holy' right again! I have to give special thanks to Bill and Jean Young, Peter and all at Pittington St. John's – 'The Church whom I loved (!)' – a place where many continue to experience their hearts 'strangely warmed'. I'm overjoyed the Open Day was such a success though my legs are quite tired from the 500 house leaflet trek! I wish Pittington many more blessed years serving their community.

There have been many people who have taken care of me in the smallest but most significant ways. Maureen, my neighbour, has kept me replenished with all

types of fruit (especially mango!) and the best fruit of them all, coconut bounty bars. I always enjoyed our lunches and coffees out. Hilary and Bryan have treated me as their own grandson giving me pizzas, lectures on linguistics and a warm cup of Ribena on a Saturday afternoon - hospitality at its finest. As a Scot with an English accent, my English friend Alison with a Scottish accent has always been there for an intriguing discussion on various subjects. I wonder if we will ever categorically prove the Transfiguration event occurred on Mount Tabor...?

Finally, my thanks to my family. My Dad has given me hard to swallow advice throughout this PhD which has very often been right. All the best for your retirement this year! I'm sure it won't stop you from keeping busy or from driving everyone across the country. My regular calls with my Mum are always the highlight of my day. It was always a welcome surprise to receive a card or postcard from Mum featuring a picture of a funny looking animal on it. I'm glad to see you looking so well... and with hair! My sister Michaela has thankfully stopped asking me for legal advice. By which I mean, she has stopped asking me for advice on her qualification to be a solicitor, instead discovering she is legally gifted herself and I am sadly not. All the best for both of us in our job searches!

I dla Oliwii, mimo że poznaliśmy się dopiero na koniec mojego doktoratu, twoje wsparcie emocjonalne było kluczowe do wysłania mojej pracy. Dziękuję, za te wszystkie nasze wspólne odklejki! Założe się, że wykupiłaś już wszystkie książki z The Collected, zanim to przeczytasz (więc docenisz tę!). Wszystkiego najlepszego na nowej drodze jako najwspanialszy nauczyciel naukowy w historii The Oaks.

Declaration

The work in this thesis is based on research carried out at the Quantum Light and Matter Group, Department of Physics, University of Durham, England. No part of this thesis has been submitted elsewhere for any other degree or qualification, and it is the sole work of the author unless referenced to the contrary in the text.

Relevant Articles

F. S. Ponciano-Ojeda, F. D. Logue, and I. G. Hughes. Absorption spectroscopy and Stokes polarimetry in a ^{87}Rb vapour in the Voigt geometry with a 1.5 T external magnetic field. *Journal of Physics B: Atomic, Molecular and Optical Physics*, **54**(1): 015401, (2020). https://doi.org/10.1088/1361-6455/abc7ff [1]

F. D. Logue, J. D. Briscoe, D. Pizzey, S. A. Wrathmall, and I. G. Hughes. Better magneto-optical filters with cascaded vapor cells. *Optics Letters*, **47**(12):2975-2978, (2022). https://doi.org/10.1364/OL.459291 [2].

D. Pizzey, J. D. Briscoe, F. D. Logue, F. S. Ponciano-Ojeda, S. A. Wrathmall, and I. G. Hughes. Laser spectroscopy of hot atomic vapours: from 'scope to theoretical fit. *New Journal of Physics*, **24**:125001, (2022).https://doi.org/10.1088/1367-2630/ac9cfe [3].

J. D. Briscoe, F. D. Logue, D. Pizzey, S. A. Wrathmall, and I. G. Hughes. Voigt transmission windows in optically thick atomic vapours: a method to create single-peaked line centre filters. *Journal of Optical Physics B: Atomic, Molecular and Optical Physics*, **56**(10):105403 (2023). https://doi.org/10.1088/1361-6455/acc49c [4].

F. D. Logue, J. D. Briscoe, D. Pizzey, S. A. Wrathmall, and I. G. Hughes. Exploiting non-orthogonal eigenmodes in a non-Hermitian optical system to realize sub-100 MHz magneto-optical filters. *ArXiv Preprint*, 2303.00081, (2023). https://doi.org/10.48550/arXiv.2303.00081 [5]

List of Figures

Chapter 1

Introduction

All text written without the use of AI.

1.1 A Brief Review of Magneto-Optical Filters

The history of magneto-optical filters starts with the Faraday effect [6]. In the mid-19th century, Michael Faraday [7] discovered that a magnetic field applied to certain crystals along the direction of the light's passage would cause the plane of polarisation to rotate - a revolutionary phenomenon only to be fully understood if light were an electromagnetic wave. For the next half century, a variety of new optical phenomena were observed and given names including Kerr (1875, 1877) [8, 9], Christiansen (1884) [10, 11], Cotton (1895) [12], Zeeman (1896) [13], Righi [14, 15], Macaluso-Corbino (1898) [16], Voigt (1898) [17, 18], Pockels (1898) [19] and Cotton-Mouton (1905) [20]. In a sea of names, questions remained: were any of these effects related, and if so, how? When light passed through an atomic vapour, the Macaluso-Corbino effect[2] showed a large polarisation change in the light output near an atomic resonance. Could atoms exhibit a Faraday-like effect? The full picture could not be fully understood without the aid of quantum mechanics. Having

[2]Macaluso-Corbino always refers to an effect where polarisation rotation is observed in the vicinity of a resonance [21, 6, 22]. However, [21] offers a more specific definition: an effect which causes anomalous dispersion. Anomalous dispersion generally occurs in a much smaller region near the resonance. Readers should be careful to note how each writer is using the term.

confirmed the existence of spin as a quantum number alongside orbital angular momentum in the Stern-Gerlach experiment [23, 24], the Zeeman effect explained how these atomic resonances were split by magnetic sub-level and became frequency separated with an applied magnetic field. Righi observed that these split resonances preferentially absorbed different polarisations. With this knowledge, one need only place a polariser after the vapour and create an ultra-narrow frequency bandpass device. The magnetic field could be applied parallel to the propagation direction of the light, as in the original Faraday experiment, or perpendicular, as Voigt[1] observed. Other effects, listed above or otherwise unmentioned, were found to be more distant cousins to the Faraday effect. Though many have been employed in the creation of polarisation selection devices (Pockels cells [25, 26, 27, 28, 29], Kerr Shutters [30, 31, 32, 33], Christiansen filters [34, 35, 36, 37] and others predicted [38]), magneto-optical filters are the best performing frequency filtering devices by far having typical bandwidths 10,000 times narrower than Christiansen filters [39].

The development of magneto-optical filters begins as a tale of two continents. In 1950s Stockholm, the Swedish astrophysicist Yngve Öhman [40] proposed and realised a sodium magneto-optical filter for astronomical imaging. This joined the French Lyot (sometimes Lyot-Öhman) [41, 42, 43, 44, 45] and Czech Šolc filters [46, 47, 48, 49] as feasible devices to be incorporated in telescopes. For a history of early astronomical filters, see [50]. Lyot and Šolc filters are constructed from alternating stacks of birefringent material and polarisers as opposed to an atomic source. As such, they are the only reliable options currently available for certain wavelengths, e.g. the hydrogen lines [51] given the difficulties encountered working with monatomic hydrogen [52]. However, as a consequence, they are not absolutely tied to the spectral line of interest which can lead to drifting [53, 54, 55]. Lyot and Šolc filters are highly tunable when liquid crystal retarders or crystal defects are incorporated [56, 57, 58, 59, 60, 61, 62, 63]. Magneto-optical filters show com-

[1] The Voigt effect is sometimes called the Cotton-Mouton effect. In condensed matter contexts, both terms are often used to describe quadratic effects. In this thesis, we use Voigt to refer to a linear response to a magnetic field applied perpendicular to the propagation direction of the light.

parable tunability (as a fraction of bandwidth) however their central frequency is fixed by the atoms [64]. Each filter type has a different platform. Lyot and Šolc elements can be made out of quartz [65, 66, 67] or liquid crystal and integrated in optical fibres [68, 69, 70]. For magneto-optical filters, the atoms can be heated in glass cells [71, 72, 73] or held at room temperature in a hollow cathode lamp [74, 75, 76]. Nevertheless, in this competitive field, the absolute frequency standard provided by magneto-optical filters [77] gave them a permanent position in solar weather analysis. Through the latter half of the 20th century, the Osservatorio di Roma [78, 79, 80] developed magneto-optical designs which were used to create detailed solar magnetograms and take velocity measurements of solar wind. Magneto-optical filters are now being used in two major international collaborations, SAMNet [81] and SAMM [82], to study solar weather in an effort to protect Earth's infrastructure from solar storms [83].

Meanwhile, across the pond in mid-century America, there was great interest in mercury [84, 85, 86, 87] as a possible metrological standard for length [88, 89]. In 1960, the *11th General Conference on Weights and Measures* decided that the orange 606 nm transition in ^{86}Kr would define the metre [90, 91, 92, 93]. However, The National Bureau of Standards in Washington D.C. turned their attention to the ultraviolet 254 nm transition in ^{198}Hg. In a series of experiments, a linewidth 2.5 times narrower than the Krypton transition was realised using a 'Zeeman filter' [94, 95, 96]. The Zeeman filter was used as a second atomic medium which would extinguish transmission from a prior atomic medium thus narrowing it and refining its profile. Unlike Öhman's filter which rejected all light outside a transmission region, the Zeeman filter allowed light outside the vicinity of the resonance to transmit completely. In true cold war fashion, the first paper dedicated to the details of the Zeeman filter [97] was published in 1965, the same year a cadmium 'Filtration' device [98] was announced in St. Petersburg. This cadmium device was based on similar sodium [99] and mercury [100] filtration setups used to realise fast amplitude modulation of light. In fact, all three of these devices were not

dissimilar to that built by Hanle back in Europe [101] who is perhaps responsible for the earliest bandpass magneto-optical filter in 1933.

As the decade closed, the proliferation of lasers [102, 103, 104, 105, 106] brought significant changes to atomic physics labs. Nevertheless, magneto-optical filters remained at the forefront. In 1969, the first Faraday filter for laser frequency stabilisation was built at IBM [107] transmitting away from the resonance on either side (the 'wings'). This technique was improved in the late 1970s at the University of Kyoto [108, 109] which also achieved transmission at line centre. The 'Faraday laser' [110, 111, 112, 113, 114, 115, 116, 117, 118, 119] as it has come to be known competes directly with cavity lens devices [120, 121, 122] amongst other techniques. Typically, cavity lenses have bandwidths 100 times narrower than magneto-optical filters though optical pumping [123] and Doppler cooling techniques [124] can reduce this disparity by at least an order of magnitude. Nevertheless, cavity lenses have less tunability than magneto-optical filters and are also subject to frequency drift [64]. Most recently, Peking University has incorporated Faraday lasers in atomic clock setups [125, 126, 127, 128] and Shanxi University has demonstrated frequency comb mode selection [129, 130] continuing the legacy of magneto-optical filters in metrology.

It is a testament to the value of the magneto-optical filter that it has been considered and developed independently in wildly different spectral filtering applications. It is clear that each field lacked knowledge of the other until fairly recently. The first American astronomy paper to cite the work at the Osservatorio di Roma [131] appeared unaware of the amplitude modulation and Zeeman experiments on the East Coast. In the 1990s, the Osservatorio di Roma collaborated with astronomers from several West Coast universities [132, 133, 134] and yet were unaware of filters created at the University of California [135]. Geography appeared not to be the issue. Additionally, the application-driven focus of filter research has often left investigations into the working principles far behind. As late as the 2010s, it was shown that several magneto-optical filters had been incorrectly categorised. The Faraday

anomalous dispersion optical filter (FADOF) was an inappropriate, though popular, name for many published magneto-optical filters where anomalous dispersion accounted for very little of their performance [21]. Vastly improved performance on filter setups [136, 137] almost identical to those used fifty years previously show how little was understood about the parameter dependencies. Yeh's 1980s review papers which addressed the astronomical Lyot and Šolc [138], magneto-optical [139] and other filters [140, 141] played a large role in recognising the common work in different fields and the need to dedicate more resources to building robust theoretical models. This led to a renaissance of modelling, parameter studies and experimental filters in various alkali metals including potassium [142, 143, 144], caesium [145, 146, 147, 148, 149], sodium [150, 151] and rubidium [152, 153, 154].

Filter research in the 2020s is in a strong position. Experimental work is underpinned by some excellent theory models including *ElecSus* [155, 156], *Atomic Density Matrix* [157, 158] and a *Mathematica* demonstrations project [159, 160, 161], all of which are open source software packages that can calculate and fit spectra in seconds. Many packages have graphical user interfaces (GUI) allowing those with less coding experience to access the theory needed. Development of theory is still needed for systems involving more than two-levels [162, 163, 123, 143, 164, 165, 166, 167, 168], intense light fields [169, 166, 170, 171, 172], and for transitions beyond the alkali metals [173, 174, 175]. Encouragingly, current literature demonstrates an interest in analysing these specific cases and slowly building theory alongside experiment. Nevertheless, the author believes the ease of access to theory as it stands is responsible for an explosion of new applications areas. The most exciting of these include:

- *Quantum hybrid systems* [176, 177, 178, 179]: the frequency of single photons from a quantum dot source are anchored to an absolute atomic reference via a magneto-optical filter.
- *Ghost Imaging* [180]: an imaging technique that relies upon corrleations be-

tween photons rather than viewing the light reflected from the object of interest.

- *Detecting rocket plumes* [181, 182]: The concentration of potassium can be used to detect security threats as part of an early warning system.

- *Real time visualisation of gases* [183, 184, 185]: The motion of nitric oxide (NO) gas can be viewed in real time by passing the images though a magneto-optical filter with molecular NO as the active medium.

- *Free Space Communication* [186]: including underwater [187, 188, 189, 190] and for quantum key distribution [191].

- *Cold Atom Filters* [124, 192, 193]: Very narrow line centre filters using cold atoms.[1]

- *Light Detection and Ranging (LIDAR)* [195, 196, 197, 198, 199]: A more established application dating back to the 1990s [200, 201, 202]. Laser light is emitted into the atmosphere or towards terrestial objects and reflected back to form a 3D relief map. Magneto-optical filters are vital as weak-signal detection devices permitting studies of the mesophere during solar eclipses [203] and in light polluted cities [204]. There is also interest in measuring ocean temperature profiles [205, 206].

1.2 The Aim of This Thesis

We hold to the belief that a great deal is yet to be understood about simple magneto-optical filters. We also believe that additional insight will inevitably lead to improved performance. In this thesis, we choose to study two aspects that can be readily modelled with current theory:

- a) vapour cell cascading

[1] Of interest, the same group has also proposed a solid state magneto-optical filter [194].

- b) exerting magnetic fields at oblique angles to the propagation direction of the light.

Vapour cell cascading has been performed at the Osservatorio di Roma where it was used to select for wing features far away from resonance and rejecting transmission everywhere else [77]. It was also performed at the National Bureau of Standards as a notch filter permitting transmission everywhere except for two finite regions either side of line centre [96]. A general treatise on how cascading cells improves performance has not been presented nor has any cascaded line center filter ever been published.

Most filters cited above are in the *Faraday* geometry; the magnetic field is parallel with the propagation direction of the light. A few are in the *Voigt* geometry with magnetic field perpendicular to the propagation direction [148, 182, 164]. From our understanding, only four papers have experimentally realised filters with oblique magnetic fields [148, 207, 208, 64]. Once again, no general treatise on how oblique magnetic fields affect performance has been presented. Additionally, oblique cells have never been used in cascading investigations before.

In the following chapters, we give treatises on these two subjects. Using our new knowledge, we realise filters with competitive performance that are better quantitatively using several metrics (e.g. Figure of Merit, Equivalent Noise Bandwidth and Peak Full Width Half Maximum) and whose profiles are qualitatively more suited to various applications. We also predict several high performing filters not realised in this thesis.

Beyond this thesis, we hope magneto-optical filters will continue to be investigated from a foundational point of view. We commend our verified filter designs to be tested in suitable applications. We invite others to study the predicted filters in this thesis that they may be constructed in the near future.

1.3 Overview of Thesis

We present a quick summary of the chapters in this thesis:

Chapter 2 outlines an approach to studying magneto-optical filters. The theory of light propagating through a naturally abundant Rb vapour cell is presented. We construct susceptibility lineshapes, refractive indices and eigenmodes which fully characterise the birefringent and dichroic qualities of the vapour. From this, we model various kinds of filters including wing and line centre types and discuss desirable features for different applications. We introduce quantitative and qualitative performance metrics to compare filters. To gain additional insight into the magneto-optical rotation, we introduce measurable observables including invariant polarisations and the Stokes parameters which describe polarisation evolution.

Chapter 3 investigates the effect of cascading two vapour cells on magneto-filter performance where light passes through one cell before passing through the other. We consider two independent cells of the same atomic species with each cell in either the Faraday or Voigt geometry. When parameters are optimised, the two cells perform different roles; one cell rotates the light while the other predominately absorbs. Additionally, the combination of cell geometries permits the selection of wing or line centre features with high suppression of other features in the spectrum. We theoretically characterise and realise a Faraday-Faraday wing type and Faraday-Voigt line centre type filter with one-peak profiles.

Chapter 4 investigates the effect of oblique magnetic field angles, neither parallel or perpendicular to the propagation direction of the light, on magneto-optical filter performance. In this geometry, the magneto-optical rotation is unique given that the propagation eigenmodes are non-orthogonal and frequency dependent. These properties are responsible for narrower line centre filters with better suppression of features near the peak. We theoretically characterise and realise two line centre filters approaching $\sim$ 100 MHz full width half maximum, an order of magnitude

smaller than the Doppler width. This geometry also permits the selection of line centre or wing features without the need to reconstruct the setup.

Chapter 5 uses non-Hermitian analysis to justify why the oblique geometry exhibits non-orthogonal eigenmodes. We go further and predict the existence of exceptional points of degeneracy in the oblique parameter space where the propagation eigenmodes completely coalesce and become parallel. We present line centre filters relying on exceptional points with full width half maximums of < 50 MHz. We study the parameter space and find that the filter profiles are ultra-sensitive to small deviations from optimal parameters. As a result, we were unable to realise these filters experimentally. We identify inhomogeneous fields, computational uncertainty and model assumptions as factors likely to have hindered the experiment.

Chapter 6 summarises the thesis and gives an outlook. We argue with experimental evidence that cascading vapour cells and applying oblique magnetic fields leads to better filter performance quantitatively with lower equivalent noise bandwidths and higher figures of merit. We also see qualitative improvement with the ability to select for desirable lineshape features dependent on application requirements. Exceptional points of degeneracy show promise for future improvements in performance. Such improvement hinges upon the development of more homogeneous oblique magnetic fields at $\sim$ cm scales and a thorough investigation of the oblique refractive index and eigenmode solutions.

Chapter 2

Theory of Single Cell Magneto-Optical Filters

Author completed all theoretical computations, and created all figures presented in this chapter. All text written without the use of AI. Work is related to the published article:

D. Pizzey, J. D. Briscoe, F. D. Logue, F. S. Ponciano-Ojeda, S. A. Wrathmall, and I. G. Hughes, 'Laser spectroscopy of hot atomic vapours: from 'scope to theoretical fit.', *New Journal of Physics*, **24**:125001, (2022). https://doi.org/10.1088/1367-2630/ac9cfe [3].

2.1 Background

To aid our discussions going forward, it is important that we have a solid grounding in the workings of the simplest magneto optical filter: light directed at a single cell filled with an alkali atomic vapour. Atom light interactions with alkali metals are well understood [209, 210, 211], so much so, that data has been presented that agrees with theory to 99.5% [212]. Typically, the atomic vapour is heated, a magnetic field is applied and other optical elements are added to the setup. As such, we require additional tools to help us understand the parameter space and

analyse the function of every optical component. More philosophically, we need to be able to answer: what is a *good* filter? How can we measure this quantitatively? How can we more holistically measure how well a filter meets the requirements of its intended application.

In this chapter, we give a comprehensive review of the theory and tools needed to study single cell magneto-optical filters. Using natural abundance rubidium as our atomic vapour of choice, we begin with the atomic transitions between the hyperfine ground and excited states. By considering natural and Doppler broadening, we calculate the susceptibilities due to the three electric dipole allowed transitions, $\sigma^{+/-}$ and π.

By defining the cell geometry, i.e. the angle the magnetic field makes with the k-vector of the fully polarised light beam, we calculate the two refractive indices of the birefringent vapour and their associated eigenmodes and invariant polarisations. With this, we are able to calculate our first spectrum.

We describe three formalisms to help us approach magneto-optical filter studies throughout this thesis: Jones Calculus which calculates the output electric field, projection operators which give an explicit relationship between input polarisation and induced transitions, and the Stokes parameters, which uniquely describe the polarisation state of light.

We then model the vapour cell placed between two crossed polarisers which is known as a bandpass filter. We study how the filter rejects all light far away from the transition resonances, transmitting light only in birefringent and dichroic regions where magneto-optical rotation occurs.

We introduce metrics to study filter performance quantitatively including Figure of Merit (FOM), Equivalent Noise Bandwith (ENBW) and Peak Full Width Half Maximum (FWHM). We also discuss qualitative metrics by considering case studies of filters in the literature with beneficial lineshapes for their applications.

In our outlook, we consider how we will build on the single cell case in the following

chapters by adding a second cell (cascading) and applying oblique magnetic fields. We briefly discuss modification routes that we have chosen not to take including incorporating a pump laser or laser cooling our atoms. We detail our reasons.

2.2 From Atomic Transitions to Susceptibilities

While today there exist several platforms for ultra-narrow band filtering of light, we are interested in using alkali thermal vapours, in particular Rubidium, confined in glass cells. Vapour cells are compact and resilient [213, 214, 71, 3]. Moreover, vapours can readily be modelled using programs like *ElecSus* [155, 156], *Atomic Density Matrix* [157, 158] and Antoine Weiss' *Mathematica* demonstrations program [159, 160, 161].

We consider the 780 nm D2 transition driven by a laser from $5^2S_{j=1/2} \rightarrow 5^2P_{j=3/2}$ in natural abundance Rb with 72% ^{85}Rb ($I = 5/2$) and 28% ^{87}Rb ($I = 3/2$). In addition to the Rubidium fine structure, a hyperfine structure arises due to the interaction of the nuclear spin I with the total electronic angular momentum J. In the absence of any magnetic field, a good quantum number $\hat{\mathbf{F}} = \hat{\mathbf{I}} + \hat{\mathbf{J}}$ can be constructed representing the total atomic angular momentum.

From this we can write down the selection rules. Our transition is electric dipole with the orbital angular momentum increasing by 1 ($S \rightarrow P \Leftrightarrow L = 0 \rightarrow L = 1$). The transition does not change electronic spin, S, or I. Given $\hat{\mathbf{J}} = \hat{\mathbf{L}} + \hat{\mathbf{S}}$, the $\hat{\mathbf{J}}$ and $\hat{\mathbf{F}}$ operators have analogous selection rules:

$$\begin{aligned} J' &= J - 1, J, J + 1, \\ F' &= F - 1, F, F + 1, \end{aligned} \tag{2.1}$$

with any transition of the form $0 \rightarrow 0$ forbidden. Fig. 2.1 shows energy level diagrams for ^{85}Rb and ^{87}Rb showing all allowed $F \rightarrow F'$ transitions in zero field. The plotted relative linestrengths C^2 are derived from the Clebsch-Gordon coefficients,

more information on which can be found in [3]. The transition strength for a given $F \to F'$ transition is proportional to $C^2 d^2$ where d is the reduced matrix element for the D2 transition.

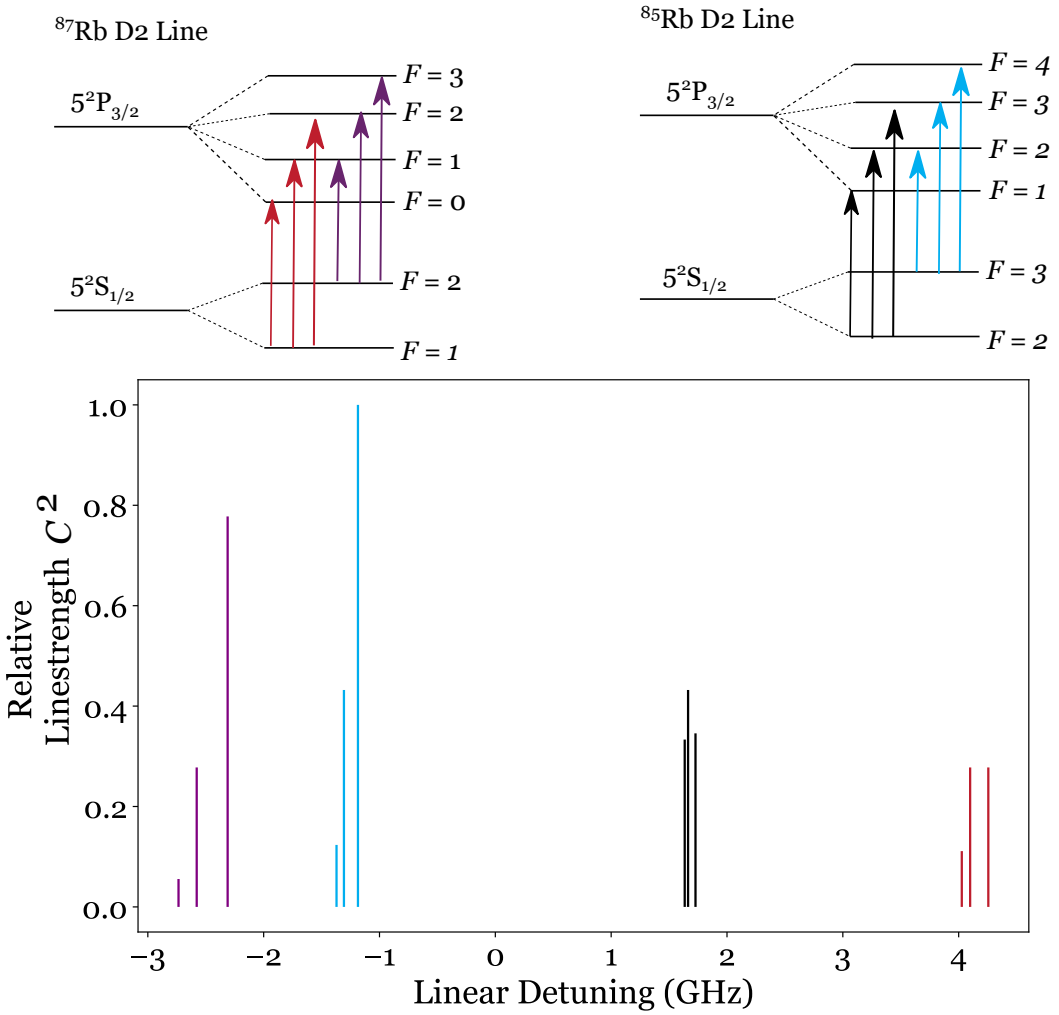

Figure 2.1: Energy level diagrams for ^{85}Rb and ^{87}Rb showing the transitions allowed by eq. 2.1 in zero field. The transition frequencies are plotted on a detuning axis where 0 GHz represents the weighted transition line centre of the two isotopes. The colour of the transition indicates the ground state F number with ^{87}Rb $F = 1 \to F'$ (purple), ^{87}Rb $F = 2 \to F'$ (red),^{85}Rb $F = 2 \to F'$ (black), ^{85}Rb $F = 3 \to F'$ (blue). The relative linestrengths C^2 are calculated from the Clebsch-Gordon coefficients.

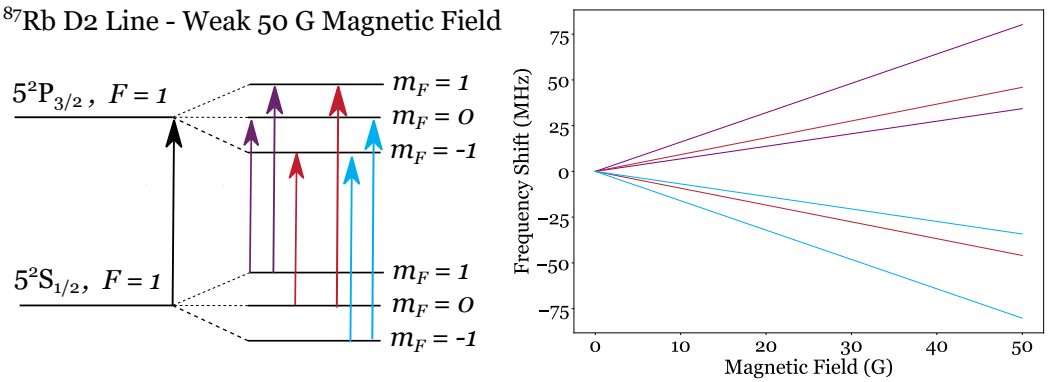

Figure 2.2: An energy level diagram for one of the hyperfine transitions (^{87}Rb $F = 1 \rightarrow F' = 1$) with a degeneracy lifted due to a weak 50 G magnetic field being applied across the vapour. The original transition resolves into 6 $m_F \rightarrow m'_F$ transitions obeying the selection rules in eq. 2.2. The plot shows the frequency shift of the 6 transitions away from the zero field 4.099 GHz transition which for sufficiently small magnetic fields changes linearly.

By exerting a weak magnetic field across the vapour, a degeneracy is lifted and transitions take place between magnetic sublevels $m_F \rightarrow m'_F$:

$$\begin{aligned} m'_I &= m_I, \\ m'_J &= m_{J-1}, m_J, m_{J+1}, \\ m'_F &= m_{F-1}, m_F, m_{F+1}, \end{aligned} \tag{2.2}$$

with $0 \rightarrow 0$ transitions once again forbidden. Fig. 2.2 shows how the ^{87}Rb $F = 1 \rightarrow F' = 1$ splits into 6 transitions which become frequency separated due to the Zeeman effect [13]. We note in weak fields up to ~ 50 G the frequency shift $\Delta\nu$ in ^{87}Rb transitions is linear with field, B:

$$h \cdot \Delta\nu = \mu_{\mathrm{B}} B (g'_F m'_F - g_F m_F), \tag{2.3}$$

where h is Planck's constant, μ_{B} is the Bohr magneton and g_F and g'_F are the gyromagnetic ratios of the F and F' states [215, 216]. On the other hand, for very large magnetic fields (~ 1 T in ^{87}Rb), the nuclear and electronic angular momenta decouple and F and m_F are no longer good quantum numbers. This is called

the hyperfine Paschen-Back regime [217, 218, 219] where transitions are labelled $|m_J, m_I\rangle \rightarrow |m'_J, m'_I\rangle$ and follow the appropriate selection rules in eq. 2.2.

In this thesis, we consider weak fields where F and m_F are good quantum numbers and fields in an intermediate regime where transitions take place between superpositions of $|m_J, m_I\rangle$ ground states and strongly decoupled excited states $|m_J, m_I\rangle$. Our largest field measured is ~ 4000 G which approaches the hyperfine Paschen-Back regime in the ground state [220]. For all magnetic field magnitudes, it is useful to classify the $m_J \rightarrow m'_J$ transitions:

$$\begin{aligned} \pi &: m_J = m'_J, \\ \sigma^{+/-} &: m_J = m'_J \pm 1. \end{aligned} \tag{2.4}$$

While the resonances are localised at the transition frequencies, they are broadened by several processes. Firstly, there is natural Lorentzian broadening due to the 26 ns lifetime of the excited state [221] before the rubidium atom spontaneously decays back to the ground state. This corresponds in frequency to a $\Gamma = 2\pi \cdot 6$ MHz broadening distributed as a function of linear detuning $\Delta/2\pi$:

$$\mathcal{L}(\Delta) = \frac{\mathrm{i}}{\frac{\Gamma}{2} - \mathrm{i}\Delta}. \tag{2.5}$$

Self broadening [222] due to atomic collisions at high temperatures and interactions with buffer gases [223] introduced to the vapour cell are responsible for additional Lorentzian broadening. These broadening mechanisms will not be considered in this thesis. Additionally, there is a Gaussian broadening mechanism. This is due to atoms experiencing a Doppler shift in the laser frequency as atoms move towards and away from the propagation direction, or k-vector, of the light. The Doppler shift is dependent on the atomic velocity v and is modelled as a Maxwell-Boltzmann distribution [155]:

$$\mathcal{D}(v) = \frac{1}{U\sqrt{\pi}}\exp\left(\frac{-v^2}{U^2}\right), \tag{2.6}$$

$$U = \sqrt{\frac{2k_{\mathrm{B}}T}{m}}, \tag{2.7}$$

with U being a function of the mass of the atom, m, the temperature T and the Boltzmann constant, k_{B}. To find the resultant lineshape, we convolve the Lorentzian and Gaussian lineshapes to arrive at a Voigt lineshape, $\mathcal{V}(\Delta)$. Fig. 2.3 shows example real and imaginary lineshapes associated with the Lorentzian and Voigt distributions. Detuning is measured from an arbitrary transition frequency.

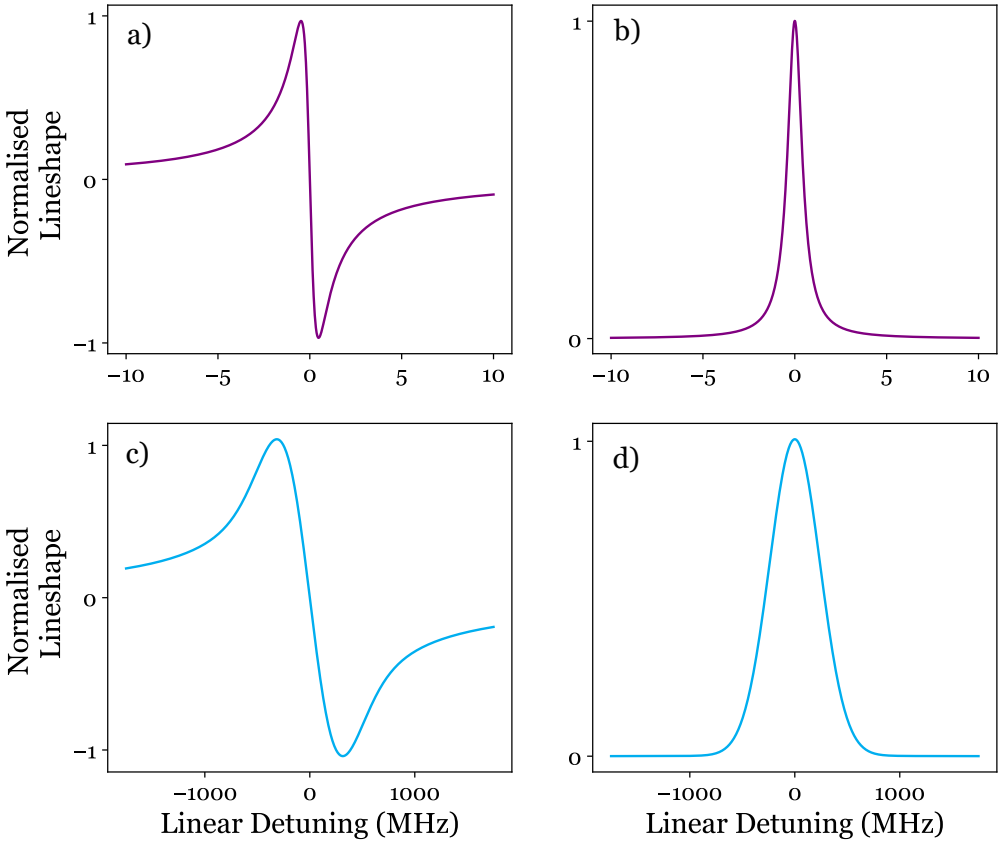

Figure 2.3: Real and imaginary lineshapes of the Lorentzian and Voigt distributions centred at a single zero field hyperfine transition. Detuning is measured with respect to the transition frequency. a) and b) show the real and imaginary parts of the 6 MHz naturally broadened Lorentzian distribution calculated using eq. 2.5. c) and d) show the real and imaginary parts of the Voigt distribution respectively, a convolution of the Lorentzian lineshapes in a) and b) with Doppler broadening due to thermal motion at 86° C. The Voigt width at half the maximum value (FWHM) is approximately 500 MHz.

Of interest, we note that the Voigt width is approximately 500 MHz, i.e. much greater than the Lorentzian width. We shall discover that the Doppler width has often been the limiting factor in creating narrow magneto-optical filters. The Voigt linewidth shows characteristic features of both lineshapes. It approximates a Gaussian close to resonance but decays slowly like a Lorentzian for far detuned frequencies [224].

We are now in a position to calculate the electric susceptibilities which describe the response of the vapour to the electric field. The susceptibility, χ_i due to transition i is:

$$\begin{aligned} \chi_i &= \frac{C_i^2 d^2 \mathcal{N}_a}{\epsilon_0 h} \cdot \mathcal{V}(\Delta), \\ \mathcal{N}_a &= \frac{F_a \mathcal{N}}{2(2I+1)}, \end{aligned} \tag{2.8}$$

where F_a is the isotopic fraction and N is the number density of atoms in the vapour state with which the light can interact. It is interesting to note that the temperature, T, of the vapour has two contributions to the susceptibility. Firstly, the Doppler width has a $\sqrt{T}$ dependence. Secondly T is proportional to the number density with higher T increasing the number of atom-light interactions. In words, the susceptibility is the transition strength ($C_i^2 d^2$) multiplied by the number of vapourised atoms in each magnetic sublevel ($\mathcal{N}_a$) modified by the Voigt lineshape, $\mathcal{V}(\Delta)$. By adding the susceptibilities from each transition together [1], we can arrive at the complex susceptibilities for the σ^+, σ^- and π transitions as shown in Fig. 2.4.

[1] *ElecSus* calculates the lineshape over a detuning range by adding together the susceptibility contributions due to each transition [155]. This has been found to give very good agreement (>99%) in experiments [212]. We have not explored whether it is possible that the susceptibility due to a particular transition is modified by its neighbouring transitions.

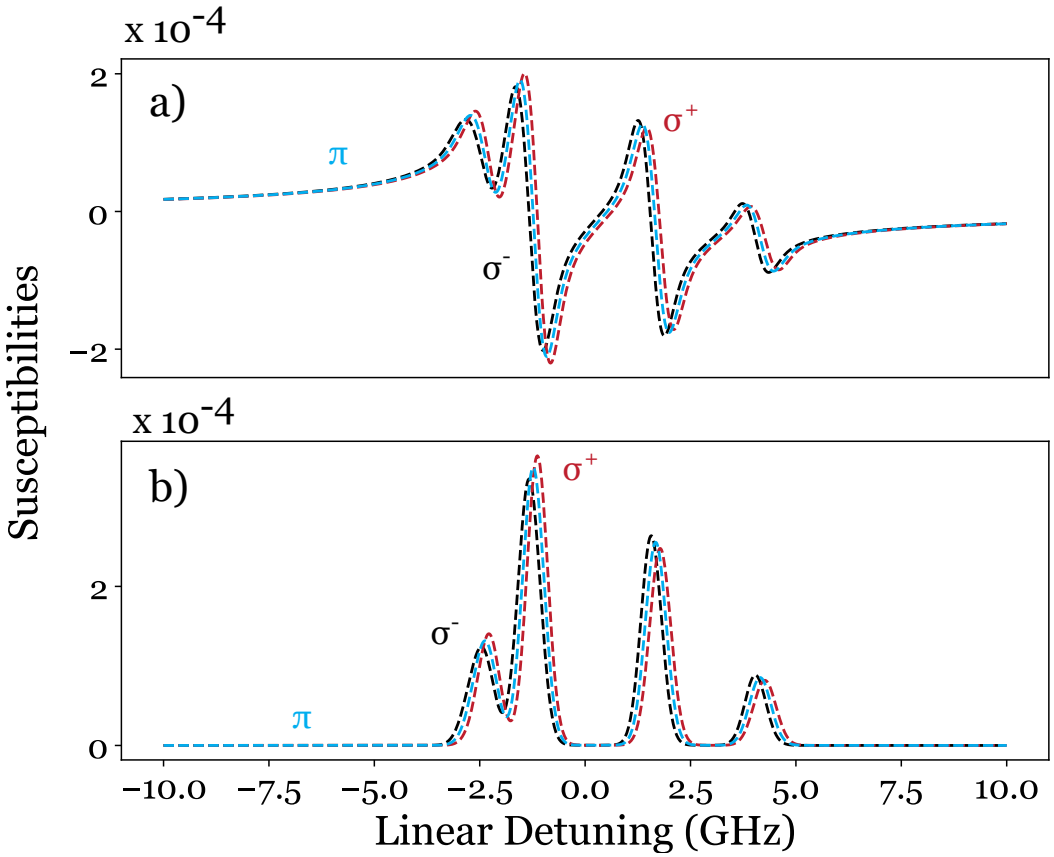

Figure 2.4: The a) real and b) imaginary parts of the susceptibility curves calculated for a temperature of 86 °C and magnetic field of 49 G. There are three curves corresponding to the susceptibilities due to each of the three electric dipole allowed transitions, π ($m_J = m'_J$) and $\sigma^{+/-}$ ($m_J = m'_J \pm 1$).

This has been a very brief overview of the theory up to this point. We encourage interested readers to refer to [225, 212, 226, 221, 155]. Susceptibility calculations follow the same process for all filters in this thesis and are completed using our model *ElecSus* [155, 156].

2.3 From Cell Geometry to Propagation Matrix

So far we have considered the impact of temperature and magnetic field magnitude on the three $\sigma^{+/-}$ and π susceptibilities. In doing so, we were careful to consider that angular momentum was always conserved e.g. when light with one unit of angular momentum is absorbed resulting in an atom moving from an S to a P state.

How are the projected angular momenta, m_J, conserved when inducing $\sigma^{+/-}$ and π transitions? Projecting the angular momenta of light is equivalent to considering its *polarisation*. For simplicity, we consider the light to be fully polarised upon entering and exiting the cell. In practice this is practically achievable in the lab by adding a high grade polariser to purify the laser light. The magnetic field direction acts as a quantisation axis for the angular momentum projections since it aligns the individual atomic magnetic dipoles. Fig. 2.5 shows electric field polarisations with angular momentum projections $m_J = -1, 0, 1$ which induce σ^-, π, σ^+ transitions respectively.

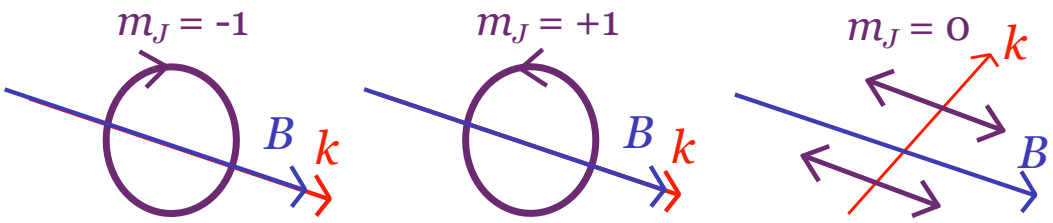

Figure 2.5: Pictorial representations of polarisations that have angular momentum projections $m_J = -1, 0, 1$ along the magnetic field (B) quantisation axis. The k-vector points in the propagation direction of the light. We can say that $m_J = \pm 1$ is anti-clockwise/clockwise or left/right hand circular. $m_J = 0$ is linearly horizontal. The k-vector is parallel with the magnetic field for $m_J = \pm 1$ and perpendicular for $m_J = 0$.

While the magnetic field is a quantisation axis for angular momentum projections, the k-vector is also a quantisation axis defining the polarisation state. As such, the angle between the k-vector and the magnetic field, θ, defines the relationship between input polarisation and vapour response. A dispersion relation can be posed with the susceptibilities χ_i and θ as arguments [207]:

$$\begin{bmatrix} (\frac{\epsilon_x}{\epsilon_0} - n^2)\cos\theta & \frac{\epsilon_{xy}}{\epsilon_0} & \frac{\epsilon_x}{\epsilon_0}\sin\theta \\ -\frac{\epsilon_{xy}}{\epsilon_0}\cos\theta & \frac{\epsilon_x}{\epsilon_0} - n^2 & -\frac{\epsilon_{xy}}{\epsilon_0}\sin\theta \\ (n^2 - \frac{\epsilon_z}{\epsilon_0})\sin\theta & 0 & \frac{\epsilon_z}{\epsilon_0}\cos\theta \end{bmatrix} \cdot \begin{bmatrix} E_x \\ E_y \\ 0 \end{bmatrix} = 0, \tag{2.9}$$

with:

$$\begin{aligned}\epsilon_x &= \frac{\epsilon_0}{2}(2+\chi_{\sigma^+}+\chi_{\sigma^-}),\\ \epsilon_{xy} &= \frac{\mathrm{i}\epsilon_0}{2}(\chi_{\sigma^-}-\chi_{\sigma^+}),\\ \epsilon_z &= \epsilon_0(1+\chi_\pi).\end{aligned} \tag{2.10}$$

For $\theta = 0$, i.e. the k-vector and magnetic field parallel, there are two refractive index solutions, n, which are plotted in Fig. 2.6:

$$\begin{aligned}n_a &= \sqrt{1+\chi_\sigma^+},\\ n_b &= \sqrt{1+\chi_\sigma^-}.\end{aligned} \tag{2.11}$$

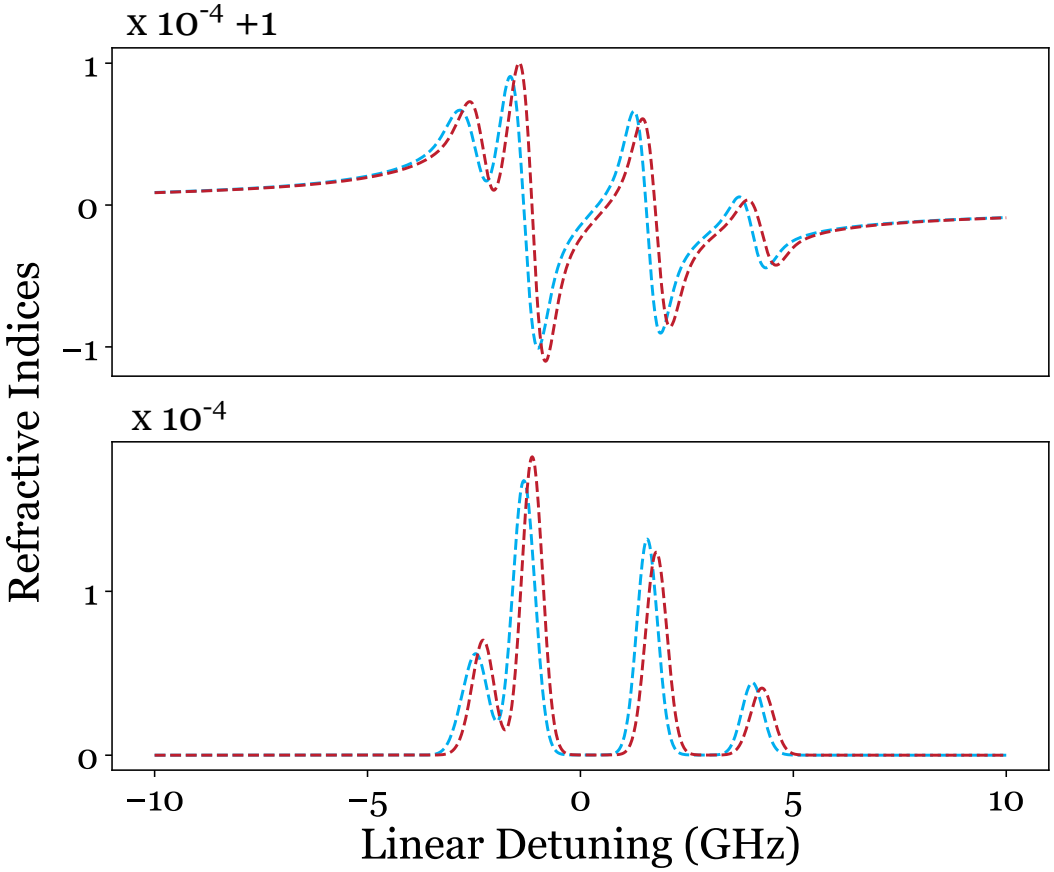

Figure 2.6: The a) real part and b) imaginary part of the refractive indices n_a and n_b for a vapour cell at 86° C and magnetic field of 49 G parallel with the k-vector (Faraday geometry). The blue and red lines are the refractive indices associated with the right hand/left hand circular propagation eigenmodes respectively.

The refractive indices n describe how two distinct polarisations of light exhibit a dispersive response (real part) and attenuating response (imaginary part) to the vapour. The fact that there are two solutions demonstrates that the vapour is in general birefringent with different input polarisations resulting in different responses. To find these two polarisations, we substitute the two refractive indices back into eq. 2.9:

$$\frac{1}{2}\begin{bmatrix} \pm(\chi_{\sigma^+} - \chi_{\sigma^-}) & -\mathrm{i}(\chi_{\sigma^+} - \chi_{\sigma^-}) & 0 \\ \mathrm{i}(\chi_{\sigma^+} - \chi_{\sigma^-}) & \pm(\chi_{\sigma^+} - \chi_{\sigma^-}) & 0 \\ 0 & 0 & 2\cdot(1+\chi_\pi) \end{bmatrix} \cdot \begin{bmatrix} E_x \\ E_y \\ 0 \end{bmatrix} = 0, \tag{2.12}$$

$$\implies \vec{a} = \begin{bmatrix} 1 \\ \mathrm{i} \end{bmatrix}, \quad \vec{b} = \begin{bmatrix} 1 \\ -\mathrm{i} \end{bmatrix}.$$

For $\theta = 0$, the two polarisations $\vec{a}$ and $\vec{b}$, called *eigenmodes*, are left hand and right hand circular light (not normalised). With this information the propagation matrix, $\mathcal{P}$ can be constructed:

$$\begin{bmatrix} a_1^* & a_2^* \\ b_1^* & b_2^* \end{bmatrix}^{-1} \begin{bmatrix} f(n_a) & 0 \\ 0 & f(n_b) \end{bmatrix} \begin{bmatrix} a_1^* & a_2^* \\ b_1^* & b_2^* \end{bmatrix}, \tag{2.13}$$

$$f(n_a) = \exp\left(\frac{2\pi \mathrm{i} n_a L}{\lambda}\right). \tag{2.14}$$

where a_i and b_i are the vectors entries of $\vec{a}$ and $\vec{b}$, * denotes the complex conjugate, L is the cell length and λ is the wavelength. In words, the input electric field is transformed into the eigenmode basis, its components are acted upon by the refractive indices over a cell length L before being transformed back into the original basis as an output electric field. Note that due to the nature of the calculation we do not need to normalise the eigenmodes and can avoid unnecessary factor terms.

Fig. 2.7 shows two possible cell geometries with different values of θ alongside pictures of their eigenmodes. If the magnetic field is parallel to the k-vector, i.e.

$\theta = 0$ we say the cell is in the *Faraday* geometry. Its eigenmodes are left and right hand circular light. Likewise, if the magnetic field is perpendicular to the k-vector, i.e. $\theta = 90°$ we say it is in the *Voigt* geometry with linearly horizontal and vertical light as eigenmodes. Oblique filters can also be created with the field at neither 0 or 90° but we delay discussion on this until Chapter 4.

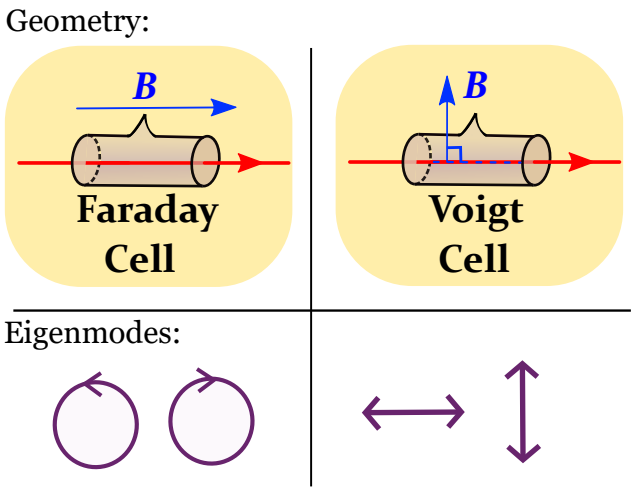

Figure 2.7: A schematic showing a Faraday and Voigt cell alongside their respective eigenmodes derived from the dispersion relation. The Faraday cell has a magnetic field exerted across it which is parallel with the k-vector of the light. Its eigenmodes are left/right hand circular light. On the other hand, a Voigt cell has a magnetic field exerted across it which is perpendicular to the k-vector of the light. Its eigenmodes are linearly horizontal and vertical light.

A final polarisation concept of note are the invariant polarisations, $\vec{p}$ and $\vec{q}$ which are orthogonal to the eigenmodes $\vec{a}$ and $\vec{b}$ respectively:

$$\vec{p} = c_1 \begin{pmatrix} -a_2 \\ a_1 \end{pmatrix}^*, \quad \vec{q} = c_2 \begin{pmatrix} -b_2 \\ b_1 \end{pmatrix}^*, \tag{2.15}$$

$$\vec{a} = \begin{pmatrix} a_1 \\ a_2 \end{pmatrix}, \quad \vec{b} = \begin{pmatrix} b_1 \\ b_2 \end{pmatrix}, \tag{2.16}$$

where c_1 and c_2 are suitable normalisation factors. Since each polarisation is orthogonal to one eigenmode, they are only acted upon by a function, f, of one refractive index in the propagation matrix. This means that while they may be

attenuated in the vapour, their polarisation state will not change. We will explore this further in 2.6. In the Faraday case, the invariant polarisations are also left and right hand circular light since the eigenmodes are mutually orthogonal. However the eigenmodes and invariant polarisations are distinct in general (See 2.8). The eigenmodes form a calculation basis for electric field propagation in the vapour, while the invariant polarisations form a polarisation transformation basis for understanding how polarisations evolve through the vapour.

2.4 First Filter Spectra

Having constructed the propagation matrix, $\mathcal{P}$, we are now in a position to calculate our first filter spectra. The simplest such filter is a single cell notch filter depicted in Fig. 2.8. Fully polarised linear light passes through the cell and the intensity across a given detuning range where the refractive indices differ from one is detected. For our parameters the notch filter extinguishes the light entirely in three regions while transmitting partially or fully elsewhere. For reference, the zero transmission regions are on the order of $\sim$ 1 GHz wide corresponding to $\sim$ 0.002 nm. As such, our notch filter has highly selective attenuating regions when compared with commercially available solid state notch filters (typically 10s nm).

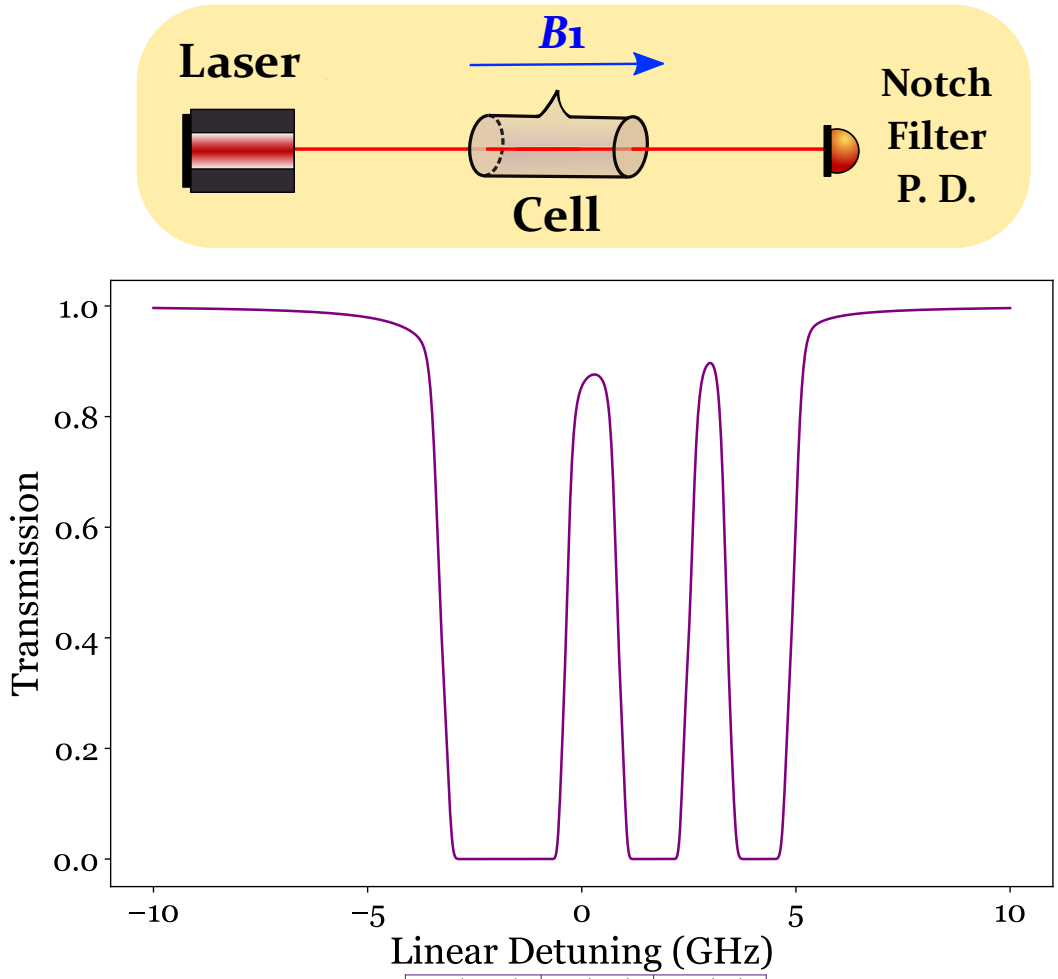

L (mm)	T(°C)	B (G)
75	85.6	48.9

Figure 2.8: Schematic and theory curve for a notch filter setup. Fully polarised linear laser light passes through a 75 mm Rb vapour cell with magnetic field, B_1, parallel to the light k-vector. The output light is detected by a photodetector (P.D). The detected light intensity (Transmission) across a 20 GHz detuning range is shown with 0 GHz corresponding to the weighted line centre of the two Rb isotopes' D2 transitions. We note three major absorption regions. From left to the right, the first absorption region is due to ^{87}Rb $F = 2 \rightarrow F'$ and ^{85}Rb $F = 3 \rightarrow F'$ transitions. The second is due to ^{85}Rb $F = 2 \rightarrow F'$ and the third is due to ^{87}Rb $F = 1 \rightarrow F'$.

Using the same cell, one can create a bandpass filter which unlike the notch filter rejects all light far away from transition resonances which we depict in Fig. 2.9. To do this, we make use of polarisers. A perfect polariser transmits one linear polarisation while rejecting the orthogonal linear state. For instance, a polariser

can be rotated to transmit linearly horizontal light while rejecting vertically linear light. In practice, polarisers are not perfect and also erroneously transmit partially for the orthogonal polarisation. As such, in an experiment we would use Glan-Taylor polarisers for their high extinction ratio of 100,000:1 [227], i.e. the polariser only erroneously transmits other polarisations with a power 100,000 less than that of the correct polarisation.

In the bandpass filter setup, we *cross* the two polarisers. That is to say the first polariser is rotated to transmit one linear polarisation state and the other is rotated accordingly to transmit an orthogonal linear polarisation. For example, one polariser could transmit linearly horizontal light and the other linearly vertical light. In the absence of the cell, there is no transmission since the light transmitted by the first polariser would then be completely rejected by the second polariser since the light polarisation does not change upon propagation. However, by adding the cell between the crossed polarisers, it is possible for the polarisation of light to be transformed in the region of the transition resonances. In fact, we see multiple transmission features corresponding to light whose polarisation has been transformed from the cell to be partially selected by the second polariser.

This polarisation transformation facilitated by the vapour is called *magneto-optical rotation* and we can study this mechanism after equipping ourselves with a number of analytical tools in the next section. Once again, we can see the transmission regions are on the order of GHz or 100s MHz wide (0.0002-0.002 nm) making them much narrower than those offered by commercial solid state bandpass filters (1 - 10 nm). Many of these features can be studied easier with names. Features a) and d) are called wing features due to their long tails which decay slowly as we move further from line centre. (approximately decaying as one over the fourth power of linear detuning [228]) We call feature b), centred at ~ 270 MHz, a line centre peak.

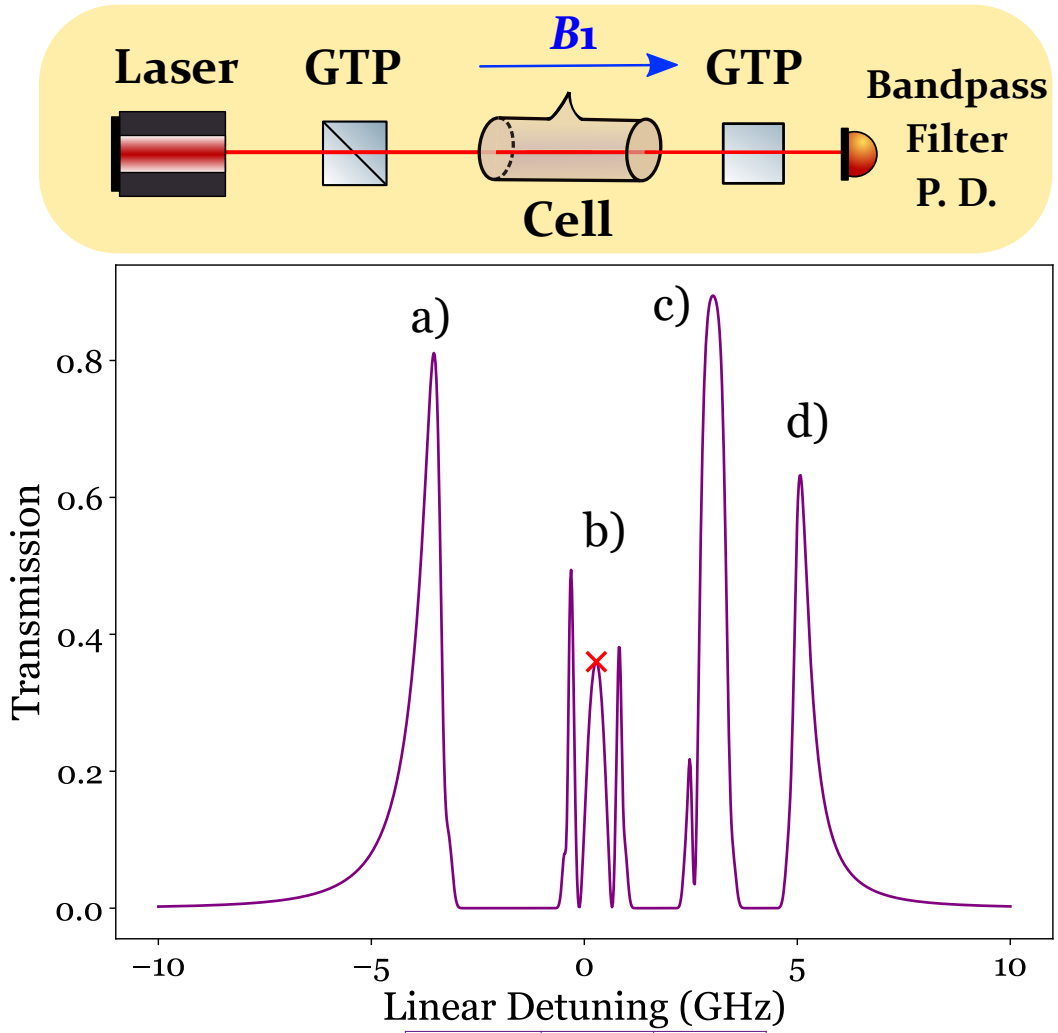

L (mm)	T(°C)	B (G)
75	85.6	48.9

Figure 2.9: Schematic and theory curve for a bandpass filter setup. Fully polarised linear laser light passes through a 75 mm Rb vapour cell with magnetic field, B_1, parallel to the light k-vector. The cell is placed between two crossed Glan-Taylor polarisers (GTP) with the second polariser selecting for polarisations orthogonal to those selected by the first. The output light is detected by a photodetector (P.D). The detected light intensity (Transmission) across a 20 GHz detuning range is shown with 0 GHz corresponding to the weighted line centre of the two Rb isotopes' D2 transitions. Features labelled a) and d) are called wing features while b) is a line centre feature. The red x marks 270 MHz where the line centre feature has peak transmission.

2.5 Formalisms

Having generated our first filter spectra, we require some additional tools to generalise the spectral calculation process and provide analysis of filter function. In this thesis, we rely on three main formalisms: Jones Calculus, Stokes Parameters and Projection Operators.

2.5.1 Jones Calculus

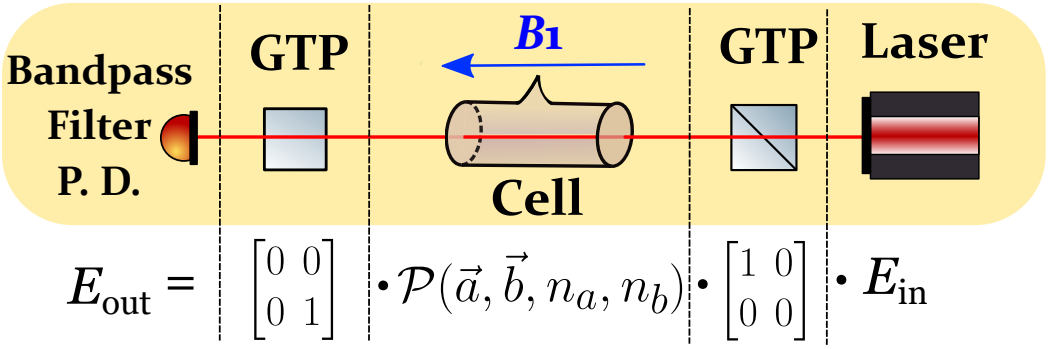

Figure 2.10: A schematic of the same bandpass filter as in Fig. 2.9. Underneath each component is its associated Jones matrix. The Glan-Taylor polarisers (GTP) are rotated such that the first and second select for linearly horizontal and vertical light respectively. The Jones matrix for the vapour cell is the *Propagation* matrix, $\mathcal{P}$, and is a function of the two eigenmodes $\vec{a}$ and $\vec{b}$ and their associated refractive indices n_a and n_b. $\mathcal{P}$ is additionally a function of cell length and the wavelength.

Defining an electric field vector:

$$E_{\text{in}} = \begin{bmatrix} E_x \\ E_y \end{bmatrix}, \tag{2.17}$$

with horizontal E_x and vertical E_y components, the output electric field E_{out} through an arbitrary filter setup composed of vapour cells and other optical components can be derived through Jones Calculus [229]. As shown in Fig. 2.10, each component in our bandpass filter has an associated 2 x 2 matrix. Pre-multiplying the electric field by a Jones matrix results in an intermediary electric field which

is the output electric field after that component. By pre-multiplying E_{in} by the matrix associated with any electric field altering component in turn, one arrives at E_{out}. Jones matrices for common optical components such as polarisers and waveplates are shown in the Figure A.2. The Jones matrix for a vapour cell, is the propagation matrix $\mathcal{P}$, calculated in 2.3. $\mathcal{P}$ is a function of the cell length, wavelength, eigenmodes and refractive indices. All spectra calculations, including Fig. 2.8 and 2.9 in this thesis are completed using Jones Calculus. We dedicate Appendix A to a complete discussion on the subject.

2.5.2 Stokes Parameters

The function of a filter is determined by the polarisation input, not the electric field. By calculating the output electric field, the polarisation state of the light can be extracted and uniquely defined in terms of three variables, called the Stokes parameters:

$$S_1 = \frac{(I_{\leftrightarrow} - I_{\updownarrow})}{N}, \quad S_2 = \frac{(I_{\swarrow} - I_{\nwarrow})}{N}, \quad S_3 = \frac{(I_{\circlearrowright} - I_{\circlearrowleft})}{N}, \tag{2.18}$$

where the animations represent the output intensities for various polarisation states. $\leftrightarrow$ and $\updownarrow$ represent linearly horizontal and vertical light respectively $\swarrow$ and $\nwarrow$ represent linearly diagonal light at $+45°$ and $-45°$ respectively, and $\circlearrowright$ and $\circlearrowleft$ represent circular right and left handed light respectively. N is a normalisation factor. $\tilde{S}_i$ denotes the Stokes parameters normalised by the output intensity, $N = I_{\text{out}}$ which gives information about polarisation state but not loss. $\tilde{S}'_i$ denotes the Stokes parameters normalised by the input intensity $N = I_{\text{in}}$ which gives information about polarisation state and loss. Note since we assume fully polarised input and output beams neither set of Stokes parameters measures decoherence or dephasing. We also denote a zeroth Stokes parameter as:

$$S'_0 = \frac{I_{\text{out}}}{I_{\text{in}}}, \tag{2.19}$$

which is the total normalised intensity detected. When plotting spectra, we may label some y-axes, 'Transmission' to denote the output from a filter and 'S_0'' to denote the output from a vapour cell as a component in a wider filter setup. However, note, for example, Fig. 2.8 is both a 'Transmission' and a 'S_0'' profile.

The Stokes parameters can give us insight into filter performance. Fig. 2.11 shows how $\tilde{S}_i$ plotted as a function of distance through the cell can depict the polarisation evolution of one frequency of light as it passes through vapour. In this case we choose a frequency of 270 MHz i.e. the detuning marked with a red x in Fig. 2.9.

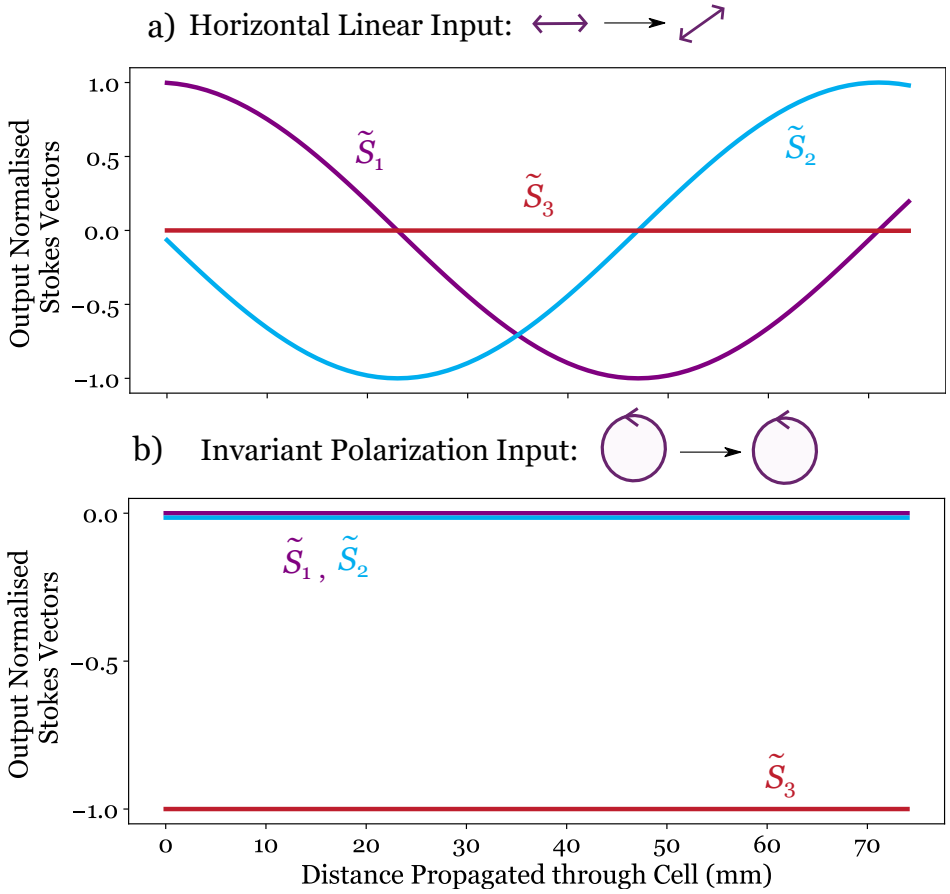

Figure 2.11: Plots of $\tilde{S}_i$ as a function of length propagated through the cell for the bandpass filter in Fig. 2.9. The frequency of light is 270 MHz indicated by a red x in the original figure. Panel a) and b) respectively show the case where linearly horizontal and left hand circular light are input. Left hand circular light is an invariant polarisation in the Faraday geometry. Pictorial representations of the polarisations at 0 and 75 mm are shown. Note in panel a), the output polarisation is not quite diagonal.

Panel b) shows one of the invariant polarisations of the bandpass filter in Fig. 2.9, left hand circular light. $\tilde{S}_1$ and $\tilde{S}_2$ are zero since left hand circular light can be broken into an equal combination of linearly horizontal and vertical light (similarly for linearly diagonal light). $\tilde{S}_3 = -1$ since there is no right hand circular component. The values of $\tilde{S}_i$ do not change as the light passes through the cell proving the polarisation is invariant. On the other hand, panel a) shows that linearly horizontal light evolves to become neither horizontal or vertical. In this case, $\tilde{S}_3 = 0$ initially since horizontal and diagonal light can be broken into an equal combination of left and right handed circular light. Additionally $\tilde{S}_3$ remaining zero throughout tells us that the polarisation transformation always remains linear i.e. the Faraday effect. In fact, the $\tilde{S}_1$ and $\tilde{S}_2$ curves show that the horizontal light rotates its plane of polarisation to become diagonal light.

For the same bandpass filter we can also plot S_i' against linear detuning for all frequencies of interest which describes the frequency dependence of the polarisation evolution.

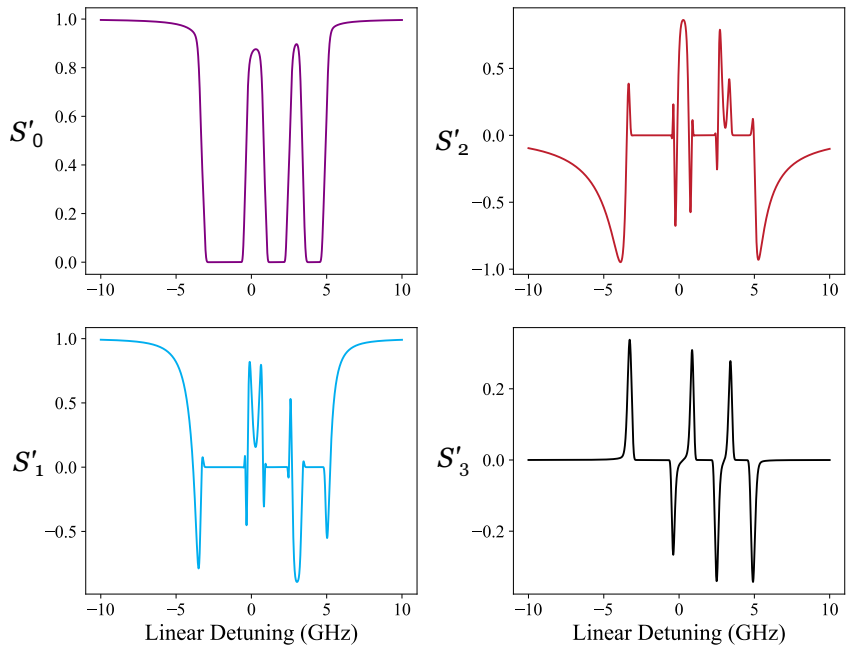

Figure 2.12: S_i' plotted against linear detuning for the vapour cell in the bandpass filter in Fig. 2.9. We note that S_0' by definition is the intensity recorded after the vapour cell and as such shares the same profile with the notch filter in Fig. 2.8.

S_0' returns the same spectrum as the transmission of the notch filter in Fig. 2.8. S_0' is the total normalised intensity recorded after the vapour cell which is by definition a notch filter transmission. From S_1' and S_2' we can make out the (sometimes inverted) bandpass filter features including the wings and centre line. The filter features are those with S_1' and S_2' values which are selected by the second polariser. The S_3' shows light output at frequencies with small handed components, typically either side of the larger transmitted filter features.

Stokes parameters will be the main analysis tool used in later chapters.

2.5.3 Projection Operators

A final analytical tool can be found in the projection operators. The projection operators give an *explicit* relationship between input polarisations and dipole transitions induced and are determined by the cell geometry. A state orthogonal to a projection operator for transitions X_i will not induce transitions X_i. For example, for a plane wave in the Faraday cell, left/right hand circular light are the projection operators for the $\sigma^{+/-}$ transitions while π transitions cannot be induced.

We can plot S_0' against linear detuning for the projection operators as input polarisations. By doing so, we can show the effect different transitions have on the spectrum as well as the detuning spread of the transition frequencies. In Fig. 4.5, we note the S_0' curves corresponding to $\sigma^{+/-}$ transitions are positively/negatively detuned slightly. This is expected since the bandpass filter has a small magnetic field of ~ 50 G leading to a small Zeeman effect. We dedicate Appendix C to a complete discussion on projection operators.

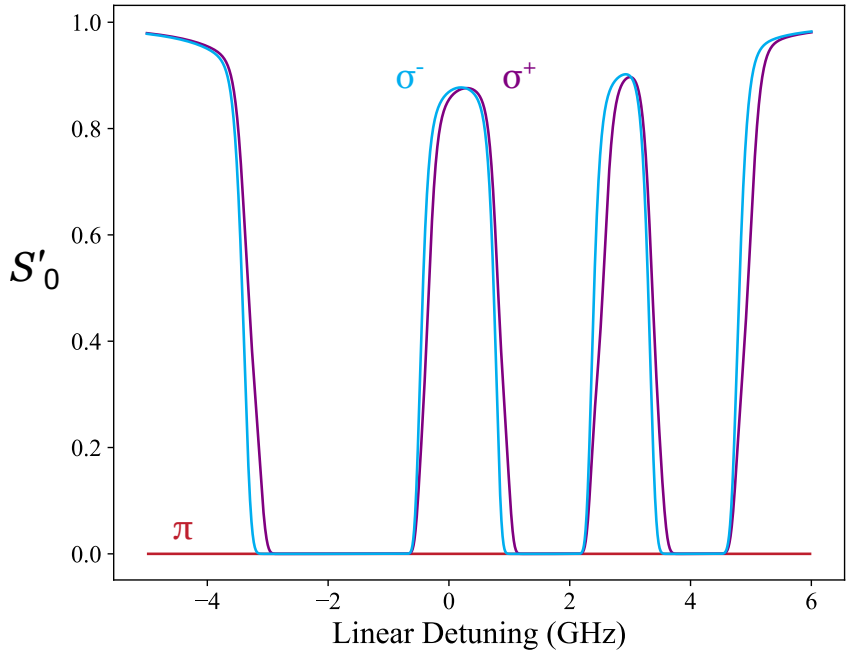

Figure 2.13: S'_0 outputs when projection operators are input polarisations to the vapour cell in Fig. 2.8 and 2.9. These include σ^+ : left hand circular (purple) and σ^- : right hand circular (blue). For a plane wave in the Faraday geometry, the π projection operator (red) is the zero vector.

2.6 Magneto-Optical Rotation

We now have all the necessary tools to explain the magneto-optical rotation of the vapour which accounts for the performance of the bandpass filter. As discussed in 2.3, the invariant polarisations form a good basis to study magneto-optical rotation. In Fig. 2.14, we plot the four features of the bandpass filter from Fig. 2.9 in purple for linear light input. The red and yellow S'_0 profiles are plotted for the two invariant polarisations, left and right hand circular light, respectively. Their overlap is shown in orange.

We can identify two regions: the *birefringent region* where there is some transmission of both of the invariant polarisations and the *dichroic region* where there is transmission of mainly one invariant polarisation. Note that the birefringent regions are not strictly contained within the orange overlaps as there is non-zero transmission of both invariant polarisations outside of these overlaps. If linear light

is input at a frequency in the dichroic region, there will be no transmission due to one of the invariant polarisations i.e. the polarisation after passing through the vapour can be described as:

$$E_{\text{out}} = (E_{\text{in}} \cdot \vec{p}) \cdot \vec{p} \mathrm{e}^{f(n_a)}, \tag{2.20}$$

with f defined in 2.3 and $\vec{p}$, an invariant polarisation. E_{in} will be refracted and attenuated. However, the refraction only changes the speed of propagation having no noticeable effect on the output polarisation state. This leaves only the attenuating effects. The component of E_{in} along the invariant polarisation $\vec{p}$ will continue to be attenuated as it moves through the vapour. Since the invariant polarisation is circular light, after sufficient vapour, the circular handed component of E_{in} will be attenuated such that the resulting output polarisation will be the opposite circular hand. This is the case since linear light can be broken into equal parts left and right circular light. This polarisation transformation results in transmission by the second crossed polariser.

We can see this effect at play in the S_3' plot in Fig. 2.12 where either side of the main features, the output light is handed. In Fig. 2.14, we note small features not exceeding 50% in the dichroic regions due to the attenuation required to transform the polarisation.

However, in the birefringent region, we can write the output electric field as:

$$E_{\text{out}} = (E_{\text{in}} \cdot \vec{p}) \cdot \vec{p} \mathrm{e}^{f(n_a)} + (E_{\text{in}} \cdot \vec{q}) \cdot \vec{q} \mathrm{e}^{f(n_b)}. \tag{2.21}$$

In this case, we have refraction and attenuation due to both invariant polarisations. This time given that in general both polarisations will be refracted by different values, differential refraction takes place which has a noticeable effect on polarisation. A local phase arising between the two components can result in polarisation transformation without relying on attenuation. We can see the highly transmitted features a), c) and d) reside mostly in the birefringent region.

We note that the wing features appear to slowly decay in transmission while still remaining in the birefringent region. The reason for this is that the two refractive indices far away from resonance are slowly tending towards the same value of 1. This means that differential refraction effects tend to become negligible. Nevertheless the slow decays are a result of the refractive index lineshapes approaching 1 relatively slowly despite being far detuned from the transition frequencies.

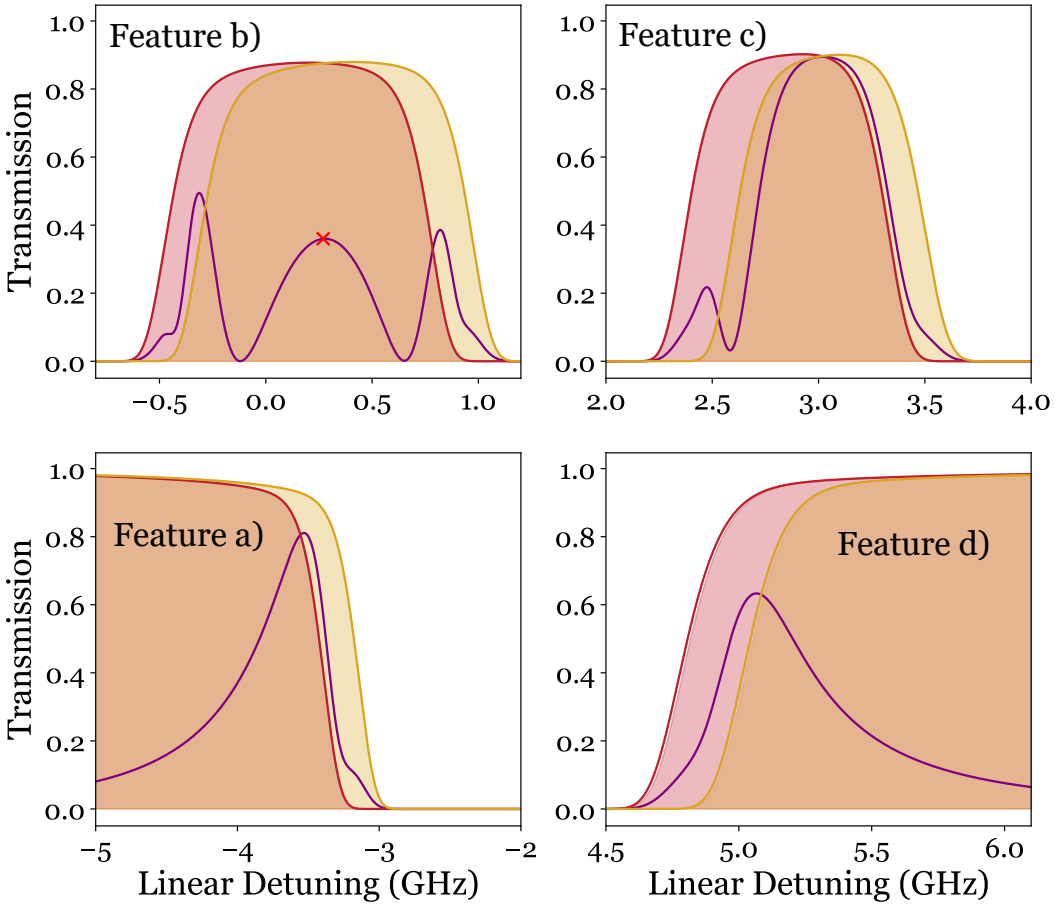

Figure 2.14: The four features of the bandpass filter in Fig. 2.9 plotted in purple. The S_0' outputs are shown in red and yellow corresponding to input polarisations of left hand and right hand circular light respectively. These are the invariant polarisations. Their overlap is shown in orange. Note that the birefringent regions are not entirely contained in the orange overlaps as there exists transmission of both invariant polarisations outside of these overlaps. The regions beyond birefringence are called the *dichroic regions*.

We can use the projection operators to explain the magneto-optical rotation in terms of the underlying transitions. In the Faraday case, it happens that the pro-

jection operators for the $\sigma^{+/-}$ transitions are the same polarisation states as the invariant polarisations, i.e. left/right hand circular light. Therefore, our filter operates in dichroic regions as a σ^+ or σ^- driven attenuator. In the birefringent regions, differential refraction between σ^+ and σ^- transitions results in high transmission polarisation transformation.

2.7 Filter Performance Metrics

Having understood the basics of filter performance, we still do not have a notion of what makes a good filter. Comparing the notch filter in Fig. 2.8 to the bandpass filter in Fig. 2.9, we might intuitively favour the performance of the bandpass filter for its ability to reject all light away from the resonances. Having said this, filter performance will be highly application specific and notch filters have been used in single molecule detection in DNA [230]. In this section, we introduce some quantitative and qualitative metrics we will use to determine filter performance going forwards.

We are interested in bandpass filters. In an ideal world, a bandpass filter could transmit one frequency at 100% transmission and reject all other frequencies. Of course, for many reasons this is impossible but we can build quantitative metrics which score filters relative to this ideal case. The Equivalent Noise Bandwidth (ENBW) is defined as:

$$\text{ENBW} = \int \frac{\mathcal{T}(\nu)\mathrm{d}\nu}{\mathcal{T}(\nu_\mathrm{s})}, \tag{2.22}$$

where $\mathcal{T}(\nu)$ is the transmission at frequency, ν, and ν_s is the signal frequency, generally chosen to be the frequency with maximum transmission. In words, the ENBW is the area subtended between the transmission curve and the horizontal axis. We seek to minimise ENBW everywhere except at ν_s. However, a computer struggles to optimise with this metric given that a flatline filter with no transmission

has an ENBW of 0. Therefore, we want to consider a metric that gives equal parity to minimising ENBW as it does to maximising the transmission at ν_s. We call this metric, the Figure of Merit (FOM) [228],

$$\mathrm{FOM} = \frac{\mathcal{T}(\nu_\mathrm{s})}{\mathrm{ENBW}}, \tag{2.23}$$

which we seek to maximise. For our bandpass filter, the ENBW and FOM are 2540 MHz and 0.38 GHz^{-1} respectively. On the other hand, our notch filter has an infinite ENBW as transmission continues as we detune away from the resonances leading to a FOM of 0. Another useful metric is the Full Width Half Maximum (FWHM) of the filter peak of interest:

$$\mathrm{FWHM} = \nu_R - \nu_L, \tag{2.24}$$

where ν_R and ν_L are two frequencies positively and negatively detuned from the signal frequency ν_s, where maximum transmission occurs. ν_R and ν_L are transmitted at half the intensity of ν_s,

$$\begin{gathered}\mathcal{T}(\nu_L) = \mathcal{T}(\nu_R) = 0.5 \cdot \mathcal{T}(\nu_s), \\ \nu_L < \nu_s < \nu_R.\end{gathered} \tag{2.25}$$

The FWHM is a useful metric if there is one dominant peak in the transmission spectrum with other features having low transmission. It can also be used with care to consider the FWHM of spectra with multiple peaks. In general we seek to minimise FWHM to have narrow peaks.

However, beyond quantitative metrics, the application determines the qualitative features that are beneficial. Fig. 2.15 shows four published filter profiles generated from single cell bandpass filters. The spectra and their quantitative metrics vary considerably and yet each filter is well designed for its application.

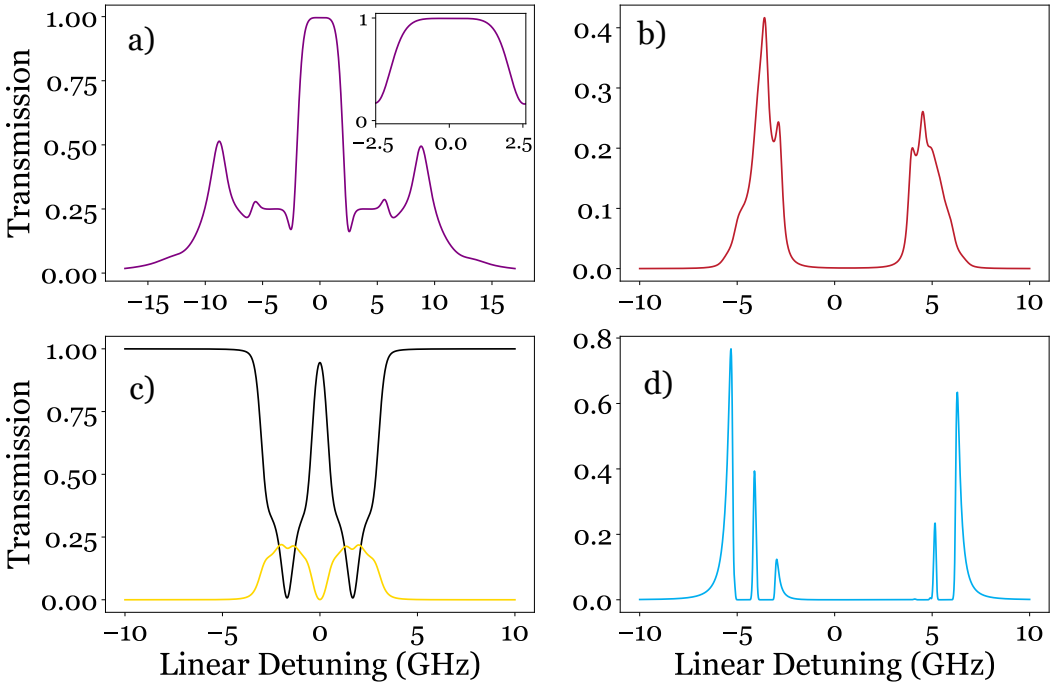

Filter	Element & D-line	Cell Length	T (°C)	B (G)	ENBW (MHz)	FOM (GHz^{-1})
a) [198]	Na-D2	20	182	3000	9560	0.10
b) [118]	Cs-D2	30	30	330	2510	0.16
c) [182]	K-D1	71.8	81	1200	4780	0.05
d) [137]	Cs-D1	75	68	45.3	960	0.80

Figure 2.15: Theoretical filter profiles from various published papers with their parameters alongside ENBW and FOM in table. a), b) and d) are Faraday filters with the magnetic field parallel with the k-vector. c) represents a Voigt filter with magnetic field perpendicular to the k-vector. Linear light at +45° to the horizontal is input to the cell in c) while any linear polarisation can be input into a), b) and d). The yellow and black curves represent the output light polarised linearly at −45° and +45° to the horizontal respectively.

Filter a) [198] is used in the sodium LIDAR apparatus at the Wuhan Institute of Physics and Mathematics to take long term measurements of the mesosphere. For this, they require a broadband laser with bandwidth 1.2 GHz. Given that the spectrum can change greatly over the interval of a GHz and their laser experiences frequency drifts, they require a profile with flat transmission for several GHz. The inset shows the transmission remains high and uniform for > 3 GHz.

Filter b) [118] from Peking University is double peaked with one peak corresponding to transitions from the ^{85}Rb $F = 4$ ground state and the other from $F = 3$.

This was designed in response to a new sub-Doppler spectroscopy scheme for laser frequency stabilisation [231]. A dual frequency laser centred on two Cs hyperfine transitions can result in inverted sub-Doppler features with much larger transmission dips than the conventional scheme offering improved stabilisation. For more information on sub-Doppler spectroscopy, see Appendix D.

Filter c) [182] is a Voigt filter with magnetic field perpendicular to the k-vector. Linear light at 45° is input and the system outputs both the bandpass filter light linearly polarised at $-45°$ (yellow) and the light that is rejected by the bandpass (black) linearly polarised at 45°. Here the aim of capturing both signals is to construct a calibration scheme to account for imperfect polarisers. With this, North Carolina State University hopes to improve imaging of rocket plumes.

Filter d) [137], found in the lab in Durham, is the largest FOM single cell filter in the Faraday geometry owing to its very narrow peaks. In this thesis, we will judge our filter designs by both quantitative and qualitative metrics.

2.8 A Word of Warning

In this introductory chapter, we have introduced several concepts that for the bandpass filter plotted in Fig. 2.9 *appear* to be related or equivalent. These include polarisation concepts such as the eigenmodes, invariant polarisations and projection operators. These also include atom-light concepts such as the susceptibilities and refractive indices. These are all in general distinct concepts. Applying these concepts in their correct context will be essential in analysing filters considered in later chapters. We provide a concise summary:

- The *eigenmodes* are the two vector solutions of the dispersion relation and are essential for constructing the propagation matrix, $\mathcal{P}$ for Jones Calculus computations. (See 2.3, 2.5.1 and Appendix A).

- The *invariant polarisations* are the two polarisations for which $\tilde{S}_i$ remains constant upon propagation. In short, while an invariant polarisation might be attenuated upon propagation, the polarisation state does not change. See 2.3.

- A state orthogonal to a *projection operator* for transitions X_i will not induce transitions X_i. (See 4.5 and Appendix C).

- An electric *susceptibility* is associated with either the σ^+, σ^- or π transitions. Their real and imaginary parts describe the dispersive and attenuating properties respectively of the vapour due to the associated transition. The electric susceptibilities are *independent* of cell geometry (See 2.2).

- A *refractive index* is associated with an eigenmode and is also essential for constructing the propagation matrix $\mathcal{P}$. Their real and imaginary parts describe how the eigenmode as an input polarisation is refracted and attenuated respectively. The refractive indices are *dependent* on cell geometry (See 2.3, 2.5.1 and Appendix A).

2.9 Outlook

In this chapter, we have introduced the theory and tools needs to study single cell filters. We generated atomic spectra in two parts. Firstly, we calculated the electric susceptibilities from the Zeeman shifted atomic transitions and line strengths and accounted for natural and Doppler broadening. In the second part, we calculated the refractive indices, eigenmodes and invariant polarisations which relied on the cell geometry. This thesis has a specific focus on cell geometry and we will frequently refer back to this part of the calculation. From this, we created a notch filter that relied on attenuation and a bandpass filter which relied predominantly on magneto-optical rotation. We introduced three formalisms that gave us the calculation and analytical tools needed to study filters. In particular, the

Stokes parameters will form the basis of much of our filter analysis. We studied the transmission profile of the bandpass filter noting the birefringent and dichroic regions where the polarisation was transformed to be selected by the second polariser. Finally, we measured important metrics like FOM, FWHM and ENBW which allowed us to compare the bandpass filter profile with others. We made clear that filter performance is highly application specific and we studied various qualitative lineshape features.

Through the rest of this thesis, we will consider the implications of two modifications to the single cell case: adding a second vapour cell (cascading) and applying an oblique magnetic field (at an angle neither 0 or 90° to the k-vector). We note that these modifications maintain a *passive* filter design. That is to say, we do not make use of additional pumping lasers and could theoretically replace our probe laser with a broadband source. This is essential in astronomical applications where celestial light enters the filter, not laser light. These designs are the most flexible in their purpose as they can theoretically filter any light source.

Other filter designs are considered *active*. For instance, excited state transitions and multi level schemes [162, 163, 123, 143, 164, 165, 166, 167] incorporate an additional laser for optical pumping. As such, they offer new operating wavelengths for magneto-optical filters and can even generate filters with sub-natural linewidths at ~ 70 % transmission [168]. More recently, laser cooled atomic designs [124, 192, 193] have also been considered which typically incorporate additional pump, cooling and repump lasers. In doing so, these designs are able to reduce the Doppler widths to sub-natural linewidths at $< 20\%$ transmission. However, adding lasers increases the complexity of the setup considerably and may make it difficult to take outside a lab setup. Moreover, many of these designs use a frequency locked probe laser and therefore cannot be replaced by an arbitrary light source. Nevertheless, we would like to note that these are exciting directions which are not only producing great experimental results but provide much needed theoretical insight.

Our compact robust passive designs will...:

1. ...justify our thesis in Chapter 1 that huge performance improvements can be achieved via small modifications to the single cell case combined with more theoretical study.

2. ...include some of the best passive designs recorded in the literature by quantitative metrics.

3. ...include designs which are competitive with active designs with all the advantages of passive designs.

Chapter 3

A Study of Cascading Vapour Cells

Author completed all theoretical computations, collected and processed all data and created all figures presented in this chapter. Figures 3.5 and 3.6 were created using code by Jack D. Briscoe. Figures 3.10, 3.11 and 3.12 were created using code by Thomas Robertson-Browne. All text written without the use of AI. Work is related to the published article:

F. D. Logue, J. D. Briscoe, D. Pizzey, S. A. Wrathmall, and I. G. Hughes, 'Better magneto-optical filters with cascaded vapor cells.', *Optics Letters*, **47**(12):2975-2978, (2022). https://doi.org/10.1364/OL.459291 [2].

3.1 Background

In the previous chapter, we introduced single cell magneto-optical filters. Decades after their invention, these filters remain competitive devices delivering high FOM and low ENBW values alongside their compact setups [3]. The table in [137] gives predicted optimized parameters for all alkali metals in the weak probe regime [169] with best FOM and ENBW at 0.8 GHz^{-1} and 960 MHz (plotted in Fig. 2.15). These metrics act as a baseline for further improving filter performance. However,

quantitative metrics do not tell the full story. Qualitative metrics such as tailored lineshape features [198], flexibility of operation [129] and robustness to the elements [190] are desirable and often essential in various applications.

Perhaps the most intuitively simple way to modify the single cell case is to add another cell such that the light passes through each in turn in a cascade. This is the basic principle behind the work at the Osservatorio di Roma and later at the Sapienza Università where two cells, both in the Faraday geometry, are cascaded [77, 78, 79, 80, 132, 133, 134, 232]. When parameters are tuned appropriately, one or both of the filter's transmitted wing features can be selected with all other features suppressed. This setup continues to be of use in two international solar weather monitoring networks [81, 82]. Additionally, the same setup with minor modifications was realised [154] for filtering background optical noise in free space laser communications. However, none of these works explain the working principle behind these filters. Such knowledge would not only be important when exporting these ideas outside their original applications but in considering other feature-selection mechanisms.

For instance, is it possible for a line centre filter to be constructed which suppresses all features other than the central peak? While the early Zeeman filter [94, 97] selected for a central peak, it was a notch filter, and a bandpass line centre filter has yet to be constructed. Such a filter would be very useful in laser frequency stabilisation [110, 111, 112, 113, 114, 115, 116, 117, 118, 119] where laser drift could be limited to a central region around the transition frequency.

In this chapter, we present the theory behind two cascaded filters: a wing filter and the first line centre filter. We analyse the function of each filter by studying the output polarisation through each component using the Stokes parameters [233, 234, 235]. The Faraday-Faraday wing filter is composed of two cells in the Faraday geometry while the Faraday-Voigt line centre filter is composed of a cell in the Faraday geometry and a cell in the Voigt geometry. We find that for both filters, both cells address different roles: one *transforms* the polarisation to create the

feature of interest while the other *extinguishes* unwanted features. We show that the geometry of the cell, Faraday or Voigt, determines the relationship between input polarisation and transitions induced. As such, different geometries can be used to extinguish different detuning regions.

We then describe the setup for realising these two filters. We use solenoids and permanent NdFeB magnets to create the axial and transverse fields necessary which are verified using the python package *Magpylib* [236].

We present fitted data which show excellent agreement with theory. We show that by turning a waveplate, the wing filter can select for both wings or either wing. In our outlook, we show that our analysis is not an exhaustive treatment of cascading's many benefits. We present two theoretical two-cell cascaded filters engineered for applications in cavity lens stabilisation [64] and cryptography [237] respectively.

3.2 Theory

3.2.1 The Role of the Second Cell

To begin our discussion, let's assume we have fixed first cell parameters. For instance, let's consider the single cell natural abundance Rb filter plotted in Fig. 2.9. How can we use a second cell to substantially improve performance? By inspecting the transmission profile, we see four peaks. If the second cell had an *extinguishing* role and suppressed the transmission of undesired features, we could create a single peak filter. This would undoubtedly decrease ENBW and hence increase FOM and qualitatively would give better control over the lineshape.

To do this, we require the cell to extinguish over certain detuning regions while still transmitting highly in others. For this, we can make use of the Zeeman shift of transitions [13, 238, 217, 218, 239]. As a progressively larger magnetic field is exerted across an alkali metal, the π ($m_J = m'_J$) and $\sigma^{+/-}$ ($m_J = m'_J \pm 1$) electric dipole allowed transitions shift in frequency. For a large field, $\sigma^{+/-}$ transitions

are shifted positively/negatively from line centre. π transitions are also shifted positively and negatively from line centre but the shift is substantially less than the $\sigma^{+/-}$ transitions. This shifting can be studied using ground (Breit-Rabi) and excited state manifold diagrams [226, 221]. Note that for low fields, i.e. outside the Hyperfine Paschen-Back regime [219, 1, 220], the shift is non-linear. Therefore with a large enough field and an ability to exclusively select for certain transitions, we can extinguish specific detuning regions of interest.

Projection operators (derived in Appendix C) give an explicit relationship between polarisation input and transitions induced for a particular cell geometry. In the Faraday geometry, the projection operators are:

$$\begin{aligned} \sigma^{+} &: \frac{\hat{x} + \mathrm{i}\hat{y}}{\sqrt{2}} \\ \sigma^{-} &: \frac{\hat{x} - \mathrm{i}\hat{y}}{\sqrt{2}} \end{aligned} \tag{3.1}$$

i.e. left/right hand circular light exclusively induces σ^{+} or σ^{-} transitions respectively. Panel a) of Fig 3.1 shows how a Faraday cell can be used to create extinguishing wells whose centres are positively/negatively detuned. We note that the wells extinguish almost completely with only very small transmission regions. To realise this, we need a combined temperature and magnetic field high enough to increase the Doppler widths and increase the frequency spacing between transitions respectively. A Faraday extinguishing cell would be very useful at selecting peaks on the extremities of spectra i.e. wings.

In the Voigt geometry, the projection operators are:

$$\begin{aligned} \sigma^{+/-} &: \hat{y} \\ \pi &: \hat{x} \end{aligned} \tag{3.2}$$

i.e. horizontally linear light induces π transitions and vertically linear light induces a linear combination of $\sigma^{+/-}$ transitions. Panel b) of Fig. 3.1 shows two wells realised with a Voigt extinguishing cell. The π well has a smaller extent than the $\sigma^{+/-}$ well and we note that the $\sigma^{+/-}$ well has a small transmission region at centre. As such the $\sigma^{+/-}$ well would function as a line centre peak selector extinguishing

all features apart from the central peak. We note that for a higher magnetic field it is also possible to create the same transmission window with the π well which was shown in [4].

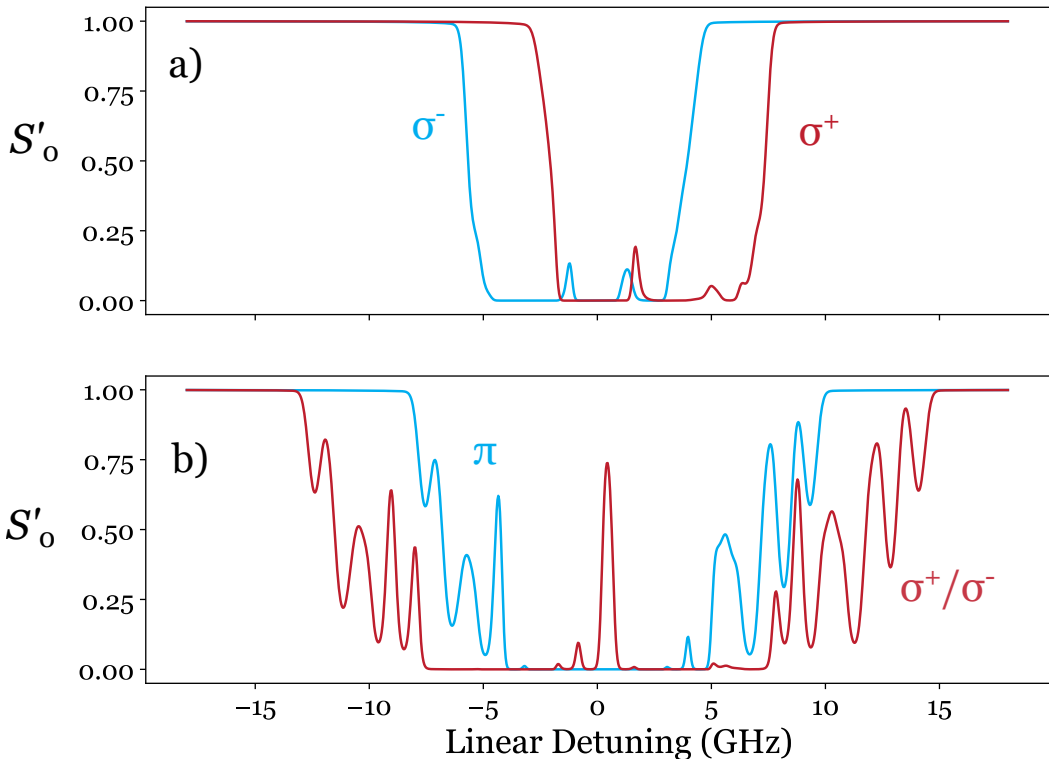

Figure 3.1: a) The theoretical S_0' outputs for a 5 mm natural abundance Rb Faraday cell with $T = 110$ °C and $B = 747$ G. By inputting the Faraday projection operators for $\sigma^{+/-}$ transitions (i.e. left/right hand circular light), the extinguishing well is positively/negatively detuned. b) The theoretical S_0' outputs for a 5 mm natural abundance Rb Voigt cell with $T = 121$ °C and $B = 2528$ G. Similarly, by inputting the Voigt projection operators for $\sigma^{+/-}$ and π transitions (i.e. vertically and horizontally linear light.), the extinguishing well has a larger/smaller frequency extent. In particular, the extent of the $\sigma^{+/-}$ well is so large that a transmission region is created at centre where the Doppler widths of the σ^+ and σ^- transitions no longer overlap.

Our approach so far has assumed a separation of cell roles. One cell *transforms* the polarisation state of the light to create filter transmission regions and the other *extinguishes* the unwanted regions. Such an approach is beneficial since it makes it easier to understand the function of each cell. It turns out that this is *not* a naïve approach. Computer optimisations show that FOM can be maximised when we assume separation of roles. A.3.3 and A.4.2 give justification for this fact.

3.2.2 Stokes Parameter Description

Having understood the two cells' roles, we are in a position to start designing filters. As discussed, polarisation plays a large role in filter operation. The polarisation transformation from cell(s) between crossed polarisers determines the output after passing the second polariser. Likewise the lineshapes of our wells in Fig. 3.1 are also polarisation dependent. To fully understand the working principles of our filters, we need to make use of the Stokes parameters defined in 2.5.2.

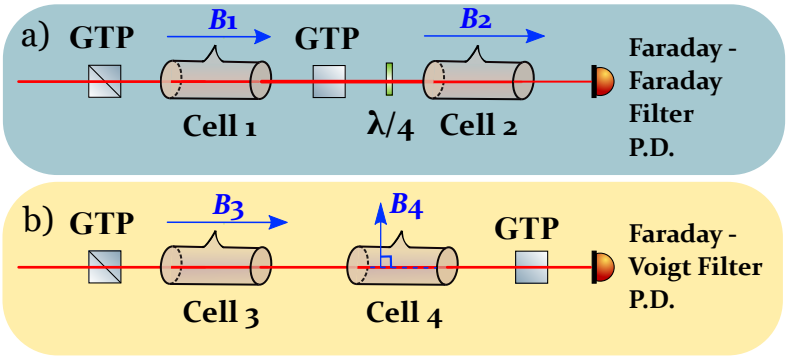

Figure 3.2: Two proposed filter designs. GTP - Glan Taylor Polariser. More details can be found in Fig. 3.7.

Our first design, shown in Fig. 3.2 a), is a Faraday-Faraday wing filter composed of two Faraday cells. It is based on the wing filter design in [154] and is similar to the wing filters realised at the Osservatorio di Roma. Fig. 3.3 plots S_i' at each stage of the filter. When horizontal light is input to the first cell, certain regions are transformed in polarisation resulting in bandpass filter peaks after the crossed polariser. This light is then transmitted through a quarter waveplate set at 45° to convert the linear vertical light to left hand circular light. In doing so, the light is in the correct polarisation state to be extinguished at centre and at positive detunings. The light at far negative detunings is transmitted through and we select for one wing. We note that rotating the waveplate axis allows us to select for the other wing or both wings which we show in 3.4.1.1.

The second design b) is a Faraday-Voigt line centre filter composed of a Faraday cell

followed by a Voigt cell. To our knowledge, no similar design has yet been theorised. As before, horizontal light from the first cell is transformed in polarisation before being input into the second cell. Light that is linear vertical induces a $\sigma^{+/-}$ well which has a small transmission region at centre. The light is then transmitted through a crossed polariser to select for one central narrow peak. We note that the peak is narrower than the central feature created by the first cell alone since the small transmission region in the Voigt cell 'carves out' a smaller peak which can be seen in panel c) in Fig. 3.5.

The reader may not be convinced that the Voigt cell's role is purely extinguishing here given it is placed within the crossed polarizers. We prove that its contribution to the final output is only extinguishing in A.3.3. While we have called cells 'First' and 'Second' by their sequence position, the order of the cells can be rearranged along with other optical components to arrive at the same filter transmission (see A.3 and A.4). We note that in both diagrams where the intensity (S_0') approaches zero, stray light and noise from the cables linking the photodetector and oscilloscope will dominate. This will result in changes to the Stokes parameter profiles.

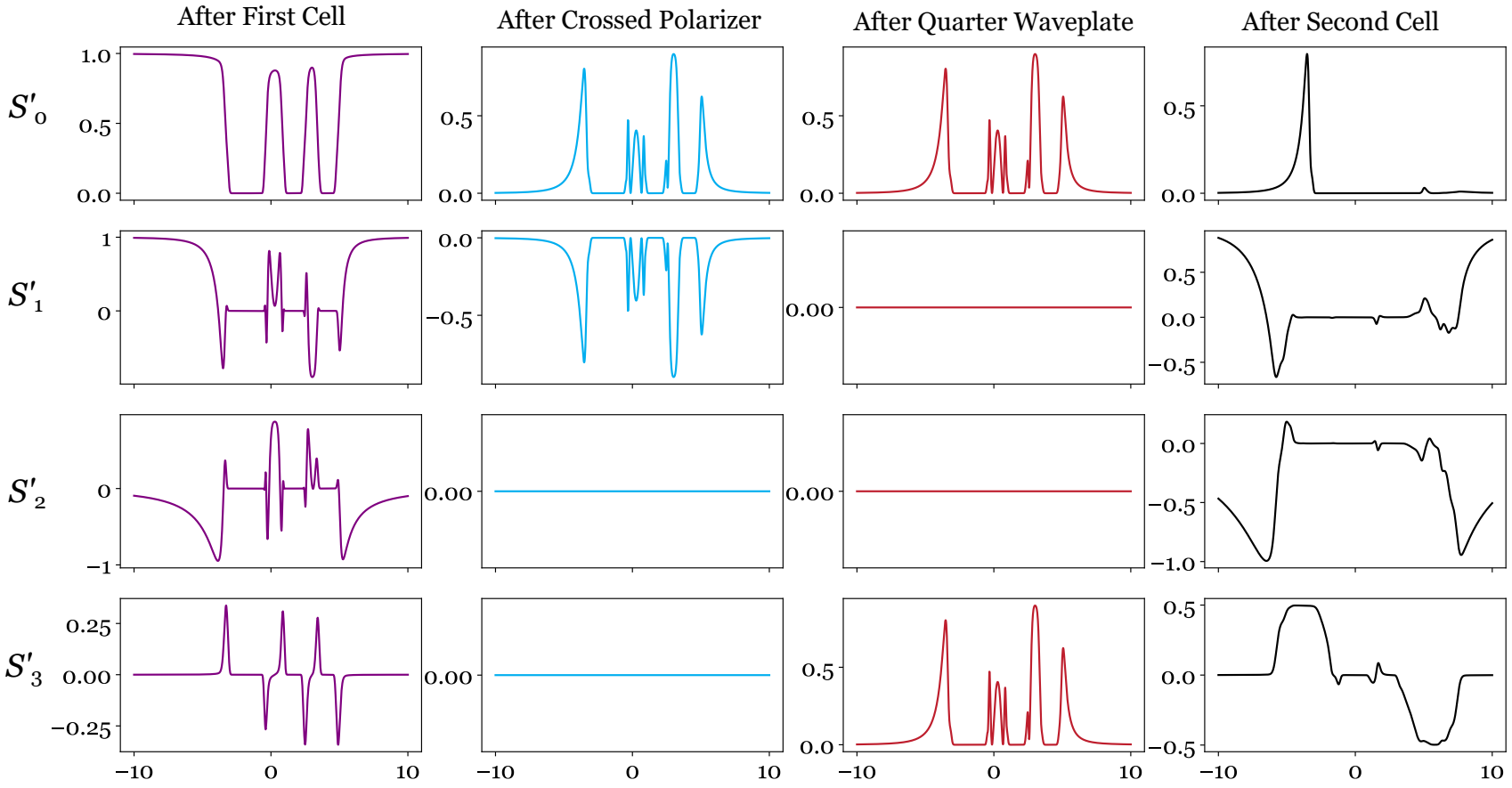

L_1/L_2 (mm)	T_1 (°C)	B_1 (G)	T_2 (°C)	B_2 (G)
75/75	85.6 ± 0.3	48.9 ± 0.5	110.1 ± 0.3	747 ± 7

Figure 3.3: The Stokes Parameters S'_i plotted at various stages of the Faraday-Faraday Wing Filter. Description in main text.

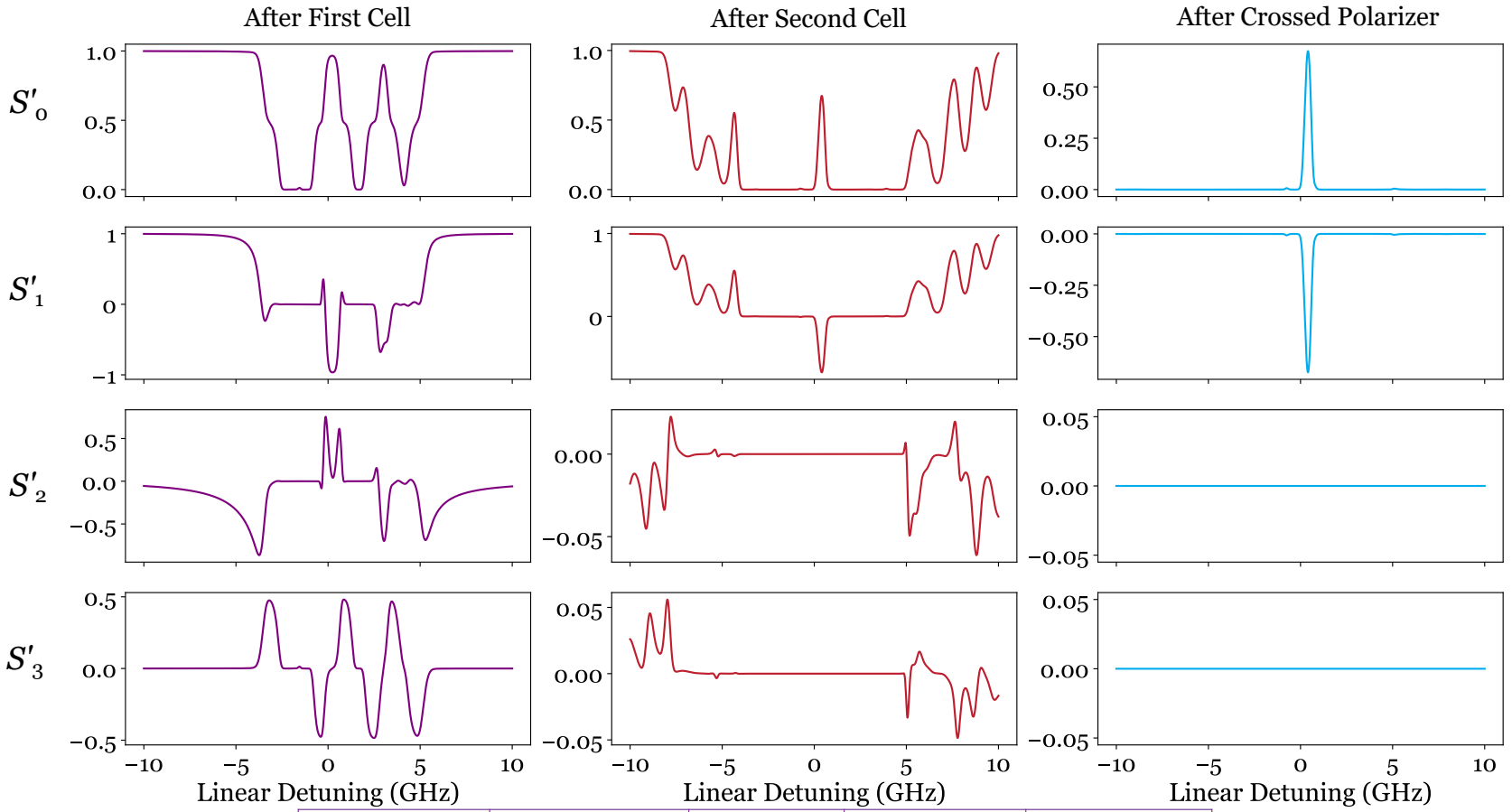

L_1/L_2 (mm)	T_1 (°C)	B_1 (G)	T_2 (°C)	B_2 (G)
75/5	100.29 ± 0.07	162.2 ± 0.3	120.79 ± 0.08	2527.6 ± 0.3

Figure 3.4: The Stokes Parameters S'_i plotted at various stages of the Faraday-Voigt Line Centre Filter. Description in main text.

3.2.3 Optimising Parameters

At this point, all that remains is finding appropriate parameters. As mentioned, computer optimisations have been used to find parameters which optimise FOM. However, understanding why these parameters give such good performance is equally important.

Figs. 3.5 and 3.6 show the variation of filter performance with second cell magnetic field. The insets to 3.13 and 3.21 show the variation of filter performance with second cell temperature. In Fig. 3.5, we see that the well experiences positive shifts in detuning with increasing magnetic field. We expect the opposite to be the case when the quarter waveplate is set at -45° such that right hand circular light is input. At low magnetic fields, the wells have gaps where there is high transmission. This is since the transition frequencies at low field are close together and their Doppler regions have high overlap. With increased magnetic field, the transitions increase in separation and their Doppler widths span a wider area. FOM remains constant after ~ 700 G where the well sufficiently extinguishes all features without detriment to the selected wing. This leads us to choose the parameters in the table.

In Fig. 3.6, the key magnetic field to consider is the value at which the central transmission region appears. This is where the σ^+ and σ^- Doppler widths no longer overlap. We want a filter where the transmission of this central region is high and the FWHM is narrow. The width and transmission of the region increase with larger magnetic field and so we must find a field value which balances the two. The parameters in the table optimise FOM.

3.2.4 Summary of Theory

We give a summary of the theory we have presented. We discovered via computer optimisation that performance can be maximised in a two cell arrangement if both cells take on different roles. One cell *transforms* the polarisation state to create

the filter peaks and the other extinguishes the unwanted peaks leaving the desired feature(s). A cell extinguishes in a certain region dependent on the transitions induced and the Zeeman shift from the applied magnetic field. The geometry of the cell, Faraday or Voigt, determines the transitions induced for a given polarisation and as such different geometries can be used to select for different features.

We theorised two designs, a Faraday-Faraday wing filter and a Faraday-Voigt line centre filter which we studied using Stokes parameters. The magnetic field and temperature must be chosen to create extinguishing wells that span the appropriate frequency range without causing detriment to the transmission of the desired feature.

3.3 Setup

Having established the performance benefits of the Faraday-Faraday and Faraday-Voigt cascades, we set out to experimentally realise these designs. Fig. 3.7 shows the experimental setup.

We use a Toptica DL100 laser [240], an external cavity diode laser scanning over an approximate range of 20 GHz. We send part of the light towards reference optics (See Appendix D for more details) and the rest to our two filter designs. A neutral density filter lowers the power to approximately 100 nW with a $1/e^2$ width of 100 μm before each experiment. This ensures we stay within the weak probe regime [169] which can be readily modelled using *ElecSus* [155, 156]. We use Thorlabs PDA36A2 amplifying photodetectors [241] setting the gain at the highest setting available '70 dB' (See Fig. 3.9). We did not verify the actual gain achieved.

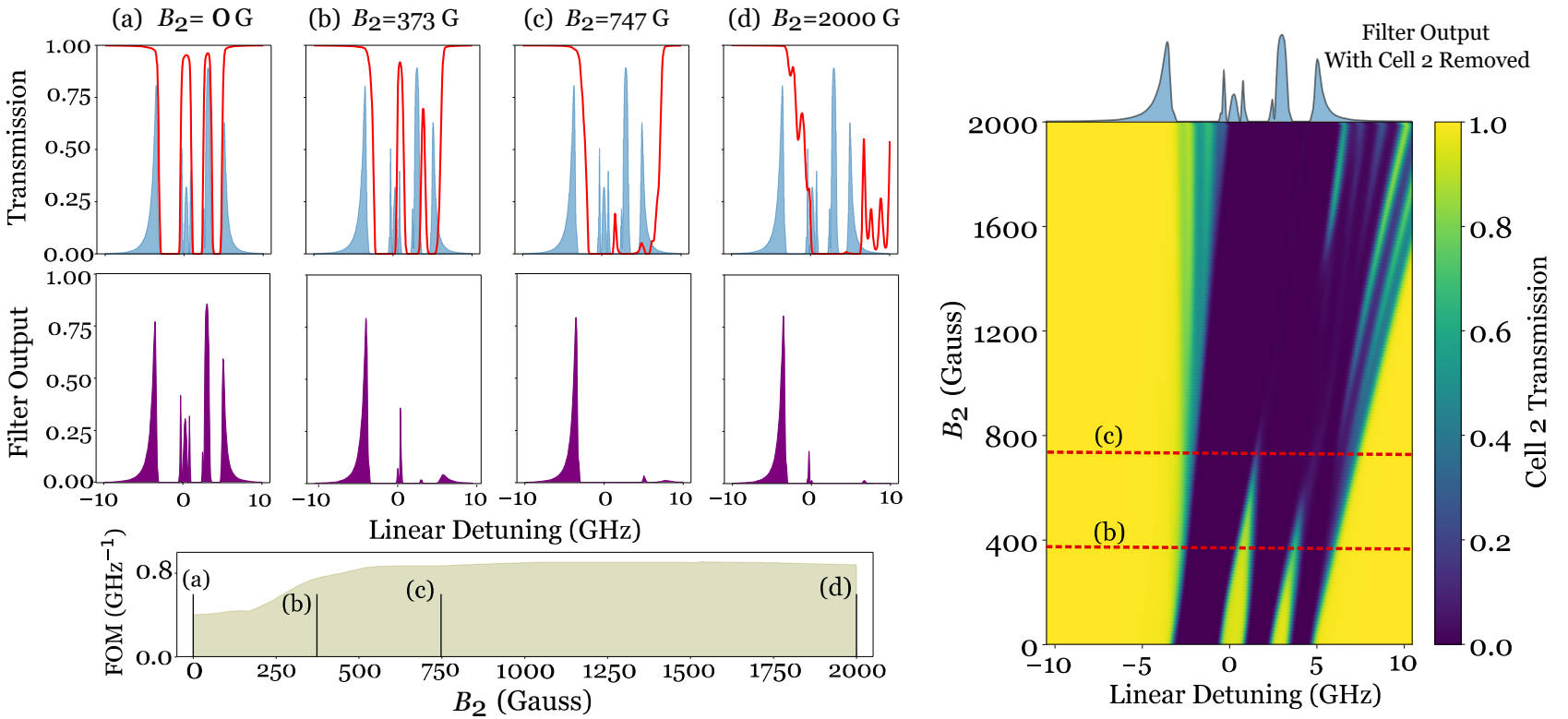

L_1/L_2 (mm)	T_1 (°C)	B_1 (G)	T_2 (°C)	B_2 (G)
75/75	86	49	110	747

Figure 3.5: The evolution of the filter profile (purple) and the second cell output (red) for various second cell B-fields, B_2. The filter transmission with second cell removed in underlayed in blue. The variation in FOM is shown in olive. To the right, a heatmap showing the maximum transmission of Cell 2 for varying B-field. The four B-fields are marked on the FOM diagram and heatmap. We notice that the extinguishing well has a positive shift in detuning as B-field increases. FOM does not increase substantially after $\sim$ 700 G since the well is wide enough and positioned to extinguish all other features without reducing the transmission of the selected peak.

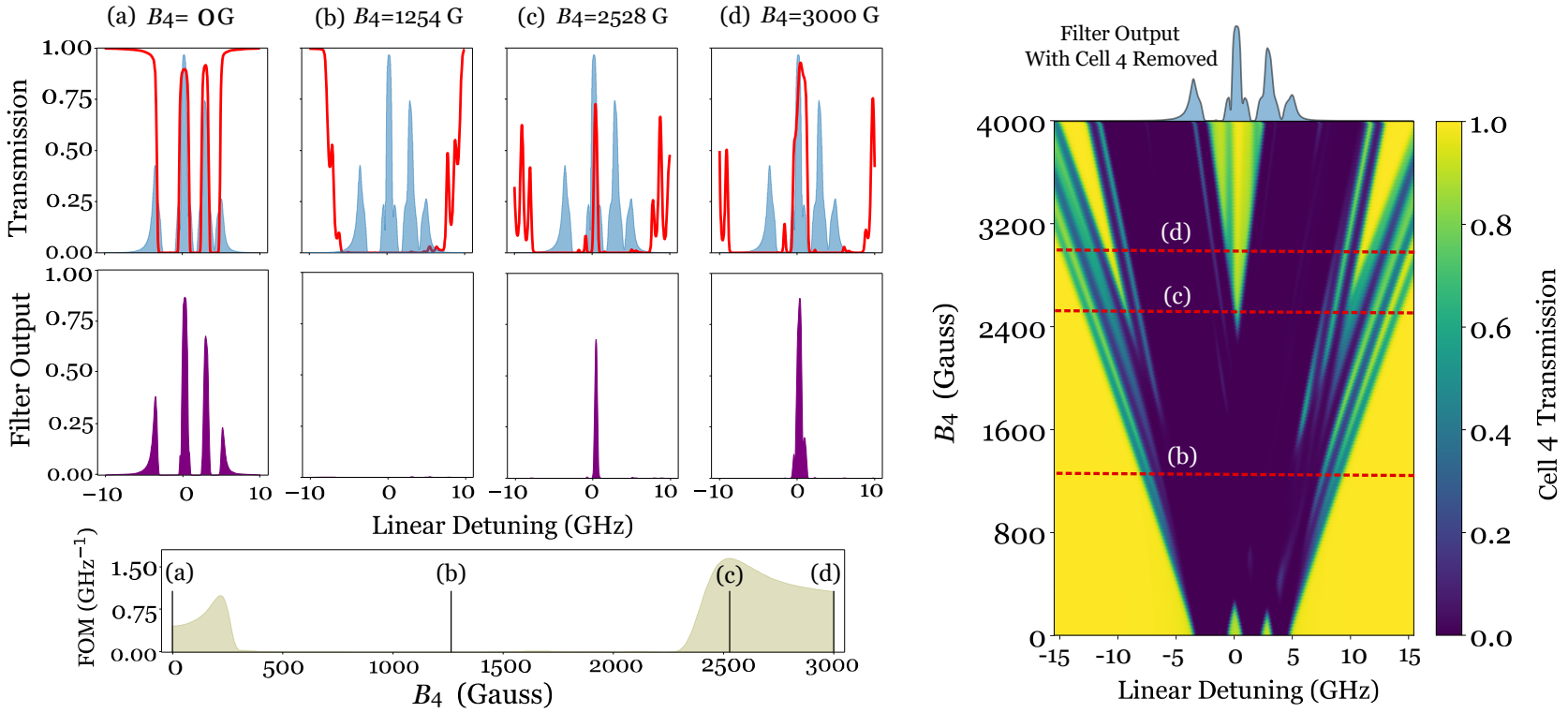

L_3/L_4 (mm)	T_3 (°C)	B_3 (G)	T_4 (°C)	B_4 (G)
75/5	100	162	121	2528

Figure 3.6: The evolution of the filter profile (purple) and the second cell output (red) for various second cell B-fields, B_4. The filter transmission with second cell removed in underlayed in blue. The variation in FOM is shown in olive. To the right, a heatmap showing the maximum transmission of Cell 4 for varying B-field. The four B-fields are marked on the FOM diagram and heatmap. We notice that a transmission region opens up in Cell 4 after $\sim$ 2400 G leading to a FOM maximum. Beyond this, the transmission region widens and the filter FWHM increases resulting in a FOM fall.

Cell 1 and Cell 3 are 75 and 5 mm natural abundance cylindrical Rb cells respectively. Both are heated by the same solenoid, shown in a) of Fig. 3.8. The solenoid also provides the required 10s-100s axial magnetic field. This arrangement is flawed in that our temperature and magnetic field control are not independent. As such, we heat the atoms to the required temperature (which is a slow process) and lower the current to achieve the required magnetic field (which is fast). We must take results immediately as the temperature falls by several degrees within a minute. An improvement was made to this arrangement in the next investigation (See 4.3) using flexible heaters. We would recommend these heaters be used if this experiment is performed again. The solenoid design is based on [242] but has a different number of coils and layers resulting in different current requirements. An example solenoid magnetic field plot calculated using the python package *magpylib* [236] is shown in Fig. 3.10. For light passing through the centre of the solenoid, the magnetic field varies by $\sim$ 20 G across the 75 mm cell for a desired field value of 49 G. We note that the magnetic field required for Cell 3 is approximately 100 G larger than that plotted in Fig. 3.10. Nevertheless, the field variation across 5 mm is substantially smaller ($\sim$ 5%).

Cells 2 and 4 are the same 5 mm cuboidal natural abundance Rb cell constructed by Dr. Danielle Pizzey and Durham Chemistry Department (see Fig. 3.9). They are placed inside a homemade copper heater with PTFE sheath which is heated by 3D printer cartridge heaters. The cell with copper heater is placed between two top hat NdFeB magnets [243, 239]. Fig. 3.11 and 3.12 show the field variation along the direction of the k-vector (z) and along the straight line connecting the centres of the two magnets (x). The magnetic field varies by less than 5% and 1% across the length of the cell and the width of the beam respectively. The cell length choices made are a compromise between minimising collisional broadening which can be achieved at lower temperatures (and hence we want longer cells to compensate for the number of atoms with which we interact) and generating homogeneous magnetic fields which is more challenging for longer cells [222].

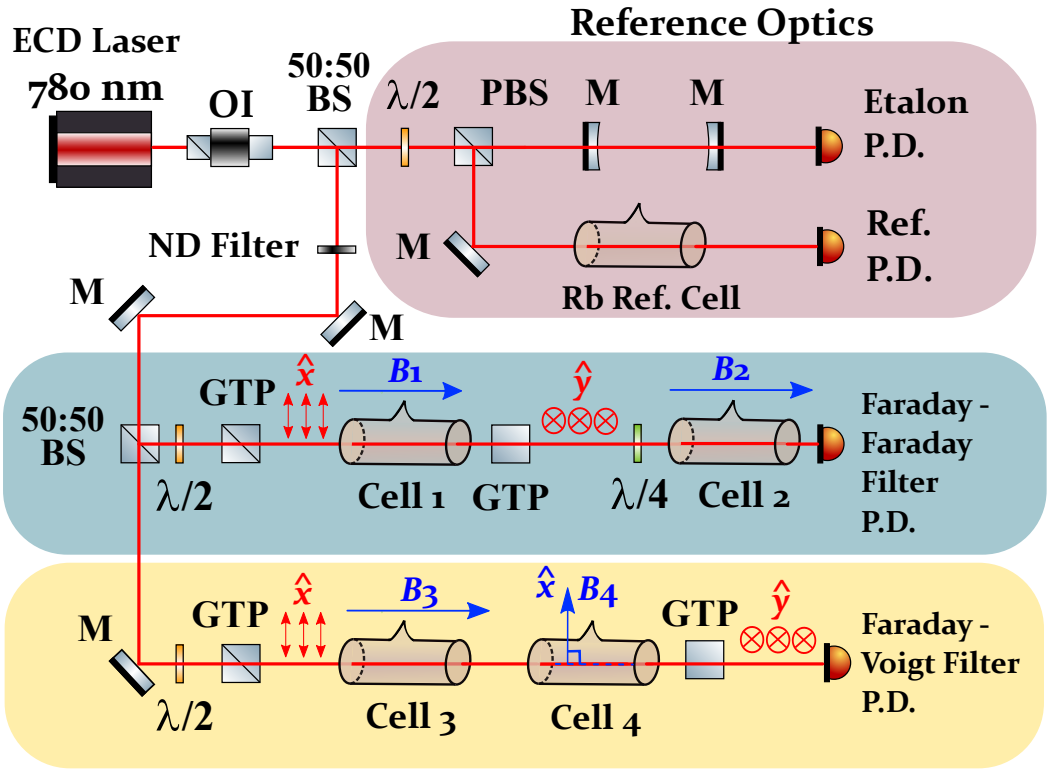

Figure 3.7: The experimental setup for the two cascaded filter experiments. 780 nm light (Rb-D2) from an external cavity diode (ECD) laser is directed towards reference optics and the experiments. The reference optics includes an etalon setup for relative frequency calibration and a zero field room temperature natural abundance Rb setup for absolute frequency calibration [3] (See Appendix D for more details). A neutral density (ND) filter is incorporated to reduce the power so as to remain in the weak probe regime [169]. The red arrows and their associated hat operators depict the polarisation state after each Glan-Taylor Polariser (GTP). Hat operators are also added to the blue magnetic field vectors for clarity in their direction. See Appendix C for a rigorous definition of the axes used throughout. The first experiment is a Faraday-Faraday filter composed of a Faraday cell between two crossed GTP followed by a quarter wave plate and an additional Faraday cell.. As such, the k-vector of the light is parallel with the magnetic fields of Cell 1, B_1, and Cell 2, B_2. The quarter waveplate can be adjusted to transform the linear light to left hand or right hand circular light by setting the fast axis at $\pm 45°$ respectively. The second experiment is a Faraday-Voigt filter which involves a Faraday and Voigt cell between crossed polarisers. Light passes through the system with k-vector parallel to the magnetic field, B_3, and perpendicular to the magnetic field, B_4. M — Mirror, (P)BS — (Polarising) Beamsplitter, OI — Optical Isolator, P.D. — Photodetector.

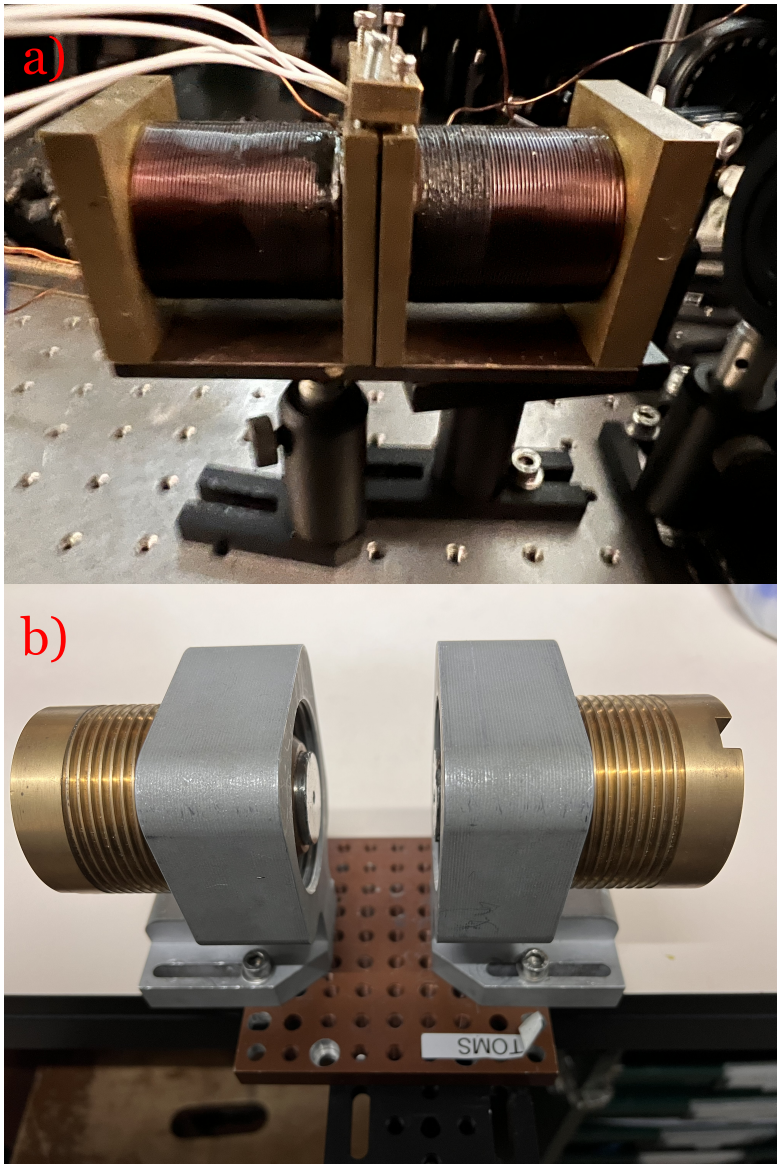

Figure 3.8: a) A photo of the solenoid used to heat and provide axial magnetic fields to Cells 1 and Cells 3. b) The annular NdFeB magnets used to apply a transverse magnetic field to Cells 2 and 4.

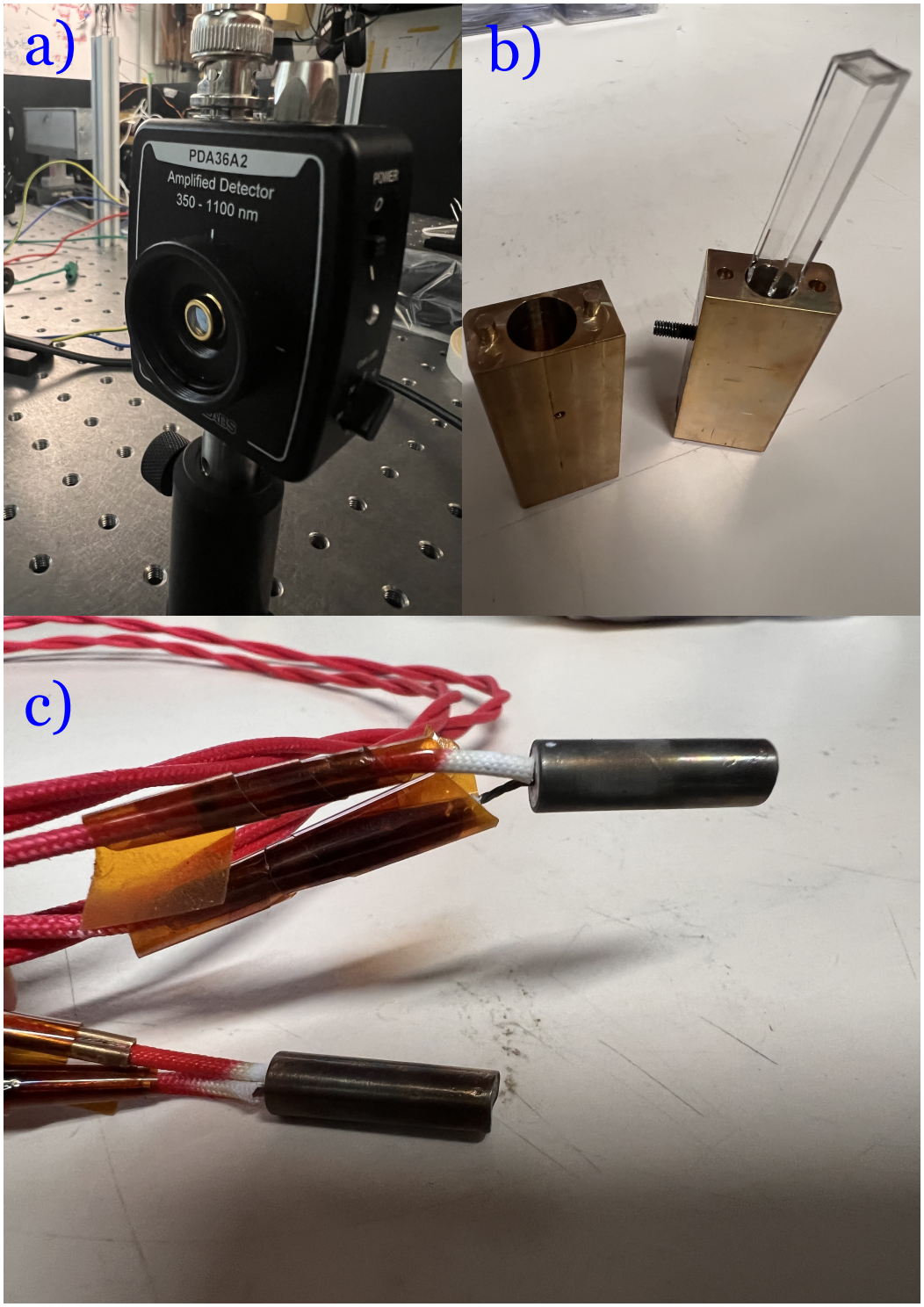

Figure 3.9: a) A photo of the photodetector used. Working in the weak probe regime and needing a high signal-to-noise ratio, we set the photodetectors at the maximum '70 dB' amplification setting for all experiments. b) A photo of the 5 mm cuboidal natural abundance Rb cell inside the copper heater. Not included in this photo is the PTFE sheath that thermally insulates the copper vessel. c) A photo of 3D printer cartridge heaters. We find they heat the copper block quickly and to high temperatures and at time of writing cost less than £5.

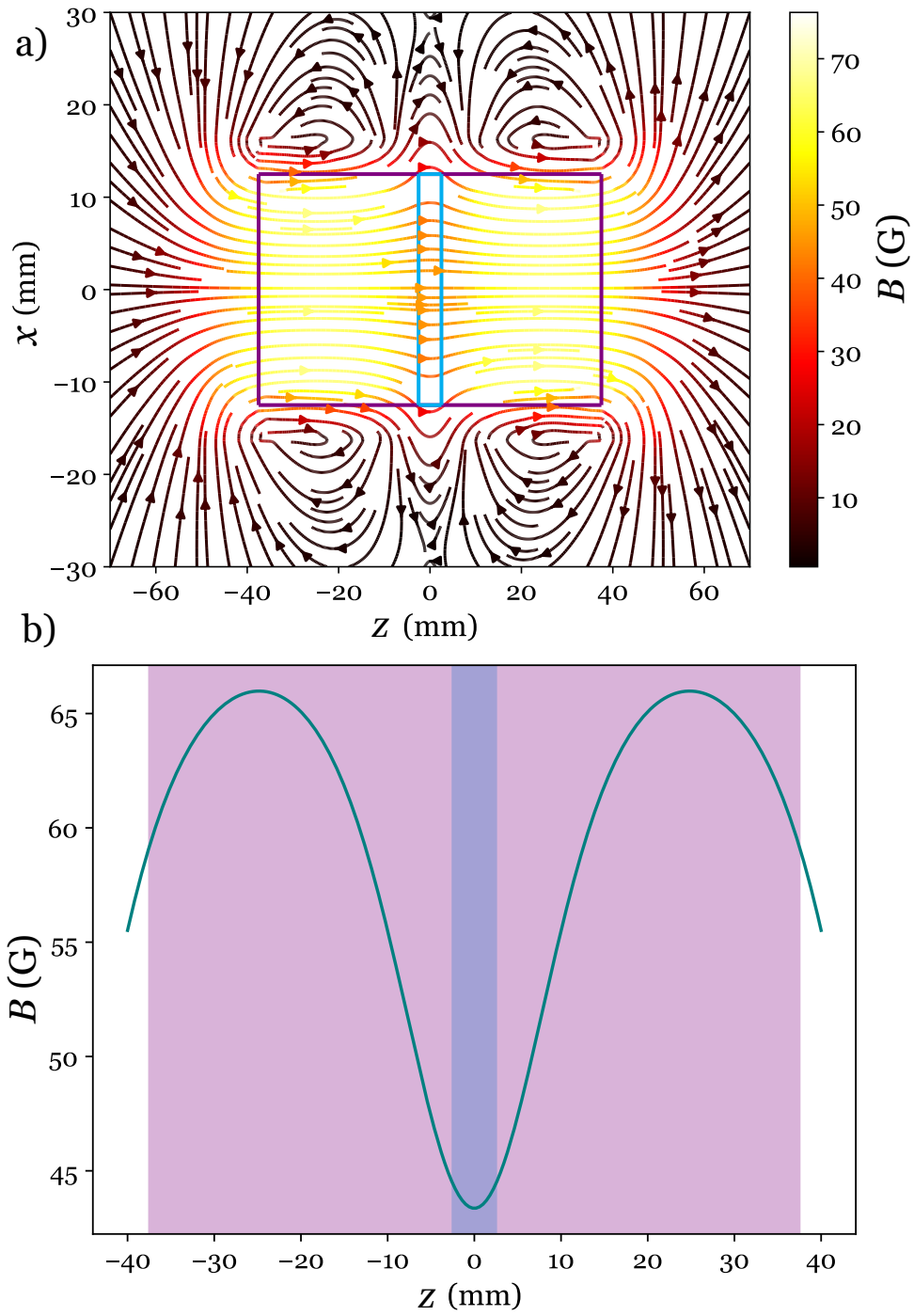

Figure 3.10: Plots of the solenoid magnetic field used to provide Cell 1 and Cell 3's axial fields calculated using *magpylib*. Panel a) shows the magnetic vector field diagram where z points in the direction of the k-vector. The purple and blue boxes mark the extent of the 75 and 5 mm cells respectively. Panel b) shows the field variation along z for $x = 0$. The purple and blue shading mark the extent of the 75 and 5 mm cells respectively. The model assumes the solenoid is broken into two parts with 12 mm separation each containing 8 layers of 53 coils with wire thickness 0.8 mm. The length of each solenoid is 43 mm. The current is 0.6 A which was used to obtain B_1, the magnetic field for Cell 1. The current for Cell 3 is ~ 2 A.

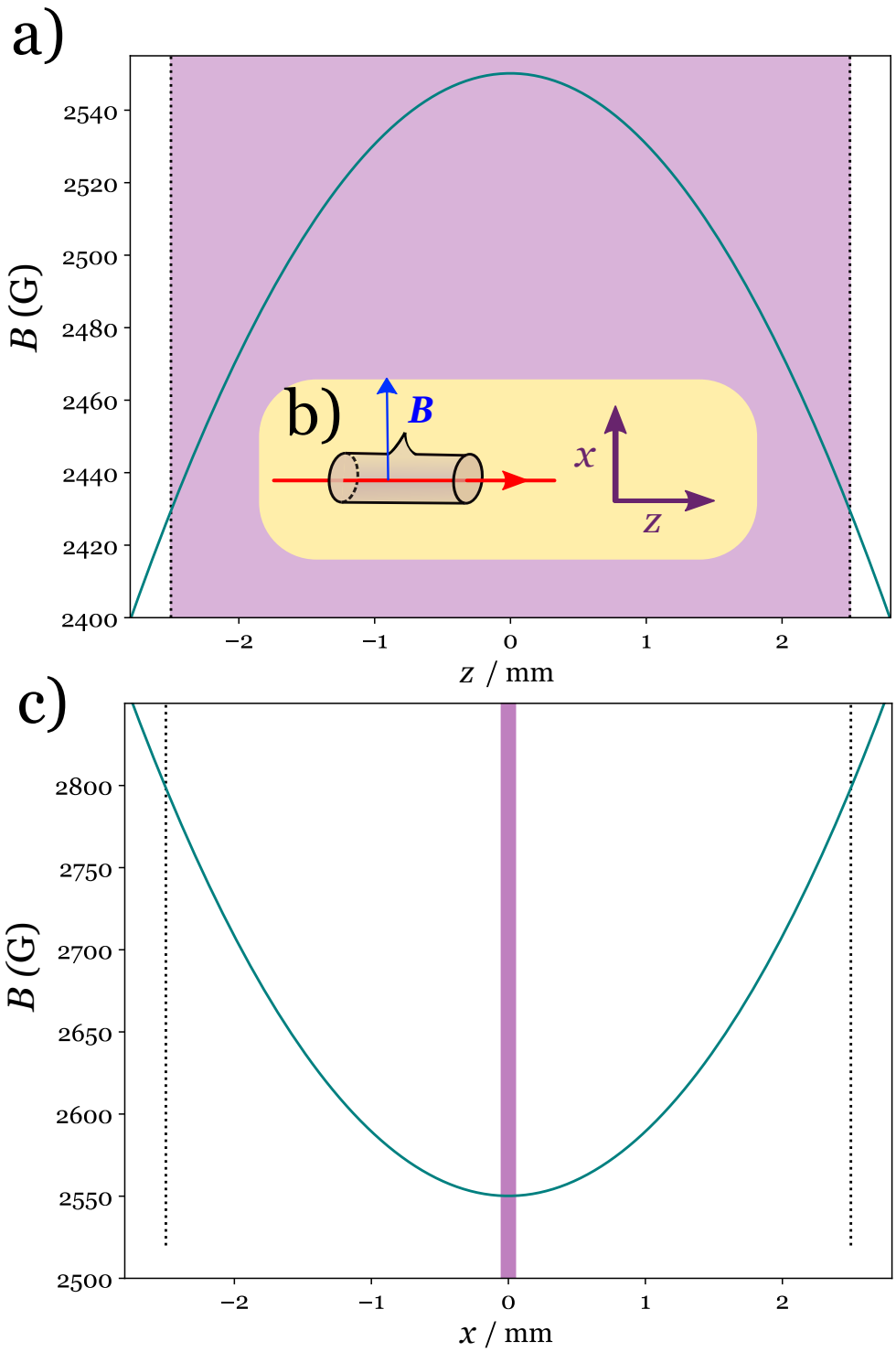

Figure 3.11: Magnetic field profiles calculated using *magpylib* for two top hat Nd-FeB magnets separated by 32.5 mm with remanence 1.42 T. b) defines the coordinate axes. x points from one top hat to the other and z is parallel with the k-vector. a) shows the field variation as the light moves in the z-direction through the 5 mm cell. c) shows the field along the x-direction. The dashed line marks the extent of the cell and the purple region is the width of the beam ($\approx 100\mu$m).

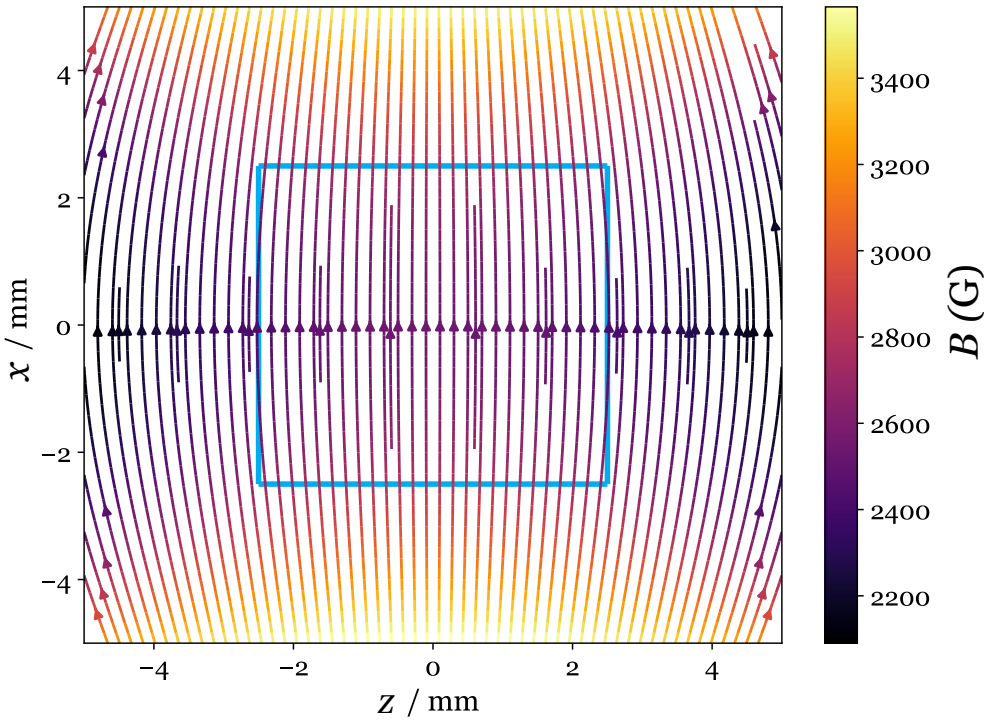

Figure 3.12: Magnetic field vector diagram for two top hat NdFeB magnets seperated by 32.5 mm with remanence 1.42 T. x points from one top hat to the other and z is parallel with the k-vector. The blue box marks the extent of the 5 x 5 mm^2 cuboidal cell. The field is perpendicular to the k-vector along the cell length.

3.4 Results

3.4.1 Faraday-Faraday Wing Filter

We first present results for the Faraday-Faraday wing filter shown in Fig. 3.13. Five sets of data were taken in quick succession via an oscilloscope capture. These datasets were fitted separately and fit parameters were obtained. We calculate mean values and standard errors from the five sets of fits which are stated in the table. Data show excellent agreement with theory [244]. The filter realised has a ENBW, FWHM and FOM of 920 ± 10 MHz, 599 ± 1 MHz and 0.86 ± 0.01 GHz^{-1} respectively. In addition we show data to verify various stages of the filter. Fig. 3.14 shows the S_0' output after the first cell. Fig. 3.15 shows the transmission after the second polariser. Fig. 3.16 shows the S_0' output of the second cell set at 45° to

select the negatively detuned wing. By setting the quarter waveplate at this angle, the light is transformed to be left hand circular. The light is then absorbed due to σ^+ transitions which are positively detuned.

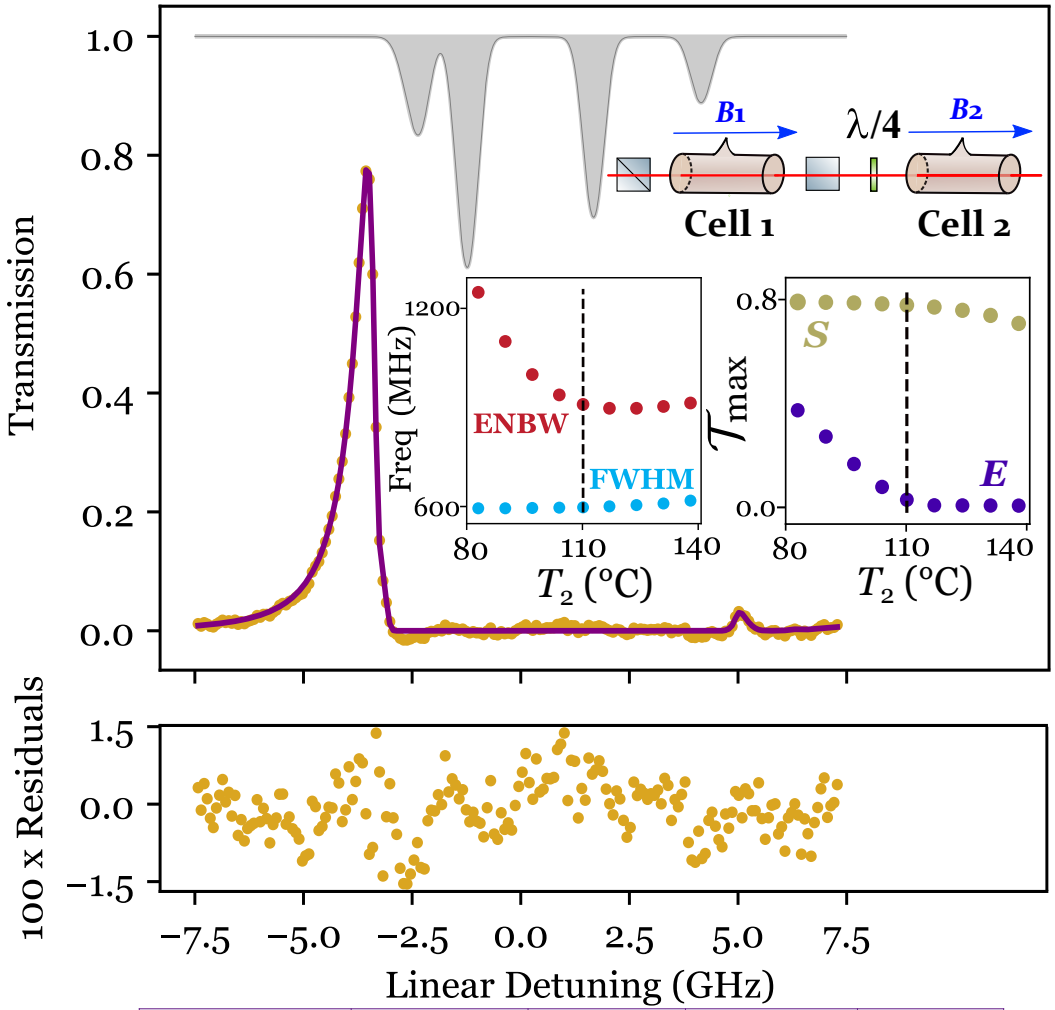

L_1/L_2 (mm)	T_1 (°C)	B_1 (G)	T_2 (°C)	B_2 (G)
75/75	85.6 ± 0.3	48.9 ± 0.5	110.1 ± 0.3	747 ± 7

Figure 3.13: Experiment (gold) with theory fit (purple) of the Faraday-Faraday wing filter using natural abundance Rb cells probed on the Rb-D2 line. Mean values and standard errors of the parameters obtained from fits of five spectra are presented in the table. Residuals are shown to show goodness of fit of the smaller features. Data and theory show excellent agreement [244]. An ENBW, FWHM and FOM of 920 ± 10 MHz, 599 ± 10 MHz and 0.86 ± 0.01 GHz^{-1} were obtained for one fit. Standard errors for these values were calculated from systematics. The quarter waveplate is set at 45° to input left hand circular light into the second cell. This results in high suppression of features positively detuned from centre and transmits the negatively detuned wing. The insets show the variation of ENBW, FWHM and the transmission values of the selected (S) and extinguished (E) peaks with second cell temperature. All other parameters are kept fixed. We note that the temperature realised is close to an ENBW minimum. Additionally the extinguished peak is almost maximally suppressed. A room temperature zero field rubidium notch spectrum is shown in grey for reference.

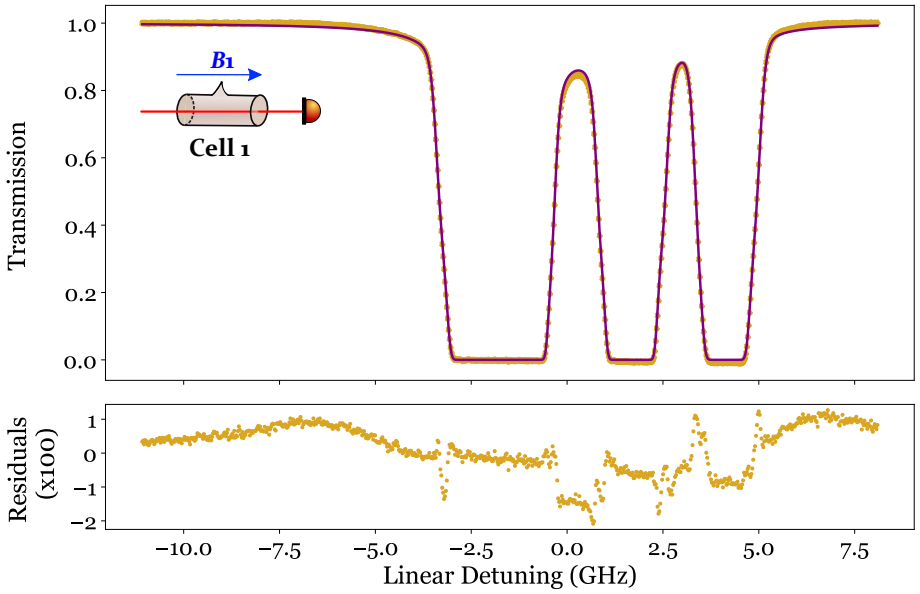

Figure 3.14: Experiment (gold) with theory (purple) for the S_0' output after the first cell of the wing filter.

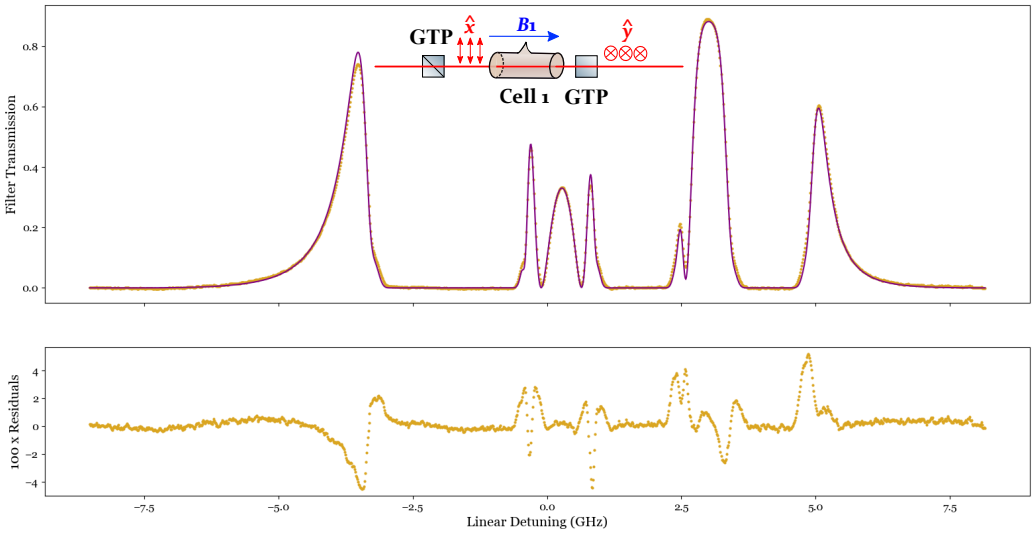

Figure 3.15: Experiment (gold) with theory fit (purple) of the S_0' output after the second polariser of the wing filter. We can see that both wings are present with additional sets of features closer to line centre.

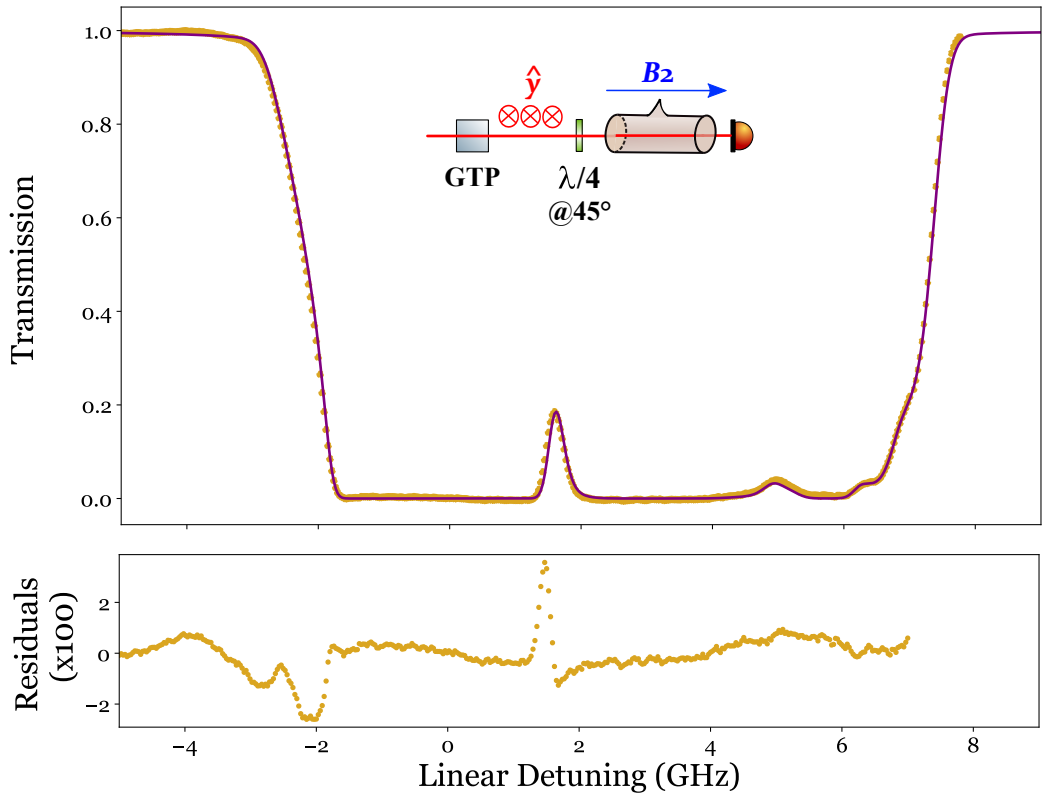

Figure 3.16: Experiment (gold) with theory fit (purple) of the S_0' output after vertical light is input to the quarter waveplate set at 45° and passes through the second cell.

3.4.1.1 Rotating the Quarter Waveplate

By rotating the quarter waveplate, we can select for the positively or negatively detuned peaks or both. Figs. 3.17 and 3.18 have the quarter waveplate set at 0° where the light remains linear and equal parts σ^+ and σ^- transitions are induced. From Figure 3.17, we see that in the central region, both transitions are induced and there is no transmission. Outside of this region there are 50% pedestals where only one of the σ transitions is induced. Since linear light can be decomposed into equal parts left and right hand circular, this means 50% of the light is extinguished and the other handed part is transmitted. Figs. 3.19 and 3.20 have the quarter waveplate set at $-45°$. In this case, the light is transformed to be right hand circular resulting in σ^- absorption. Therefore the negatively detuned region is extinguished while the positively detuned region is transmitted.

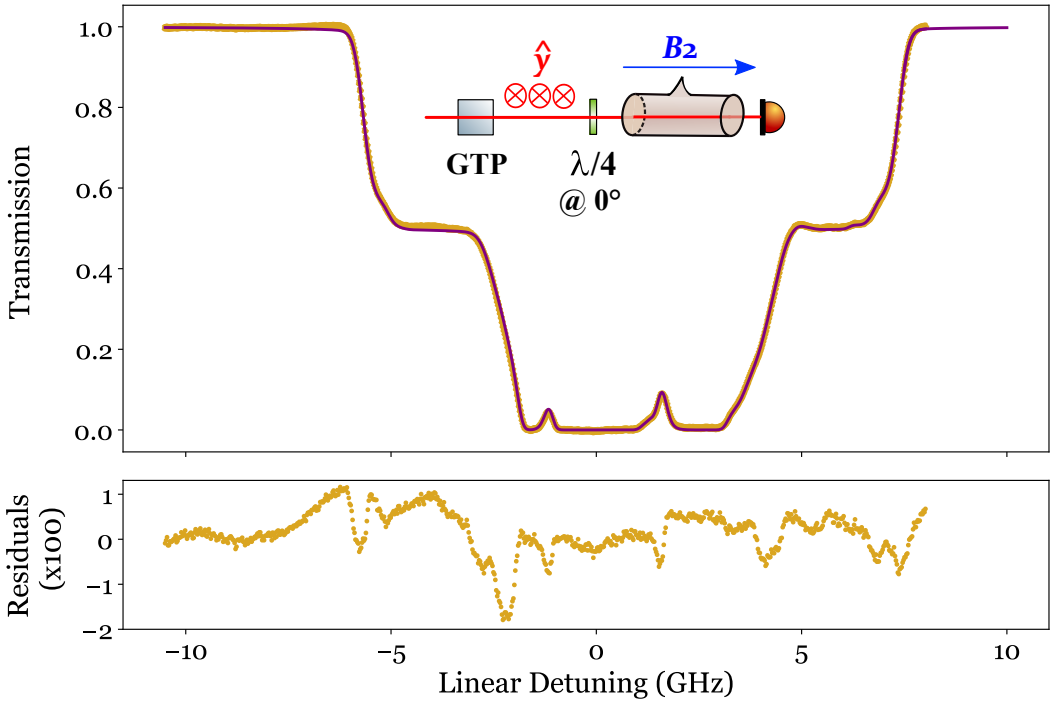

Figure 3.17: Experiment (gold) with theory fit (purple) of the S_0' output after vertical light is input to the quarter waveplate set at 0° and passes through the second cell. Note the pedestals at 50% transmission. This represents light in a mainly dichroic region where the left or right hand circular component of the linear light is extinguished leaving only the other hand.

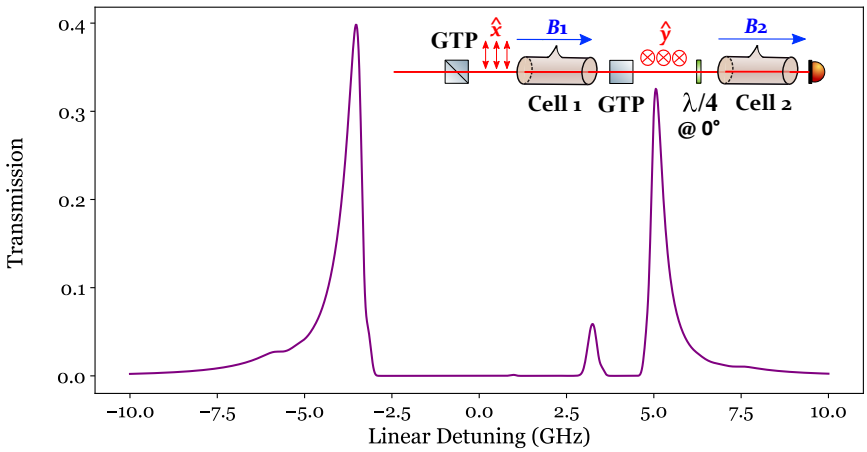

Figure 3.18: Theoretical S_0' output after vertical light is input to the quarter waveplate set at 0° and passes through the second cell. A separate smaller feature is also selected which we could reject by changing the temperature and magnetic field parameters of the second cell.

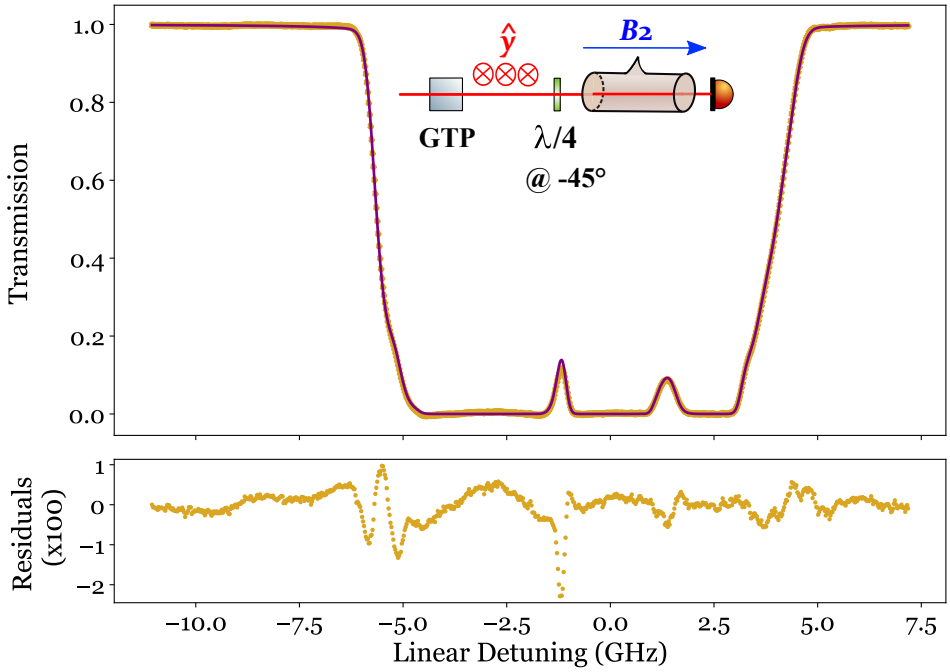

Figure 3.19: Experiment (gold) with theory fit (purple) of the S_0' output after vertical light is input to the quarter waveplate set at $-45°$ and passes through the second cell.

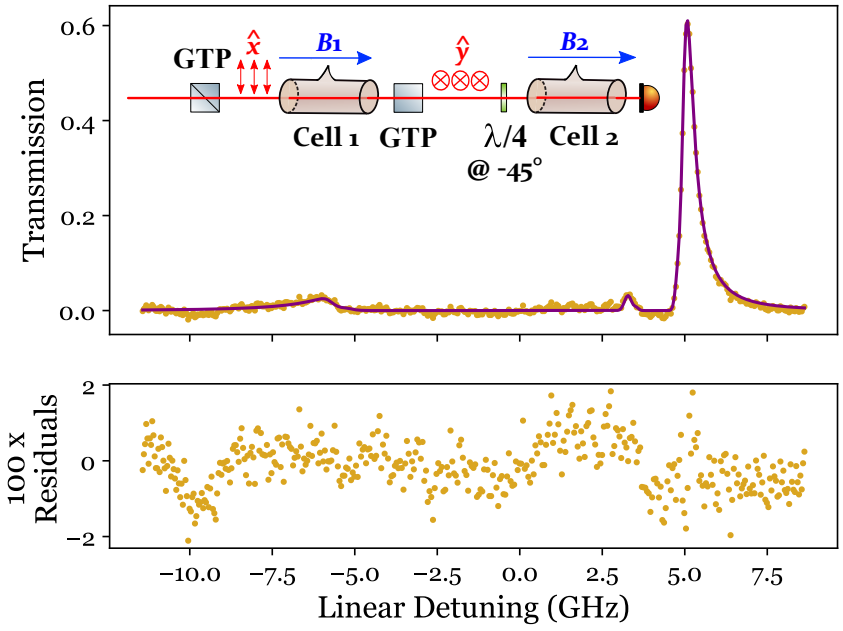

Figure 3.20: Experiment (gold) with theory fit (purple) of the Faraday-Faraday Wing filter with quarter waveplate set at $-45°$ to select the positively detuned wing.

3.4.2 Faraday-Voigt Line Centre Filter

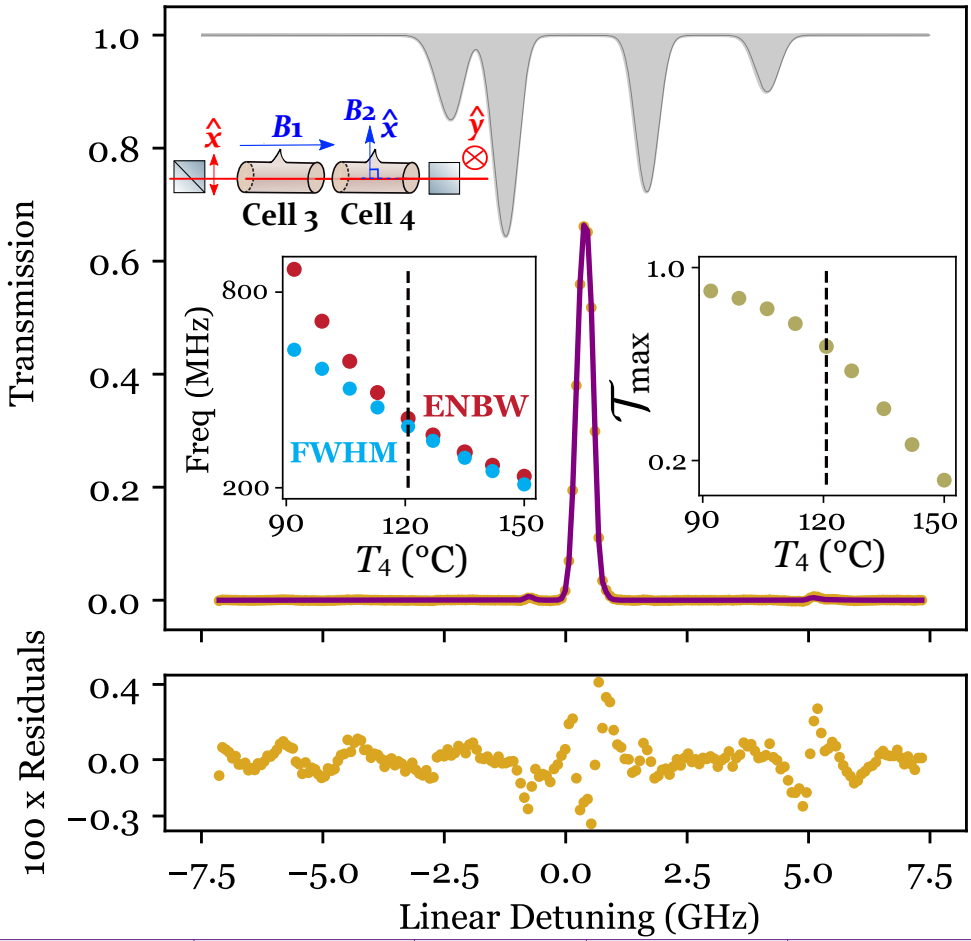

L_1/L_2 (mm)	T_1 (°C)	B_1 (G)	T_2 (°C)	B_2 (G)
75/5	100.29 ± 0.07	162.2 ± 0.3	120.79 ± 0.08	2527.6 ± 0.3

Figure 3.21: Experiment (gold) with theory fit (purple) of the Faraday-Voigt filter using natural abundance Rb cells probed on the Rb-D2 line. Mean values and standard errors of the parameters obtained from fits of five spectra are presented in the table. Data and theory show excellent agreement [244]. Residuals are shown to show goodness of fit of the smaller features. An ENBW, FWHM and FOM of 420 ± 1 MHz, 389 ± 1 MHz and 1.63 ± 0.01 GHz^{-1} respectively were obtained for one fit with standard errors being calculated from systematics. The insets show the variation of ENBW, FWHM and maximum transmission with temperature. We note that FWHM and ENBW can be improved by increasing temperature but at the detriment of maximum transmission. A room temperature zero field natural abundance rubidium notch spectrum is shown in grey for reference.

We present results for the Faraday-Voigt line centre filter in Fig. 3.21. This was the highest FOM passive filter recorded in the literature at time of publication and has

since been superseded by the filter presented in Fig. 4.11. Nevertheless, it remains a competitive single peak filter given that the next biggest peaks have less than 2% peak transmission. The second cell temperature has an approximate exponential relationship with temperature with transmission falling drastically after 120° C. This is similarly the case with the ENBW which we could minimise further at the expense of peak transmission.

3.5 Outlook

In this chapter, we have studied the effect of cascading vapour cells on filter performance. We considered two setups: the Faraday-Faraday setup adapted from [154] and a Faraday-Voigt setup that had not previously been studied. Computer optimisations show that FOM is maximised when each cell has a different role; either the cell is responsible for polarisation evolution (the 'transformation' cell) or for suppressing unwanted light (the 'extinguishing' cell). The first Faraday cell in each of the filters we realised is responsible for creating a highly transmitted filter peak centred at the desired frequency. The geometry of the second cell is critical for determining the relationship between polarisation and transitions induced and hence the light that is extinguished. The Faraday wing selecting cell extinguishes light at centre and at positively/negatively detuned values depending on the orientation of the waveplate. The Voigt line centre selector extinguishes light everywhere except at centre. We experimentally realised both filters and found excellent agreement between data and theory. The Faraday-Voigt filter was the highest FOM passive filter at the time of publication. Qualitatively, the single peak lineshapes of both filters would be highly desirable in laser frequency stabilisation applications [125, 126, 127, 128] and quantum hybrid systems [176, 177, 178, 179].

This study shows that atomic media offer many filtering functions which are hard to optimise simultaneously when one cell is required to fulfil all these roles. However, we have not given a general treatise on cascaded setups or even a complete overview

of two-cell cascades. As evidence for this, we briefly introduce some prototype filters involving two-cell cascades with quite different filter performance.

Firstly, the Faraday-Voigt setup could be cascaded with a Fabry-Pérot etalon to form an 'Atomic-Etalon' filter. As discussed in Chapter 1, Fabry-Pérot etalons can generate narrower filter peaks than magneto-optical filters but are susceptible to frequency drift over time due to mechanical and thermal vibrations [120, 121, 122, 64]. Additionally etalon peaks occur periodically with spacing given by the free spectral range, ν_{FSR}. This means etalons practically have an infinite ENBW and FOM ≈ 0 when evaluated over all frequencies. Fig. 3.22 theoretically models the output of an Atomic-Etalon filter which combines the benefits of both filter types. The Faraday-Voigt setup with the same parameters as realised in 3.21 is followed by a free space etalon. The etalon is composed of two curved confocal mirrors with $\nu_{\mathrm{FSR}} = 745$ MHz, and finesse, $\mathcal{F} = 10$ (These are the approximate specifications used in Appendix D). This results in a filter with a single peak FWHM ≈ 70 MHz with other peaks completely suppressed leading to favourable ENBW and FOM. Additionally as shown in panel (c), the filter is calibrated to reject frequency drifted signals. One can see visually that the filter peak shows assymetry after significant frequency drift (the gold and black dashed lines). After 300 MHz drift the single peak is entirely suppressed. The system could even become frequency stable if a computer was incorporated to evaluate the peak symmetry live before microadjusting the cavity mirrors using stepper motors [245, 246]. We envision metrological applications (see 4.5) as well as uses in absolute frequency calibration.

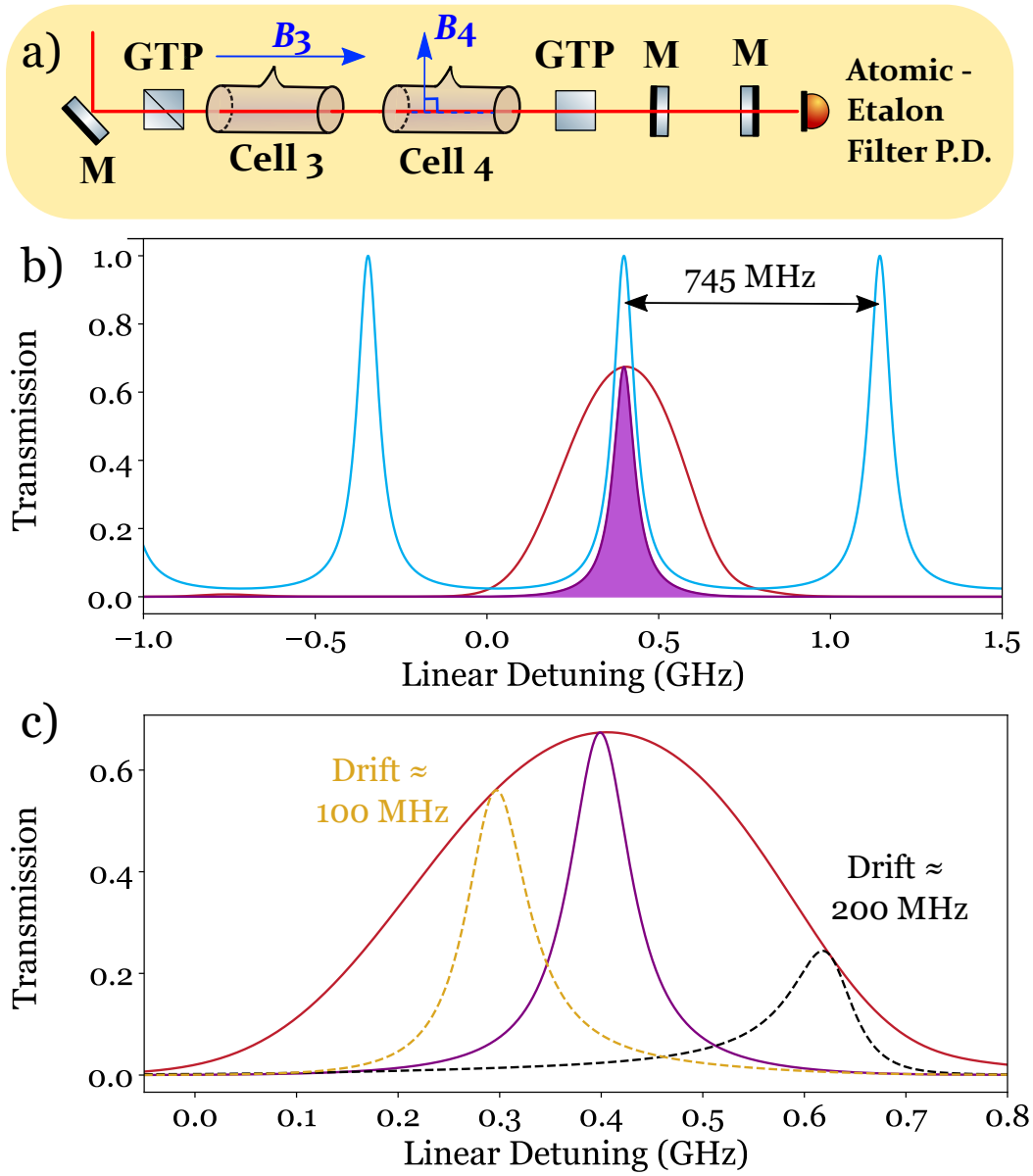

Figure 3.22: a) The experimental setup utilising the Faraday-Voigt filter with same parameters as realised in Fig. 3.21 followed by a set of confocal mirrors. The etalon has free spectral range = 745 MHz and finesse, $\mathcal{F} = 10$. Panel b) shows the etalon transmisson without the cascaded cells preceding it (blue), the cascaded filter output without the etalon following it (red) and the resultant filter transmission from the Atomic-Etalon filter (purple shading). c) shows the use of the Atomic-Etalon as a frequency drift diagnostic tool. When the etalon shows frequency drift, the resultant spectral profile is assymetric and reduced in transmission. After a certain tolerance $\sim$ 300 MHz, the peak is completely suppresed.

Secondly, we consider a prototype 'periodic' filter modelled in Fig. 3.23. The first cell is placed between two polarisers rotated at 45° and 135° respectively such

that diagonal linear light at $+45°$ is input and diagonal linear light at $-45°$ is selected by the crossed polariser. The light then enters a second cell in the Voigt geometry before being selected by a right hand circular polariser composed of a quarter waveplate and GTP. Our theory curves are calculated using two natural abundance potassium cells on the D2 line. We choose potassium cells since the equivalent realisation in Rubidium would require impractical magnetic fields and number densities. For more information on the potassium hyperfine structure, see [247].

The operation of the filter will not be considered in detail here but in short, *both* cells are involved in polarisation transformation. This results in a very different kind of filter profile which may be desirable for different applications. The first cell transforms the light to realise a central peak (blue line in panel b)). The second cell extinguishes light outside the central peak and somewhat inside the peak. Crucially, the second cell also transforms the polarisation creating the 'grooves'. Such a filter not only selects for transmission in a small region but bins the signal into smaller frequency intervals. While this may not be optimal if the user desired a smooth peak feature, such a filter may be useful in applications where additional info about the spectral data filtered is utilised, for instance, in quantum key distribution where the filter could act as a cipher [237, 191].

The predicted parameters can be practically realised. 20 mm K cells (albeit isotopically pure) have been manufactured alongside 1 mm cells in other alkali metals [81, 1]. 4000 G in the Voigt geometry over 1 mm has been realised [220] and fields slightly larger than 800 G have been realised for 20mm length scales in the Faraday geometry [248]. Heating vapour cells over 200° C [208] has also been achieved.

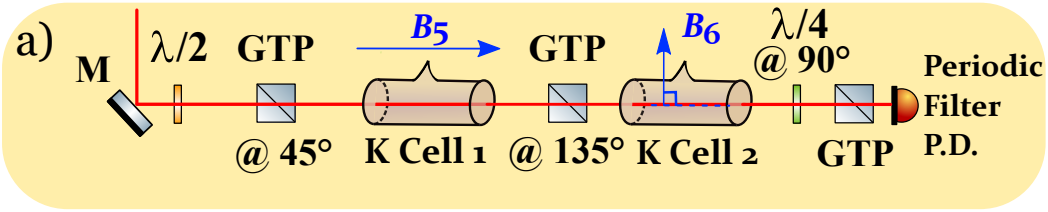

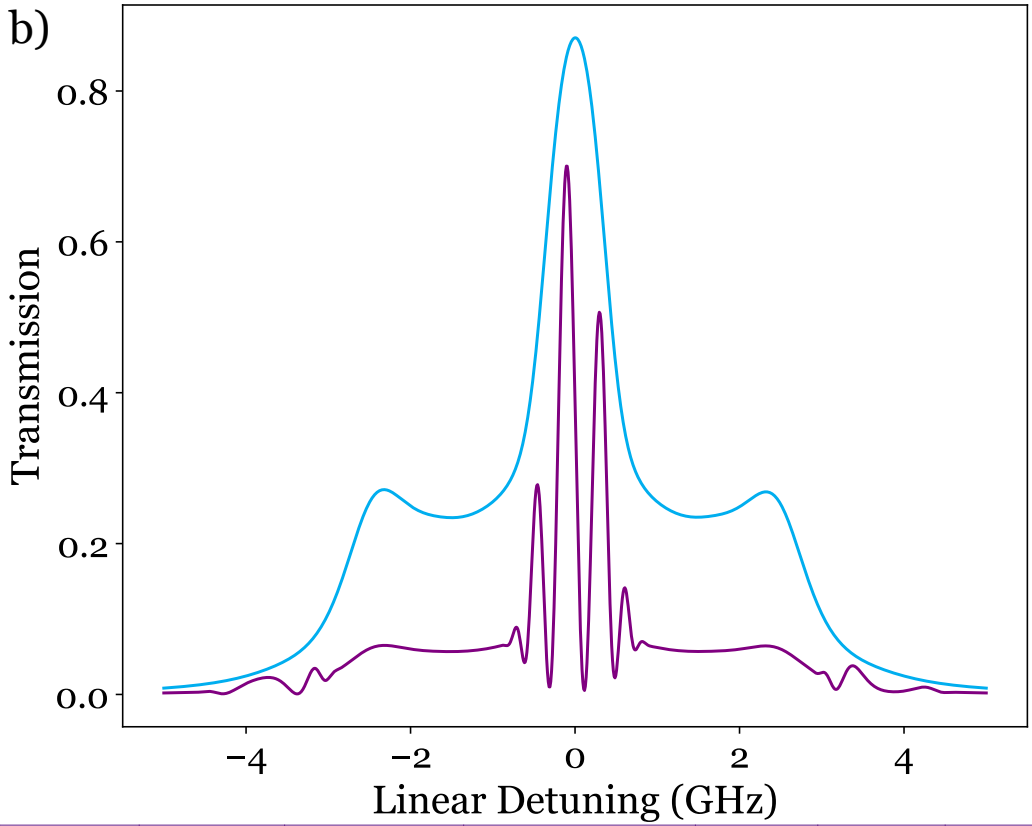

Cell	L (mm)	Geometry	Element	D-line	T (°C)	B (G)
K Cell 1	20	Faraday	Nat. Abund. K	D2	90	800
K Cell 2	1	Voigt	Nat. Abund. K	D2	200	4000

Figure 3.23: a) Experimental setup of the periodic filter. The first two GTPs are rotated at 45° and 135° respectively. After passing through the second cell, light passes through a quarter wave plate with fast axis at 90° before passing through an unrotated GTP. Parameters are shown in the table. b) The filter profile showing five grooves at centre (purple) along with the transmission after the second GTP (blue).

Chapter 4

A Study of Oblique Magnetic Fields and Filter Performance

Author completed all theoretical computations, collected and processed all data and created all figures presented in this chapter. Figures 4.9 and 4.19 were created using code by Thomas Robertson-Brown. All text written without the use of AI. Work is related to the article:

F. D. Logue, J. D. Briscoe, D. Pizzey, S. A. Wrathmall, and I. G. Hughes, 'Exploiting non-orthogonal eigenmodes in a non-Hermitian optical system to realize sub-100 MHz magneto-optical filters', *arXiv Preprint*, 2303.00081, 2023. https://doi.org/10.48550/arXiv.2303.00081 [5]

4.1 Background

In the previous chapter, we constructed magnetic fields in two specific geometries: Faraday (parallel with the k-vector) and Voigt (perpendicular with the k-vector). While these specific cases have been well studied, we believe there have only been four filters realised with a field applied *obliquely* (neither parallel or perpendicular to the k-vector) [148, 207, 208, 64]. There are both theoretical and experimental reasons for this gap in the literature. From a theoretical perspective, the

refractive index and eigenmode solutions have a more complex form. Analytic [249, 250, 251, 252] and numerical solutions [156] have been presented. However, disagreements with experiment, slow computation times, and difficulties interpreting the solutions have inhibited further research (See Appendix B for more details). Experimentally, it is challenging to design homogeneous oblique magnetic fields within the volume of the beam. Permanent magnets have achieved less than 5% inhomogeneity in 10s G [253] and less than 1% in 100s G [208, 64] for centimetre length scales. However, tuning the system to the correct field angle requires rotating the magnets which can be awkward for low tolerance field parameters. Additionally, for large enough angles, the magnets will block the path of the light. Electromagnets can be tuned by altering the current but alone are not feasible setups in oblique geometries; comparable homogeneity at 10s G has been attained but with $> 10^{\circ}$ divergence in field orientation over the same length scales [254].

Notwithstanding these obstacles, in this chapter we are able to overcome some of these issues and show improved performance of Rb filters with applied oblique fields. These include a realisation of the best FOM passive filter and the narrowest FWHM passive filter recorded to date. Beyond numerical comparisons, we incorporate cascading into our setups to suppress all but one peak as demonstrated in the last chapter. We are also able to select which peaks to transmit without interchanging magnets or rebuilding the experiment by varying input polarisation and the magnetic field vector

In this chapter, we begin by giving a theoretical background to magneto-optical rotation in the oblique geometry. We compare the polarisation evolution of light as it moves through the vapour cell in the Faraday, Voigt and oblique geometries. We visualise these polarisation evolutions by plotting Stokes parameter 'paths' on the Poincaré sphere [255, 256, 235, 257]. We discover that the oblique geometry exhibits elliptical birefringence which most notably does not guarantee orthogonal

propagation eigenmodes. We find that elliptical birefringence offers advantages over the circular and linear birefringences associated with the Faraday and Voigt geometries respectively and explain the origins of these benefits. We then describe the setup for two experiments: an Oblique-Voigt filter composed of an oblique cell and a Voigt cell and an Oblique Double Pass filter composed of one oblique cell with light passed through twice. We introduce a tunable magnetic field configuration composed of an axial field from an electromagnet (solenoid) and a transverse field from two plate magnets. The resultant oblique magnetic field is verified using the python package *Magpylib* [236]. This configuration allows us to alter the angle of the resultant field by varying the contribution from the two magnetic sources. As in the previous chapter, we discuss the roles of each cell in the cascade (or in the case of the Double Pass filter, each pass).

We present fitted data for the two filters showing excellent agreement. For the Double Pass filter, we show a different parameter set which switches the operation of the filter from line centre to both wings. We also predict input polarisations to select for either wing. In our outlook, we reflect on the competitive performance of these filters alongside their compactness and tunability. We ponder emerging applications in designing frequency comb mode selectors for use outside a laboratory [130, 258, 259].

4.2 Theory

4.2.1 Revisiting Stokes Parameters and the Poincaré Sphere

When studying cascading, we used Stokes parameters [233, 234] to describe the output polarisation of light after each optical component in our setup. When plotted as a function of detuning, we were able to gain insight into why certain frequencies were rejected, transmitted or partially transmitted in our filters. We could then tailor our filter to output desired polarisation states by choosing appropriate

geometries and parameters. However, this formalism treats the continuous polarisation change that occurs as light moves through the vapour as a black box. To gain insight into polarisation evolution, we can plot Stokes parameters (defined in 2.5.2) against distance propagated through the cell.

ElecSus can calculate the intermediate evolution of the electric field as it moves through the cell. By assuming the cell parameters are constant throughout, refractive indices are found. Then *ElecSus* can calculate the effect of these refractive indices on light travelling progressive distances through the cell. Additionally, we make use of the Poincaré Sphere as a visualisation tool. Whilst in the last chapter, we plotted 2D diagrams of each Stokes parameter, the Poincaré diagram is a 3D diagram where a single point is plotted as a function of all three Stokes parameters. Assuming that the Stokes parameters are continuous functions of the distance propagated, we can then plot paths on the Poincaré Sphere and identify patterns. Note that the Poincaré sphere representation has analogies with the Bloch [260, 261], Riemann [262, 263], Majorana [264, 265] and the *Coherence* Poincaré sphere [266, 267] in other disciplines. However, each representation is slightly different and therefore care is needed when drawing parallels.

4.2.2 Circular, Linear and Elliptical Birefringence

In Fig. 4.1, we demonstrate the Poincaré Sphere representation for a Faraday and Voigt cell. We plot frequencies with near 100% filter transmission for the setups shown in a) and b). We note that the Faraday cell shows polarisation evolution on the equator while the Voigt cell evolves through the prime meridian. In words, the linearly horizontal input light (↔) is rotated in a plane transforming to diagonal light at $-45°$ (↖↘), vertically linear light (↕), the opposite diagonal (↙↗) before becoming horizontal once again restarting the cycle. On the other hand in the Voigt cell, the left hand circular light (↺) cycles in handedness through diagonal at $-45°$ (↖↘), right hand circular light (↻), the opposite diagonal (↖↘) and back to left hand circular light.

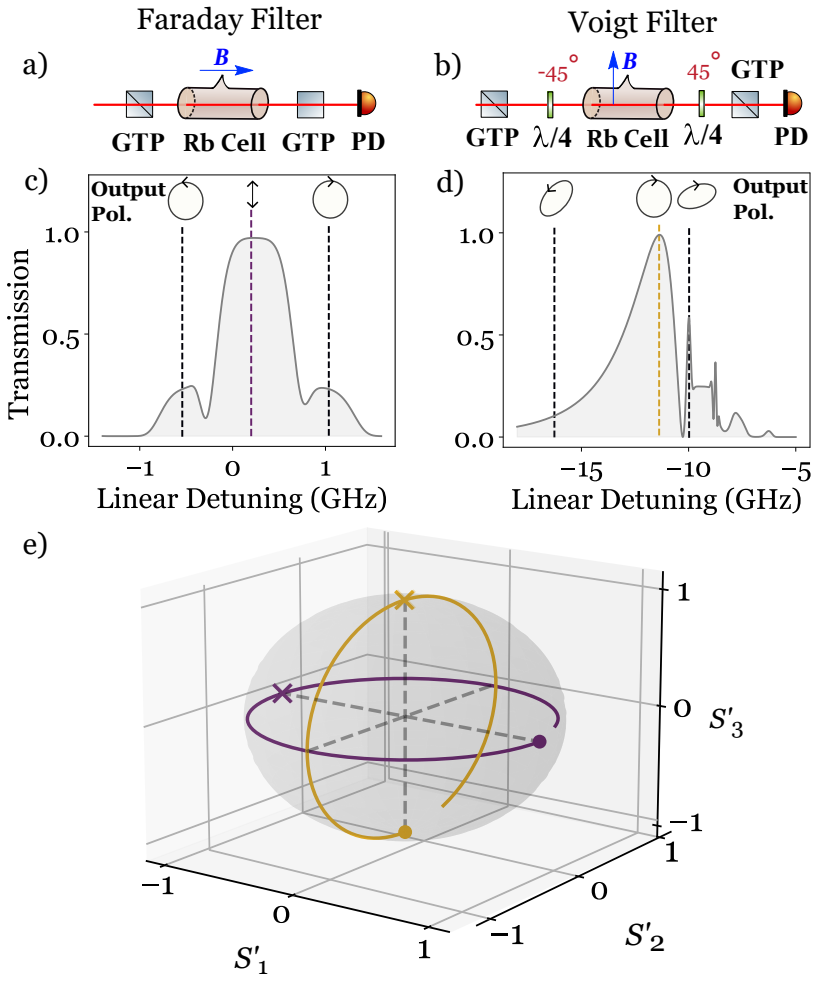

Geometry	θ (°)	D-line	T (°C)	B (G)	Inp. Pol.
Faraday	0	D2	63	160	Lin. Hor. ↔
Voigt	90	D1	100	3500	L.H. Circ. ↺

Figure 4.1: Faraday and Voigt polarisation evolutions on the Poincaré Sphere. a) and b) show the experimental setups to produce the filter profiles in c) and d) after 75 mm in natural abundance Rb cells. Parameters are in the table. Polarisation animations of the frequency dependent output polarisations are shown. e) shows curves on the Poincaré sphere for the dashed line frequencies in c) and d) as their polarisation evolves through the cell. 'x' marks the polarisation state after 75 mm propagation. f) and g) are projections on to the S'_3 and S'_1 planes.

As a reminder, thermal vapours in the presence of a magnetic field are dichroic (exhibit polarisation dependent absorption) [72] and birefringent (exhibit polarisation dependent refraction) [268]. In these examples, the attenuation is minimal so we can explain these paths solely in terms of birefringence. In the Faraday geometry, the invariant polarisations are left/right hand circular light (See A.2). From 2, this implies circular light does not evolve through new polarisation states as it moves through the cell but remains circular. Additionally, this means that circular light is differentially refracted, which we call circular birefringence. With these facts, we can justify the equatorial path of Faraday rotation. Linearly horizontal light, $|\leftrightarrow\rangle$, can be decomposed into the form (See A.2),

$$|\leftrightarrow\rangle = \frac{1}{\sqrt{2}}(|\circlearrowleft\rangle + |\circlearrowright\rangle), \tag{4.1}$$

where $|\circlearrowleft\rangle/|\circlearrowright\rangle$ are the left/right circular components of $|\leftrightarrow\rangle$. After moving through some length of the material, the left/right handed components do not evolve. However, the refractive phases γ and ζ are applied to the components[1],

$$|\text{Lin.}\rangle = \frac{1}{\sqrt{2}}(|\circlearrowleft\rangle + \mathrm{e}^{\mathrm{i}(\zeta-\gamma)}|\circlearrowright\rangle), \tag{4.2}$$

,

resulting in a new linear polarisation, $|\text{Lin.}\rangle$, which is diagonal at $\zeta - \gamma = \pm\pi/2$, vertical at $\zeta - \gamma = \pi$ and horizontal again at $\zeta - \gamma = 2\pi$. Since the refractive indices are continually applied, $\zeta - \gamma$ continually increases as the light moves through more vapour resulting in a polarisation cycle. Note that the output polarisation must be linear since it is a combination of equal magnitudes left hand circular ($\tilde{S}_3 = -1$) and right hand circular ($\tilde{S}_3 = 1$) light. Hence we observe a polarisation cycle on the $S'_1 - S'_2$ (equatorial) plane where S'_3 is always zero.

[1] Throughout this discussion we drop all global phases that do not have an impact on polarisation state

In the Voigt case, the invariant polarisations are linearly horizontal and vertical light (see A.2). Analogously, this implies horizontal/vertical light does not evolve through new polarisation states as it moves through the cell. This means linearly horizontal and vertical light are differentially refracted which we call linear birefringence. A left hand circular state, $|\circlearrowleft\rangle$, can be written as (see A.2),

$$|\circlearrowleft\rangle = \frac{1}{\sqrt{2}}(|\leftrightarrow\rangle + \mathrm{e}^{\mathrm{i}\frac{\pi}{2}}|\updownarrow\rangle), \tag{4.3}$$

where $|\leftrightarrow\rangle/|\updownarrow\rangle$ are the linearly horizontal and vertical components of $|\circlearrowleft\rangle$. After moving through some length of the vapour, the phases γ and ζ are applied,

$$|\mathrm{Pol.}\rangle = \frac{1}{\sqrt{2}}(|\leftrightarrow\rangle + \mathrm{e}^{\mathrm{i}\frac{\pi}{2}(\zeta-\gamma)}|\updownarrow\rangle), \tag{4.4}$$

resulting in a new polarisation, $|\mathrm{Pol.}\rangle$, which is linear diagonal at $\zeta - \gamma = \pm\pi/2$ and right hand circular at $\zeta - \gamma = \pi$. The S_1 component is preserved since it is a combination of equal parts horizontal ($\tilde{S}_1 = 1$) and vertical ($\tilde{S}_1 = -1$) light. Hence we observe a polarisation cycle on the $S_2' - S_3'$ plane where S_1' is always zero.

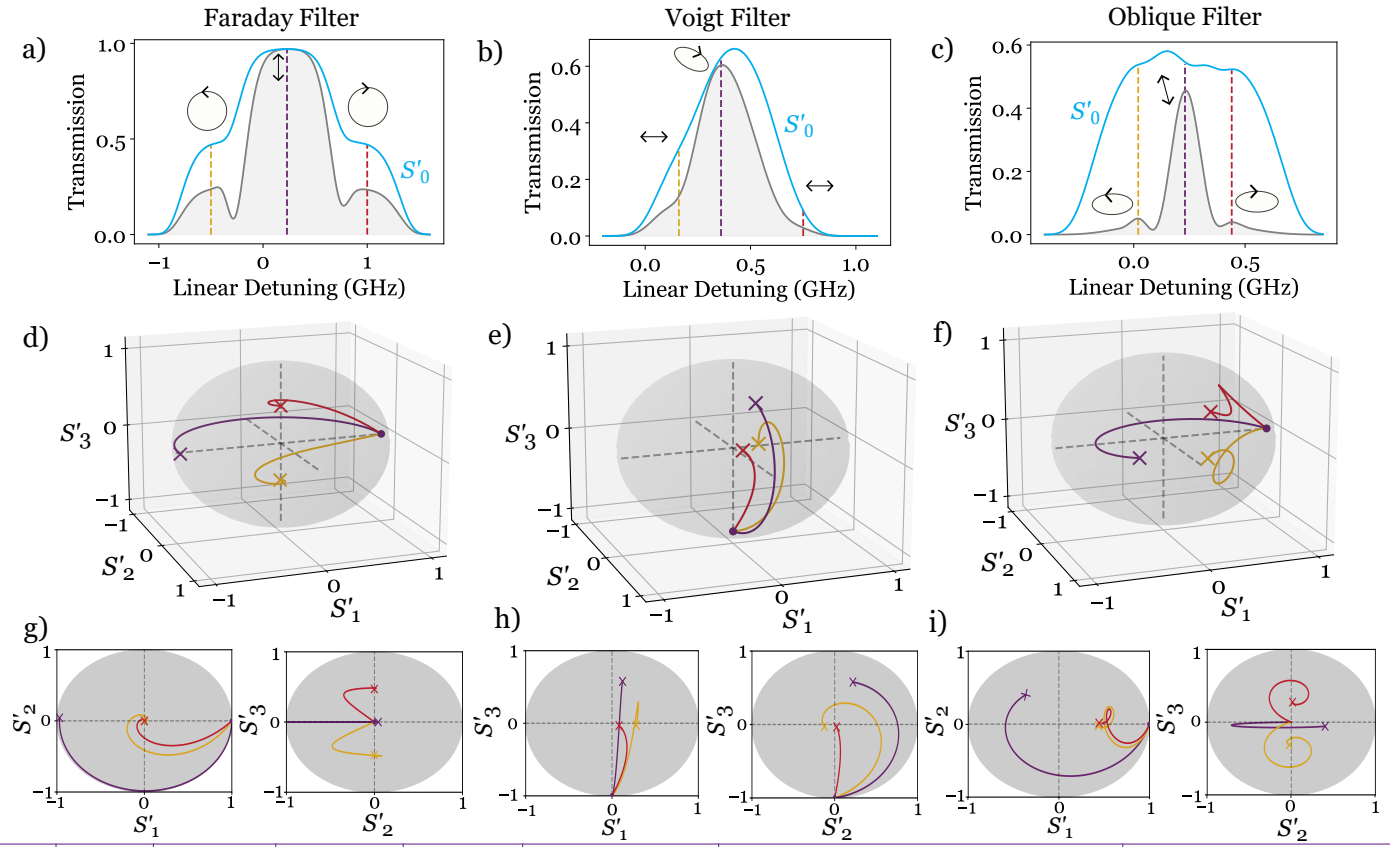

Geometry	θ (°)	D-line	T (°C)	B (G)	Inp. Pol.	% Rejection (Gold Freq.)	% Rejection (Red Freq.)
Faraday	0	D2	63	160	Lin. Hor. ↔	49	50
Voigt	90	D1	107	514	L.H. Circ. ↺	54	68
Oblique	86	D2	97	227	Lin Hor. ↔	96	92

Figure 4.2: Caption Overleaf

Figure 4.2: A comparison of light rejection outside the dominantly birefringent region in different geometries. a), b) and c) show filter profiles in the Faraday, Voigt and oblique geometries respectively using 75 mm natural abundance Rb cells. Parameters shown in the table. S_0' is also plotted in blue. Animations of the output polarisations for three frequencies indicated by a dotted vertical line are shown. The signal frequency (purple) is the maximum transmitted frequency. The gold and red frequencies are outside the dominantly birefringent region (an exception is made for the Voigt red frequency where it is close to the boundary of the birefringent region). The Faraday and oblique filters are on the D2 line for direct comparison. The D1 line is chosen for the Voigt filter since natural abundance Rb-D2 Voigt filters with a central peak profile are not competitive in their performance. d), e), f) show the polarisation evolution of the three frequencies on the Poincaré sphere. The input polarisation state propagates to a new polarisation state after 75 mm marked by 'x'. g), h) and i) are 2D projections of the same paths. The oblique filter rejects light outside the dominantly birefringent region at $> 90\%$ while other geometries reject at $\sim 50\%$.

In Fig. 4.2, we have three filter profiles incorporating a Faraday, Voigt and oblique cell ($\theta = 86°$). For each filter, we plot S_i' curves for three frequencies on the Poincaré sphere as a function of distance propagated through the cell. In this case, the signal frequencies (in purple on each filter profile) are transmitted at less than 100 % and therefore the curves do not remain on the surface of the Poincaré sphere. We choose $\theta = 86°$ for the oblique filter since it gives a desirable line centre profile with high FOM.

By eye, the oblique signal frequency appears to take a similar path to the Faraday signal frequency. However, the oblique signal is absorbed more and is not quite vertical in its output leading to lower maximum transmission. In fact the oblique rotation at this frequency approximates to circular birefringence (See Fig. 4.3). A complete picture of the oblique magneto-optical rotation at $\theta = 86°$ can be found by addressing other frequencies. The red and gold frequencies represent detunings outside the region where differential refraction occurs i.e the *birefringent region*. From 2, these frequencies lie in a region where only the dichroic features of the thermal vapour are exhibited and either one of the invariant polarisations is absorbed.

In the Faraday/Voigt cases, either one of the circular/linear invariant polarisations is absorbed. In Fig. 4.2, this is most clear in the Faraday case where absorption of one circular hand leaves left hand circular light (gold) and right hand circular light (red). In the Voigt example, vertical light is absorbed for both the red and gold frequencies leaving horizontal light. This is since the vertical transmission region is completely enclosed in the horizontal transmission region (see Fig. 4.5). In the oblique case, horizontal input light is absorbed leaving horizontal elliptical states. Unlike at the signal frequency, this is clearly not circular birefringence but evidence of elliptical dichroism. In fact, the oblique geometry in general exhibits elliptical birefringence and dichroism which is frequency dependent.

It is with this knowledge that we see the first advantage of this oblique filter over the Faraday and Voigt cases. An ideal line centre filter would reject all light outside of a selected peak i.e. high rejection of light outside the dominantly birefringent region. This would require the output polarisations at the signal and at the red and gold frequencies to be orthogonal allowing a polariser to discriminate between them. In the Faraday and Voigt cases, the red and gold frequencies are not orthogonal to the purple signal frequency. Given that the signal frequencies can be decomposed into approximately equal contributions of both invariant polarisations, the red and gold frequencies are only rejected by the crossed polariser at $\sim 50\%$.

However, in the oblique filter, the invariant polarisations are frequency dependent. Therefore it is possible for the output polarisations of the signal and red and gold frequencies to be almost orthogonal. As a result, in this example more than 90% of the light at the red and gold frequencies is rejected after passing through the crossed polariser. This results in filters with much smaller ENBWs without significant detriment to the signal frequency transmission.

4.2.3 Non-Orthogonal Eigenmodes & Invariant Polarisations

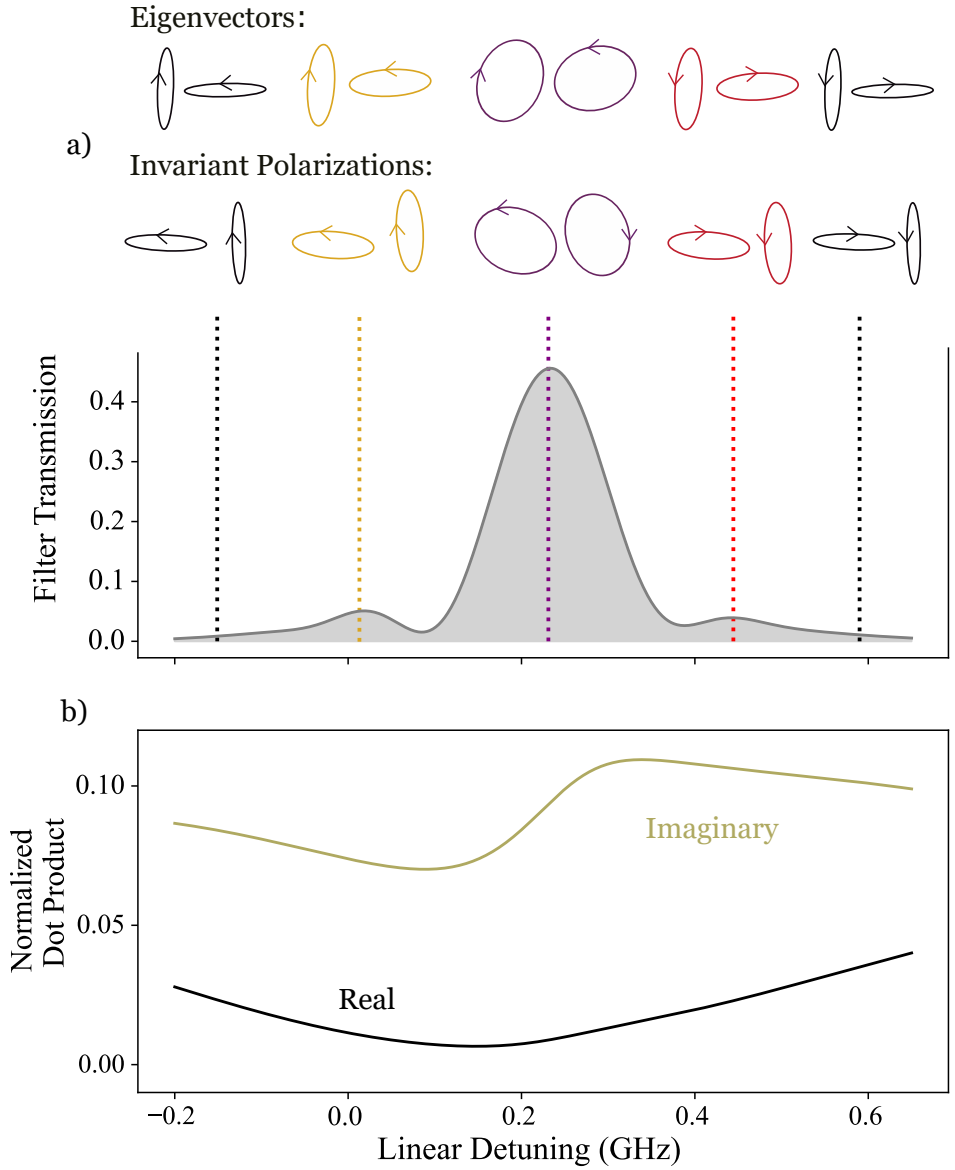

Figure 4.3: a) An oblique filter profile (Parameters shown in Fig.4.2) with animations of the frequency dependent eigenmodes and invariant polarisations for five selected frequencies above. The signal frequency eigenmodes (purple) are approximately circular. Eigenmodes are calculated using analytic solutions [252]. b) Plots of the real and imaginary parts of the normalised dot product of the eigenmodes $\vec{a}$ and $\vec{b}$: $\frac{\Sigma_i \vec{a}_i^* \cdot \vec{b}_i}{|\vec{a}||\vec{b}|}$. Here $\vec{a}^*$ denotes the complex conjugate of $\vec{a}$. Note that neither part is ever zero confirming the eigenmodes are non-orthogonal. The value of the dot product changes with frequency confirming the eigenmodes are frequency dependent and non-orthogonal.

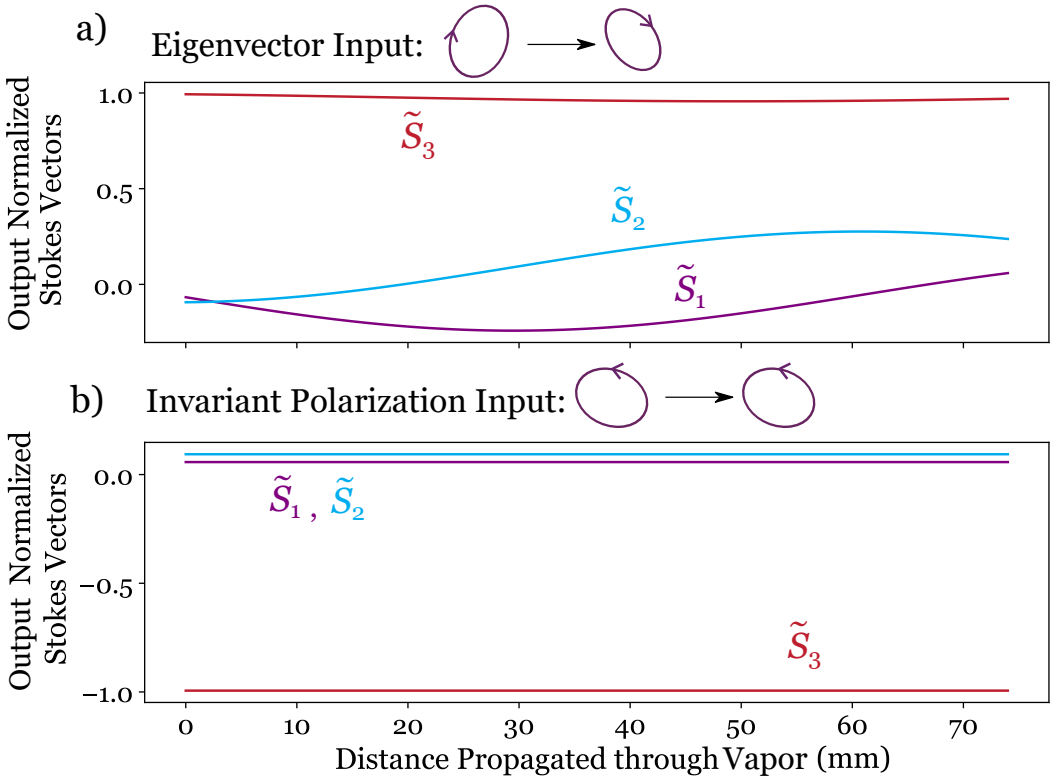

Figure 4.4: $\tilde{S}_i$ plotted for the purple frequency in Fig. 4.3 for an eigenmode and invariant polarisation input. The invariant polarisation as expected has constant $\tilde{S}_i$ since its polarisation does not evolve. However,the $\tilde{S}_i$ for the eigenmode are not constant proving the eigenmode is not invariant.

In the last subsection, we saw initial evidence for frequency dependent eigenmodes and invariant polarisations in the oblique geometry. Fig. 4.3 shows the oblique filter with animations of the eigenmodes shown for five frequencies. Below panel b) shows the normalised dot product of the eigenmodes which varies with frequency. However, it also reveals another property of the eigenmodes: given the normalised dot product is never zero, the oblique eigenmodes are non-orthogonal.

To take a step backwards, Faraday and Voigt eigenmodes are orthogonal. In Chapter 2, we discussed the difference in roles between the eigenmodes and invariant polarisations; one forms the rotation matrix used in Jones Calculus propagation and the other is a polarisation that undergoes no evolution as it moves through the cell. Up until now, this distinction has appeared overly fastidious since in the Faraday and Voigt geometry, the eigenmodes and invariant polarisations are one

and the same. In general, the invariant polarisation is orthogonal to an eigenmode. If the eigenmodes are already orthogonal then, given polarisation is defined in 2D, the invariant polarisations are just the eigenmodes. However, given the oblique eigenmodes are non-orthogonal, they are not the same state as the oblique invariant polarisations (More details can be found in A.2). In fact, as Fig. 4.4 shows, an eigenmode will not in general undergo invariant polarisation. We therefore need to be careful to use the right vector in the right context.

4.2.4 Birefringent Regions

With a better understanding of invariant polarisations, we can now calculate the dominantly birefringent regions for the Faraday, Voigt and oblique filters explictly. Fig. 4.5 shows the filter profiles alongside the transmission regions for each invariant polarisation in red and yellow. The dominantly birefringent region, where differential refraction can occur between the invariant polarisations, stretches only slightly beyond the orange overlap of the red and yellow profiles. As such the orange overlap provides a good estimate of the frequency range over which birefringence dominates. To calculate the invariant polarisations in the oblique case, we use *ElecSus* [155, 156] to output the eigenmodes for each frequency. We then find the two unique normalised vectors orthogonal to the eigenmodes lying in the $x - y$ plane in which the light is polarised. A table of the invariant polarisations used to create each region is found in Fig. 4.6.

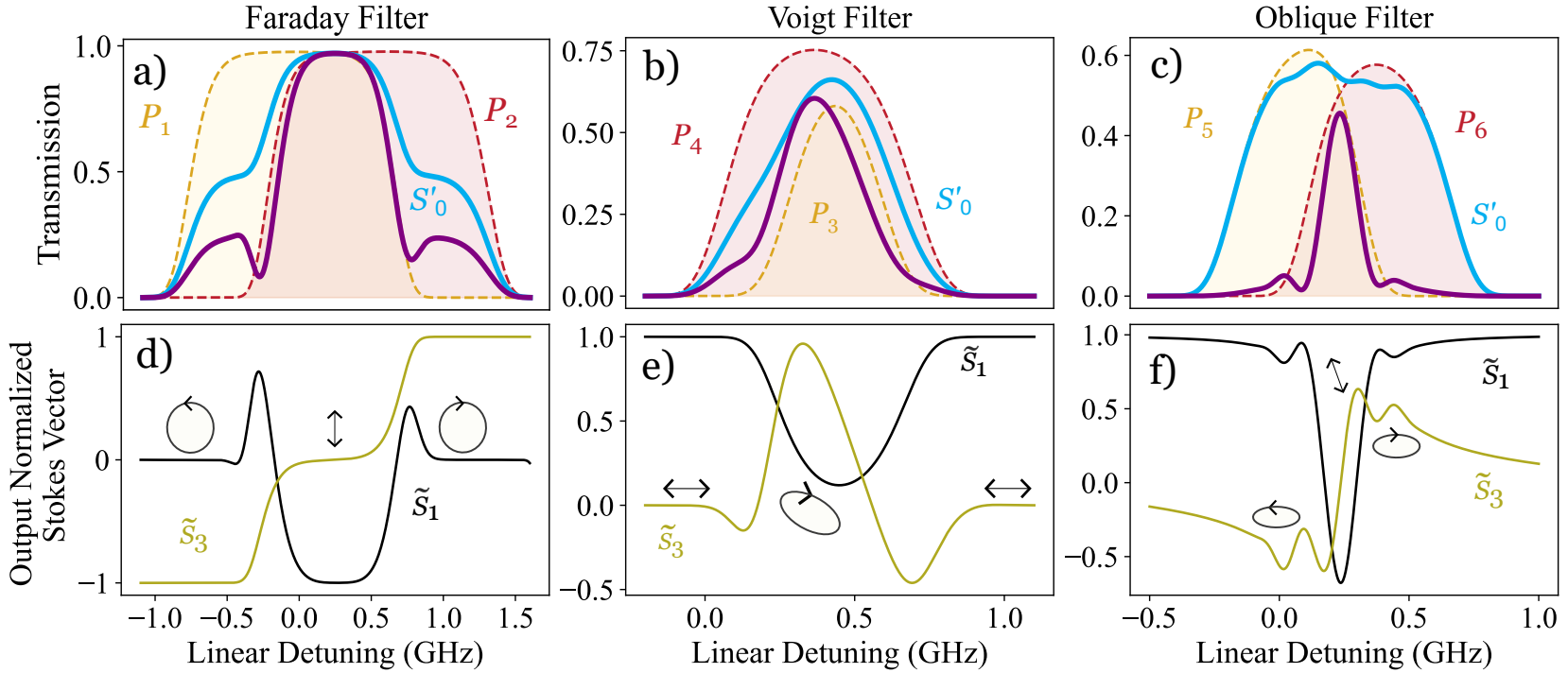

Geometry	θ(°)	D-line	T (°C)	B (G)	Inp. Pol.	Birefringent Region FWHM (MHz)	Filter FWHM (MHz)
Faraday	0	D2	63	160	Lin. Hor.↔	850	790
Voigt	90	D1	107	514	L.H. Circ. ↺	320	310
Oblique	86	D2	97	227	Lin Hor.↔	200	150

Figure 4.5: a), b), c) depict the overlap between the S'_0 regions (yellow and red) after inputting invariant polarisations, P_i (see Fig. 4.6). The orange overlaps provide a good estimate of the extent of the birefringent regions. S'_0 for the input polarisation in blue. Parameters in table, 75 mm natural abundance Rb cells used. d), e), f) show the $\tilde{S}_1$ (black) and $\tilde{S}_3$ (gold) curves with animations of the output polarisations for the three chosen frequencies in Fig. 4.2. The narrower oblique birefrigent region poses an upper limit on the FWHM.

We note that, as expected, the main peaks of each filter lie broadly within the birefringent region. An exception is the Voigt filter whose peak on the negatively detuned side has significant dichroic contribution. The oblique filter shows a much narrower birefringent region which results in the narrowest FWHM.

Transmission Region	**Invariant Pol.**	**Transitions Ind.**
P_1 (Faraday)	L.H.C ↺	σ^+
P_2 (Faraday)	R.H.C. ↻	σ^-
P_3 (Voigt)	Lin. Hor. ↔	π
P_4 (Voigt)	Ver. Hor. ↕	σ^-/σ^+
P_5 (Oblique)	Freq. Dep.	$\sigma^-/\sigma^+/\pi$
P_6 (Oblique)	Freq. Dep	$\sigma^-/\sigma^+/\pi$

Figure 4.6: A table of the invariant polarisation transmission regions plotted in Fig. 4.5. We note the polarisation state associated with the transmission region as well as the transitions induced by the polarisation state. The oblique invariant polarisations unlike the Faraday and Voigt cases are frequency dependent and may induce at least two of the three $\sigma^+/\sigma^-/\pi$ transitions.

This relationship between polarisation and transitions induced can be gained from the angular part of the dipole transition matrix which we discuss in Appendix C. We quote the oblique projection operators for our discussion which are:

$$\begin{aligned} \sigma^+ &: \frac{\widehat{x}\cos\theta + \mathrm{i}\widehat{y}}{\sqrt{\cos^2\theta + 1}}, \\ \sigma^- &: \frac{\widehat{x}\cos\theta - \mathrm{i}\widehat{y}}{\sqrt{\cos^2\theta + 1}}, \\ \pi &: \ \widehat{x}. \end{aligned} \tag{4.5}$$

i.e. left and right elliptical polarisations induce $\sigma^{+/-}$ transitions and linearly horizontal light induces π transitions. Note that it is imposible for any input polarisation to induce just one of these transitions and must induce at least two (provided the linestrengths for the two transitions are non-zero). Therefore the oblique birefrigent region has even stricter criteria then the Faraday and Voigt equivalents. The region represents the overlap between a region where at least two transitions are not induced (maybe three), and another region where at least two transitions (maybe three) are not induced.

4.2.5 Summary of Oblique Filter Advantages

To summarise, oblique filters (tuned with appropriate parameters) offer two advantages. Firstly, oblique filters reject light outside the dominantly birefringent region much more effectively. Given that the invariant polarisations are frequency dependent, the output polarisations at the signal frequency and outside the dominantly birefringent region are almost orthogonal. This allows for much larger discrepancy between the frequencies in transmission by a polariser and results in smaller ENBWs.

Secondly, the oblique birefringent regions can be narrower. This is because the overlap in the invariant polarisation transmission regions is smaller. This is since all three $\sigma^{+/-}, \pi$ transitions can be induced by both the non-orthogonal invariant polarisations which leads to narrower birefringent regions and narrower FWHMs.

Together, smaller ENBWs, narrower FWHMs, all without too much detriment to the signal transmission frequency lead to better performing line centre filters.

4.3 Setup

Having shown two advantages of the oblique filter over the Faraday and Voigt cases, we propose two filter designs: an Oblique-Voigt filter and an Oblique Double Pass filter which are both shown in Fig. 4.7.

We use the same Toptica DL100 laser [240] as used in the previous chapter's investigation scanning over an approximate range of 20 GHz. We send part of the light towards reference optics (See Appendix D for more details) and the rest to our two filter designs. A neutral density filter lowers the power to approximately 100 nW with a $1/e^2$ width of 100 μm before each experiment. This ensures we stay within the weak probe regime [169] which can be readily modelled using *ElecSus*. We use Thorlabs PDA36A2 amplifying photodetectors [241] setting the gain at the highest setting available '70 dB'. We did not verify the actual gain achieved.

Cell 1 and Cell 3 are the same 75 mm natural abundance Rb cell which is heated via two Omega Polyimide flexible heaters [269] glued down the length of the cell. The cell is then placed inside a solenoid which provides on the order of 10 G of axial field to the cell. The cell and solenoid are placed between two plate cuboidal magnets of dimensions 150 × 50 × 10 mm which provide a transverse field of 100s G. This gives a resultant field which makes an angle θ with the k-vector. Fig. 4.9 shows a magnetic field plot of the field along the propagation direction simulated using the python package *magpylib* [236]. The magnetic field strength variation is less than 10% of the mean value and the value of θ varies by less than 2° over the length of the cell. This setup is an improvement on the previous chapter's investigation where the solenoid contributed both to the heating and magnetic field. In this experiment, since the solenoid field needed is so low, the heating it offers is minimal compared to that provided by the flexible heaters. In practical terms we have independent heating and magnetic field variation within the parameter space of interest.

In the Oblique-Voigt filter, the oblique cell and the Voigt cell are placed between two crossed polarisers with linearly horizontal light emerging after the first polariser and linearly vertical light emerging after the second. The Voigt cell is the same as that in the Faraday-Voigt setup: a cuboidal 5 mm natural abundance Rb cell placed in a copper heater between two top hat NdFeB magnets [243]. More details can be found in the previous chapter. The cell choices made are a compromise between minimising collisional broadening which can be achieved at lower temperatures (and hence we want longer cells to compensate for the number of atoms with which we interact) and generating homogeneous magnetic fields which is more challenging for longer cells [222].

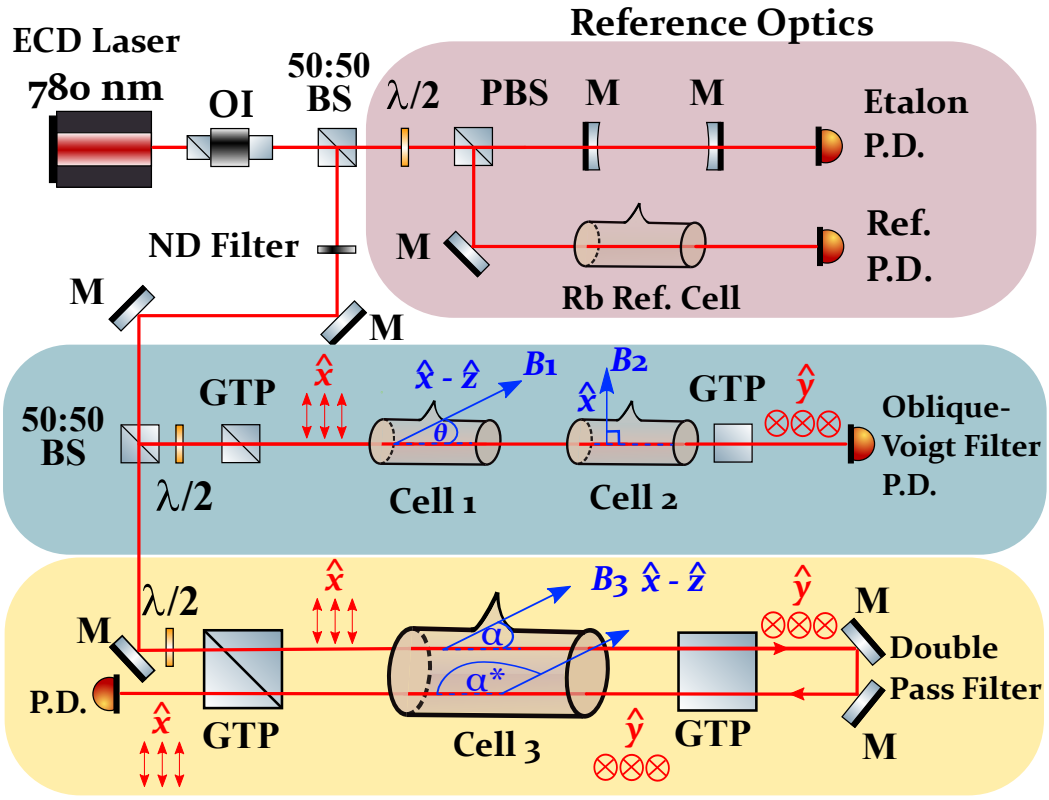

Figure 4.7: The experimental setup for the two oblique filter experiments. 780 nm light (Rb-D2) from an external cavity diode (ECD) laser is directed towards reference optics and the experiments. The reference optics includes an etalon setup for relative frequency calibration and a zero field room temperature natural abundance Rb setup for absolute frequency calibration [3] (See Appendix D for more details). A neutral density (ND) filter is incorporated to reduce the power so as to remain in the weak probe regime. The red arrows and their associated hat operators depict the polarisation state after each Glan-Taylor Polariser (GTP). Hat operators are also added to the blue magnetic field vectors for clarity in their direction. See Appendix C for a rigorous definition of the axes used throughout. The first experiment is an Oblique-Voigt filter composed of an oblique cell followed by a Voigt cell between two crossed Glan-Taylor polarisers. The k-vector of the light makes an angle θ with the the magnetic field exerted on Cell 1, B_1, and is perpendicular to the magnetic field exerted on Cell 2, B_2,. The second experiment is a Double Pass filter which involves one oblique cell between crossed polarisers. Light passes through the system with k-vector at an angle α to the magnetic field, B_3, before being reflected back through the system and making the supplementary angle, $\alpha^* = (180 - \alpha)°$, with the same magnetic field, B_3. M – Mirror, (P)BS – (Polarising) Beamsplitter, OI – Optical Isolator, P.D. – Photodetector.

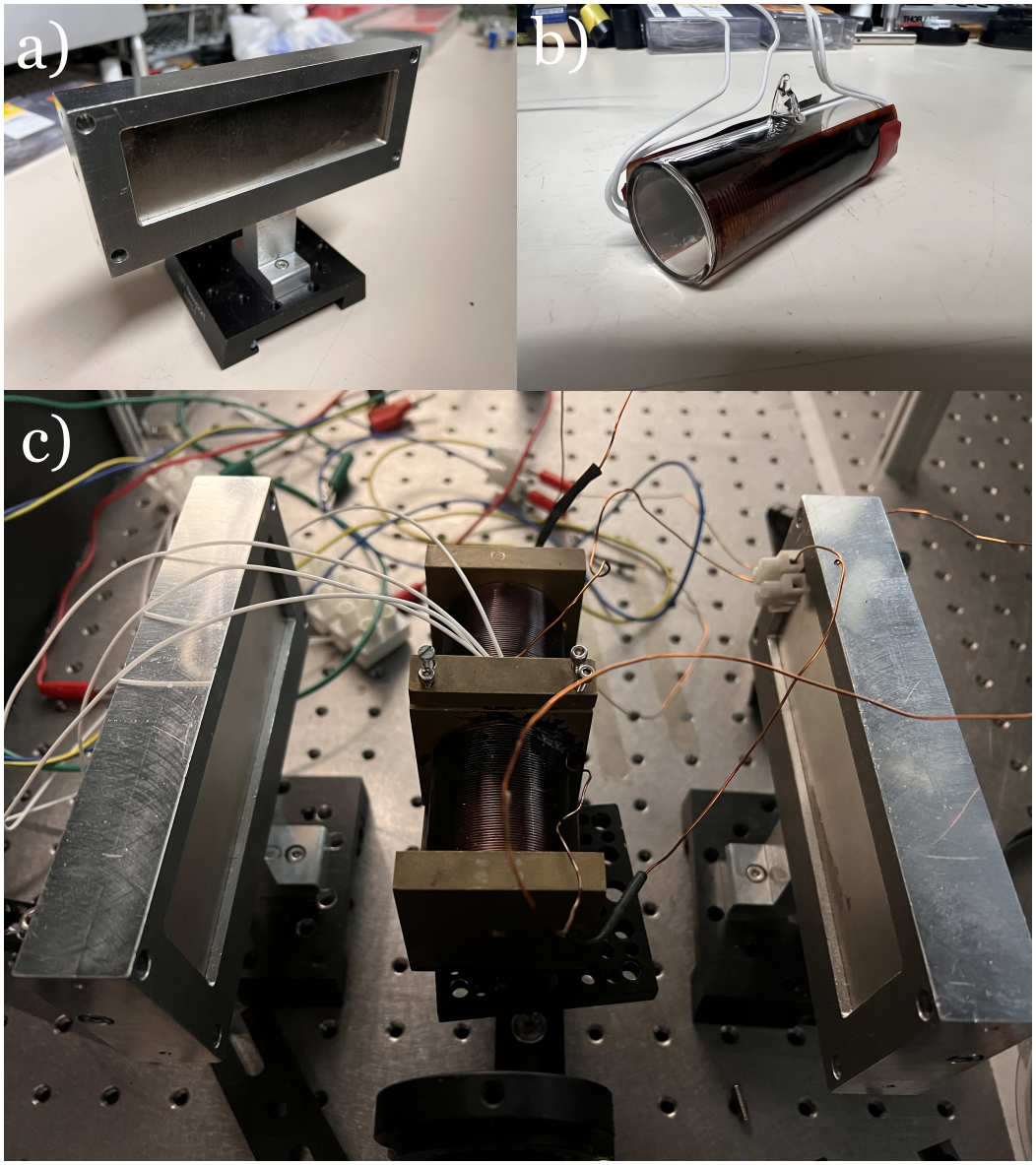

Figure 4.8: Photos from the Lab. a) One of the 150 x 50 x 10 mm cuboidal magnets. The exact material and remanence field of the magnet is estimated to be 1350 G. It has also been used in this investigation [270]. b) A 75 mm natural abundance vapour cell (which we use as Cell 1 and 3) with flexible heaters adhered along the sides. c) The setup to generate the field and temperature needed for Cell 1 and 3. The cell from panel b) is heated by adjusting the current flowing to the flexible heaters. The transverse magnetic field is generated by two magnets of the type pictured in panel a). The axial field is generated by a solenoid. Note that the required current to generate the solenoid field is low and contributes very little to heating.

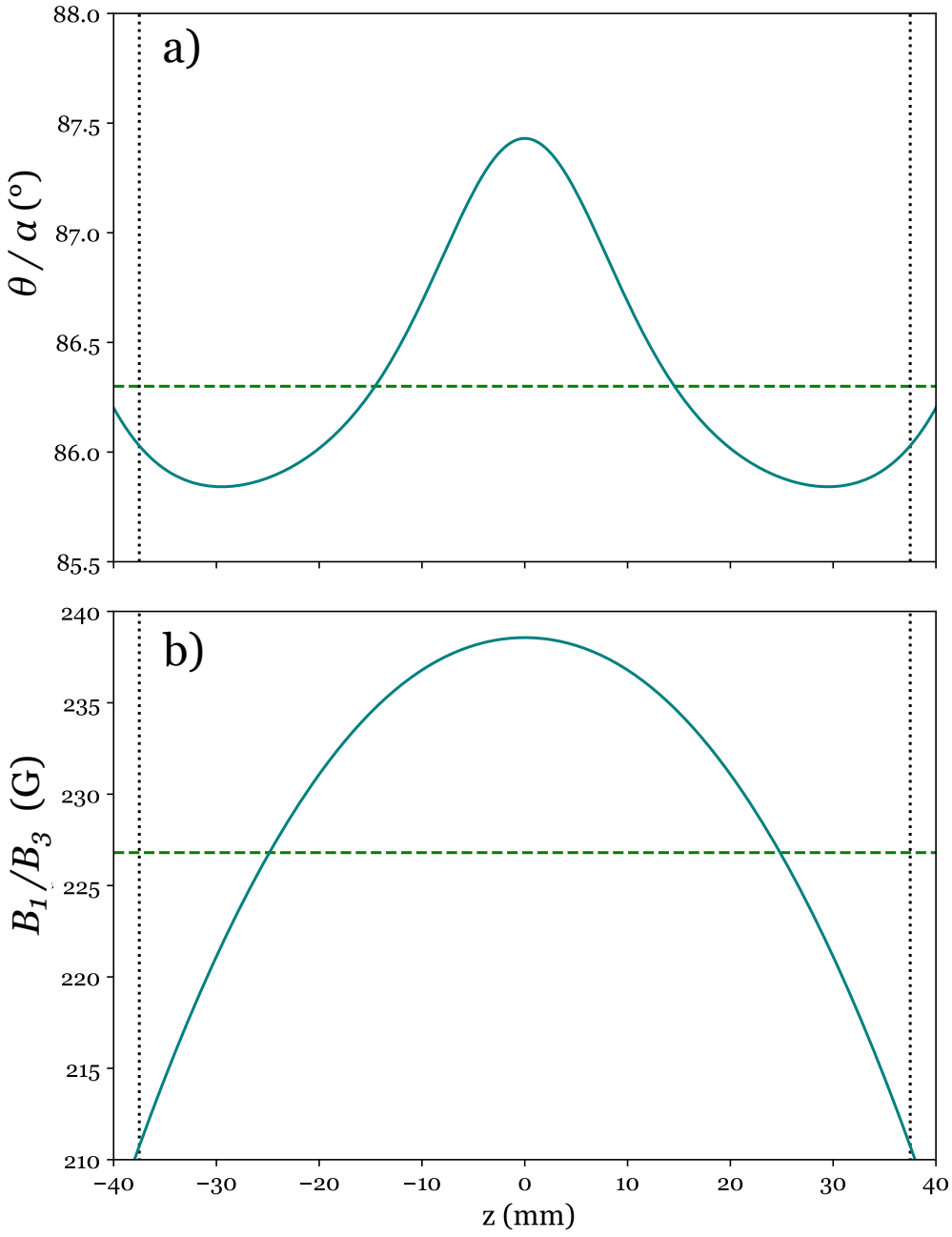

Figure 4.9: Theory plots showing the variation of the resultant magnetic field exerted upon Cell 1 and Cell 3. The vertical lines indicate the extent of the 75 mm cell. a) shows the variation of θ or α depending on whether we are considering Cell 1 or Cell 3. b) shows the variation of B_1 or B_3. The intercept of the green line on each graph is the mean value of the variable averaged over the length of the cell. Modelling was generated using *magpylib* from code developed by Thomas Robertson-Brown. It assumes the plate magnets have a remanence field of 1350 G seperated by 175 mm. The solenoid is broken into two parts with 12 mm separation each containing 8 layers of 53 coils with wire thickness 0.8 mm. The length of each solenoid is 43 mm. The current is 0.14 A.

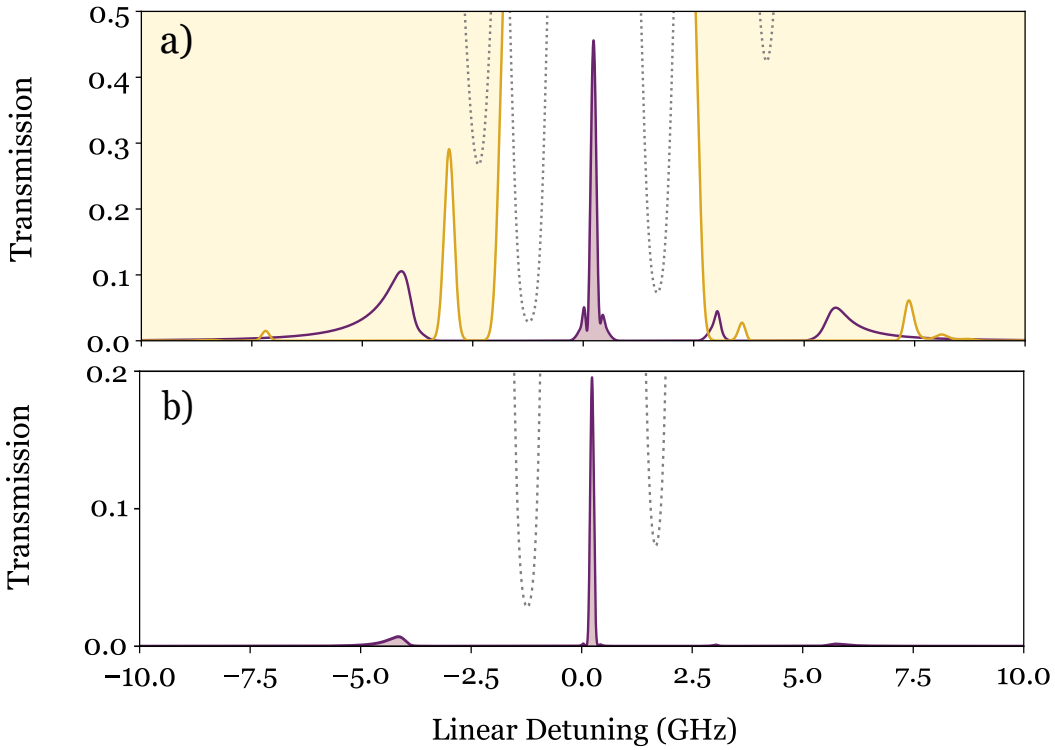

Figure 4.10: Theory curves plotted using *ElecSus* of the two filter experiments with setups described in Fig. 4.7 and similar parameters as noted in Figs. 4.11 and 4.16. a) depicts the filter transmission (purple shading) of the Oblique-Voigt filter alongside the filter transmission if the Voigt cell (Cell 2) is removed (purple line). S_0' of the Voigt cell is shown shaded in gold. b) shows the filter transmission for the Double Pass filter (purple shading). Note that the first pass of the Double Pass filter is the purple line of panel a). A high temperature zero field natural abundance Rb cell is plotted (grey dotted line) to give a sense of the detuning range.

Analogous to the Faraday-Voigt filter, the role of the oblique cell is to transform the polarisation state of the light to form the filter peaks while the Voigt cell's role is to extinguish. Linearly horizontal light is input into the oblique cell and the light is rotated to be approximately vertical at the central peak but is output as elliptical at the three other peaks. The Voigt cell absorbs vertically linear input light in the wings beyond $\sim \pm 2$ GHz (see Fig. 4.10) since the vertically polarised light is an invariant polarisation associated with $\sigma^+/-$ transitions. The high temperature and magnetic field leads to high absorption and this absorption is positively and negatively detuned from centre due to Zeeman shifts of the transition frequencies. In addition, the Voigt cell also highly absorbs invariant horizontal light associated

with π transitions between $\sim$ –5 and 6 GHz (See Fig. 4.12). As such everything between –5 and 2 GHz and, 2 and 6 GHz, where the other three peaks lie, is highly absorbed.

We note that the Voigt cell has a higher magnetic field than in the Faraday-Voigt filter leading to a much larger central window. As such the Voigt cell does not select for a narrower peak from the first cell's transmitted peak like in the Faraday-Voigt filter. It was found through optimisation that a window that was narrower than the oblique FWHM would result in significant transmission reduction. This is the first Oblique-Voigt filter recorded in the literature.

The Double Pass filter consists of only the oblique cell between two crossed polarizers. Horizontally linear light is input, passes through the vapour making an angle α with the magnetic field. Rotated vertically linear light is selected by the crossed polariser. The light is then reflected back as vertically polarised light, passes through the vapour making an angle $\alpha^* = (180 - \alpha)^\circ$ with the magnetic field before being post-selected as horizontally polarised light. Both passes individually would give identical filter transmissions. This is due to the fact that any filter composed of a cell between two crossed polarisers has equivalent output if the crossed polarisers switched positions. In addition, the two different angles of the passes amount to a change in handed convention which results in no change to linear polarisations. (See Appendix A.5). This means the second pass has an intensity squared effect reducing the transmission of each peak by its transmission value squared after the first pass. This is advantageous in our case since the three unwanted peaks have 10% or less transmission after the first pass, resulting in less than 1% transmission after the second pass. On the other hand, the central peak at 40% transmission after the first pass is transmitted at 20% after the second pass. Panel b) of Fig. 4.10 gives the filter output of the Double Pass filter. While Double Pass filters have been realised before [271, 272, 123, 273], this is the first Oblique Double Pass filter recorded in the literature.

4.4 Results

4.4.1 Oblique-Voigt filter

We first present results for the Oblique-Voigt filter. Fig. 4.11 shows the output of the Oblique Voigt-filter. Mean values of parameters obtained from five fits are shown in the table. Data show excellent agreement with theory [244]. The filter realised has a ENBW, FWHM and FOM of 181 ± 1 MHz, 145 ± 1 MHz and 2.38 ± 0.01 GHz^{-1}. This is the highest FOM passive filter recorded in the literature as of time of writing. The two peaks either side of the main peak are somewhat detrimental to the profile shape but are both less than 10% transmission. As discussed in Fig. 4.2, these small side peaks are the result of light being rejected outside the birefrigent region at more than 90%. The residuals show some structure which we attribute to magnetic field inhomogeneity. In particular, the theory curves in panel b) of Fig. 4.13 show the extreme sensitivity of the filter profile to θ with no profile at all at $\theta = 90°$, an increase of less than 4° to the mean fit θ value. Given we found that θ can vary by as much as 2° in Fig. 4.9, this will have an effect on our fits. On the other hand, variation of magnetic field and temperature, as seen in panels a) and c), gives a similar profile with higher/lower transmission with wider/narrower FWHMs.

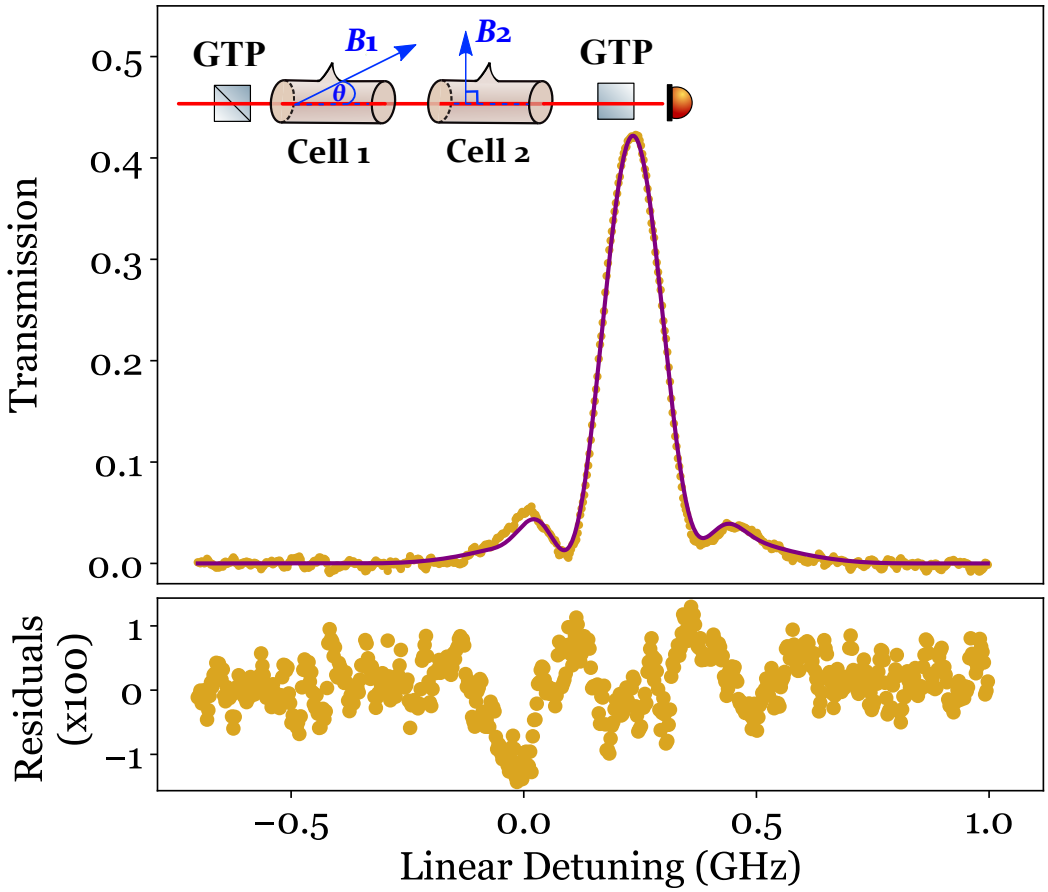

L_1/L_2 (mm)	T_1 (°C)	B_1 (G)	θ (°)	T_2 (°C)	B_2 (G)
75/5	96.8 ± 0.1	226.8 ± 0.7	86.3 ± 0.3	123.6 ± 0.2	3897 ± 3

Figure 4.11: Experiment (gold) with theory fit (purple) of the Oblique-Voigt filter using natural abundance Rb cells probed on the Rb-D2 line. Mean values and standard errors of the parameters obtained from fits of five spectra are presented in the table. Data and theory show excellent agreement [244]. An ENBW, FWHM and FOM of 181 ± 1 MHz, 145 ± 1 MHz and 2.38 ± 0.01 GHz^{-1} were obtained for one fit with standard errors being calculated from systematics.

In order to decrease uncertainty in the second cell parameter fits, we decided to fit a S_0' data curve for light passing through the second cell input linearly horizontal. Fig. 4.12 shows a fit. We plot heatmaps for the first and second cell parameter spaces (Fig. 4.14 and 4.15) which show the mean parameters obtained are near optimum, at least locally, in parameter space. Theory predicts FOMs of up to 2.7 GHz^{-1} for θ values closer to 87°.

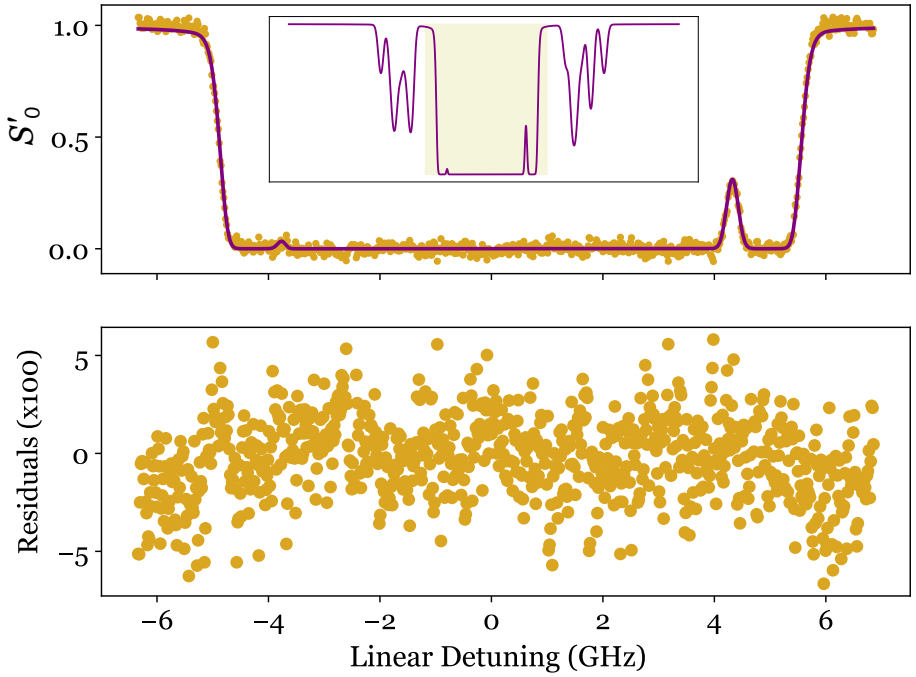

Figure 4.12: A S'_0 fit (purple) of data (gold) when linearly horizontal light was input into Cell 2. Fits of five spectra give the mean values and standard errors for Cell 2 parameters presented in Fig. 4.11. The fit is calculated over a smaller range of the spectrum as indicated by the beige area in the theory inset. Our 20 GHz scanning range is not able to capture the full spectrum. For normalisation we need to reduce the area of interest further so that the extremes of the spectrum return to approximately 100% transmission (See D).

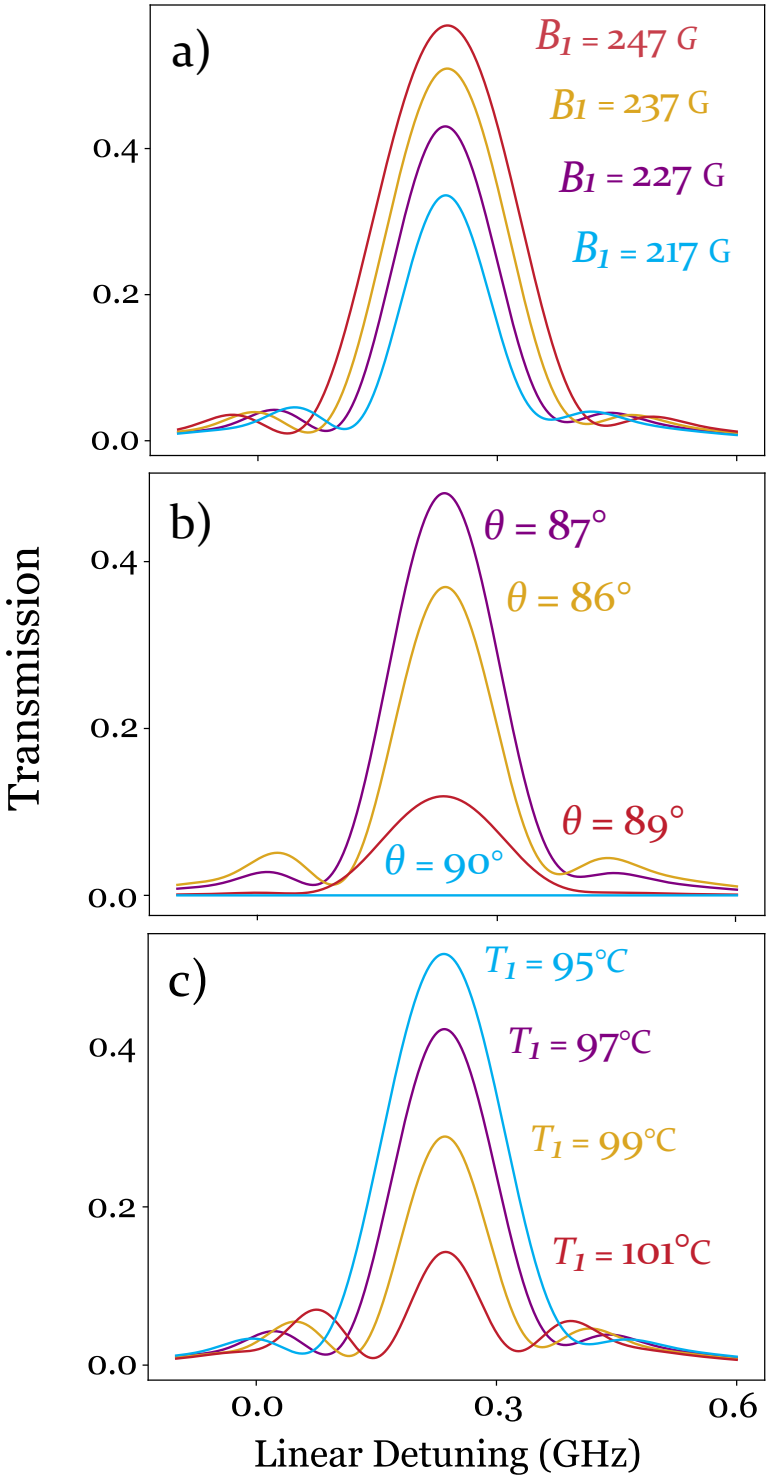

Figure 4.13: Theory curves showing the dependence of the Oblique-Voigt filter profile on a) B_1, b) θ and c) T_1. All other parameters are kept constant and are listed in Fig. 4.11. Note that in panel b) setting $\theta = 90°$ gives no filter transmission since the geometry is now Voigt and linear horizontal input light is an invariant polarisation.

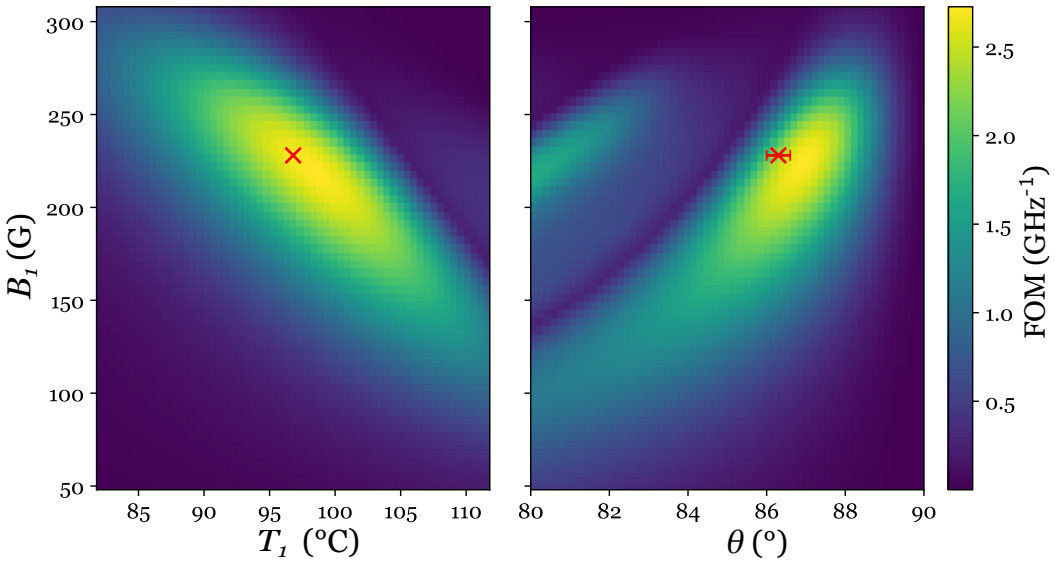

Figure 4.14: Heatmaps showing Figure of Merit values for the Oblique-Voigt filter varying B_1 against T_1 and B_1 against θ. All other parameters remain constant and are those listed in Fig. 4.11. The quoted standard errors in the table are plotted as error bars. Only the error on θ is large enough to be visible. The filter realised is at near optimum performance with respect to these parameters although θ, being so sensitive, could be enlarged to $\sim 87°$. We note the catastrophic drop off of FOM at $\theta = 90°$. The cell at 90° is in the Voigt geometry where the input linearly horizontal light is not transformed as it is an invariant polarisation.

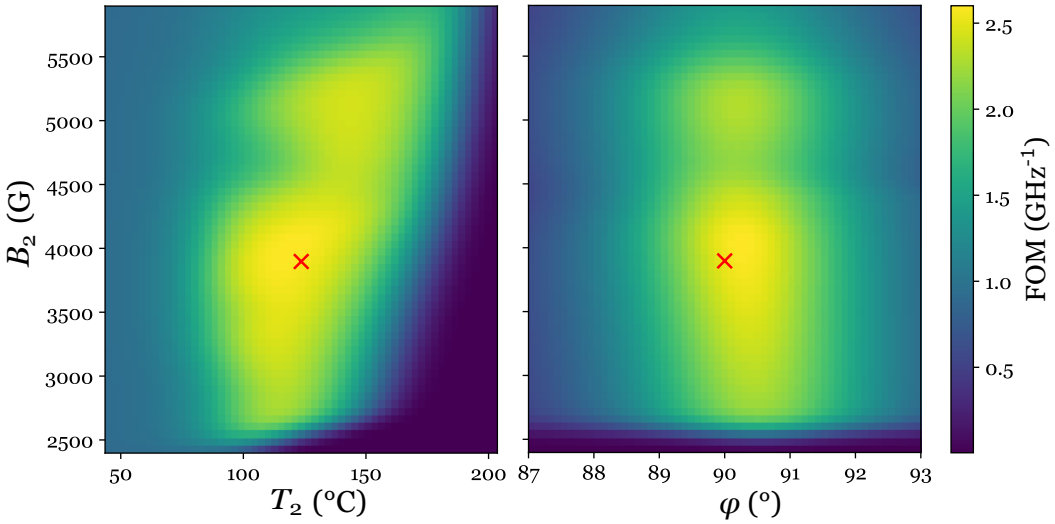

Figure 4.15: Heatmaps showing Figure of Merit values for the Oblique-Voigt filter varying B_2 against T_2 and B_2 against φ, the angle the magnetic field makes with the k-vector as it passes through the second cell. All other parameters remain constant and are those listed in Fig. 4.11. The quoted standard errors in the table are too small to be seen on the plot. The second cell parameters are much less sensitive than the first cell parameters owing to having a much simpler function. We need only a high temperature and magnetic field for large absorption. We also need the magnetic field to be tuned somewhat to give the correct Zeeman shifts.

4.4.2 Double Pass Filter

We present fitted data for the Double Pass filter in Fig. 4.16. The data show excellent agreement everywhere [244] apart from a shoulder. The ENBW, FWHM and FOM obtained from one fit are 140 ± 1 MHz, 93 ± 1 MHz and 1.20 ± 0.01 GHz^{-1} However, the FWHM increases to approximately 100 MHz given the shoulder. Nonetheless, this is the narrowest FWHM passive filter recorded to date and demonstrates that doppler broadened vapours could be manipulated to produce sub-100 MHz single peak filters.

We note a slightly lower maximum transmission than theoretically predicted. As explained in D, we normalise transmission against the 100% transmission line of an I_x curve taken using the same setup. This can be achieved by rotating the second polariser so that the two polarisers are no longer crossed.[1] Therefore, we do not take losses at each optical component into account. As a result, we believe the loss of transmission is due to lack of polarisation preservation which probably occurs as the light is reflected back by the mirrors for the second pass.

It is unclear the cause of the shoulder particularly since the Double Pass filter relies on an intensity squared effect of the Oblique Voigt profile which is largely symmetric. We therefore believe that the Oblique-Voigt filter is proof that a filter profile without a shoulder could have been realised with more time. The two sets of data where taken months apart and the setup was taken apart and rebuilt within that time period. We believe that magnetic field inhomogeneity, especially of angle, played a significant role. The cuboidal magnets providing the transverse field are much more suited for 50 mm cells leading to inhomogeneity at the edges of the cell. In short, more work is needed to theoretically analyse and design more robust magnetic fields for vapour cell designs. This is particularly true where the magnetic field requirements have stricter tolerances, for example in vapour magnetometry schemes [274, 275, 276, 225, 277].

[1] It should be noted that other methods including intensity stabilisation [22] alongside taking other intensity measurements would give a much more reliable measure of 100% transmission.

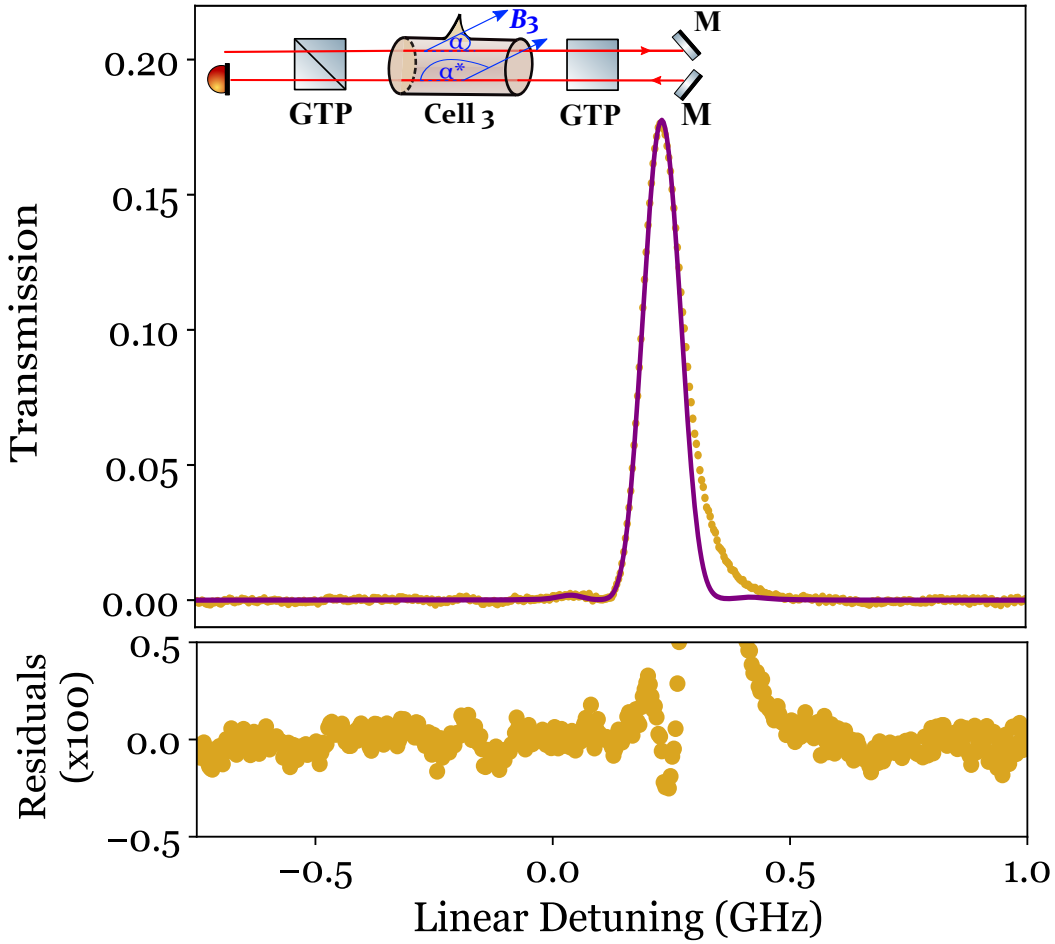

L_3 (mm)	T_3 (°C)	B_3 (G)	α (°)
75	99.4 ± 0.4	226.3 ± 1.2	87.4 ± 0.3

Figure 4.16: Experiment (gold) with theory fit (purple) of the Double Pass filter using natural abundance Rb cells probed on the Rb-D2 line. Mean parameters and standard errors obtained from from fits of five spectra are shown in the table. Data and theory show excellent agreement [244] apart from a shoulder. An ENBW, FWHM and FOM of 140 ± 1 MHz, 93 ± 1 MHz and 1.20 ± 0.01 GHz were obtained for one fit with standard errors being calculated from systematics. The actual FWHM of the data with the shoulder is 102 MHz.

We plot heatmaps for the cell parameters in Fig. 4.17 and show we are somewhat near local optimum parameters. It is informative to compare these with the heatmaps of the first cell parameters of the Oblique Voigt filter in Fig. 4.14 which show similar shape but are less sensitive. FOMs up to 2 GHz^{-1} are achievable for a slightly lower temperature and field.

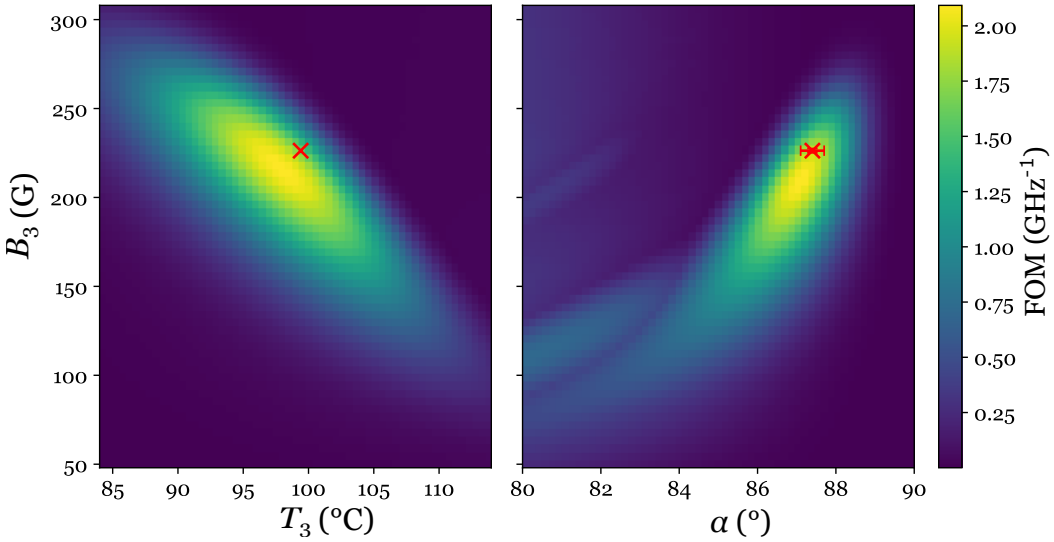

Figure 4.17: Heatmaps showing Figure of Merit values for the Double Pass filter varying B_3 against T_3 and B_3 against α. All other parameters remain constant and are those listed in Fig. 4.16. The quoted standard errors in the table are plotted as error bars. Only the error on θ is large enough to be visible. Note that the location of the mean parameters on the heatmaps has a FOM much higher than that recorded for one fit in the table. However note that the mean parameters are only statistical values and are not realised simultaneously in one set of data.

4.4.2.1 Reconfigurability

An additional property of the Double Pass filter is that it can be tuned to select for the wings rather than line centre without rebuilding the experiment (as was required in the investigation in Chapter 3). Fig. 4.18 shows data for a Double Pass filter in both wing operation which show excellent agreement with theory [244]. Parameters are shown in the table and were realised practically by decreasing the separation of the cuboidal magnets by ~ 2 cm and increasing the current through the solenoid. The change to the resultant magnetic field is shown in the plots in Fig. 4.19 with α decreasing to 69°. It is also possible to select for one wing either positively or negatively detuned from line centre by inputting elliptical light into the system as shown theoretically in 4.18.

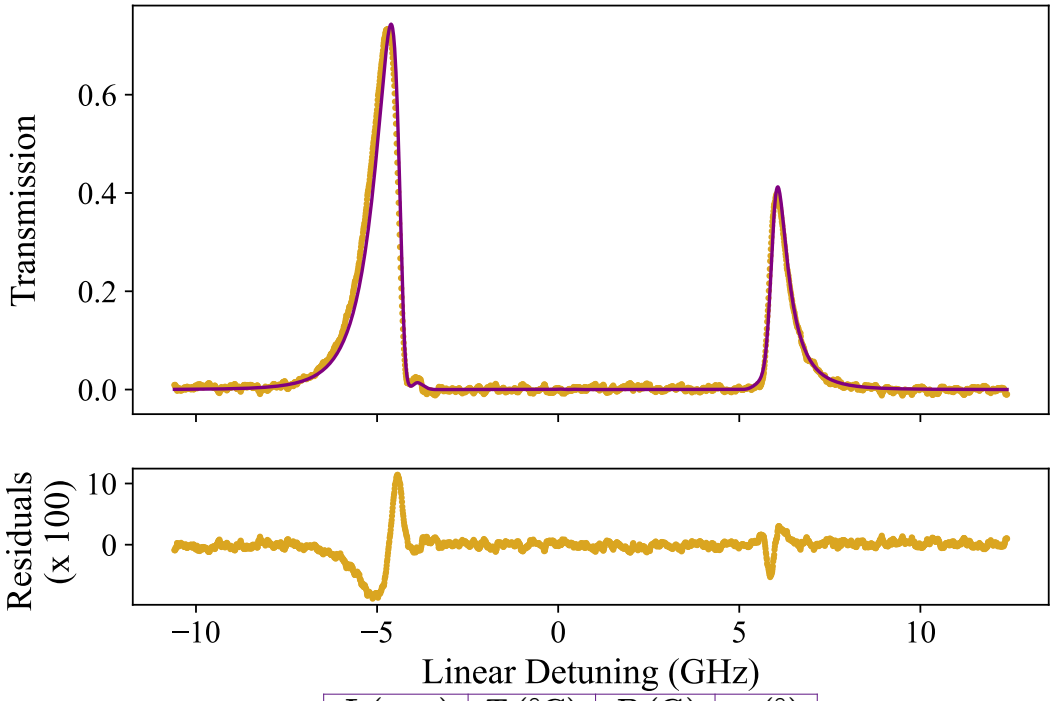

L (mm)	T (°C)	B (G)	α (°)
75	92	310	69

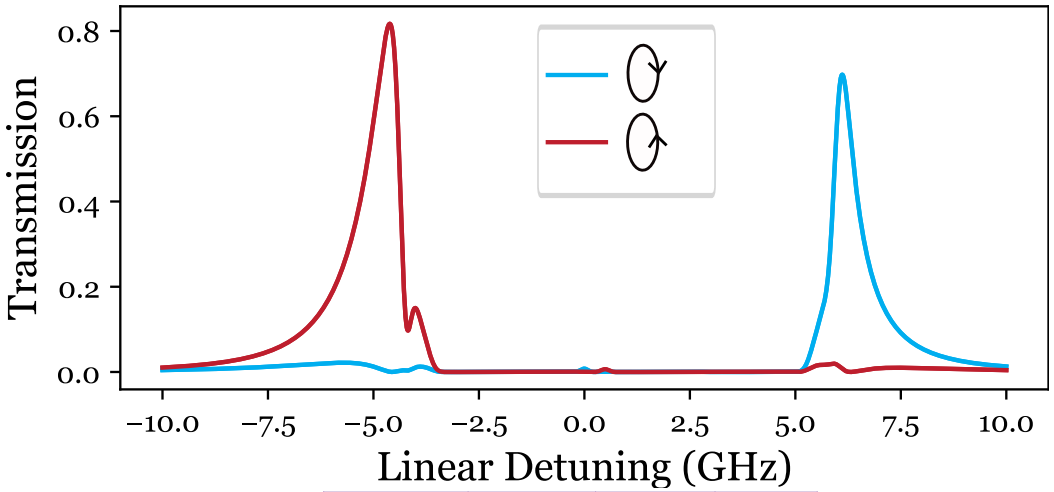

L (mm)	T (°C)	B (G)	α (°)
75	320	100	80

Figure 4.18: (Top) Data (gold) and theory (purple) of the Double Pass filter reconfigured to select both wings. Fit parameters shown in the table. (Bottom) Theory curves for the Double Pass filter setup reconfigured to output single wings. Parameters shown in the table. Selecting for the negatively/positively detuned wing requires left/right hand elliptically polarised light input. In this case the input light has a vertical major axis that is twice as long as the minor horizontal axis (see animations) with Jones vector representations of $\begin{pmatrix} 1 \\ \pm 2\mathrm{i} \end{pmatrix}$.

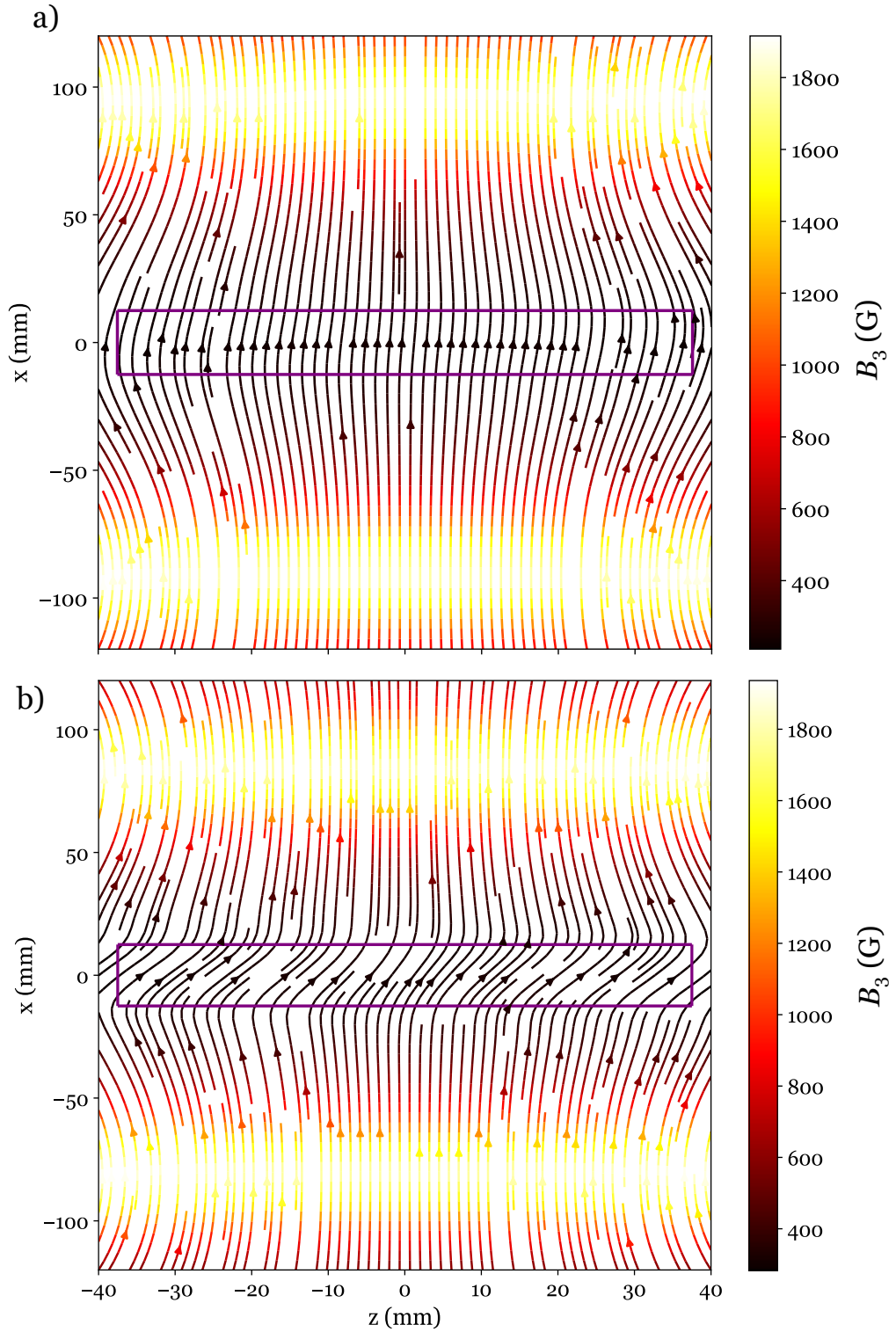

Figure 4.19: Vector field plots of the Double Pass magentic field in the $x-z$ plane with light moving in the z-direction. The purple boxes mark the extent of the 75 mm cell. a) shows the vector field for line centre operation with same field properties as discussed in Fig. 4.9. b) shows the same magnetic setup reconfigured to select for both wings. The cuboidal magnets are separated by 155 mm and the current in the solenoids is increased to 1.12 A. The mean field strength and angle with the k-vector are now 310 G and 69°. Plots realised using code developed by Thomas Robertson-Brown with *magypylib*.

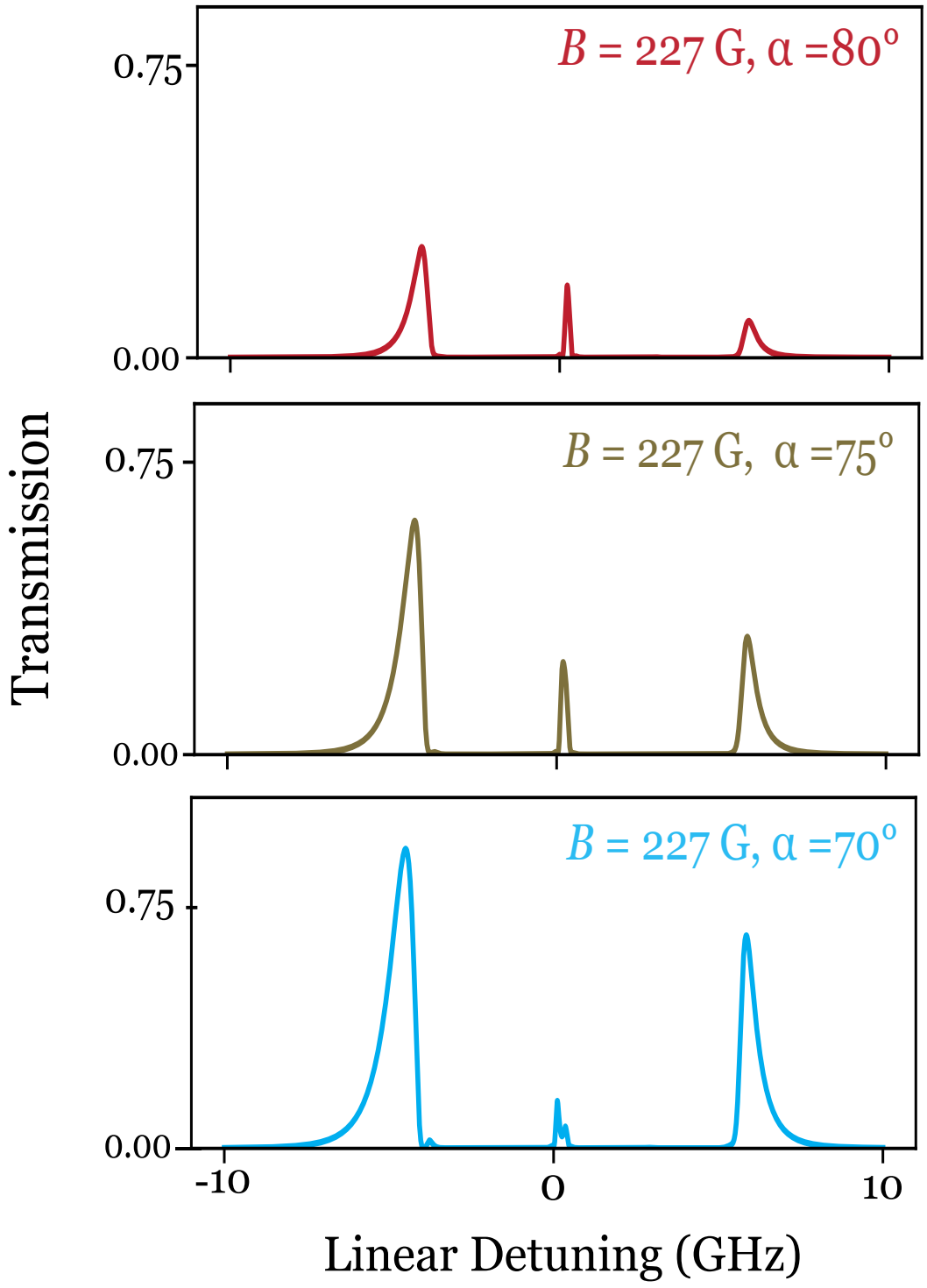

Figure 4.20: Plots showing how the Double Pass filter changes operation by decreasing the value of α while keeping the magnetic field strength constant.

Flexible operation of filters is becoming more important in different applications. Filters have been published that work on both D-lines [129] with greater tolerance [198] designed to be used in harsh environments such as shallow water [190] and in unmonitored settings year round [81]. On demand remote tuning of profiles will be an essential feature in many future out-of-the-lab filter setups.

4.5 Outlook

In this chapter, we have given an introduction to light moving through a cell in the oblique geometry. We have shown that the oblique geometry exhibits elliptical birefringence with frequency dependent non-orthogonal eigenmodes. This means that the eigenmodes and invariant polarisations are in general different vectors. With this background, we gave theoretical justification to two advantages of oblique filters. Firstly, they reject light outside of the dominantly birefringent region beyond the 50% barrier of the Faraday and Voigt filters. Secondly, the oblique birefringent region can be made narrower leading to FWHMs approaching 100 MHz. With this knowledge we designed two filters, an Oblique-Voigt cascaded filter and a single oblique cell Double Pass filter. We realised these filters experimentally and found excellent agreement with theory. The Oblique-Voigt filter is the highest FOM passive filter recorded as of time of writing while the Oblique Double Pass filter is the narrowest FWHM passive filter. We demonstrated experimentally the reconfigurability of the Double Pass filter to select for the two wings. We also discussed theoretically the ability to select one wing by inputting elliptically polarised light.

A paper has recently been published [130] which made use of a natural abundance Rb Faraday cell as a mode selector for an optical frequency comb. The filter profiles used had multiple peaks with FWHMs > 400 MHz. With this setup, the authors were able to select for three teeth of a commercial comb with 250 MHz repetition frequency. The two filters realised in this chapter could feasibly select for one tooth (See Fig. 4.21). Combining this proposition with the reconfigurability of the

Double Pass filter, it may also be possible to switch selection to teeth either side (albeit the wings, having larger FWHM, would select at least three teeth).

This method of mode selection is a recent contribution to the field and competes with other methods including optical injection which incorporates additional lasers as active filters [278, 279, 280], optical phase locking with 150 MHz tunability [281, 282] and Brillouin scattering methods [283] which present noise challenges [284]. Magneto-optical filters could stand as a highly tunable and compact option in this emerging landscape. This is to be borne in mind particularly as white papers are being written for NASA's *Decadal Survey on Life and Physical Sciences Research in Space* which include three papers on frequency combs [258, 259, 285]. All three comment optimistically on the future of frequency combs to be flight tested and eventually deployed on satelites. However, size, weight and power constraints (SWaP) are still an issue. Tailoring frequency comb pulses is an important part of being able to exploit the comb for its intended application. We can envision our filters being scaled down, thermally insulated and shielded magnetically to provide a compact and robust single mode selector for use outside the lab.

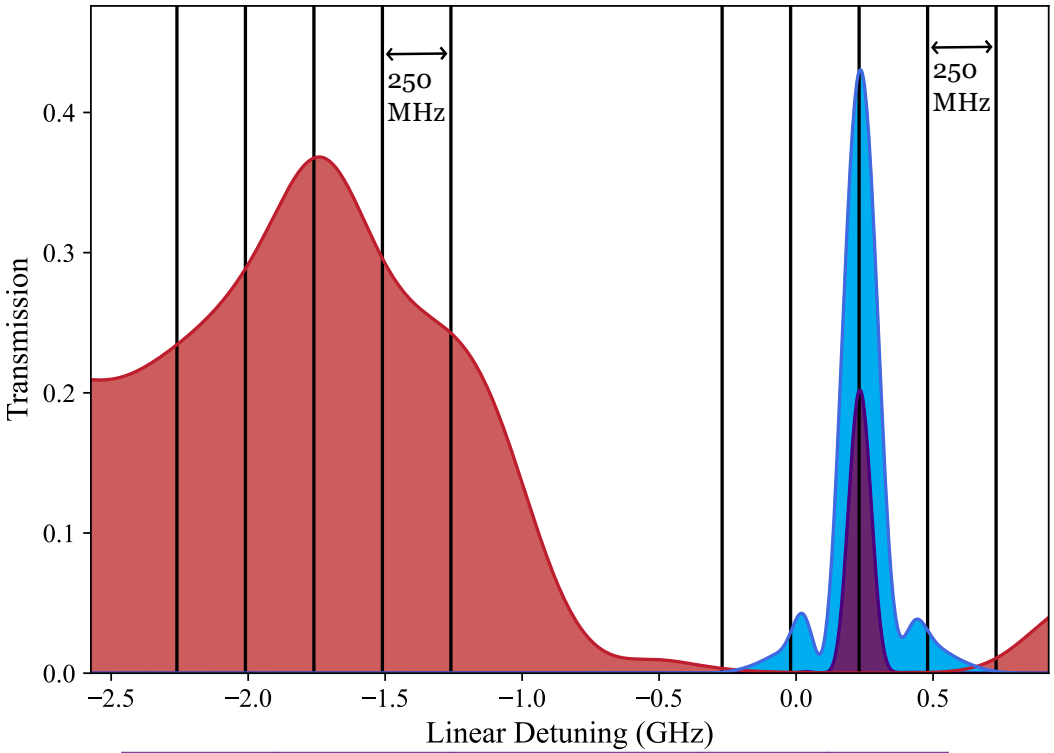

Filter	Geometry	L (mm)	T (°C)	B (G)
Red [130]	Faraday	7 (Extrapolated)	720	80

Figure 4.21: Three filter profiles including the Oblique-Voigt (blue) and Double Pass oblique filter (purple) and the profile used as a frequency comb mode selector in a recent publication (red), parameters for which can be found in the table. All three profiles are calculated using *ElecSus*. The black vertical lines mark two sets of teeth in a frequency comb with 250 MHz separation centred at the red filter peak and the purple filter peak. We note that in [130], the optical power of the teeth either side of the red central peak are very weak. As such, the red filter profile is effectively narrower than is presented here and selects for three teeth. The Oblique Voigt filter selects for one tooth at high transmission with two others at less than 10% transmission. The Oblique Double Pass filter selects for one tooth at roughly half the transmission of the red filter. We believe these oblique filters are well suited for optical frequency mode selection.

Chapter 5

An Investigation of Non-Hermitian Physics and Filter Performance

Author completed all theoretical computations, collected and processed all data and created all figures presented in this chapter. Figure 5.16 was created using code by Thomas Robertson-Browne. We discuss filter predictions first presented by masters student Alex Webber. All text written without the use of AI. Work is related to the article:

F. D. Logue, J. D. Briscoe, D. Pizzey, S. A. Wrathmall, and I. G. Hughes, 'Exploiting non-orthogonal eigenmodes in a non-Hermitian optical system to realize sub-100 MHz magneto-optical filters', *arXiv Preprint*, 2303.00081, 2023. https://doi.org/10.48550/arXiv.2303.00081 [5]

5.1 Background

In the last two chapters, we introduced two modifications to the single cell filter case: cascading and oblique magnetic fields. With these changes, we have shown improved filter performance and better understanding of filter mechanisms.

However, much of the theory introduced in the context of oblique fields appeared counter-intuitive and raised some important questions. Why do oblique cells have non-orthogonal eigenmodes? Do Faraday and Voigt cells have special symmetries? What is the best framework for understanding the physics at play?

In the 1990s, a landmark paper was published by Bender and Boettcher [286] birthing the field of *non-Hermitian* quantum mechanics [287, 288, 289]. Previously, it was demanded that Hamiltonians representing physical observables were Hermitian to guarantee real eigenvalues. Bender and Boettcher demonstrated that non-Hermitian Hamiltonians obeying the weaker condition of PT-symmetry also had real eigenvalues [290, 291, 292].

This began a tendency in multiple areas of physics to expand the set of matrices that could represent physical situations including anti-PT symmetric matrices [293, 294, 295] and even matrices with no symmetries [296, 297] that had imaginary and complex eigenvalues respectively. In optics, it had long been the case for measurable gain and loss to be represented by an imaginary value. Therefore, optics too became a natural platform for non-Hermitian physics [298, 299, 300, 301, 291] finding applications in omnipolarisers [302, 303, 304], sensing [305, 306, 307] and tailored laser output [308, 309, 310]. Typically Hamiltonians tend to be the most studied matrices [311], but non-Hermitian Linblad equations [312, 313] scattering matrices [314, 315] and density-of-state models [316, 317] are also studied. In short, any physical system described by a matrix can benefit from non-Hermitian analysis.

The consequence of lost matrix symmetries is that many basic assumptions of Hermitian physics do not hold including the orthogonality of eigenvectors. We assert that non-Hermitian physics gives the explanation for the oblique geometry's unusual properties.

In this chapter, we will show the non-Hermitian properties of the oblique cell case showing that the *dispersion relation* matrix used to calculate the eigenmodes lacks Hermitian symmetries found in the Faraday and Voigt cases. We explain how

oblique cells in general have non-orthogonal eigenvectors and introduce the fact that oblique refractive indices exhibit avoided crossings.

With this formalism, we discuss the concept of an *exceptional point of degeneracy*, a theoretical point in parameter space where the eigenmodes become parallel and the difference between the refractive indices goes to zero. In the vicinity of these points, the coalescence can change rapidly corresponding to changes in magneto-optical rotation over small frequency ranges. We suggest such a mechanism could lead to even narrower filters.

We propose two filter designs which exploit the magneto-optical rotation associated with exceptional points. Both filters are cascades of a Faraday and an oblique Rb cell. The first Rb filter is based on predictions presented by masters student Alex Webber [252] and has a peak FWHM of 11 MHz while the second revised filter has a peak FWHM of 40 MHz. We study the parameter space of the two filters and find the parameters of the Webber filter too intolerant to construct in our lab. We investigate the second revised 40 MHz filter but are unable to observe the expected feature.

We dedicate the rest of the chapter to analysing why the filter was unable to be realised. We believe the most important factors to consider are magnetic field inhomogeneity and uncertainty in calculated susceptibility values.

We conclude by considering Faraday-Oblique filters as active frequency standards in atomic clocks. The quantum limited linewidths that would be achievable are competitive with the narrowest laser lineshapes achieved whilst being compact and robust setups. As such, we make the case that although these filters have posed experimental problems, the benefits they could bring are worth the time and energy to investigate further.

5.2 Theory

5.2.1 Non-Hermitian Dispersion Relation Matrix

As introduced in Chapter 2, the calculation of atomic spectra can be split into two parts. The first calculates the susceptibilities: $\chi_{\sigma^{+/-},\pi}$ due to the $\sigma^{+/-}$ and π electric dipole allowed transitions. The second part uses these susceptibilities to calculate the refractive indices and eigenmodes. As we are interested in the symmetries leading to orthogonal or non-orthogonal eigenmodes, we consider the latter part.

From [207], the eigenvectors and refractive indices are calculated by solving the dispersion relation:

$$\begin{bmatrix} \frac{\epsilon_x}{\epsilon_0} - n^2\cos^2\theta & \frac{\epsilon_{xy}}{\epsilon_0} & n^2\cos\theta\sin\theta \\ -\frac{\epsilon_{xy}}{\epsilon_0} & \frac{\epsilon_x}{\epsilon_0} - n^2 & 0 \\ n^2\cos\theta\sin\theta & 0 & \frac{\epsilon_z}{\epsilon_0} - n^2\sin^2\theta \end{bmatrix} \begin{bmatrix} E_x \\ E_y \\ E_z \end{bmatrix} = 0, \tag{5.1}$$

where there are two possible refractive index values, n, and the permittivities ϵ_i are defined in terms of the susceptibilities:

$$\begin{aligned} \epsilon_x &= \frac{\epsilon_0}{2}(2 + \chi_{\sigma^+} + \chi_{\sigma^-}), \\ \epsilon_{xy} &= \frac{\mathrm{i}\cdot\epsilon_0}{2}(\chi_{\sigma^-} - \chi_{\sigma^+}), \\ \epsilon_z &= \epsilon_0(1 + \chi_\pi). \end{aligned} \tag{5.2}$$

The polarisation of a plane wave of light has components along x, y and z given by E_x, E_y and E_z. Note the matrix in this form assumes the magnetic field, *not* the k-vector points along z. In our calculations and discussions in the rest of this thesis, we always assume the k-vector points along z allowing us to set $E_z = 0$. However, the current co-ordinate system allows us to reveal the symmetries of the

system more readily. For more details on the solutions above, see Appendix B. Solving eq. 5.1 for n, we have

$$n_{a,b}^2 = \frac{A \pm \sqrt{B}}{C}, \tag{5.3}$$

$$\begin{aligned} A &= 2 \cdot \epsilon_x \epsilon_z + (\epsilon_x^2 - \epsilon_x \epsilon_z + e_{xy}^2) \sin^2 \theta, \\ B &= (\epsilon_x^2 - \epsilon_x \epsilon_z + \epsilon_{xy}^2)^2 \sin^4 \theta - 4 \cdot \epsilon_{xy}^2 \epsilon_z^2 \cos^2 \theta, \\ C &= 2 \cdot (\epsilon_x \sin^2 \theta + \epsilon_z \cos^2 \theta). \end{aligned} \tag{5.4}$$

We refer to the 3 x 3 matrix in eq. 5.1 as the *dispersion relation* matrix and we now want to show its symmetries for the Faraday, Voigt and oblique cases which justify their respective orthogonal and non-orthogonal eigenmodes. In the Faraday ($\theta = 0$) case, the dispersion relation matrix simplifies to:

$$D_{\mathcal{F}} = \frac{1}{2} \begin{bmatrix} \pm(\chi_{\sigma^+} - \chi_{\sigma^-}) & -\mathrm{i}(\chi_{\sigma^+} - \chi_{\sigma^-}) & 0 \\ \mathrm{i}(\chi_{\sigma^+} - \chi_{\sigma^-}) & \pm(\chi_{\sigma^+} - \chi_{\sigma^-}) & 0 \\ 0 & 0 & 2 \cdot (1 + \chi_\pi) \end{bmatrix}, \tag{5.5}$$

where the refractive index being considered determines whether the diagonal terms are $\pm$. Given that the susceptibilities χ_i are in general complex, $D_{\mathcal{F}}$ is non-Hermitian since $D_{\mathcal{F}} \neq D_{\mathcal{F}}^\dagger$ where $\dagger$ represents the conjugate transpose. However, $D_{\mathcal{F}}$ does possess a symmetry. By inspecting the matrix, if the susceptibilities were real, then the diagonal elements are real. Additionally the off diagonal elements have the same magnitude with opposite sign. If the susceptibilities are real, the conjugate transpose gives the same off diagonal terms. As a result we can say that if the susceptibilities are real, then the resulting matrix is Hermitian i.e.:

$$D_{\mathcal{F}}(\mathrm{Re}[\chi_i]) = D_{\mathcal{F}}^\dagger(\mathrm{Re}[\chi_i]) \tag{5.6}$$

In the Voigt ($\theta = 90°$) case, the dispersion relation matrix with n_a or n_b substituted reduces to $D_{\mathcal{V}_a}$ or $D_{\mathcal{V}_b}$:

$$D_{\mathcal{V}_a} = \frac{1}{2}\begin{bmatrix} (2+\chi_{\sigma^+}+\chi_{\sigma^-}) & -\mathrm{i}(\chi_{\sigma^+}-\chi_{\sigma^-}) & 0 \\ \mathrm{i}(\chi_{\sigma^+}-\chi_{\sigma^-}) & (\chi_{\sigma^+}+\chi_{\sigma^-}-2\cdot\chi_\pi) & 0 \\ 0 & 0 & 0 \end{bmatrix}, \tag{5.7}$$

$$D_{\mathcal{V}_b} = \frac{1}{2}\begin{bmatrix} (2+\chi_{\sigma^+}+\chi_{\sigma^-}) & -\mathrm{i}(\chi_{\sigma^+}-\chi_{\sigma^-}) & 0 \\ \mathrm{i}(\chi_{\sigma^+}-\chi_{\sigma^-}) & \zeta & 0 \\ 0 & 0 & \tau \end{bmatrix}, \tag{5.8}$$

$$\zeta = \frac{\left(-\mathrm{i}(\chi_{\sigma^+}-\chi_{\sigma^-})\right)^2}{2+\chi_{\sigma^+}+\chi_{\sigma^-}}, \tag{5.9}$$

$$\tau = 2\cdot(1+\chi_\pi) - (2+\chi_{\sigma^+}+\chi_{\sigma^-}) - \zeta$$

Similarly we note that the same symmetry as the Faraday case holds since ζ is real for real susceptibilities:

$$D_{\mathcal{V}}(\mathrm{Re}[\chi_i]) = D^\dagger_{\mathcal{V}}(\mathrm{Re}[\chi_i]) \tag{5.10}$$

Now let's consider the general oblique case. We note that B defined in eq. 5.4 has a square root term which is removable in the Faraday and Voigt case. This is not in general true in the oblique case. Given that the square root of a real input can in general be complex, the diagonal entries of 5.1 will in general be complex. As such $D_{\mathcal{O}}(\mathrm{Re}[\chi_i])$ is in general non-Hermitian. Without the additional symmetries in eq. 5.6 and 5.10, orthogonal eigenvectors are not guaranteed and we ought to expect non-orthogonal eigenmodes.

5.2.1.1 Frequency Dependence

Note however, that the frequency dependence of the oblique eigenmodes is not dictated by the non-Hermitian property. In general the eigenmodes depend on the susceptibilities which themselves are frequency dependent. In fact the Voigt eigenmodes are in general frequency dependent provided the light is polarised along the propagation direction i.e. there is a polarisation component along $\hat{z}$. Given that in our discussions we assume plane waves, only oblique eigenmodes are frequency dependent.

5.2.2 Coalescence

Having understood the non-Hermitian origin of non-orthogonal eigenmodes, we now ask how we can use them to build better filters. The literature records a phenomenon known as an *exceptional point of degeneracy* [318, 319, 320, 321, 322, 323, 306, 307, 324, 325]. This is a point in parameter space when the eigenmodes are not only non-orthogonal but are completely parallel. While there is doubt over whether the eigenmodes of a magneto-optical device can ever completely coalesce (see A.7), we can optimise our filter to find points where the normalised eigenmode dot product is high. Fig. 5.1 shows such an optimisation. The S_0' output from the oblique cell records a high dot product of more than 80% at an approximate frequency of 0.2 GHz. At this frequency we observe a narrow transmission feature of 40 MHz FWHM. We also must note that the refractive indices, unlike the Faraday refractive indices in Chapter 2, exhibit avoided crossings. This is predicted in non-Hermitian systems in [326, 319] where the degeneracy of the refractive indices is lifted as a result of a symmetry not present in the oblique geometry.

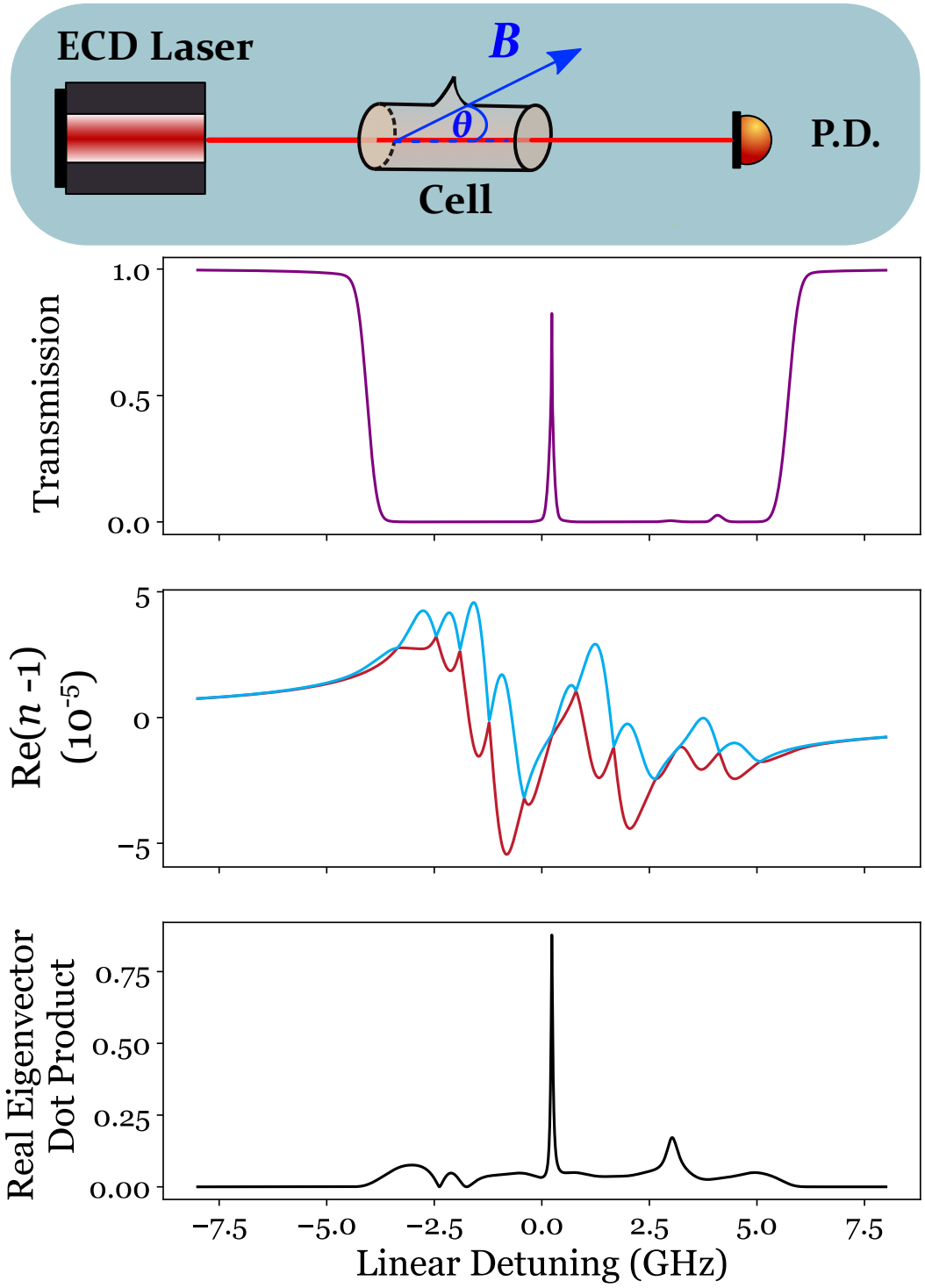

L (mm)	T (°C)	B (G)	θ (°)
75	80	295	88

Figure 5.1: Caption Overleaf

Figure 5.1: (Top) A setup to observe a S_0' output with a coalescent feature. Linearly vertical light from an external cavity diode (ECD) laser is directed into an oblique cell before being detected by a photodetector (P.D.). The S_0' output shows a narrow feature at centre occuring at an avoided crossing in the refractive indices. The real part of the normalised eigenvector dot product between eigenmodes, $\vec{a}$ and $\vec{b}$: $\frac{\Sigma_i \vec{a}_i^* \cdot \vec{b}_i}{|\vec{a}||\vec{b}|}$. is plotted. $\vec{a}^*$ denotes the complex conjugate of $\vec{a}$. At the frequency position of the narrow feature, there is a large increase in the dot product to over 80%. This implies that at this frequency, the eigenmodes are close to an exceptional point of degeneracy where the eigenmodes coalesce.

The relationship between this narrow feature and the coalescene of the eigenmodes is shown in Fig. 5.2. The coalescene of the eigenmodes in such a small frequency range results in a change in the invariant polarisations over the same interval. This results in magneto-optical rotation schemes that vary for each of the input frequencies as can be seen for the three frequencies plotted in the a), b) and c). In essence, the behaviour is no different from a standard transmission resonance. However, while the standard transmission resonances are largely dictated by the positions of transition frequencies, the coalescence emulates the same behaviour in a smaller frequency range. This shows great promise for further improving filter performance and we provide some concrete predictions in the next chapter.

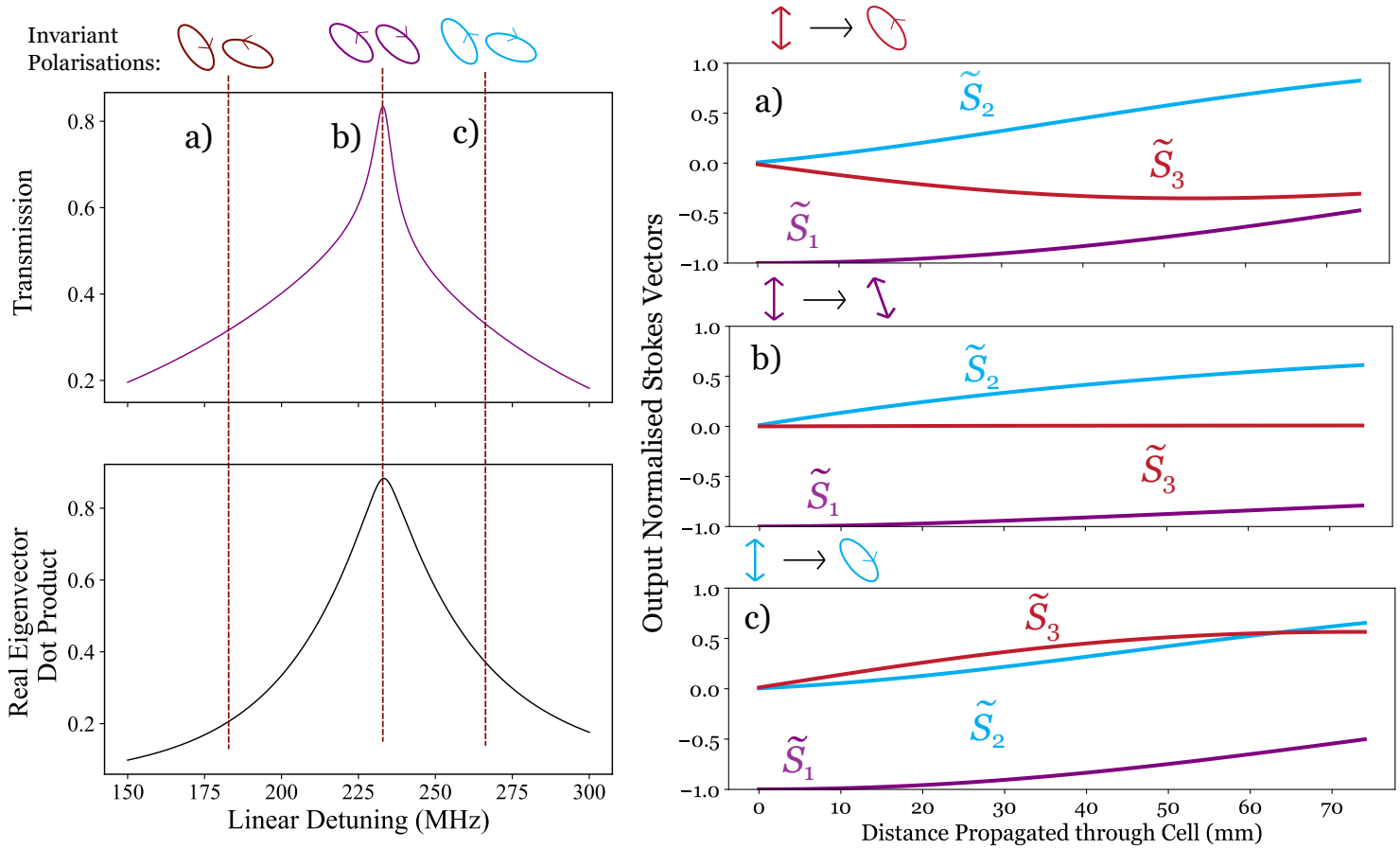

Figure 5.2: A plot of the central transmission feature of the S_0' output in Fig. 5.1 alongside the normalised eigenmode dot product. Animations of the invariant polarisations are shown for three frequencies a), b) and c). The output normalised Stokes vectors are plotted as a function of distance propagated through the cell for these three frequencies. Animations of the input and output polarisations are shown above each diagram.

5.3 Predictions

Having understood the rapid dispersion associated with a coalescent feature, we endeavour to find even narrower filters. Fig. 5.3 shows our proposed setup. Our design is a Faraday-Oblique filter composed of a Faraday and an oblique cell between crossed polarisers. Both cells have axial fields generated by solenoids. A transverse field from a pair of plate magnets is also applied to the oblique cell giving a resultant oblique field to the k-vector of the light.

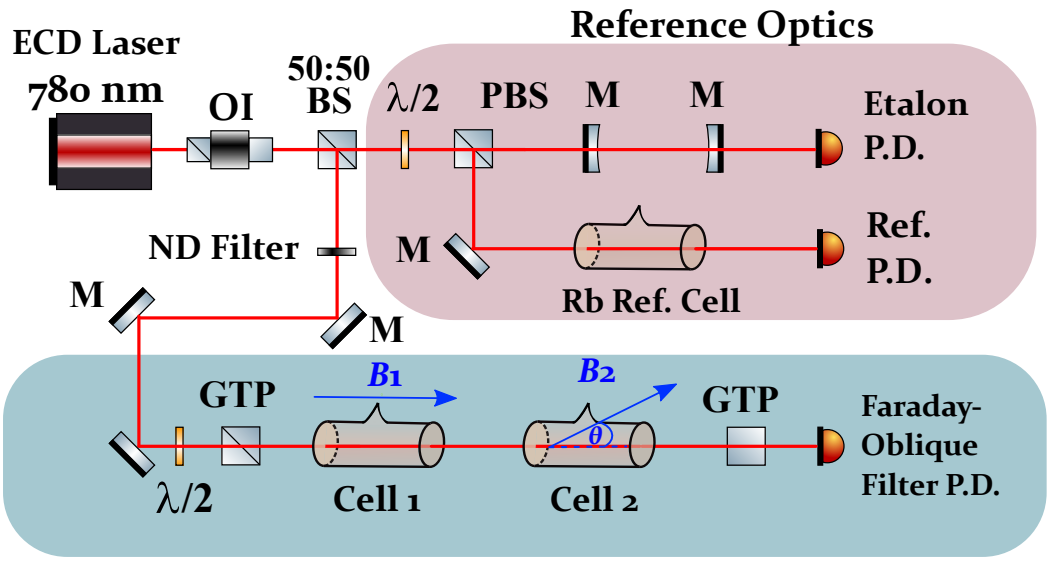

Figure 5.3: A schematic of the setup used to realise filters relying on coalescent features. Light on the Rb-D2 line passes through an optical isolator (OI) and is split into reference (see Appendix D) and experiment optics. The power in the experiment is lowered using a neutral density (ND) filter and the $\lambda/2$ waveplate. The Faraday-Oblique filter is composed of two cells between two crossed Glan-Taylor polarisers (GTP). The first cell is in the Faraday geometry and has magnetic field provided by a solenoid. The second cell is in the oblique geometry and has magnetic field provided by a combination of solenoid and plate magnets. Light is detected by photodetectors (P. D.). P(BS) - Polarising Beamsplitter, M - Mirror.

5.3.1 Webber Faraday-Oblique Filter

A masters student, Alex Webber, originally discovered the narrow lineshapes that could be obtained by relying on coalescent features. Webber achieved this by developing analytic solutions (see Appendix B) permitting faster optimisations with

finer detuning grids. A computer optimisation of two oblique cells between crossed polarisers led to a peak with sub-natural linewidth FWHM and FOM over 4 GHz^{-1}. Angles between the k-vector and magnetic field were 83.56° and 92.77° respectively. We have simplified this design to a Faraday-Oblique filter with linearly horizontal light input. This design, which we designate as the Webber filter, maintains a narrow profile widened only to 11 MHz FWHM. The other features towards the wings are less than 5% in transmission. However, one could also extinguish them by adding an additional Voigt cell to the cascade with $\sim$ 4000 G exerted upon it (see 4.3). The Stokes parameter plots (Fig. 5.5) and their zoom ins (Fig. 5.6) show the operation of the filter.

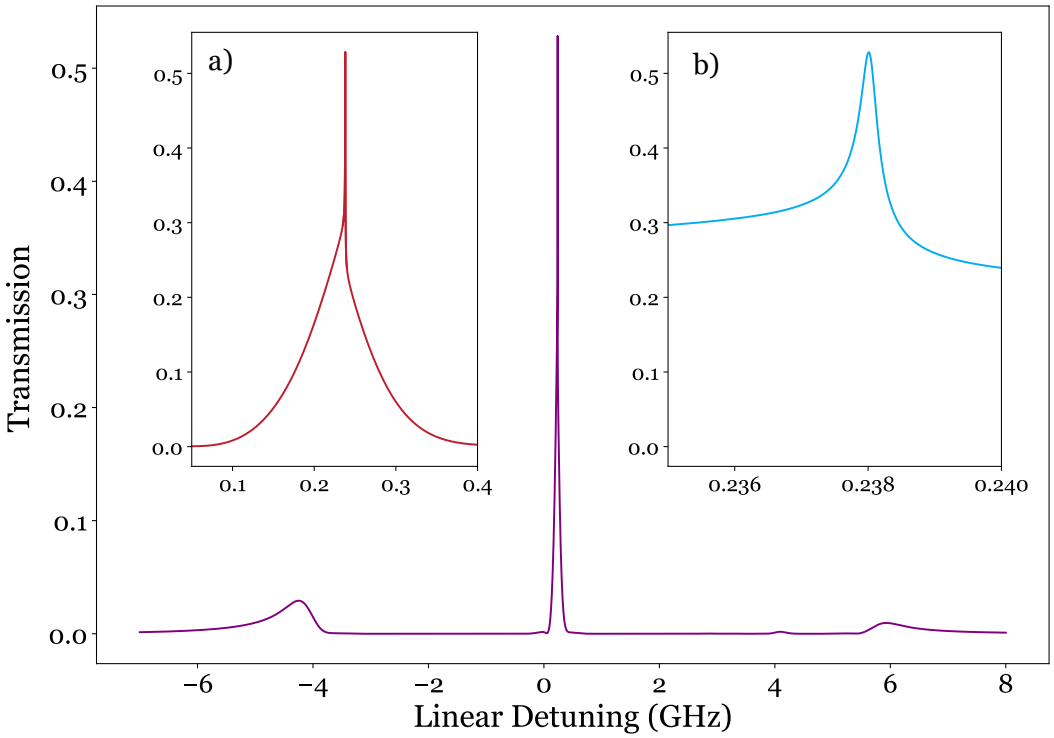

L_1/L_2 (mm)	T_1 (°C)	B_1 (G)	T_2 (°C)	B_2 (G)	θ(°)
5/5	91.5	269	126.47	292.60	92.40

Figure 5.4: The transmission profile of a Faraday-Oblique filter based on Alex Webber's original predictions. The main plot shows the transmission from -6 GHz to 8 GHz after linearly horizontal light is input while the insets a) and b) show zoom-ins at relevant frequencies. The FWHM, ENBW and FOM are 11 MHz, 133 MHz and 3.98 GHz^{-1}. Note the precision of the values given in the table. The filter is sensitive to some parameters to two decimal places.

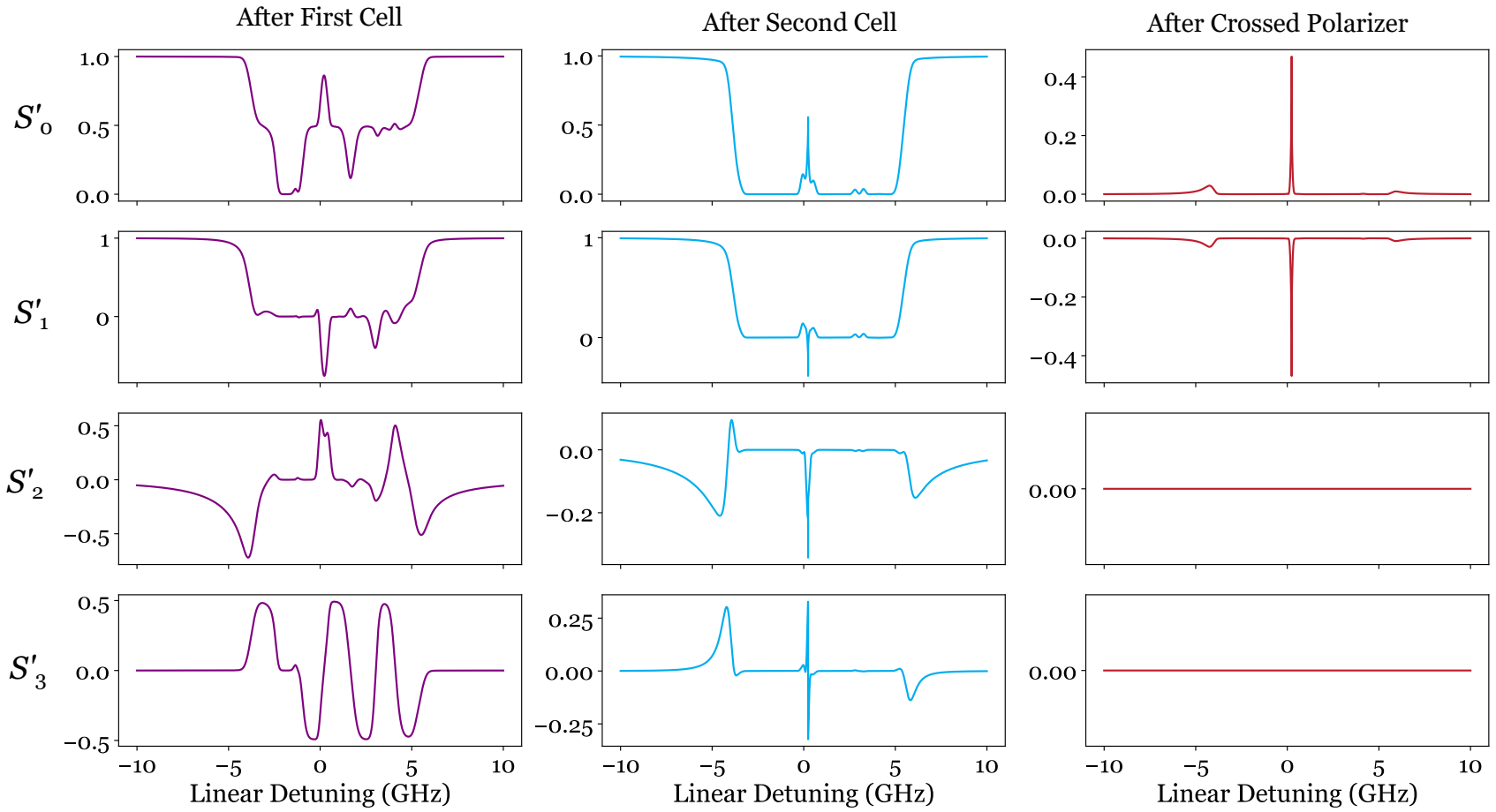

Figure 5.5: Plots of the Stokes Parameters after each component in the Webber filter. The S_i are input normalised and show polarisation transformation and loss.

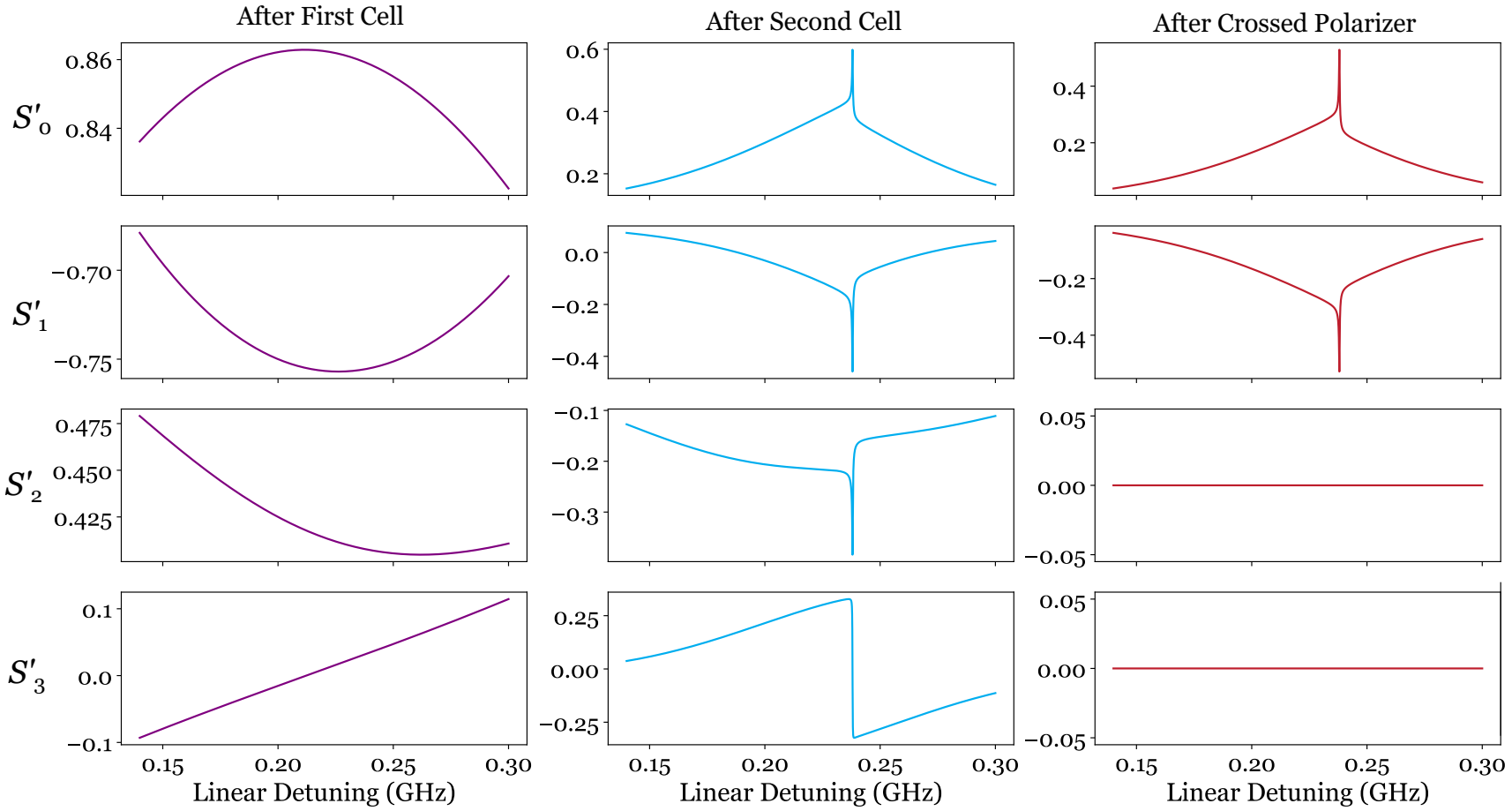

Figure 5.6: The same Stokes parameters after each component of the Webber filter as plotted in Fig. 5.5. We have zoomed in on the central detuning region where the narrow lineshape emerges.

The first Faraday cell's role is to transform the linearly horizontal light at resonant frequencies to linearly vertical light. The second oblique cell's role is to extinguish unwanted regions away from centre line. The second cell has a key additional role of transforming the polarisation in a very small region between $\sim$ 0.15 and 0.30 GHz. In this region, the S_3' value is dispersive remaining positive and growing up until 0.23 GHz. After which S_3' rapidly becomes negative before growing steadily once again. As such the light in this region leads to a resonance peak in the filter transmission which is so narrow due to the small frequency range over which this dispersive behaviour occurs.

As much as the Webber filter has high performance, its parameter sensitivity makes practical realisation in our lab currently impossible. The parameter sensitivity was somewhat mitigated by replacing Webber's original Oblique first cell with a Faraday cell since Faraday fields are much easier to generate. In fact, the first cell is largely invariant to field angle, ψ (See Fig. 5.7). The variation of B_1 and T_1 also poses few problems since a value too large/small in one can be mitigated by decreasing/increasing the other.

Nevertheless, it is the parameter sensitivity of the second cell responsible for generating the 11 MHz FWHM feature that presents issues. The FOM remains high in a very small parameter region of temperature, magnetic field and angle, θ as shown in Fig. 5.8. Beyond this region, the FOM rapidly falls to less than 1 GHz^{-1}. These FOM contours are not conducive to finding parameters in a lab setting where parameters are tuned by monitoring the small changes in performance for small adjustements in the setup. While approaching the correct values from one side of the contour shows steady improvement, from the other, the performance remains low before rapidly increasing in performance.

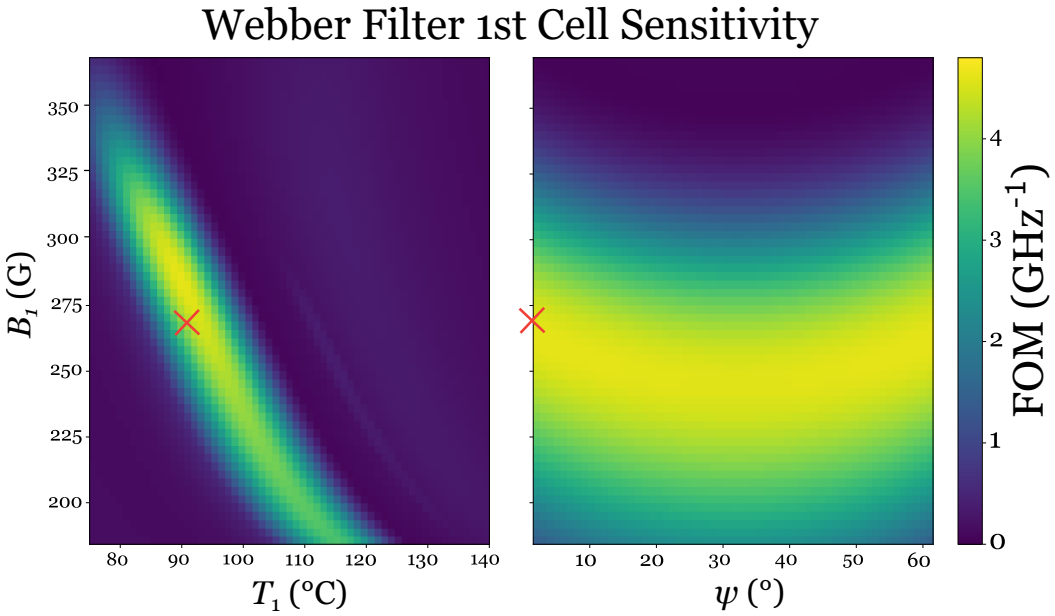

Figure 5.7: Heat maps showing the sensitivity of FOM to variation of Cell 1's three parameters: the magnetic field, B_1, the temperature, T_1 and angle between the magnetic field and k-vector which is ψ for the first Faraday cell. Red crosses mark the parameters plotted in Fig. 5.4. The FOM of the first cell is largely invariant with changing ψ while a small increase/decrease in the magnetic field can be mitigated by decreasing/increasing the temperature.

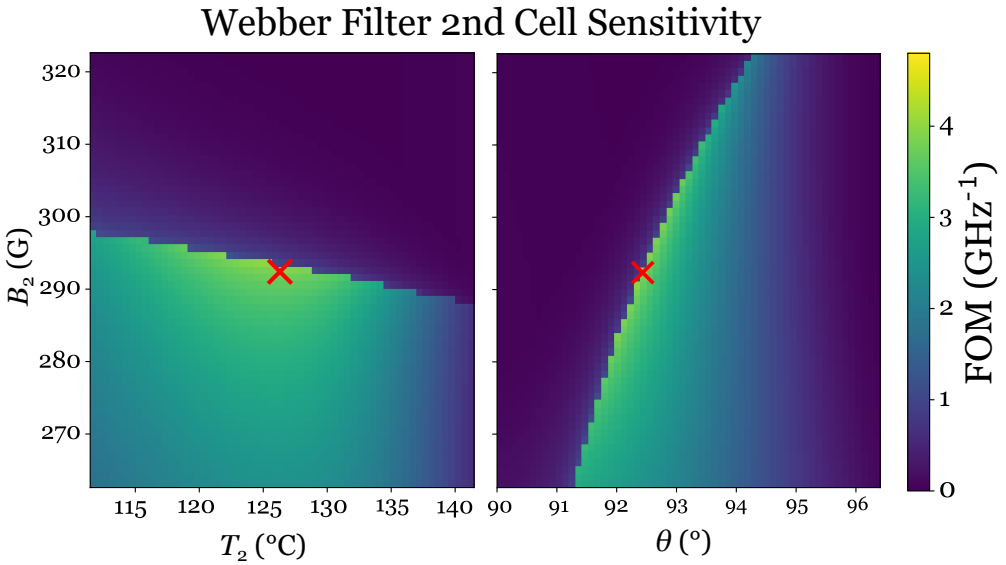

Figure 5.8: Heat maps showing the sensitivity of FOM to variation of Cell 2's three parameters: the magnetic field, B_2, the temperature, T_2 and angle between the magnetic field and k-vector which is θ for the second oblique cell. Red crosses mark the parameters plotted in Fig. 5.4. The FOM is ultra-sensitive to Cell 2's parameters remaining high along a small region. By increasing the field or decreasing θ beyond this region, the filter performance rapidly drops to less than 1 GHz^{-1}.

This ultra-sensitivity is also seen in the dependence of filter lineshape on second cell parameters. Fig. 5.9 shows the effect of varying θ on lineshape. By decreasing θ by 0.2°, the filter peak becomes a trough and by increasing θ by 0.2°, the narrow 11 MHz feature disappears. We can see that while variation in θ is small, changes in the refractive index profiles and coalescence of the eigenmodes are responsible for this behaviour. The crossing and avoided crossing shape exhibited for 92.2° and 92.4° dissapears for 92.6° despite only very small differences in the refractive index values between the three cases. The eigenmode coalescence remains high for all three cases but for 92.4°, we observe a cusp like peak behaviour, not observed in the other two cases.

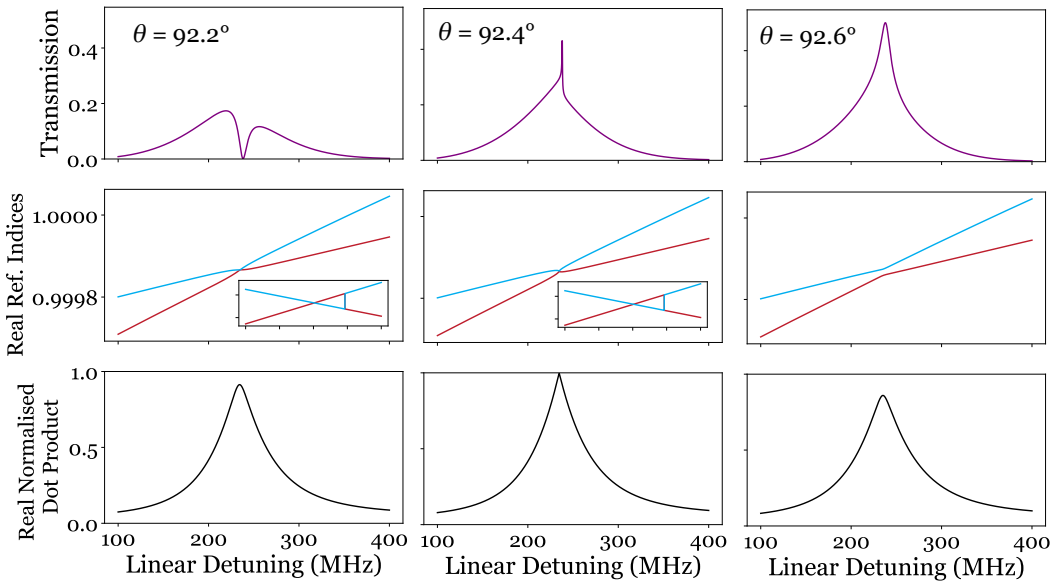

Figure 5.9: Plots showing the extreme sensitivity of the Webber filter to variation in θ. Decreasing θ by 0.2° results in the peak becoming a trough and increasing θ by 0.2° results in the 11 MHz FWHM feature being lost. This makes the Webber filter impratical to implement in our current setup. The real refractive indices and real part of the normalised eigenmode dot product show the small but significant changes that result in this ultra-sensitive behaviour.

As such, we have found that the additional magneto-optical rotation provided by coalescent features has the downside of creating ultra-sensitive filters. Of course, we might think more positively and realise that we have created a high quality magnetometer. Indeed, there has already been much work in utilising non-Hermitian

physics in sensing [307, 306, 305].

5.3.2 40 MHz FWHM Revised Filter

We note that the profile of the 92.4° case in Fig. 5.9 is still high performance given its 40 MHz FWHM. Once could reoptimise the filter for this lineshape and find a less sensitive yet competitive filter. We call this new set of parameters, the *Revised* Filter. Computer optimisations find that such a lineshape can be obtained for a higher maximum transmission than the Webber filter compensating somewhat for its wider FWHM. Nevertheless the wing features of the Revised filter have larger transmission and a Voigt cell at ~ 4000 G would be required for the Revised FOM to be comparable with the Webber FOM. Once again we plot the Stokes parameters and find the function of the filter to be analogous to the Webber filter with the S_3' dispersive feature occuring over a larger detuning range leading to a larger FWHM.

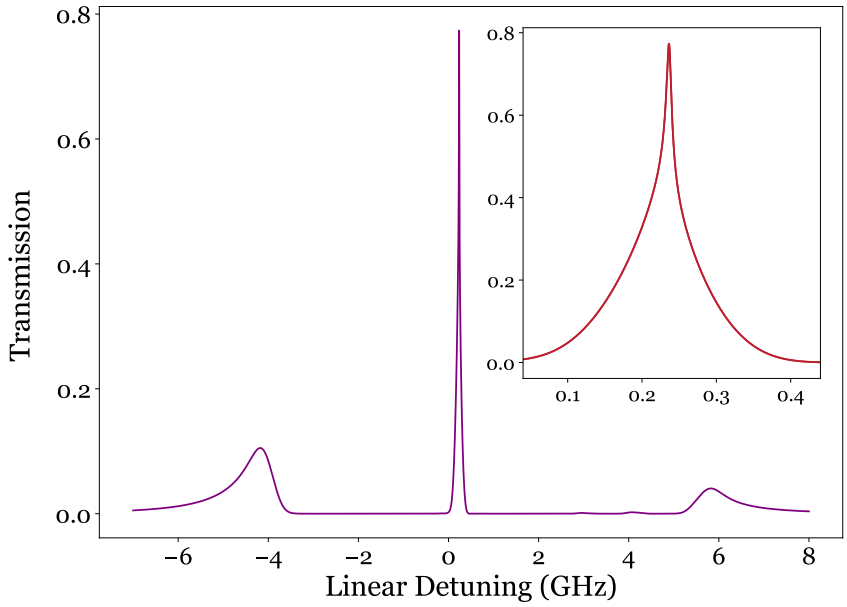

L_1/L_2 (mm)	T_1 (°C)	B_1 (G)	T_2 (°C)	B_2 (G)	θ(°)
75/75	60	176	80	295	88

Figure 5.10: The transmission profile of a Faraday-Oblique filter based on revised parameters. The main plot shows the transmission from –7 GHz to 8 GHz after linearly horizontal light is input while the inset shows a zoom-in of the central feature. The FWHM, ENBW and FOM are 41 MHz, 313 MHz and 2.48 GHz^{-1}.

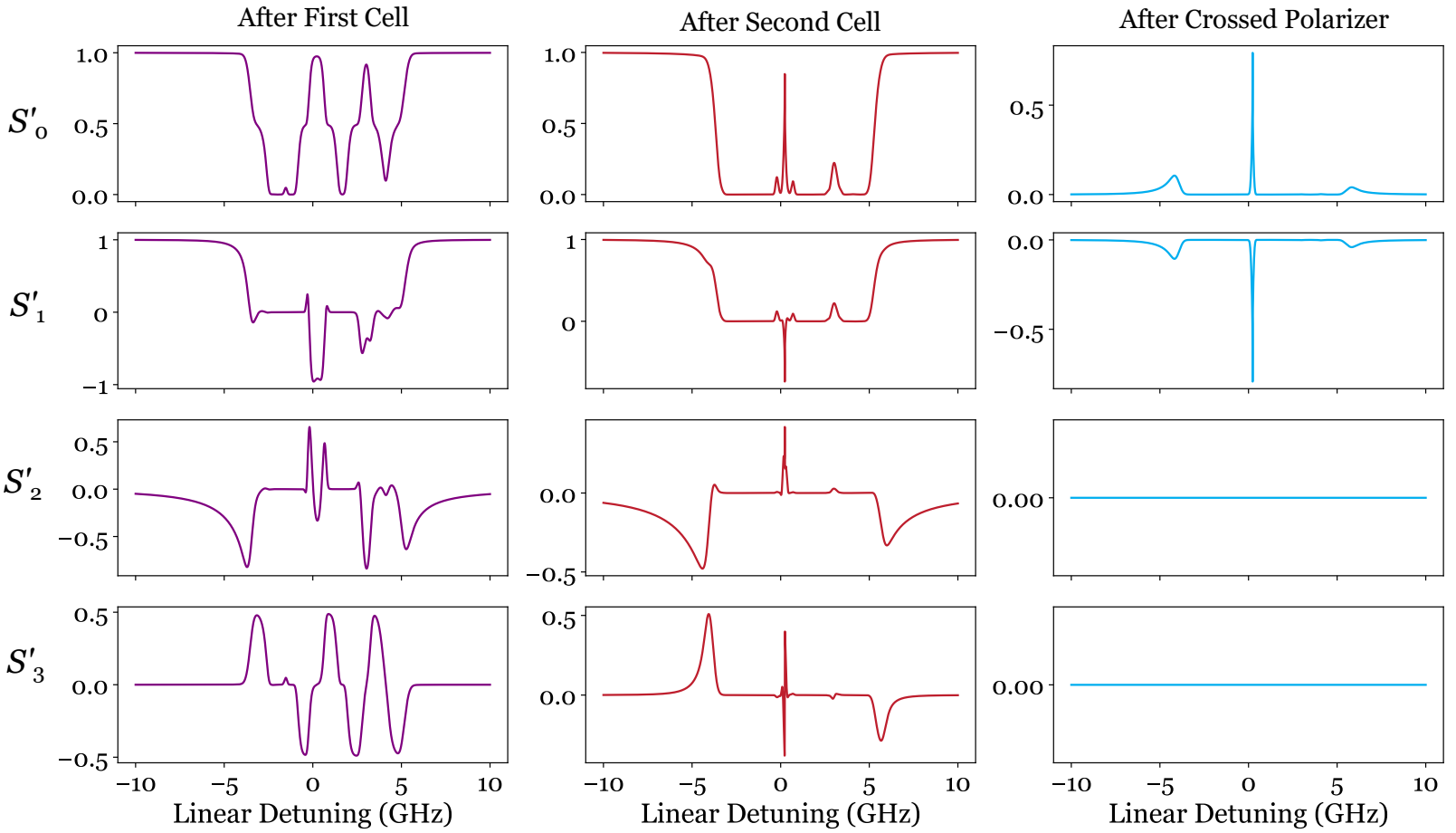

Figure 5.11: Plots of the Stokes Parameters after each component in the Revised filter. The S_i are input normalised and show polarisation transformation and loss.

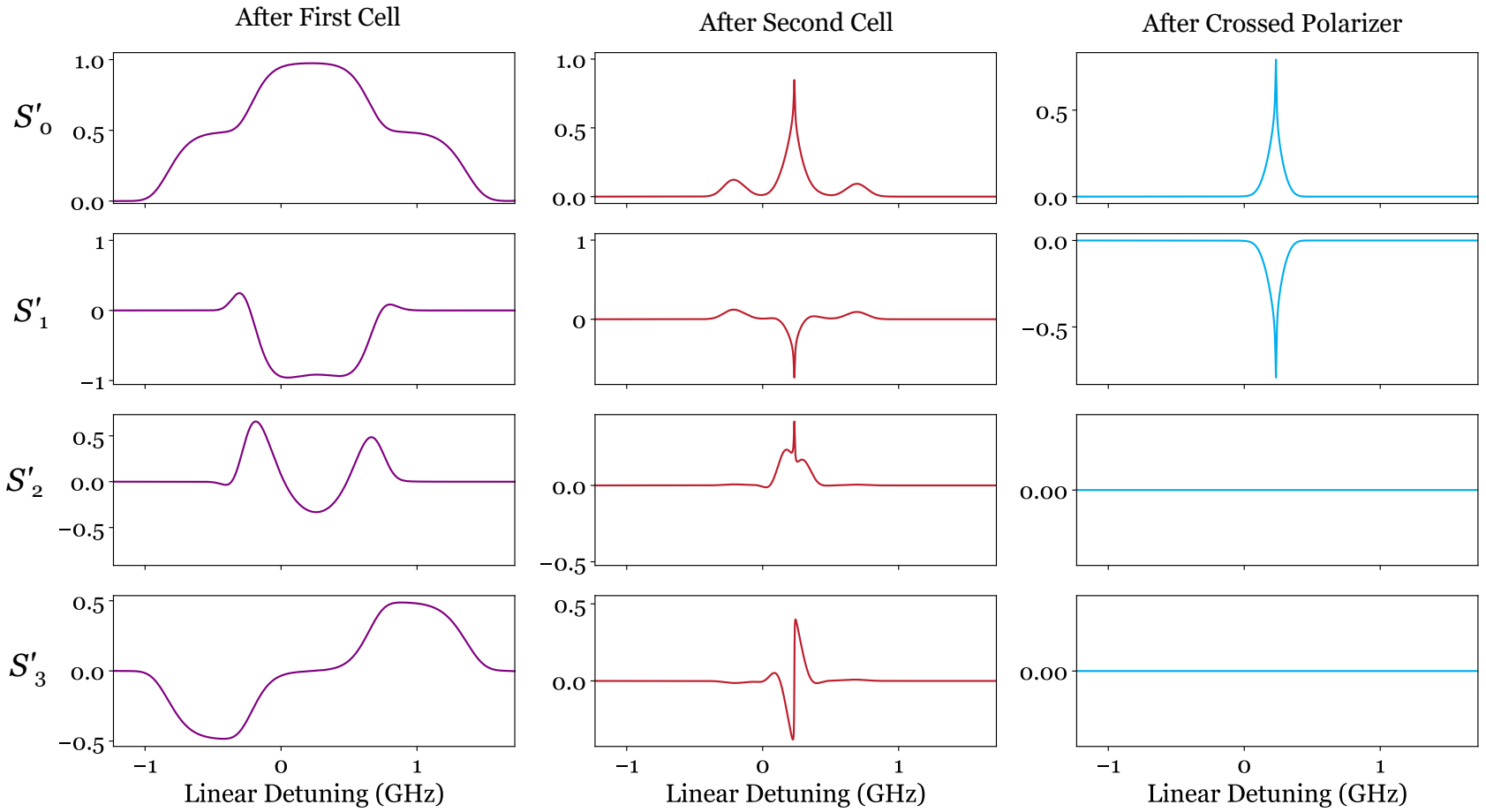

Figure 5.12: The same Stokes parameters after each component of the Revised filter as plotted in Fig. 5.5. We have zoomed in on the central detuning region where the narrow lineshape is located.

The sensitivity of the second cell Revised filter parameters to FOM shows similar contours to that of the Webber filter (compare Fig. 5.8 and 5.13). However, the region close in value to maximum FOM (albeit lower for the Revised filter) is larger shown by a larger yellow region. Fig. 5.14 further confirms the practical realisability of the Revised filter. By varying the magnetic field and temperature of the second cell alongside θ, we find that although the lineshapes are sensitive to small changes in each parameter, the narrow feature remains either as a peak or a trough. This is in contrast to the Webber filter where the narrow 11 MHz feature disappears altogether. This lineshape dependence lends itself to easier optimisation in a lab setting. The feature can initially be realised by coarse parameter variation and fine tuned to optimise.

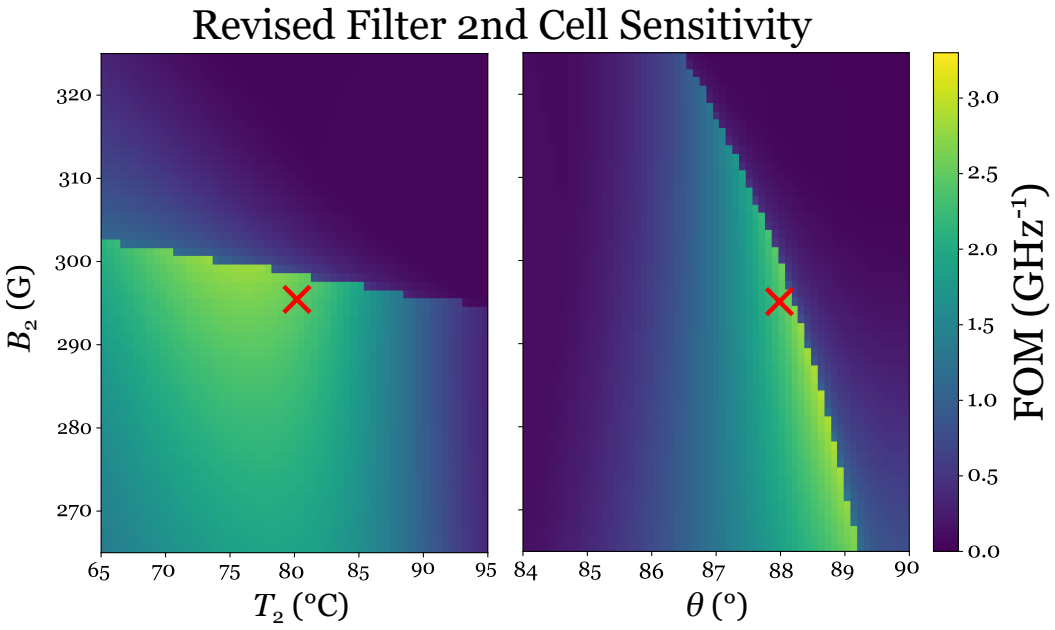

Figure 5.13: Heatmaps showing the sensitivity of FOM in the Revised filter to variation of Cell 2's three parameters: the magnetic field, B_2, the temperature, T_2 and angle between the magnetic field and k-vector which is θ for the second oblique cell. Red crosses mark the parameters plotted in Fig. 5.10. The FOM remains sensitive to Cell 2's parameters. However, one can compare the yellow regions with Fig. 5.8 and see that FOM remains close to maximum value for a larger region before plummeting to less than 1 GHz^{-1}

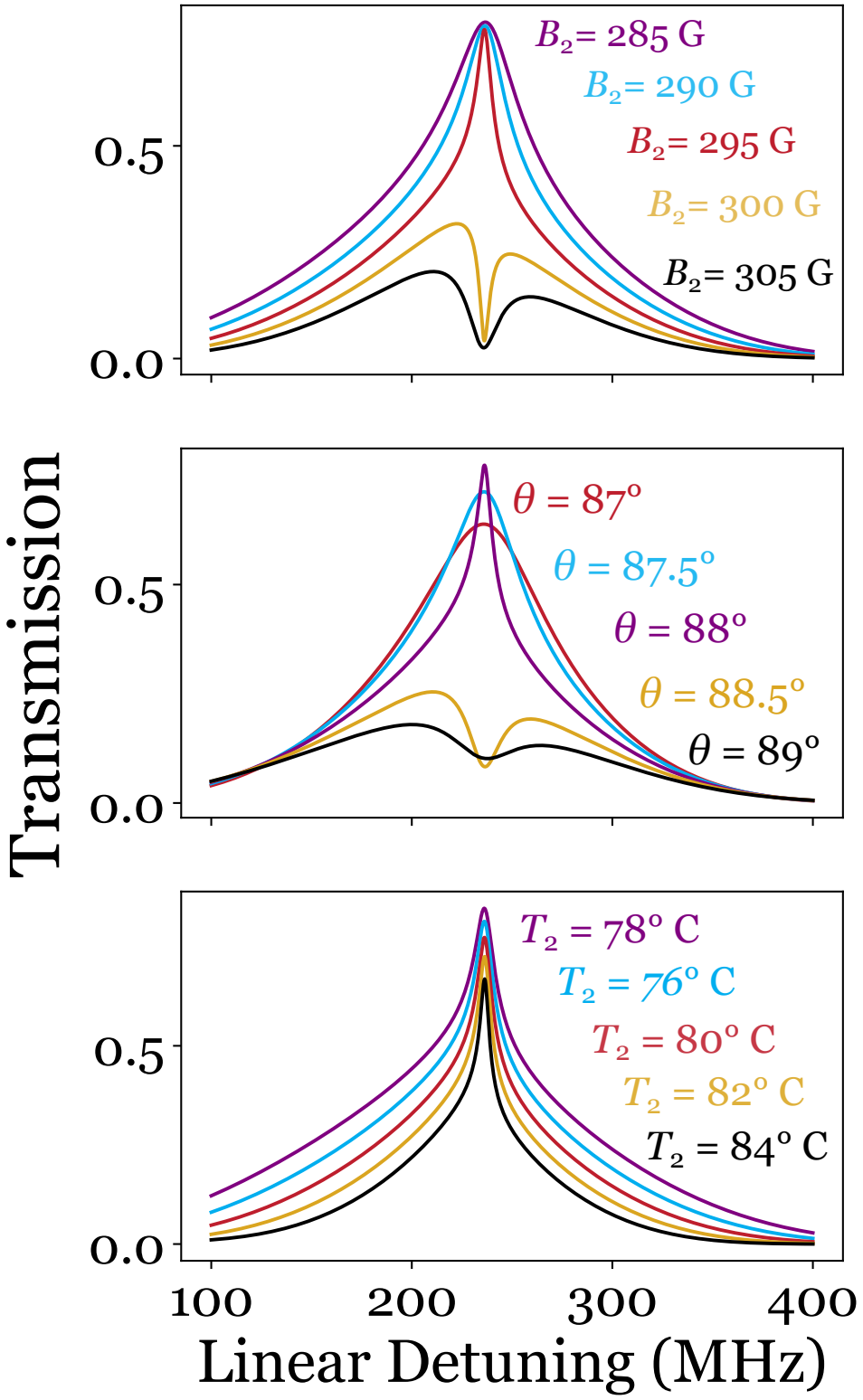

Figure 5.14: Lineshapes of the revised filter central peak for variation in B_2, θ and T_1. Lineshape remains a peak after varying the field by $\pm$ 5 G, and reducing θ by 1°. Varying temperature alters FWHM but maintains the peak lineshape.

5.4 Analysis

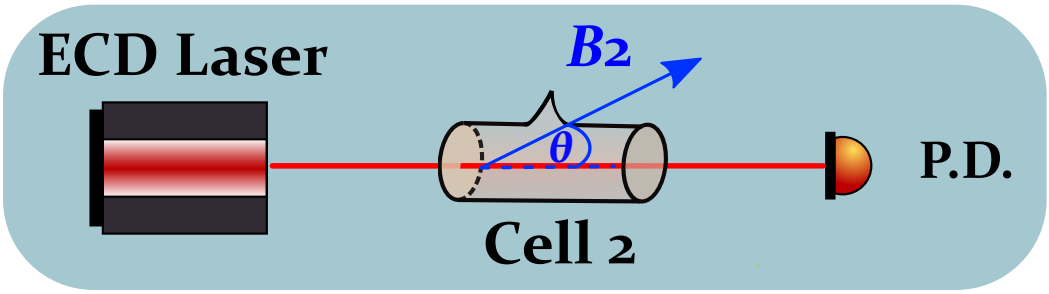

Figure 5.15: An experimental scheme used in an attempt to realise narrow transmission features resulting from coalescent eigenvectors. An external cavity diode (ECD) laser directs light through a cell with oblique magnetic field provided by a solenoid and plate magnet configuration discussed in 4.3. Light is detected by a photodetector (P.D.).

Having predicted the Revised filter with parameter sensitivities that could reasonably be realised, we conducted initial tests on a single oblique cell (see Fig. 5.15). Light from a Toptica DL100 laser in the weak probe regime was directed through Cell 2 of the Revised filter before being detected by a photodetector. The magnetic field was provided axially by a solenoid and transversely by a pair of plate magnets, more details can be found in 4.3. The aim was to detect any sub-100 MHz transmission features either peaks or troughs. For this we also considered other parameter sets, predicted by *ElecSus*, that may not have generated good filter profiles but may nevertheless exhibit these sharp features. We were unable to find any evidence of these features with our current setup. Therefore in this section, we consider some possible factors to explore in understanding why experiment currently does not match theory.

5.4.1 Inhomogeneities and Other Field Problems

Fig. 5.16 shows how the magnetic field magnitude and angle θ varied over the 75 mm cell. The field magnitude and angle are inhomogeneous to 7 % and < 1 % of their respective mean values. As demonstrated in the previous section, parameter

variation of this magnitude can cause coalescent peaks at high transmission to deteriorate to low transmission troughs.

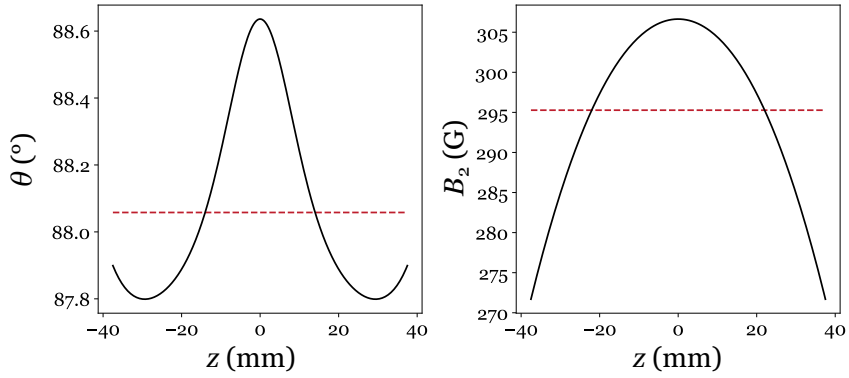

Figure 5.16: Theoretical magnetic field profile of the Revised filter oblique cell. The red dotted line marks the mean value over 75 mm which are 88.0° and 295 G. Plots calculated using the python package *magpylib* using code developed by Thomas Robertson-Browne.

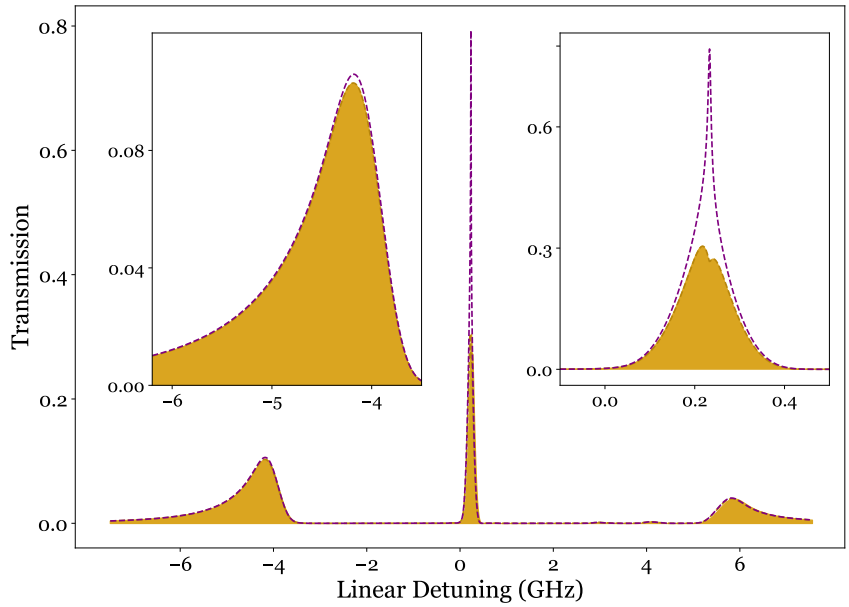

L (mm)	T (°C)	B (G)	θ (°)
75	60	295	88

Figure 5.17: Theory curves of the Revised Filter transmission for a perfectly homogeneous field (purple) and for the predicted field profile shown in Fig. 5.16 (goldenrod). Parameters for the perfectly homogeonous filter are shown in the table. All other parameters remain the same for both filters. We note that the predicted field filter has a lower transmission and higher FWHM of ~ 100 MHz.

Fig. 5.17 shows the effect that an inhomogeonous field can have on filter transmis-

sion. The central peak is far reduced in transmission and has a higher FWHM of ~ 100 MHz. It is therefore possible that our field generation limited our ability to view these narrow features. However, we note that even features of ~ 100 MHz width were not seen in single pass experiments. This may be due to further compounding issues in our field generation. In particular, we struggled to calibrate our plate magnets such that we would not exert an axial field. It is believed that the magnet dimensions used were too short along the cell length to provide a zero axial field. Additionally, changing the separation of the magnets to scan over different field magnitudes was achieved by moving the magnets by hand as space did not permit a more sophisticated approach. This was a clunky method and made it difficult to scan the parameter space in small increments.

One might ask why we do not optimise with a realistic magnetic field involving inhomogeneities. In theory, this is possible. Considering only the plate magnets as an example, we could calculate the magnetic field using *magpylib* and define the magnet separation as a parameter which can be varied in an optimisation. However, in its current form, the optimisation would run very slowly. We would need to find a way to shortcut *magpylib* such that it only runs the necessary code on each iteration as the separation is varied.

Additionally, inhomogeneity may not be the only problem posed by our magnetic fields. Stray fields could disturb our atoms [327]. Indeed our own generated fields could be noisy [328] resulting in unpredicted magnetic behaviour that varies with environmental conditions. Sizaeble magnetic field gradients could be present across the beam waist as the beam diverges upon propagation. In short, it is imperative we fully understand the action of our magnetic fields in the lab.

5.4.2 Computational Uncertainty and Model Assumptions

The sensitivity of the parameters may not merely pose experimental difficulties but computational ones. Appendix B addresses further the implications of computa-

tional error. The general conclusion of the Appendix is that we ought to investigate the numerical stability of our solutions though most calculations have been found to be reliable.

5.4.3 Non-Hermitian Reasoning

One might be tempted to suggest that having never seen coalescent features, there is little proof for non-Hermitian physics having a role in this domain. Particularly given that magneto-optical rotation has been studied extensively and this has never been addressed before. Firstly, we note that exceptional points of degeneracy have been explored on multi-level thermal vapour platforms [329, 293, 330] albeit not in ground state filters. Most recently, theoretical studies were conducted [331] into non-Hermitian Faraday rotation. Moreover, the work in Chapter 4 relies on eigenmode non-orthogonality (<20% real eigenmode dot product value) where we showed excellent agreement between data and theory.

Though the results are not yet convincing, there is not a reasonable alternative explanation. One can force *ElecSus* to have crossing refractive index solutions in the oblique geometry by swapping labels and similarly force orthogonal eigenmodes. However, these lead to wildly different results which are not experimentally supported and have little theoretical justification behind them. It would appear that non-Hermitian physics has unintentionally been built into our model. In this chapter, we have shown that non-Hermitian physics has a natural place in magneto-optical rotation and we ought to explore its implications further.

5.5 Outlook

In this chapter, we introduced non-Hermitian physics as an explanation as to why oblique cells exhibit non-orthogonal eigenmodes. Having studied the dispersion relation matrix, we found that the oblique matrix lacks a symmetry found in Faraday

and Voigt matrices which are Hermitian for real susceptibilities. With this knowledge, we expected to see narrower filter peaks by identifying *exceptional point of degeneracy*: points where the eigenvectors are almost parallel and the refractive indices approach an avoided crossing. We presented two filter predictions. The first was a 11 MHz FWHM filter which required parameters too sensitive to feasibly construct. The second prediction maintained a sub-50 MHz FWHM for reasonable parameters and tolerances. However, we were unable to realise this in a lab after much effort. We gave initial analysis into what may have limited us and we describe the way forward in more detail in our conclusions in Chapter 6.

For the time being, we suspend disbelief and consider a possible application for such narrow filters. Optical clocks are set to replace atomic clocks as the new time standard at a future meeting of the International Bureau of Weights and Measures [332, 333]. While most realised clocks are *passive* relying on atomic spontaneous emission as a frequency standard [334, 335], recently there has been interest in *active* optical clocks where the atomic medium is built into the lasing device and its stimulated emission becomes the frequency standard [336, 337].

Active clocks are being readily pursued to reach mHz clock laser linewidths [338] and overcome cavity noise instability by utilising so called 'bad cavities' where the cavity decay rate is much greater than the gain bandwidth [339, 340]. The group at Peking University [125] presented the first Faraday active optical clock incorporating a single cell Cs filter as the atomic medium. Their predicted quantum limited linewidth of 0.3 Hz is much smaller than the spontaneous case owing to an additional term is the Shawlow-Townes formula [337]:

$$\nu_{\text{Laser}} = \frac{h\nu_0 \cdot \Gamma_c^2}{4\pi \cdot P} \cdot \left(\frac{1}{1 + \frac{\Gamma_c}{\kappa}} \right)^2 \tag{5.11}$$

where ν_{Laser} is the quantum limited laser linewidth, h, is Planck's constant, P and ν_0, are the power and frequency input to the first cell. Γ_c is the cavity decay rate and κ is the output bandwidth of light after passing through the gain medium and cells. Note there is a correction for detuned light that we do not consider here.

Fig. 5.18 shows the setup needed to create a magneto-optical active frequency standard where a gain medium and a bandpass filter are placed in a cavity. The table shows quantum limited linewidths of the Peking group Faraday filter alongside various filters presented in this thesis. In particular the Webber filter linewidth limit is ten times smaller than the best laser linewidths achieved to date using the Pound-Drever Hall technique [341, 294, 342]. There is therefore huge incentive to explore how we can realise these new filters especially since they do not require a pump laser which was a cited as a major source of instability in [125] and the atoms do not have to be cooled [124, 192, 193].

Of course we are unable to estimate the systematics or expected frequency uncertainties currently but it it possible that the simplicity of the vapour cell setup could translate into more manageable error mitigation. We note that systematics have a large effect on linewidths in reported results. The Peking group demonstrated a laser linewidth of $\sim$ 100 Hz, a factor of 300 greater than the minimum. A group from the University of Copenhagen recently produced a laser linewidth of $\sim$ 800 Hz in ^{88}Sr [343], a factor of 1600 greater than minimum linewidth.

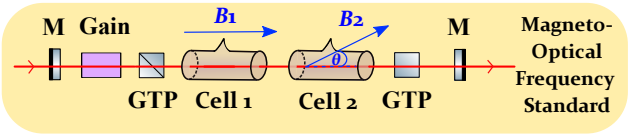

Active Frequency Standard	Quantum Limited Linewidth (Hz)
Line Centre Filter (Fig. 3.21)	8
Oblique-Voigt Filter (Fig. 4.11)	3
Double Pass Filter (Fig. 4.16)	2
Strontium Gas 689 nm Laser [336]	0.5
Cs Excited State 852 nm Filter [125]	0.3
40 MHz Faraday-Oblique FWHM Filter	0.35
Webber Faraday-Oblique Filter	0.03

Figure 5.18: A schematic of a magneto optical active frequency standard which could be used as an optical clock. Two vapour cells with magnetic fields, B_1 and B_2, exerted at angles θ and ψ to the k-vector, are placed between crossed Glan-Taylor polarisers (GTP) forming a bandpass filter. The filter is placed with a gain medium (Gain) inside a cavity formed of two mirrors (M). The cavity satisfies the bad cavity condition where $\kappa << \Gamma_c$. Light from an initial laser transmits into the cavity and photons produced via stimulated emission leave the cavity to further experiments. The table shows theoretical quantum limited linewidths of various active frequency standards using $\Gamma_c = 300$ MHz and $P = 75$ μW from [125]. If the active frequency standard is a filter, we substitute FWHM for κ. The filters experimentally realised in this thesis remain above > 1 Hz while the theoretical filters predicted in this chapter are sub-Hz.

Chapter 6

Conclusions

At the beginning of this thesis, we showed that magneto-optical filters had played integral roles in various applications and continue to do so today. Nevertheless, decades after their invention, basic principles of filter operation were still unknown. In order for filters to reach their true potential, more theoretical and proof of principle work was needed.

We ambitiously suggested that two simple modifications to the single cell filter case could improve quantitative metrics such as ENBW tenfold and increase lineshape tailoring abilities considerably. Through Chapters 3 and 4, we set out the theory behind adding a second cell (cascading) and exerting oblique magnetic fields. The experimental results met these high expectations. We can now realise filters with 100 MHz FWHMs, ENBWs not far behind, and FOMs approaching three times greater than those in the single cell case. We can select for wing or line centre features and change between operation via solenoid current variation. Additionally our chapter outlooks have highlighted several new applications where these filters may find utility including cryptography, cavity lens stabilisation and frequency comb mode selection. While we first considered oblique fields to be a small modification, the theory behind them became increasingly complicated. In Chapter 5, we argued that non-Hermitian analysis, which has become of increasing interest since the late 1990s, would benefit the study of oblique magneto-optical filters. We

predicted that with better understanding of the non-orthogonal propagation eigenmodes and their coalescence, filters could even approach FWHMs less than the natural linewidth. This represents a paradigm shift in our understanding of filter capabilities. We list the specific and general achievements of this thesis below:

Specific Achievements

- Realised the first line centre filter (Fig. 3.21).
- Realised the best passive filter design by FOM (Fig. 4.11).
- Realised the narrowest passive filter design by FWHM. (Fig. 4.16)

General Achievements

- Provided insight into the working principles of cascaded and oblique filters (Chapters 3 and 4).
- Introduced non-Hermitian analysis into magneto-optical filter studies (Chapters 4 and 5).

Having said this, we were unable to realise the filters relying on eigenvector coalescence predicted in Chapter 5. We proposed several reasons why this may be the case including inhomogeneous magnetic fields, our model assumptions and computational uncertainty. We dedicate the rest of this conclusion to outline a possible plan moving forwards.

Field homogeneity ought to be the first item to investigate. Many of our field plots throughout this thesis show inhomogeneities of $> 5\%$ over the length of the cell. Indeed, we believe the disagreement between data and theory for the Double pass oblique filter in Chapter 4 (See Fig. 4.16) was due to the short length of our plate magnets relative to the cell. Computer optimisations have shown that longer cells exhibit higher transmission coalescent features. Though we are unsure why, this is one reason why we want to consider improved field generation rather than

swapping longer cells for shorter ones. A manuscript in preparation by Sharaa Alqarni *et al.* demonstrates improved homogeneity for the combined solenoid and permanent magnet setup. Alqarni *et al.* have achieved this by replacing the plate magnets with a row of smaller bar magnets held in place by a custom built holder. The advantage is that now we can feasibly build more homogeneous magnetic fields over longer cell lengths for low cost and short build times. However, the remanence field can vary from bar magnet to bar magnet. As such each one must be analysed before constructing the setup. Indeed, more generally, recent progress in our lab has shown that manufacturing more homogeneous fields is very possible. It is merely the case that our niche requirements have rarely been considered in the literature. The work at the Université de Toulouse has been extremely valuable to us in the past. They have manufactured permanent magnets with $\sim$ 1 T fields suitable for 1 mm cells [344] which have been shipped and used in our lab resulting in a publication [1]. We note that a group in Nizhny Novgorod [345, 346] have also built similar competitive permanent magnets. While the magnetic field requirements are different to our previous work, there may be value in collaborating with these groups. Nevertheless, we have not yet established *how* homogeneous our field must be and this needs to be quantified before going forwards.

Our model makes certain assumptions that may not accurately describe the experimental situation. For instance, we have not considered the role of even a small quantity of buffer gases in our cells. Buffer gases can cause additional Lorentzian broadening and shifts in transition frequencies [223]. Indeed, it is possible that the role buffer gases play is more complicated than adding an additional Lorentzian broadening term to the susceptibility calculation (See Appendix A in [225]). There is scope for a project at Durham to consider the total effect buffer gases have on the susceptibility curves and whether this could account for our missing coalescent features. These investigations should not be confused with the effects of higher order susceptibilities that have been considered in harmonic generation and nonlinear optics. Such discussions are not relevant here as we still remain in the weak

probe regime. We should also not confuse these discussions with computational error which may also play a part. We consider the numerical stability of our solutions in Appendix B but further understanding in this area lies within the arena of computer science.

Finally, this thesis has only been an introduction to non-Hermitian physics in two level atomic vapours. Is it possible that there are obvious reasons arising from non-Hermitian physics as to why we are not observing these effects? We hope that the results of Chapter 4 encourage researchers with non-Hermitian backgrounds to consider exploring this question. As always, Durham is open to collaboration.

The future for magneto-optical filters looks bright. We believe that the filters predicted, while unfeasible now, hint at a very real filter mechanism evidenced by robust non-Hermitian analysis. We think the implications of an exceptional point filter are exciting enough for researchers to dedicate time and energy towards. The writer of this thesis looks forward to seeing progress in this area.

Appendix A

Jones Calculus

Author completed all theoretical computations, derived all proofs, created all figures presented in this appendix. All text written without use of AI. Work is related to the articles:

F. D. Logue, J. D. Briscoe, D. Pizzey, S. A. Wrathmall, and I. G. Hughes, 'Better magneto-optical filters with cascaded vapor cells', *Optics Letters*, 47(12):2975–2978, 2022. https://doi.org/10.1364/OL.459291 [2]

F. D. Logue, J. D. Briscoe, D. Pizzey, S. A. Wrathmall, and I. G. Hughes, 'Exploiting non-orthogonal eigenmodes in a non-Hermitian optical system to realize sub-100 MHz magneto-optical filters', *arXiv Preprint*, 2303.00081, 2023. https://doi.org/10.48550/arXiv.2303.00081 [5]

In this appendix, we use Jones Calculus [229] to mathematically justify various statements made in this thesis. As we have done throughout, we define z as the propagation direction of the light and assume the light is a plane wave. As such, since a plane wave can only be polarised transversely, the wave is polarised in the 2D $x-y$ plane. This completely polarised wave is represented by a 2 x 1 Jones column vector and propagated through optical elements represented by 2 x 2 matrices that transform the input electric field to its output. If the beam is partially polarised or unpolarised, a generalised Mueller calculus [347, 348] can be used involving 4 x

4 matrices, however, this is outside the scope of this thesis. Tables A.1 and A.2 define some standard Jones vectors and matrices used in this appendix.

When discussing polarisation, we have often used the language of Stokes parameters rather than Jones vectors and it is important to note the differences in the two representations. The three real Stokes parameters uniquely define each polarisation state. On the other hand, a Jones vector contains two complex entries, or four independent values, that uniquely determine the 2D electric field:

$$\mathbf{J} = \begin{pmatrix} x \\ y \end{pmatrix} = \begin{pmatrix} |x|e^{\mathrm{i}\gamma} \\ |y|e^{\mathrm{i}\zeta} \end{pmatrix}, \qquad \mathbf{S} = (S_1, S_2, S_3).$$

The global phases, γ and ζ, defined by the imaginary part of the electric field entries, are required for propagation calculations. Post-calculation, since we are interested in the polarization state and not the electric field vector, we can eliminate (or indeed add) global phases leaving only the relative phase, $\zeta - \gamma$, which determines handedness. Hence, Stokes parameters are the best representation scheme for polarisation. However, an extra degree of freedom is required to calculate the output electric field making Jones Calculus indispensable in polarisation studies [349, 350, 351, 352, 353, 354, 355].

Unnormalised Jones Vector	Polarisation
$\begin{pmatrix}1\\0\end{pmatrix}$	Horizontally Linear ↔
$\begin{pmatrix}0\\1\end{pmatrix}$	Vertically Linear ↕
$\begin{pmatrix}1\\1\end{pmatrix}$	Diagonally Linear at 45° ↘
$\begin{pmatrix}-1\\1\end{pmatrix}$	Diagonally Linear at −45° ↙
$\begin{pmatrix}1\\\mathrm{i}\end{pmatrix}$	Left Hand Circular ↺
$\begin{pmatrix}1\\-\mathrm{i}\end{pmatrix}$	Right Hand Circular ↻

Figure A.1: Definitions of standard unnormalised Jones vectors. Polarisation animations drawn as viewed looking *towards* the source. Sign conventions taken from [356].

Jones Matrix	Function
$\begin{pmatrix}1&0\\0&0\end{pmatrix}$	Horizontal Linear Polariser
$\begin{pmatrix}0&0\\0&1\end{pmatrix}$	Vertical Linear Polariser
$\frac{1}{2}\begin{pmatrix}1&-\mathrm{i}\\\mathrm{i}&1\end{pmatrix}$	Left Circular Polariser
$\frac{1}{2}\begin{pmatrix}1&\mathrm{i}\\-\mathrm{i}&1\end{pmatrix}$	Right Circular Polariser
$\frac{1}{2}\begin{pmatrix}1+\mathrm{i}&1-\mathrm{i}\\1-\mathrm{i}&1+\mathrm{i}\end{pmatrix}$	Quarter Waveplate, Fast Axis at 45°
$\frac{1}{2}\begin{pmatrix}1+\mathrm{i}&\mathrm{i}-1\\\mathrm{i}-1&1+\mathrm{i}\end{pmatrix}$	Quarter Waveplate, Fast Axis at −45°

Figure A.2: Definitions of standard Jones matrices.

A.1 Propagating an Electromagnetic Wave through a Birefringent Vapour

Rubidium vapour in the presence of a magnetic field is characterised as having two propagation eigenmodes[1], $\vec{a}$ and $\vec{b}$ [207]:

$$\vec{a} = \begin{bmatrix} a_1 \\ a_2 \end{bmatrix}, \qquad \vec{b} = \begin{bmatrix} b_1 \\ b_2 \end{bmatrix}. \tag{A.1}$$

These vectors together form the hermitian conjugated (†) change-of-basis matrix,

$$\mathbf{R} = \begin{bmatrix} a_1 & b_1 \\ a_2 & b_2 \end{bmatrix}^\dagger. \tag{A.2}$$

Associated with these eigenmodes are refractive index eigenvalues n_a and n_b. Defining a function f, we can construct a diagonal matrix $\mathbf{T}$,

$$\mathbf{T} = \begin{bmatrix} f(n_a) & 0 \\ 0 & f(n_b) \end{bmatrix}, \tag{A.3}$$

such that the input electric field $\mathbf{E_{in}}$ is propagated to the output electric field $\mathbf{E_{out}}$ as,

$$\mathbf{E_{out}} = \overbrace{\mathbf{R^{-1}} \cdot \mathbf{T} \cdot \mathbf{R}}^{\mathcal{P}} \cdot \mathbf{E_{in}}. \tag{A.4}$$

We label the resultant propagation matrix, $\mathcal{P}$. In the sections that follow, we will use eq. A.4 to prove facts about filter outputs discussed in this thesis. Fig. A.3 gives a sequential visual explanation of how $\mathcal{P}$ acts on $\mathbf{E_{in}}$ to output $\mathbf{E_{out}}$.

[1] For the reader interested as to why there are not three propagation eigenmodes, see § 12, (*The allowance for spatial dispersion in an anisotropic medium*) of [357].

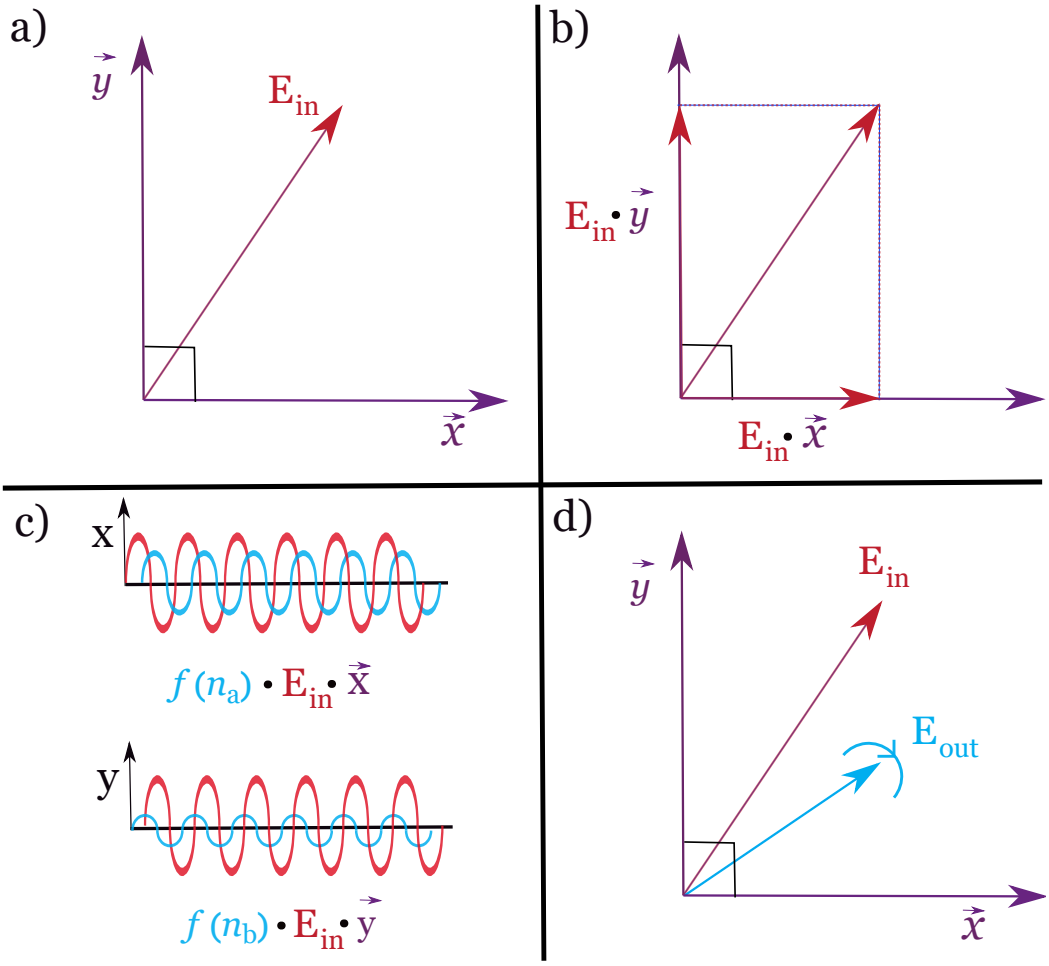

Figure A.3: A visualisation of the matrix propagation from input to output electric fields in a birefringent vapour. We choose the Voigt geometry as an example. a) The eigenmodes of the system (purple) which are linearly horizontal ($\vec{x}$) and vertical ($\vec{y}$) light, the eigenmodes in the Voigt geometry. The input electric field, $\mathbf{E_{in}}$, in red. b) The input electric field is decomposed on to the two eigenvectors. c) The two decomposed vectors are acted upon by either the function $f(n_a)$ or $f(n_b)$. This results in absorption as shown by the output vectors (blue) having smaller amplitude than the original decomposed vectors (red). The decomposed vectors also gain a phase. In this case, one gains a positive and the other a negative phase. d) The transformed vectors in c) are added resulting in an output electric field $\mathbf{E}_{\text{out}}$ that is smaller in amplitude, rotated in the linear plane and right handed.

A.2 Comparison of Propagation in the Faraday, Voigt and Oblique Geometries

In this section, we construct propagation matrices, $\mathcal{P}$, in the Faraday, Voigt and oblique geometries. Using these matrices, we find the invariant polarisations that

when input to the cell are output in the same polarisation state. We show that the invariant polarisations are the orthogonal states to the eigenmodes. We also demonstrate that in the Faraday and Voigt geometries, this means the eigenmodes are the invariant polarisations since they are mutually orthogonal. In the oblique geometry, the eigenmodes are not invariant since the eigenmodes are not in general mutually orthogonal.

A.2.1 Faraday Propagation

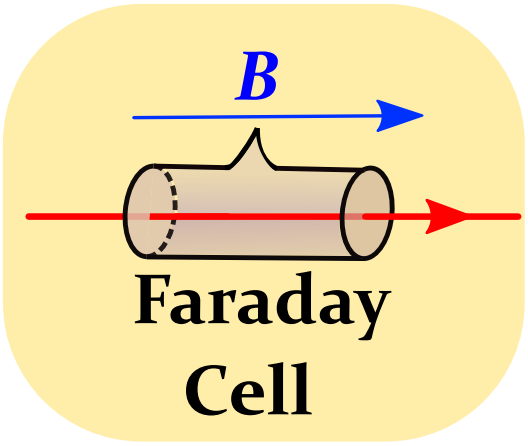

Figure A.4: A thermal vapour cell in the Faraday geometry with the k-vector of the light parallel with the applied magnetic field (B).

Fig. A.4 depicts a cell in the Faraday geometry. Solving the wave equation, one finds that the Faraday geometry has left and right hand circular light as eigenmodes [356]. From eq. A.4 and using the Jones vector expressions in Table A.1, the Faraday propagation matrix, $\mathcal{P}_{\mathrm{F}}$, is

$$\begin{aligned}\mathcal{P}_{\mathrm{F}} &= \frac{1}{2}\begin{bmatrix}1 & 1\\ \mathrm{i} & -\mathrm{i}\end{bmatrix}\cdot\begin{bmatrix}f(n_a) & 0\\ 0 & f(n_b)\end{bmatrix}\cdot\overbrace{\begin{bmatrix}1 & -\mathrm{i}\\ 1 & \mathrm{i}\end{bmatrix}}^{\circlearrowleft,\circlearrowright} \\ &= \frac{1}{2}\begin{bmatrix}f(n_a)+f(n_b) & -\mathrm{i}(f(n_a)-f(n_b))\\ \mathrm{i}(f(n_a)-f(n_b)) & f(n_a)+f(n_b)\end{bmatrix}.\end{aligned} \tag{A.5}$$

Note that the eigenmodes in $\mathbf{R}$ do not need to be normalised since the inverse reverses any scaling by $\mathbf{R}$ at the end of the calculation. Similarly, the positions of $\vec{a}$ and $\vec{b}$ can be interchanged in $\mathbf{R}$ if the positions of $f(n_a)$ and $f(n_b)$ are interchanged in $\mathbf{T}$. Suppose we input left hand circular light into this Faraday system:

$$\begin{aligned}\mathbf{E_{out}} &= \frac{1}{2}\begin{bmatrix} f(n_a)+f(n_b) & -\mathrm{i}(f(n_a)-f(n_b)) \\ \mathrm{i}(f(n_a)-f(n_b)) & f(n_a)+f(n_b)\end{bmatrix}\cdot\overbrace{\begin{bmatrix}1\\ \mathrm{i}\end{bmatrix}} \\ &= \begin{bmatrix} f(n_a) \\ \mathrm{i}\cdot f(n_a)\end{bmatrix} \\ &= f(n_a)\cdot\begin{bmatrix}1\\ \mathrm{i}\end{bmatrix}.\end{aligned} \tag{A.6}$$

The output electric field, $\mathbf{E_{out}}$, has the same direction as the input, therefore the polarisation has not changed. In fact, it has been acted upon by a factor dependent on the refractive index, n_a. In magneto-optical rotation terms, this results in a phase added and some absorption. The phase added is global and so has no physical impact on the polarisation state and the absorption ensures the output is of a lower intensity than its input. For completeness, we input right handed circular light,

$$\begin{aligned}\mathbf{E_{out}} &= \frac{1}{2}\begin{bmatrix} f(n_a)+f(n_b) & -\mathrm{i}(f(n_a)-f(n_b)) \\ \mathrm{i}(f(n_a)-f(n_b)) & f(n_a)+f(n_b)\end{bmatrix}\cdot\overbrace{\begin{bmatrix}1\\ -\mathrm{i}\end{bmatrix}} \\ &= \begin{bmatrix} f(n_b) \\ -\mathrm{i}\cdot f(n_b)\end{bmatrix} \\ &= f(n_b)\cdot\begin{bmatrix}1\\ -\mathrm{i}\end{bmatrix},\end{aligned} \tag{A.7}$$

and find the case to be analogous but with a factor dependent on n_b. In short, the eigenmodes of a Faraday cell are invariant polarisations.

A.2.2 Voigt Propagation

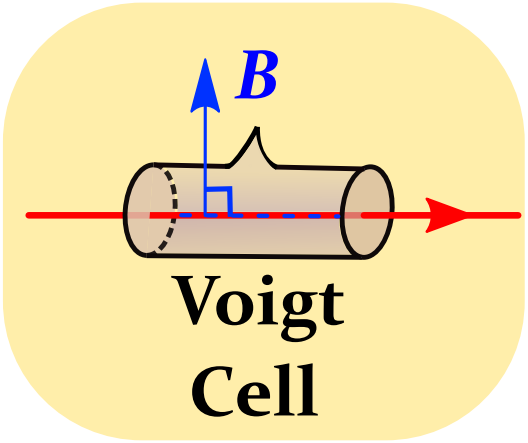

Figure A.5: A thermal vapour cell in the Voigt geometry with the k-vector of the light perpendicular to the applied magnetic field (B).

Fig. A.5 depicts a cell in the Voigt geometry. A Voigt cell has linearly horizontal and vertical light as eigenmodes [207]. Once again from eq. A.4 and using Jones vectors from Table A.1, we have the Voigt propagation matrix, $\mathcal{P}_{\mathrm{V}}$:

$$\begin{aligned}\mathcal{P}_{\mathrm{V}} &= \begin{bmatrix}1 & 0\\ 0 & 1\end{bmatrix}\cdot\begin{bmatrix}f(n_a) & 0\\ 0 & f(n_b)\end{bmatrix}\cdot\overbrace{\begin{bmatrix}1 & 0\\ 0 & 1\end{bmatrix}}^{\longleftrightarrow,\updownarrow}\\ &= \begin{bmatrix}f(n_a) & 0)\\ 0 & f(n_b)\end{bmatrix}.\end{aligned} \tag{A.8}$$

We input an eigenmode, linearly horizontal light, into the Voigt system and find:

$$\begin{aligned}\mathbf{E_{out}} &= \begin{bmatrix} f(n_a) & 0) \\ 0 & f(n_b) \end{bmatrix} \cdot \overbrace{\begin{bmatrix} 1 \\ 0 \end{bmatrix}}^{\longleftrightarrow} \\ &= \begin{bmatrix} f(n_a) \\ 0 \end{bmatrix} \\ &= f(n_a) \cdot \begin{bmatrix} 1 \\ 0 \end{bmatrix}.\end{aligned} \tag{A.9}$$

Like the Faraday case, inputting an eigenmode results in invariant polarisation. Showing this is the case when inputting the other eigenmode, linearly vertical light, follows trivially.

A.2.3 Oblique Propagation

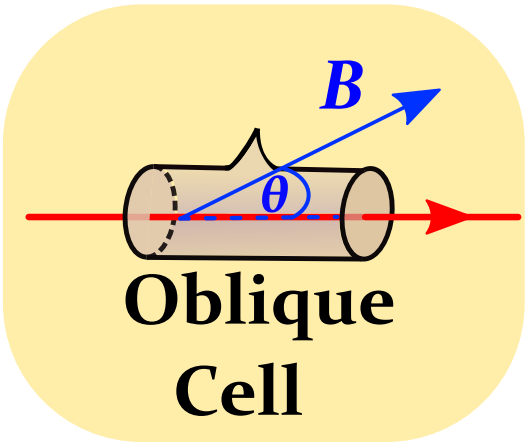

Figure A.6: A thermal vapour cell in the oblique geometry with the applied magnetic field (B) making an angle θ, neither 0° or 90°, to the k-vector of the light.

Fig. A.6 depicts a cell in the oblique geometry. As discussed in Chapter 4, eigenmode solutions to the wave equation are non-orthogonal and frequency dependent in the oblique geometry. We construct a toy system with non-orthogonal eigenmodes: horizontally linear and diagonally linear at 45° light. Fig. A.7 shows all

the polarisation vectors involved in this example. The propagation matrix, $\mathcal{P}_{\mathrm{O}}$, is given as:

$$\begin{aligned}\mathcal{P}_{\mathrm{O}} &= \begin{bmatrix} 1 & 0 \\ -1 & 1 \end{bmatrix} \cdot \begin{bmatrix} f(n_a) & 0 \\ 0 & f(n_b) \end{bmatrix} \cdot \overbrace{\begin{bmatrix} 1 & 0 \\ 1 & 1 \end{bmatrix}}^{\longleftrightarrow,\ \swarrow\!\!\nearrow} \\ &= \begin{bmatrix} f(n_a) & 0 \\ f(n_b) - f(n_a) & f(n_b) \end{bmatrix}.\end{aligned} \tag{A.10}$$

We input the eigenmodes linearly horizontal light, in eq. A.11 and diagonal light at 45°, in eq. A.12:

$$\begin{aligned}\mathbf{E_{out}} &= \begin{bmatrix} f(n_a) & 0 \\ f(n_b) - f(n_a) & f(n_b) \end{bmatrix} \cdot \overbrace{\begin{bmatrix} 1 \\ 0 \end{bmatrix}}^{\longleftrightarrow} \\ &= \begin{bmatrix} f(n_a) \\ f(n_b) - f(n_a) \end{bmatrix} \\ &= f(n_b) \cdot \overbrace{\begin{bmatrix} 0 \\ 1 \end{bmatrix}}^{\updownarrow} - f(n_a) \cdot \overbrace{\begin{bmatrix} -1 \\ 1 \end{bmatrix}}^{\nwarrow\!\!\searrow},\end{aligned} \tag{A.11}$$

$$\begin{aligned}\mathbf{E_{out}} &= \begin{bmatrix} f(n_a) & 0 \\ f(n_b) - f(n_a) & f(n_b) \end{bmatrix} \cdot \overbrace{\begin{bmatrix} 1 \\ 1 \end{bmatrix}}^{\swarrow\!\!\nearrow} \\ &= \begin{bmatrix} f(n_a) \\ 2 \cdot f(n_b) - f(n_a) \end{bmatrix} \\ &= 2 \cdot f(n_b) \cdot \overbrace{\begin{bmatrix} 0 \\ 1 \end{bmatrix}}^{\updownarrow} - f(n_a) \cdot \overbrace{\begin{bmatrix} -1 \\ 1 \end{bmatrix}}^{\nwarrow\!\!\searrow}.\end{aligned} \tag{A.12}$$

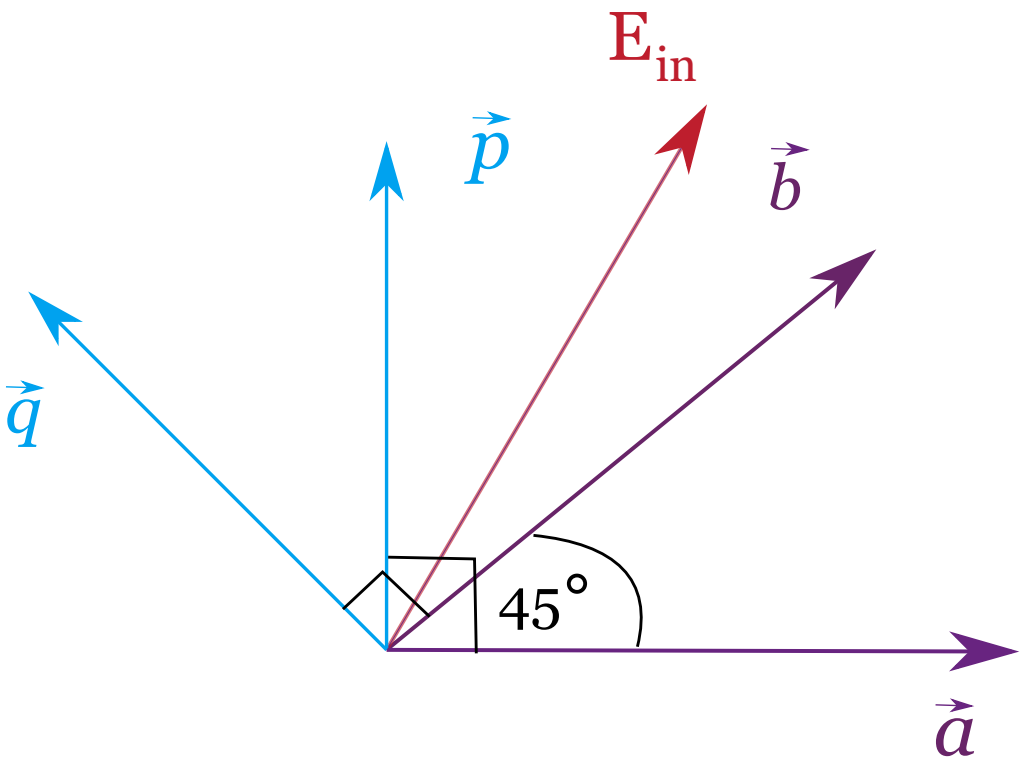

Figure A.7: A diagram of the vectors used in the toy example. An arbitrary input electric field, $\mathbf{E_{in}}$, is shown in red. $\vec{a}$ and $\vec{b}$ (purple) are the non-orthogonal eigenmodes, linearly horizontal and linear diagonal light at 45° respectively. $\vec{p}$ and $\vec{q}$ (blue) are the invariant polarisations, linearly vertical and linear diagonal light at −45° respectively. Note that each invariant polarisation is orthogonal to one eigenmode which eq. A.16 shows is a general principle across Faraday, Voigt and oblique systems.

While we have input eigenmodes in both cases, neither case is an example of an invariant propagation. The two entries, x and y of the input Jones vector have been modified in the output by different factors and as such the output polarization state is different to the input. In both cases, we are able to decompose the output polarization into a linear combination of the same polarizations, linearly vertical and linear diagonal light at −45°. These are in fact the invariant polarisations of the system. We input linearly vertical light (eq. A.13) and linear diagonal light at −45° (eq. A.14) into the system,

$$\begin{aligned}\begin{bmatrix} f(n_a) & 0 \\ f(n_b) - f(n_a) & f(n_b) \end{bmatrix} \cdot \begin{bmatrix} 0 \\ 1 \end{bmatrix} \\ = \begin{bmatrix} 0 \\ f(n_b) \end{bmatrix} \\ = f(n_b) \cdot \begin{bmatrix} 0 \\ 1 \end{bmatrix},\end{aligned} \tag{A.13}$$

$$\begin{aligned}\begin{bmatrix} f(n_a) & 0 \\ f(n_b) - f(n_a) & f(n_b) \end{bmatrix} \cdot \begin{bmatrix} -1 \\ 1 \end{bmatrix} \\ = \begin{bmatrix} -f(n_a) \\ f(n_a) \end{bmatrix} \\ = f(n_a) \cdot \begin{bmatrix} -1 \\ 1 \end{bmatrix},\end{aligned} \tag{A.14}$$

and prove they are indeed invariant polarisations. While the non-orthogonal eigenmode system constructed is a toy example, the general principle that the invariant polarisations and the eigenmodes are not one and the same holds in the oblique geometry. For more information on the constraints on eigenmodes in the oblique geometry, see Section A.6.

A.2.4 General Expression for Invariant Polarisations

An invariant polarisation when propagated cannot be acted upon by functions of both refractive indices otherwise a relative phase may be applied to the electric field leading to polarisation transformation. Hence, a polarisation is invariant if it is orthogonal to one of the eigenmodes. This leads to the general expression to find the invariant polarisations, $\vec{p}$ and $\vec{q}$, in terms of the entries in the eigenmodes, $\vec{a}$ and $\vec{b}$,

$$\vec{p} = \begin{pmatrix} -a_2^* \\ a_1^* \end{pmatrix}, \quad \vec{q} = \begin{pmatrix} -b_2^* \\ b_1^* \end{pmatrix}, \tag{A.15}$$

$$\vec{a} = \begin{pmatrix} a_1 \\ a_2 \end{pmatrix}, \quad \vec{b} = \begin{pmatrix} b_1 \\ b_2 \end{pmatrix}, \tag{A.16}$$

where $*$ incidates the complex conjugate. This is a general expression applicable to the Faraday, Voigt and oblique geometries. In the Faraday and Voigt cases, since the eigenmodes are mutually orthogonal, each eigenmode is the invariant polarisation of the other eigenmode. The reader can verify that the invariant polarisations in the toy example (Section A.2.3) are indeed those described in eq A.16. This fact can also be seen visually in Fig. A.7. We say that the invariant polarisations and the eigenmodes, if normalised, together form a *biorthogonal* system [358, 359, 360, 361].

A.3 Faraday-Voigt and Voigt-Faraday Filters Have Equivalent Outputs

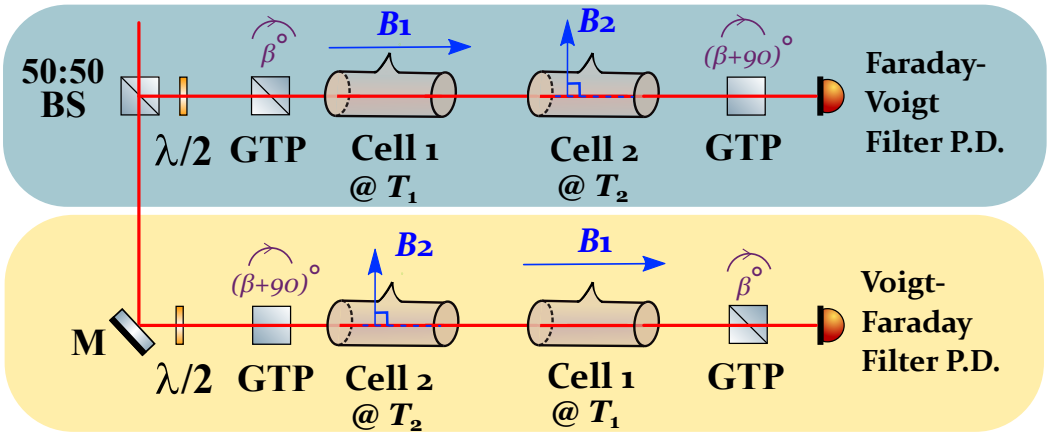

Figure A.8: A diagram of a Faraday-Voigt filter and a Voigt-Faraday filter with equivalent outputs. In the blue box, the Faraday-Voigt filter is composed of two cells with cell lengths L_1 and L_2 at temperatures and magnetic fields T_i and B_i. The first cell is in the Faraday geometry and the second is in the Voigt with both cells between two crossed polarisers. The first polariser is rotated out of the page by angle $\beta°$. In the yellow box, the Voigt-Faraday filter is composed of cells with the same parameters as in the Faraday-Voigt filter but with their positions interchanged. As such the first cell is in the Voigt geometry and the second is in the Faraday. Once again, the cells are between crossed polarisers which are both rotated 90° out of the page relative to the orientation of the polarisers in the Faraday-Voigt filter. Alternatively, one can interchange the positions of the polarisers. M — Mirror, BS — Beamsplitter, GTP — Glan-Taylor Polariser, P.D. — Photodetector.

In Chapter 3, it is stated that a Faraday-Voigt filter has the same output as a Voigt-Faraday filter where the positions of cells are interchanged as well as the positions of the polarisers. In this section, we prove this statement for the specific case where linearly horizontal/vertical light is input into the Faraday-Voigt/Voigt-Faraday cell, and more generally. We plot the theory intensity curves of the two filter setups and comment on the role of the Voigt cell in each filter and its effect on the filter profile.

Fig. A.8 shows an example experimental setup for the two filters. Note for clarity, when the cell positions are interchanged, the parameters of each cell are unchanged such that the first cell in sequence now has a temperature of T_2 and the second, T_1.

In a two-cell cascade, the output electric field is given by applying two propagation matrices, $\mathcal{P}_i$, one for each cell,

$$\mathbf{E_{out}} = \overbrace{\mathcal{P}_2 \cdot \mathcal{P}_1}^{\mathcal{P}_{1,2}} \cdot \mathbf{E_{in}}, \tag{A.17}$$

where $\mathcal{P}_1$ and $\mathcal{P}_2$ are the propagation matrices of the first and second cells respectively (defined in eq. A.4) and $\mathcal{P}_{1,2}$ is the resultant propagation matrix from both cells. For a Faraday cell followed by a Voigt cell and a Voigt cell followed by a Faraday cell, $\mathcal{P}_{\mathrm{F,V}}$ and $\mathcal{P}_{\mathrm{V,F}}$ respectively are,

$$\begin{aligned}\mathcal{P}_{\mathrm{F,V}} &= \begin{bmatrix} g(n_a) & 0) \\ 0 & g(n_b) \end{bmatrix} \cdot \frac{1}{2} \begin{bmatrix} f(n_a)+f(n_b) & -\mathrm{i}(f(n_a)-f(n_b)) \\ \mathrm{i}(f(n_a)-f(n_b)) & f(n_a)+f(n_b) \end{bmatrix} \\ &= \frac{1}{2} \begin{bmatrix} g(n_a)\cdot(f(n_a)+f(n_b)) & -\mathrm{i}\cdot g(n_a)\cdot(f(n_a)-f(n_b)) \\ \mathrm{i}\cdot g(n_b)\cdot(f(n_a)-f(n_b)) & g(n_b)\cdot(f(n_a)+f(n_b)) \end{bmatrix},\end{aligned} \tag{A.18}$$

$$\begin{aligned}\mathcal{P}_{\mathrm{V,F}} &= \frac{1}{2} \begin{bmatrix} f(n_a)+f(n_b) & -\mathrm{i}(f(n_a)-f(n_b)) \\ \mathrm{i}(f(n_a)-f(n_b)) & f(n_a)+f(n_b) \end{bmatrix} \cdot \begin{bmatrix} g(n_a) & 0 \\ 0 & g(n_b) \end{bmatrix} \\ &= \frac{1}{2} \begin{bmatrix} g(n_a)\cdot(f(n_a)+f(n_b)) & -\mathrm{i}\cdot g(n_b)\cdot(f(n_a)-f(n_b)) \\ \mathrm{i}\cdot g(n_a)\cdot(f(n_a)-f(n_b)) & g(n_b)\cdot(f(n_a)+f(n_b)) \end{bmatrix}.\end{aligned} \tag{A.19}$$

$$\mathcal{P}_{\mathrm{F,V}} \neq \mathcal{P}_{\mathrm{V,F}} \tag{A.20}$$

A.3.1 Specific Case

We start with a specific case where horizontal linear light is input into a Faraday-Voigt filter and we post-select for vertical light using a vertical polarizer (as defined in Table A.2):

$$\begin{aligned}
\mathbf{E_{out}} &= \begin{bmatrix} 0 & 0 \\ 0 & 1 \end{bmatrix} \cdot \frac{1}{2} \begin{bmatrix} g(n_a) \cdot (f(n_a) + f(n_b)) & -\mathrm{i} \cdot g(n_a) \cdot (f(n_a) - f(n_b)) \\ \mathrm{i} \cdot g(n_b) \cdot (f(n_a) - f(n_b)) & g(n_b) \cdot (f(n_a) + f(n_b)) \end{bmatrix} \cdot \overbrace{\begin{bmatrix} 1 \\ 0 \end{bmatrix}}^{\leftrightarrow} \\
&= \begin{bmatrix} 0 & 0 \\ 0 & 1 \end{bmatrix} \cdot \frac{1}{2} \cdot \begin{bmatrix} g(n_a) \cdot (f(n_a) + f(n_b)) \\ \mathrm{i} \cdot g(n_b) \cdot (f(n_a) - f(n_b)) \end{bmatrix} \\
&= \frac{1}{2} \cdot \mathrm{i} \cdot g(n_b)((f(n_a) - f(n_b)) \cdot \overbrace{\begin{bmatrix} 0 \\ 1 \end{bmatrix}}^{\updownarrow}.
\end{aligned} \tag{A.21}$$

We similarly model a Voigt-Faraday filter where vertically linear light is input and we post-select for linear horizontal light using a horizontal polarizer (see Table A.2):

$$\begin{aligned}
\mathbf{E_{out}} &= \begin{bmatrix} 1 & 0 \\ 0 & 0 \end{bmatrix} \cdot \frac{1}{2} \begin{bmatrix} g(n_a) \cdot (f(n_a) + f(n_b)) & -\mathrm{i} \cdot g(n_b) \cdot (f(n_a) - f(n_b)) \\ \mathrm{i} \cdot g(n_a) \cdot (f(n_a) - f(n_b)) & g(n_b) \cdot (f(n_a) + f(n_b)) \end{bmatrix} \cdot \overbrace{\begin{bmatrix} 0 \\ 1 \end{bmatrix}}^{\updownarrow} \\
&= \begin{bmatrix} 1 & 0 \\ 0 & 0 \end{bmatrix} \cdot \frac{1}{2} \cdot \begin{bmatrix} -\mathrm{i} \cdot g(n_b) \cdot (f(n_a) - f(n_b)) \\ g(n_b) \cdot (f(n_a) + f(n_b)) \end{bmatrix} \\
&= -\frac{1}{2} \cdot \mathrm{i} \cdot g(n_b)((f(n_a) - f(n_b)) \cdot \overbrace{\begin{bmatrix} 1 \\ 0 \end{bmatrix}}^{\leftrightarrow}.
\end{aligned} \tag{A.22}$$

Given we are interested in filter transmission, we calculate the intensity $\mathcal{I} \propto |\mathbf{E_{out}}|^2$ and find that both filters have the same intensity value proving the equivalent filter outputs in this case,

A.3.2 General Proof

We now generalise this equivalence and prove that the output from a Faraday-Voigt filter with first polariser set at $\beta°$ rotating out of the page, (see Fig. A.8), is the same as the output from a Voigt-Faraday filter with first polariser set at $(\beta+90)°$.

In our Faraday-Voigt filter, we input linear light, $\mathbf{E_{rot}}$, at an angle β to the horizontal axis and we define a crossed polariser at $(\beta+90)°$, $\mathbf{V_{rot}}$. We create these objects by applying appropriate rotation matrices to linearly horizontal light and a vertical polarising matrix respectively:

$$\mathbf{E_{rot}} = \begin{bmatrix} \cos\beta & -\sin\beta \\ \sin\beta & \cos\beta \end{bmatrix} \cdot \begin{bmatrix} 1 \\ 0 \end{bmatrix} = \begin{bmatrix} \cos\beta \\ \sin\beta \end{bmatrix}, \tag{A.23}$$

$$\begin{aligned} \mathbf{V_{rot}} &= \begin{bmatrix} \cos\beta & -\sin\beta \\ \sin\beta & \cos\beta \end{bmatrix} \cdot \begin{bmatrix} 0 & 0 \\ 0 & 1 \end{bmatrix} \cdot \begin{bmatrix} \cos\beta & -\sin\beta \\ \sin\beta & \cos\beta \end{bmatrix}^{-1} \\ &= \begin{bmatrix} \sin^2\beta & -\cos\beta\cdot\sin\beta \\ -\cos\beta\cdot\sin\beta & \cos^2\beta \end{bmatrix}. \end{aligned} \tag{A.24}$$

Substituting these rotated values into A.17 we obtain,

$$\begin{aligned} \mathbf{E_{out}} &= \begin{bmatrix} \sin^2\beta & -\cos\beta\cdot\sin\beta \\ -\cos\beta\cdot\sin\beta & \cos^2\beta \end{bmatrix} \cdot \mathcal{P}_{\mathrm{F,V}} \cdot \begin{bmatrix} \cos\beta \\ \sin\beta \end{bmatrix} \\ &= \frac{1}{2}[f(n_b)(\cos\beta + \mathrm{i}\sin\beta)(g(n_a)\sin\beta + \mathrm{i}g(n_b)\cos\beta) \\ &-f(n_a)(\mathrm{i}\sin\beta - \cos\beta)(g(n_a)\sin\beta - \mathrm{i}g(n_b)\cos\beta)] \begin{bmatrix} -\sin\beta \\ \cos\beta \end{bmatrix}. \end{aligned} \tag{A.25}$$

For the generalised Voigt-Faraday filter, we input linear light at $(90+\beta)°$ to the horizontal axis and set the second polariser at β. To obtain these expressions, we apply rotation matrices in the same way as in A.23 and A.24 to linearly vertical light and a horizontal polarising matrix respectively. Substituting into A.17 again, we derive a similar result,

$$\begin{aligned}\mathbf{E_{out}} &= \begin{bmatrix} \cos^2\beta & -\cos\beta\cdot\sin\beta \\ -\cos\beta\cdot\sin\beta & \sin^2\beta \end{bmatrix} \cdot \mathcal{P}_{\mathrm{V,F}} \cdot \begin{bmatrix} -\sin\beta \\ \cos\beta \end{bmatrix} \\ &= \frac{1}{2}[f(n_b)(\cos\beta + \mathrm{i}\sin\beta)(g(n_a)\sin\beta + \mathrm{i}g(n_b)\cos\beta) \\ &-f(n_a)(\mathrm{i}\sin\beta - \cos\beta)(g(n_a)\sin\beta - \mathrm{i}g(n_b)\cos\beta)] \begin{bmatrix} \cos\beta \\ \sin\beta \end{bmatrix}.\end{aligned} \tag{A.26}$$

The prefactors in the output electric field for both A.25 and A.26 are the same. As such squaring the output electric field to find the intensity yields the same value for both cases since $\sin^2\beta + \cos^2\beta = 1$ ■

A.3.3 Comparing the Role of the Voigt Cell in Both Filters

Fig. A.9 shows theoretical intensity curves for the two filters as described in eqs. A.21 and A.22 showing the outputs after each cell and the final polariser. A key conclusion in Chapter 3 was that in the Faraday-Voigt filter, the Faraday cell rotates the plane of polarisation while the Voigt cell absorbs away from line-centre. Fig. [Ref Chapter 3] showed that while the Voigt cell also had a dispersive effect on the propagating light, it did not contribute to the final filter output. In the Voigt-Faraday filter, linearly vertical light — which is a Voigt eigenmode — is input into the Voigt cell and therefore the Voigt cell only absorbs in this case. Fig. A.9 shows the difference in the transmission profiles after the second cell highlighting the all-absorbing role vs absorbing with some dispersion role the Voigt cell plays. However, given the filter outputs are equivalent, we have shown again that the dispersive role of the Voigt cell does not contribute to the final filter.

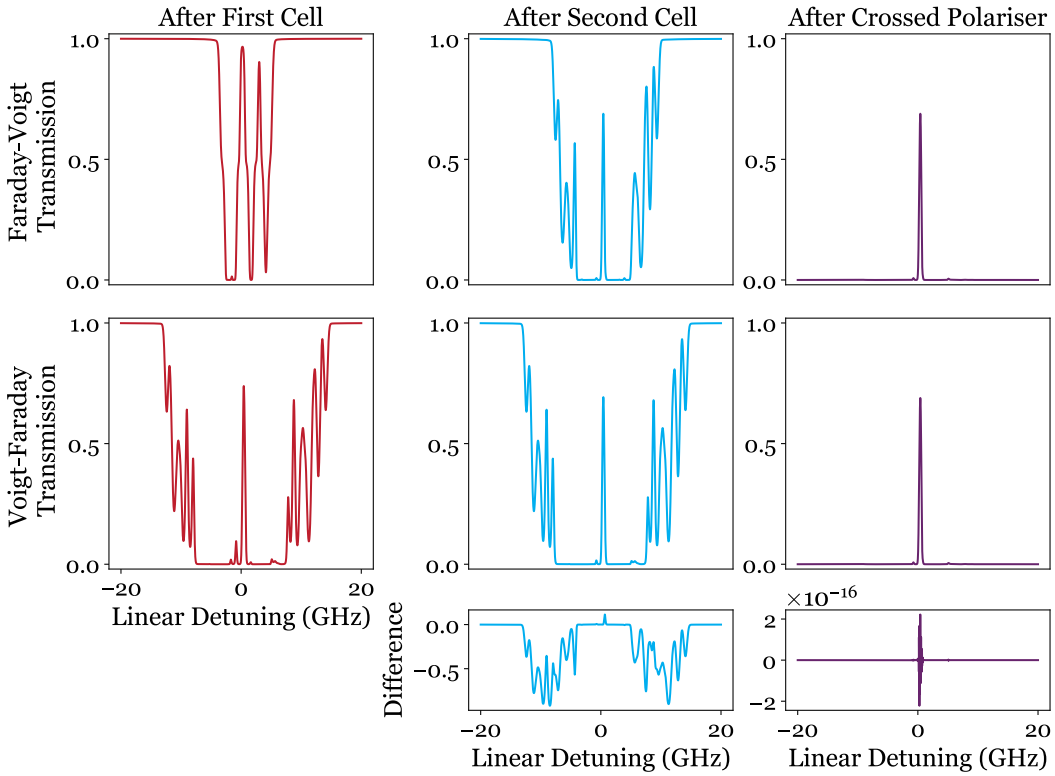

D-line	T_1 (°C)	B_1 (G)	T_2 (°C)	B_2 (G)	L_1 (mm)	L_2 (mm)
D2	100	162	121	2528	5	5

Figure A.9: Theoretical intensity curves for outputs at different stages of the Faraday-Voigt and Voigt-Faraday natural abundance Rb filters modelled using *ElecSus*. Parameters are given in the table. The columns depict the transmission seen if a photodetector is placed after the first (red) and second (blue) cells and if it is placed after the crossed polariser (purple). Residuals are shown for the final two columns. After the second cell, both filter outputs have similar shapes but are not the same due to the additional dispersive properties of the Voigt cell in the Faraday-Voigt case. However, both setups lead to equivalent filter output demonstrating that the dispersive properties of the Voigt cell do not contribute to the filter profile. The disagreement between the two final filter curves is very small and can most likely be attributed to computational floating point arithmetic error [362, 363].

A.4 Faraday-Faraday Wing Filter with Equivalent Filter Outputs

In Chapter 3, it is stated that the described Faraday-Faraday filter has the same output as a Faraday-Faraday filter with optics and cells rearranged as shown in Fig. A.10. In other words, one can Zeeman select for positively/negatively detuned light

and rotate the plane of polarisation of the light in either order and arrive at the same filter profile. In this section, we prove this statement and plot theory intensity curves comparing the two filter setups.

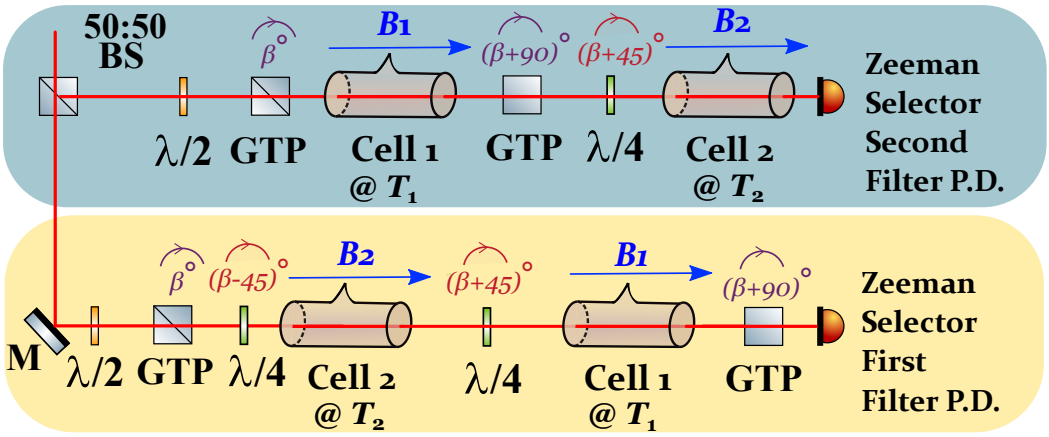

Figure A.10: A diagram of two Faraday-Faraday filters with equivalent outputs, one where the Zeeman selector follows rotation of the plane of polarisation and the other when the Zeeman selector precedes it. In the blue box, the Faraday-Faraday filter is composed of two cells with cell lengths L_1 and L_2 at temperatures and magnetic fields T_i and B_i with both cells in the Faraday geometry. The light passes through the first cell between crossed polarisers with first polariser rotated $\beta°$ out of the page. The light then passes through a quarter waveplate set at $(\beta + 45)°$ before passing through the second cell. In the yellow box, the cells with the same parameters are used but with their order swapped. The light passes through a quarter waveplate at $(\beta - 45)°$ before being directed into Cell 2. The light passes through a second waveplate at $(\beta + 45)°$ before passing through Cell 1. M — Mirror, BS — Beamsplitter, GTP — Glan-Taylor Polariser, P.D. — Photodetector.

In Fig. A.10, light of an arbitrary polarisation is directed into each experiment. In the Zeeman Selector Second filter, the light is first polarised to be linear by passing through a Glan-Taylor polariser (GTP). Having exited the second GTP, the light is directed through a quarter waveplate where it becomes left handed before entering the second cell. In the Zeeman Selector First experiment, light passing through the GTP and the quarter waveplate ensures the light entering Cell 2 is also left handed before it is converted back to linear light by the second quarter waveplate. Note that if we want to select for the other wing and direct right handed light into the Zeeman selector, two equivalent filters can be acheived by swapping quarter waveplates at $(\beta + 45)°$ for $(\beta - 45)°$ and vice versa.

A.4.1 General Proof

Noting that the he rotation angle experienced for linear input in a Faraday cell is independent of β, we can choose to prove this statement for a specific value and it will hold in general. We set $\beta = 0$ and therefore after the first polariser in each filter have linearly horizontal light. From eq. A.5, we define $\mathcal{P}_{\mathrm{F}_1}$ and $\mathcal{P}_{\mathrm{F}_2}$, the Faraday cell propagation matrices for Cell 1 and 2 respectively,

$$\mathcal{P}_{\mathrm{F}_1} = \frac{1}{2}\begin{bmatrix} f(n_a)+f(n_b) & -\mathrm{i}(f(n_a)-f(n_b)) \\ \mathrm{i}(f(n_a)-f(n_b)) & f(n_a)+f(n_b) \end{bmatrix}, \tag{A.27}$$

$$\mathcal{P}_{\mathrm{F}_2} = \frac{1}{2}\begin{bmatrix} g(n_a)+g(n_b) & -\mathrm{i}(g(n_a)-g(n_b)) \\ \mathrm{i}(g(n_a)-g(n_b)) & g(n_a)+g(n_b) \end{bmatrix}. \tag{A.28}$$

Using Jones vectors and matrices defined in Tables A.1 and A.2, we calculate the filter output from the Zeeman Selector Second filter,

$$\begin{aligned} \mathrm{E}_{\mathrm{out}} &= \mathcal{P}_{\mathrm{F}_2} \cdot \frac{1}{2}\begin{bmatrix} 1+\mathrm{i} & 1-\mathrm{i} \\ 1-\mathrm{i} & 1+\mathrm{i} \end{bmatrix} \cdot \begin{bmatrix} 0 & 0 \\ 0 & 1 \end{bmatrix} \cdot \mathcal{P}_{\mathrm{F}_1} \cdot \begin{bmatrix} 1 \\ 0 \end{bmatrix} \\ &= \frac{1}{4} \cdot g(n_a) \cdot (f(n_a)-f(n_b)) \begin{bmatrix} 1+\mathrm{i} \\ \mathrm{i}-1 \end{bmatrix}, \end{aligned} \tag{A.29}$$

and from the Zeeman Selector First filter,

$$\begin{aligned} \mathrm{E}_{\mathrm{out}} &= \begin{bmatrix} 0 & 0 \\ 0 & 1 \end{bmatrix} \cdot \mathcal{P}_{\mathrm{F}_1} \cdot \frac{1}{2}\begin{bmatrix} 1+\mathrm{i} & 1-\mathrm{i} \\ 1-\mathrm{i} & 1+\mathrm{i} \end{bmatrix} \cdot \mathcal{P}_{\mathrm{F}_2} \cdot \frac{1}{2}\begin{bmatrix} 1+\mathrm{i} & \mathrm{i}-1 \\ \mathrm{i}-1 & \mathrm{i}+1 \end{bmatrix} \cdot \begin{bmatrix} 1 \\ 0 \end{bmatrix} \\ &= -\frac{1}{2} \cdot g(n_a) \cdot (f(n_a)-f(n_b)) \begin{bmatrix} 0 \\ 1 \end{bmatrix}, \end{aligned} \tag{A.30}$$

Noting that,

$$\left\| \begin{bmatrix} 0 \\ -1 \end{bmatrix} \right\| = 1, \qquad \left\| \begin{bmatrix} 1+\mathrm{i} \\ \mathrm{i}-1 \end{bmatrix} \right\| = 2. \tag{A.31}$$

We find the intensity squared values of the two configurations are the same proving the statement,

$$\mathcal{I}_{\mathrm{F}_1,\mathrm{F}_2} = \mathcal{I}_{\mathrm{F}_2,\mathrm{F}_1} = \frac{1}{2} \cdot g(n_a)^2 (f(n_a - f(n_b))^2. \qquad \blacksquare \tag{A.32}$$

A.4.2 Comparing the Two Filter Setups

Fig. A.11 shows theoretical intensity curves for the two filters as described in eqs. A.29 and A.30 showing the outputs after each cell and the final polariser. The roles of Zeeman selector and rotator are independent and commute.

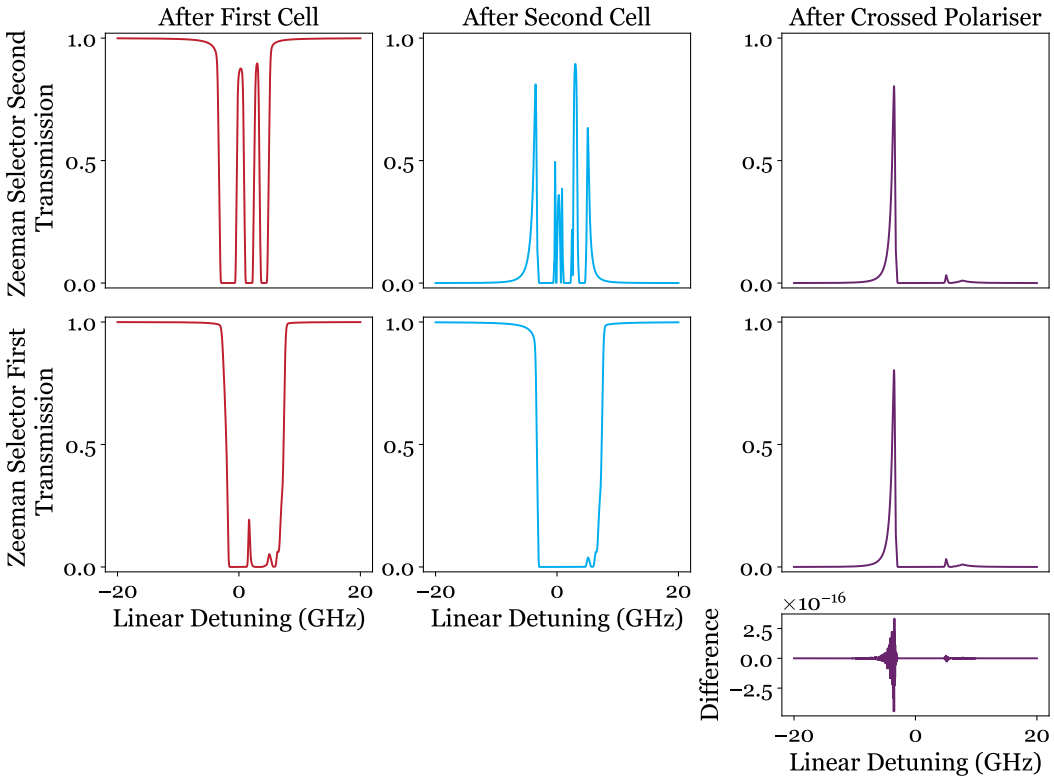

D-line	T_1 (°C)	B_1 (G)	T_2 (°C)	B_2 (G)	L_1 (mm)	L_2 (mm)
D2	86	49	110	747	75	5

Figure A.11: Theoretical intensity curves for outputs at different stages of the Zeeman Selector Second (blue box in Fig. A.10) and the Zeeman Selector First (yellow box in Fig. A.10) natural abundance Rb filters modelled using *ElecSus*. Parameters are given in the table below. The columns depict the transmission seen if a photodetector is placed after the first (red) and second (blue) cells and if placed after the crossed polariser (purple). The difference between the two filters' intensity curves are shown for the final filter output. The disagreement between the two final filter curves is very small and can most likely be attributed to computational floating point arithmetic error [362, 363].

A.5 Propagation with Magnetic Field at a Supplementary Angle to the *k*-vector

In Chapter 4, a Double Pass filter design is proposed and realised. Two passes through the vapour cell are made, the first at an arbitrary angle α to the magnetic field and the second at an angle $\alpha^* = (180 - \alpha)°$, the supplementary angle to α [364]. It is claimed that the two passes between crossed polarisers have the same

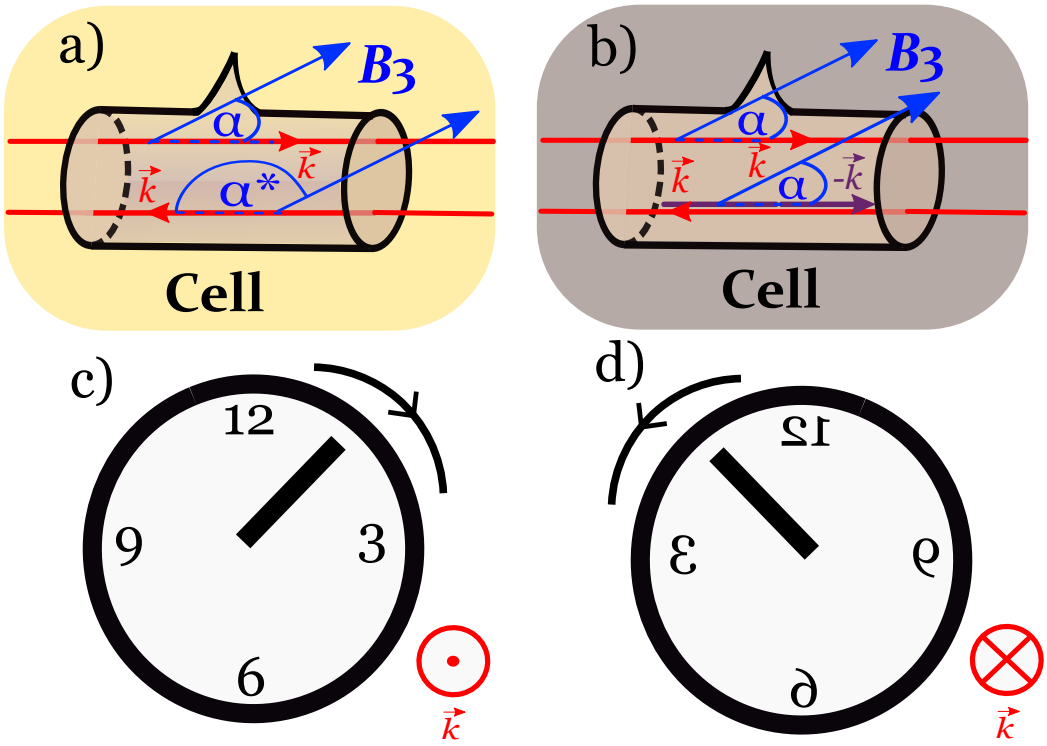

Figure A.12: A visualisation to aid in understanding how a pass at angle α differs from its supplementary angle $\alpha^* = (180 - \alpha)°$. Panel a) shows the cell in the Double Pass filter realised in Chapter 4. The propagation direction of the light on each pass is indicated by the k-vector. b) re-frames the situation by depicting the second pass as making an angle α with $-\vec{k}$. Panels c) and d) demonstrate the effect of viewing polarisations in the opposite direction to the k-vector using a clockface. With k pointing towards us, we view the clock hand moving clockwise but looking at the clock from behind, and with $\vec{k}$ pointing away from us, the clock hand appears to be moving anti-clockwise.

filter output. In this section, we prove the smaller claim that the two passes have the same S_0 value if either linearly horizontal or vertical light is input on both passes. With this claim, we prove the full statement in the next section (Section A.6).

We consider the Double Pass filter to offer intuition on the problem. Panel a) in Fig. A.12 shows a ray trace of the Double Pass setup. Panel b) shows an alternative way of viewing the situation with the second pass having the same magnetic field angle α as the first pass between the magnetic field and a vector pointing opposite to the k-vector, $-\vec{k}$.

With regards to $-\vec{k}$, the relevant point to observe polarisation is not *towards* the

source but *from* the source which means that left/right handed light (relative to k) is observed as right/left handed light (relative to -k). Similarly, diagonal light at 45° is observed at $-45°$ relative to $-\vec{k}$. Given that the passes are otherwise identical, assuming the parameters do not change across the volume of the cell, the two passes are equivalent upon interchanging the hand of the input light. Since linearly horizontal and vertical light do not depend on whether the observer looks from or towards the source, we have proved the claim.

Note that this claim can also be applied generally to the Faraday and Voigt geometries where the supplementary magnetic field angles to the k-vector are 180° and 90°. Note in the Voigt case, the supplementary angle is the same as the original angle.

A.6 Linearly Horizontal and Vertical Filters are Equivalent

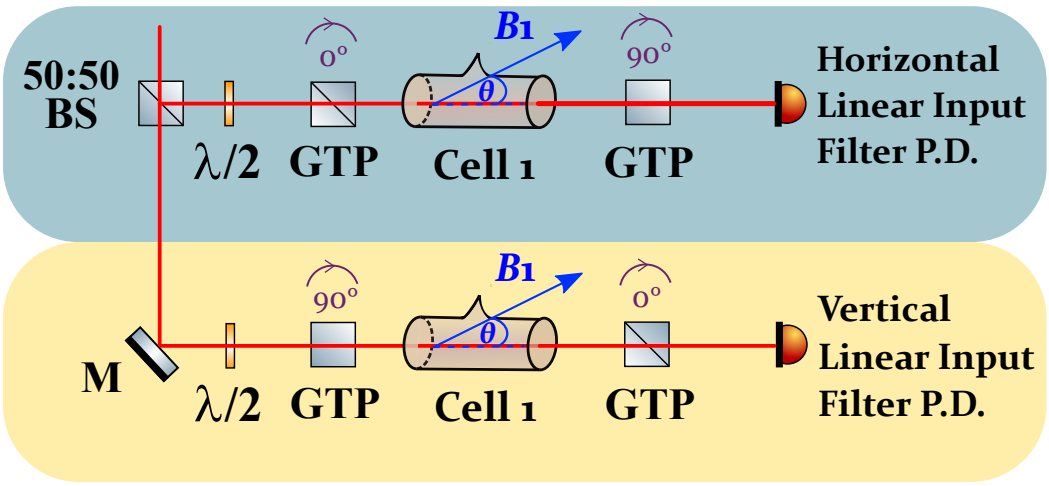

Figure A.13: A diagram of two filters constructed from a cell in any geometry between two crossed polarisers. The parameters for the cell in both filters are the same. In the blue box, the first polariser is set to 0° rotation out of the page ensuring light input into the cell is linearly horizontal. In the yellow box, the first polariser is set to 90° outputting vertical linear light. M- Mirror, BS - Beamsplitter, GTP -Glan-Taylor Polariser, P.D. - Photodetector.

In the previous section, we proved the claim that if linearly horizontal light is input into both passes of the Double Pass cell, the S_0 values will be the same. In this section, we upgrade this claim, by showing that the two passes in the Double Pass filter give the same output. In doing so, we derive a constraint on the eigenmodes valid for all geometries. We plot theory curves to show the effect of input polarisation on filter output in different geometries.

In the Double Pass filter, the input into the first pass is polarised linearly horizontal before passing through a crossed polariser, it returns for a second pass in a linearly vertical state before passing through another crossed polariser. To prove the statement, we need to show the two filters depicted in Fig. A.13 are equivalent.

A.6.1 Unitary Matrix Lemma

In this proof, we will need to make use of the fact that the normalised matrix, $\mathbf{R}/|\det(\mathbf{R})|$ (defined in eq. A.2), is unitary since it is a change-of-basis matrix [365],

$$\mathbf{R} \cdot \mathbf{R}^{\dagger} = \mathbf{R}^{\dagger} \cdot \mathbf{R} = |\det(\mathbf{R})| \cdot \mathbb{I}, \tag{A.33}$$

where $\mathbb{I}$ is the 2 x 2 identity matrix. Consider the Faraday and Voigt change of basis matrices as examples:

$$\begin{bmatrix} 1 & -\mathrm{i} \\ 1 & \mathrm{i} \end{bmatrix} \cdot \begin{bmatrix} 1 & 1 \\ \mathrm{i} & -\mathrm{i} \end{bmatrix} = \begin{bmatrix} 1 & 1 \\ \mathrm{i} & -\mathrm{i} \end{bmatrix} \cdot \begin{bmatrix} 1 & -\mathrm{i} \\ 1 & \mathrm{i} \end{bmatrix} = 2 \cdot \begin{bmatrix} 1 & 0 \\ 0 & 1 \end{bmatrix}, \tag{A.34}$$

$$\begin{bmatrix} 1 & 0 \\ 0 & 1 \end{bmatrix} \cdot \begin{bmatrix} 1 & 0 \\ 0 & 1 \end{bmatrix} = \begin{bmatrix} 1 & 0 \\ 0 & 1 \end{bmatrix}. \tag{A.35}$$

This implies a constraint on the values of $\mathbf{R}$:

$$\begin{aligned}
\mathbf{R}^{-1} &= \frac{\mathbf{R}^{\dagger}}{|\det(\mathbf{R})|}, \\
&\implies \frac{1}{a_1^* b_2^* - a_2^* b_1^*} \begin{bmatrix} b_2^* & -a_2^* \\ -b_1^* & a_1^* \end{bmatrix} = \frac{1}{|a_1 b_2 - a_2 b_1|} \begin{bmatrix} a_1 & b_1 \\ a_2 & b_2 \end{bmatrix}, \\
&\implies a_1 b_1 = a_2 b_2,
\end{aligned} \tag{A.36}$$

where we have assumed, without loss of generality, that a_1 and b_1 are real and a_2 and b_2 are complex since any polarisation state can be written as a Jones vector with a real x-entry and a complex y-entry. We can do this since different $\mathbf{R}$ can lead to to the same propagation matrix, $\mathcal{P}$, as we act again with $\mathbf{R}^{-1}$. We will use this constraint in the general proof.

A.6.2 General Proof

We want to prove the following statement:

$$||\mathbf{P}_{\updownarrow} \cdot \mathcal{P} \cdot \mathbf{E}_{\leftrightarrow}|| = ||\mathbf{P}_{\leftrightarrow} \cdot \mathcal{P} \cdot \mathbf{E}_{\updownarrow}||, \tag{A.37}$$

where $\mathbf{P}_{\updownarrow}$ and $\mathbf{P}$ are vertical and horizontal linear polarisers, $\mathcal{P}$ is the propagation matrix defined in A.4 and $E_{\updownarrow}$ and $E_{\leftrightarrow}$ are horizontal and vertical linear inputs respectively. Note in this equivalence the two filters have the same cell in the same geometry with the same parameters. All we are changing between the two situations is the input electric field and the orientation of the polariser to cross the initial polarisation.

The propagation matrix, $\mathcal{P}$, is general as we have not defined a geometry. The left and right hand side of A.37 are:

$$\begin{aligned}\mathbf{E_{out}} &= \begin{bmatrix}0 & 0\\ 0 & 1\end{bmatrix}\cdot\begin{bmatrix}A & B\\ C & D\end{bmatrix}\cdot\overbrace{\begin{bmatrix}1\\ 0\end{bmatrix}}^{\leftrightarrow}\\ &= \overbrace{\begin{bmatrix}0\\ C\end{bmatrix}}^{\updownarrow},\end{aligned} \tag{A.38}$$

$$\begin{aligned}\mathbf{E_{out}} &= \begin{bmatrix}1 & 0\\ 0 & 0\end{bmatrix}\cdot\begin{bmatrix}A & B\\ C & D\end{bmatrix}\cdot\overbrace{\begin{bmatrix}0\\ 1\end{bmatrix}}^{\updownarrow}\\ &= \overbrace{\begin{bmatrix}B\\ 0\end{bmatrix}}^{\leftrightarrow}.\end{aligned} \tag{A.39}$$

In order for the two intensities ($\propto |\mathbf{E_{out}}|^2$) to be equal we require $|B| = |C|$. We expand the general propagation matrix in terms of its definition in eq. A.4,

$$\begin{aligned}\begin{bmatrix}A & B\\ C & D\end{bmatrix} &= \mathbf{R^{-1}}\cdot\mathbf{T}\cdot\mathbf{R}\\ &= \frac{1}{a_1^*b_2^* - a_2^*b_1^*}\begin{bmatrix}b_2^* & -a_2^*\\ -b_1^* & a_1^*\end{bmatrix}\begin{bmatrix}f(n_a) & 0\\ 0 & f(n_b)\end{bmatrix}\cdot\begin{bmatrix}a_1^* & a_2^*\\ b_1^* & b_2^*\end{bmatrix}\\ &= \frac{1}{a_1^*b_2^* - a_2^*b_1^*}\begin{bmatrix}a_1^*b_2^*f(n_a) - a_2^*b_1^*f(n_b) & a_2^*b_2^*(f(n_a) - f(n_b))\\ -a_1^*b_1^*(f(n_a) - f(n_b)) & a_1^*b_2^*f(n_b) - a_2^*b_1^*f(n_a)\end{bmatrix}.\end{aligned} \tag{A.40}$$

We can read off that for $|B| = |C|$ we need,

$$|a_2b_2| = |a_1b_1|. \tag{A.41}$$

This is satisfied using the unitary constraint developed in the last subsection. ■

A.6.3 Brief Comments on Unitary Constraint

Asserting that $\mathbf{R}$ is unitary is a deeper statement since it determines a constraint as to what eigenmodes are physically possible. In section A.2, we presented a toy model of a non-orthogonal propagation but did not call it an oblique propagation. This is because the eigenmodes did not form a unitary matrix and as such the eigenmodes cannot represent an oblique cell propagation.

Note also that unitarity also implies that an analogous set of filters, one with left hand circular input and one with a right hand input, also have equivalent outputs. Using the definitions for circular polarisers in Table A.2,

$$\begin{aligned}\mathbf{E_{out}} &= \frac{1}{2}\begin{bmatrix}1 & i\\ -i & 1\end{bmatrix}\cdot\begin{bmatrix}A & B\\ C & D\end{bmatrix}\cdot\overbrace{\begin{bmatrix}1\\ i\end{bmatrix}}^{\circlearrowleft}\\ &= \frac{1}{2}[A-D+\mathrm{i}(B+C)]\cdot\overbrace{\begin{bmatrix}1\\ -i\end{bmatrix}}^{\circlearrowleft},\end{aligned} \tag{A.42}$$

$$\begin{aligned}\mathbf{E_{out}} &= \frac{1}{2}\begin{bmatrix}1 & -i\\ i & 1\end{bmatrix}\cdot\begin{bmatrix}A & B\\ C & D\end{bmatrix}\cdot\overbrace{\begin{bmatrix}1\\ -i\end{bmatrix}}^{\circlearrowleft}\\ &= \frac{1}{2}[A-D-\mathrm{i}(B+C)]\cdot\overbrace{\begin{bmatrix}1\\ i\end{bmatrix}}^{\circlearrowleft}.\end{aligned} \tag{A.43}$$

The two intensity outputs ($\propto |\mathbf{E_{out}}|^2$) are equivalent if $B = -C$ which from eq. A.40 requires the stronger condition:

$$a_2^* b_2^* = a_1^* b_1^* \implies a_2 b_2 = a_1 b_1. \tag{A.44}$$

The implication arises from the assumption we make again that a_1 and a_2 are real and b_1 and b_2 are complex and we arrive at the unitary constraint. ■

A.6.4 Effect of Input Polarisation on Filter Profiles in Different Geometries

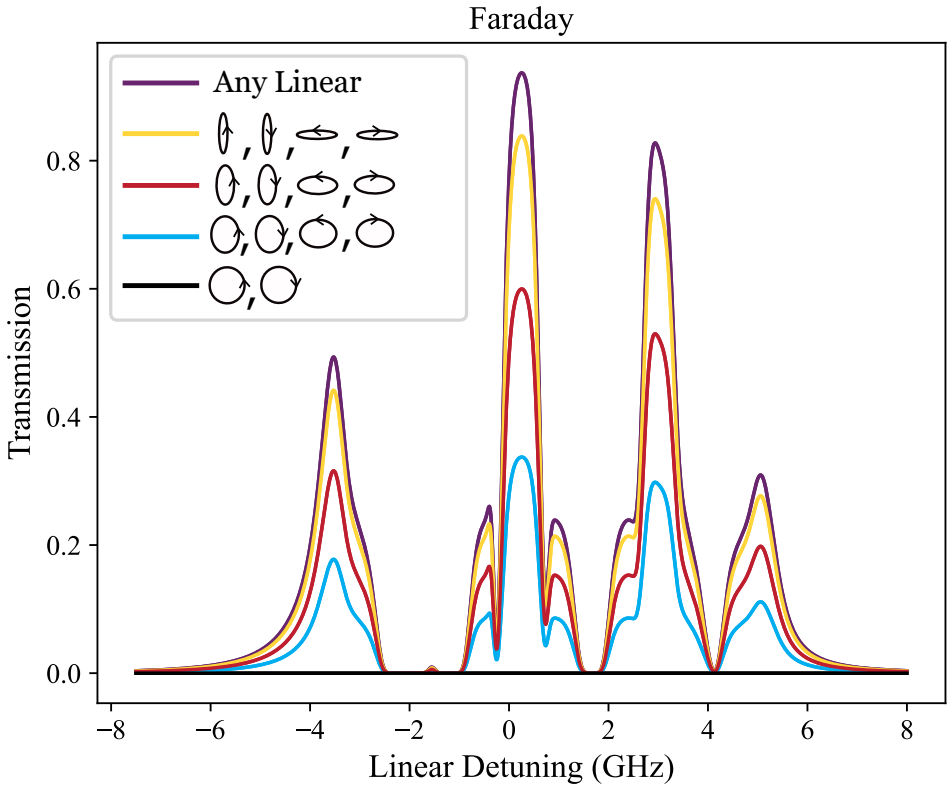

D-line	T (°C)	B (G)	L (mm)
D2	64	162	75

Figure A.14: Theory curves modelled in *ElecSus* of filter profiles for a natural abundance Rb Faraday cell. Parameters stated in table. Note that all linear inputs give the same filter ouput. Any handed polarisations give the same filter profile but with lower intensity. The invariant polarisations, left and right hand circular light, give zero filter profile since they are invariant and maintain their polarisation state through the propagation.

We plot theory curves of filter profiles in various geometries inputting different polarisations. The curves are calculated using *ElecSus* [155, 156]. Note that in all geometries linearly horizontal and vertical light give the same profile. The situation is analogous for left hand and right hand circular light.

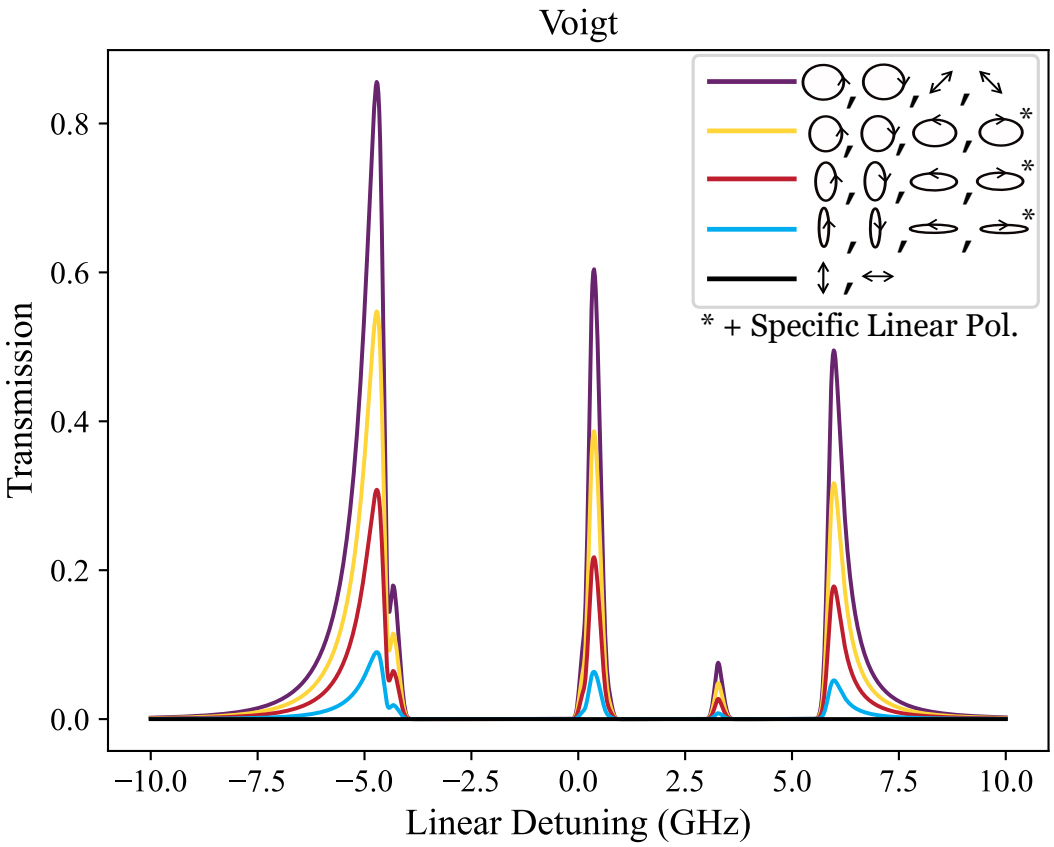

D-line	T (°C)	B (G)	L (mm)
D1	107	514	75

Figure A.15: Theory curves modelled in *ElecSus* of filter profiles for a natural abundance Rb Voigt cell. Parameters stated in table below. Note that circular and diagonal light give the highest filter output while linearly horizontal and vertical light give zero output since they are invariant polarisations. Other polarisations give the same filter profile but at different intensities. The yellow, red and blue curves could also be realised by four other linear polarisations; two largely diagonal and two largely anti-diagonal polarisations. One diagonal and anti-diagonal are evolving towards a horizontal state and the other diagonal and anti-diagonal are evolving towards a vertical state.

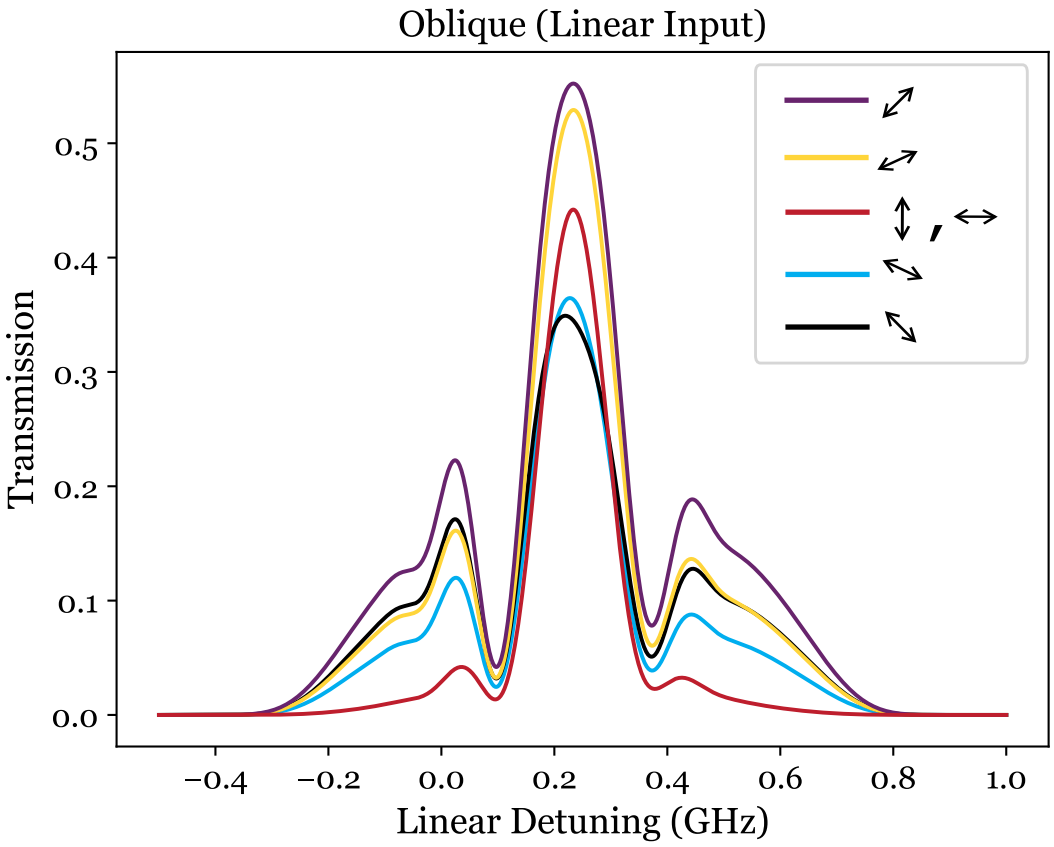

D-line	T (°C)	B (G)	θ (°)	L (mm)
D2	99	226	87	75

Figure A.16: Theory curves modelled in *ElecSus* of filter profiles for a natural abundance Rb Oblique cell. Parameters stated in table. Note that unlike the Faraday and Voigt cases, the different polarisations result in different filter profiles.

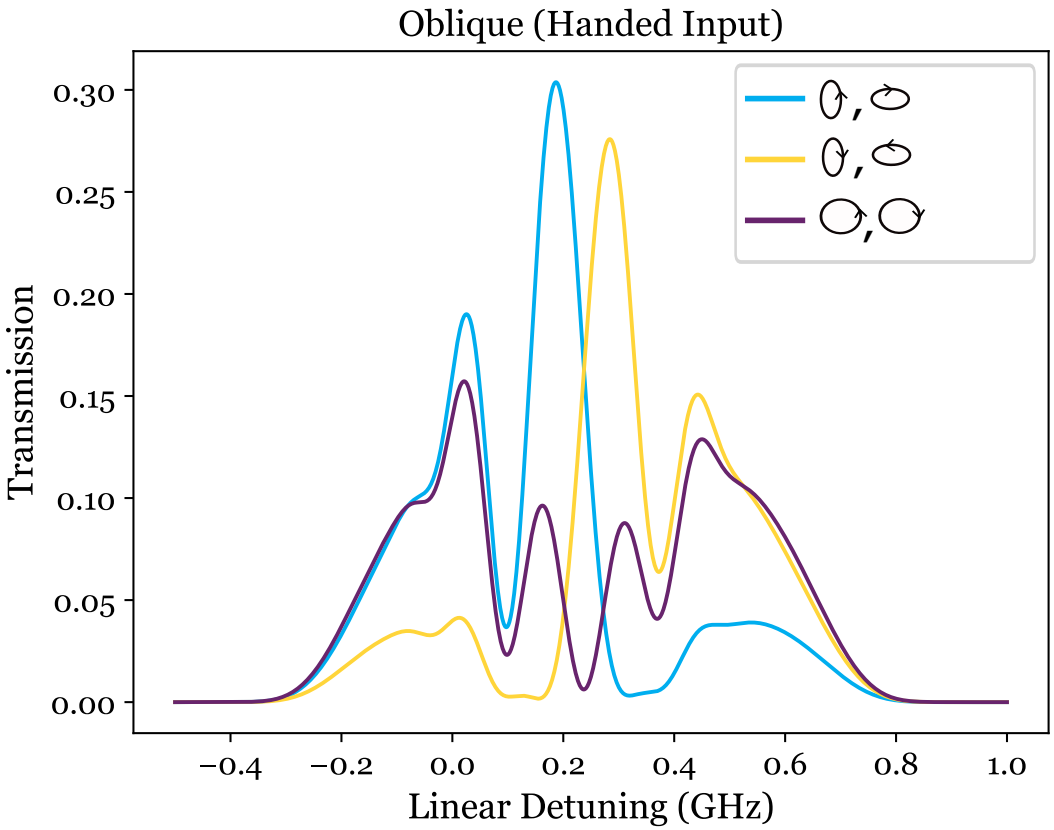

D-line	T (°C)	B (G)	θ (°)	L (mm)
D2	99	226	87	75

Figure A.17: Theory curves modelled in *ElecSus* of filter profiles for a natural abundance Rb oblique cell. Parameters stated in table. Note that unlike the Faraday and Voigt cases, the different polarisations result in different filter profiles.

A.7 Open Question: Propagation at an Exceptional Point

In Chapter 5, we introduced the concept of an exceptional point, a point in parameter space where the refractive indices become degenerate and the propagation eigenmodes coallesce. In this section, we present good practice when computing propagation near an exceptional point. We also pose an open problem with regards to propagation of light at an exceptional point.

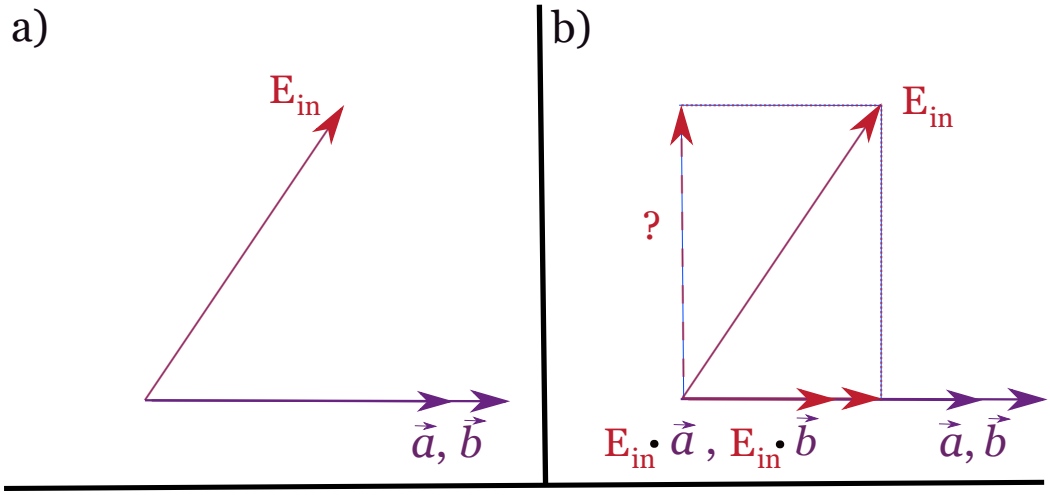

Figure A.18: A visualisation of the paradox of propagation using Jones Calculus at an exceptional point. Panel a) depicts an arbitrary input electric field, $\mathbf{E_{in}}$, in red alongside two coallescent eigenmodes, $\vec{a}$ and $\vec{b}$. Panel b) decomposes the vector in the same way as shown in panel b) of Fig. A.3. In this case, the input electric field is decomposed twice on to the same vector, once with respect to $\vec{a}$ and once with respect to $\vec{b}$. However, there exists a vector component orthogonal to the eigenmodes labelled with a question mark that is not used in the propagation calculation. This is a seemingly non-physical or at best counter-intuitive result.

Eigenmode coallescence can only occur in oblique geometries where the eigenmodes are permitted to be non-orthogonal. Near an exceptional point in parameter space, the normalised dot product of the propagation eigenmodes increases towards one. From a theoretical Jones Calculus perspective, whether near or far away from an exceptional point, propagation can be calculated as described in section A.1. Even very nearly coallescent eigenmodes remain linearly independent and as such span the 2D polarisation space [366, 367].

From a more practical computational perspective, as exploited in Chapter 6, small changes in parameter can result in large changes to spectral features near an exceptional point. Numerical stability of solutions can be understood and mitigated using numerical analysis [368, 369]. A new Python package, *PyTracer* [370], has recently been developed to analyse common Python tools such as SciPy [371] for numerical noise. Robust implementations of these tools in *ElecSus* or other theoretical models is beyond the scope of this thesis.

However, at an exceptional point, where the normalised dot product of the propagation eigenmodes is 1, the propagation method breaks down. For example, consider a system where the eigenmodes coallesce on to left hand circular light. Following section A.1, we construct the matrix $\mathbf{R}_{\text{E.P.}}$:

$$\mathbf{R}_{\text{E.P.}} = \overbrace{\begin{bmatrix} 1 & -\mathrm{i} \\ 1 & -\mathrm{i} \end{bmatrix}}^{\circlearrowleft,\circlearrowleft}. \tag{A.45}$$

This matrix now fails to be a change-of-basis matrix as it is no longer unitary when normalised:

$$\mathbf{R}_{\text{E.P.}} \cdot \mathbf{R}^{\dagger}_{\text{E.P.}} = \begin{bmatrix} 1 & -\mathrm{i} \\ 1 & -\mathrm{i} \end{bmatrix} \cdot \begin{bmatrix} 1 & 1 \\ \mathrm{i} & \mathrm{i} \end{bmatrix} = 2 \begin{bmatrix} 1 & 1 \\ 1 & 1 \end{bmatrix}. \tag{A.46}$$

If we input an orthogonal polarisation, right hand circular light, we arrive at a counter intuitive answer,

$$\mathbf{R}_{\text{E.P.}} = \begin{bmatrix} 1 & -\mathrm{i} \\ 1 & -\mathrm{i} \end{bmatrix} \cdot \overbrace{\begin{bmatrix} 1 \\ -\mathrm{i} \end{bmatrix}}^{\circlearrowright} = 0, \tag{A.47}$$

implying that the light is extinguished/scattered on contact with the medium. Fig. A.18 visualises this paradox using the same framework as the earlier Fig. A.3. This is an open question not tackled in this thesis.

There are some candidate solutions to this problem. Perhaps exceptional points can never be reached in our systems thus suggesting A.47 is non-physical. Appendix B presents the oblique eigenvalue solutions alongside the condition for an exceptional point. In this research, we have not yet found a physical criterion that would exclude this condition from holding. Rejecting these solutions on the basis of lack

of unitarity is compelling. However, given that the dimensionality of the problem decreases from 2D to 1D, we ought to expect the physics to fail to be linear at this point.

Perhaps eq. A.47 has a more intuitive consequence. It may merely imply the polarisation is not refracted and its propagation must be calculated through other means. Potentially the framework of Jones Calculus breaks down at an exceptional point. We leave this as an area for others to explore.

Appendix B

Wave Equation Solutions

Author completed all theoretical computations, collected and processed all data and created all figures presented in this appendix. We make use of Alex Webber's wave equation solutions [252] as well as other published solutions [156, 249]. All text written without the use of AI. Work is related to the published articles:

F. S. Ponciano-Ojeda, F. D. Logue, and I. G. Hughes, 'Absorption spectroscopy and Stokes polarimetry in a ^{87}Rb vapour in the Voigt geometry with a 1.5 T external magnetic field', *Journal of Physics B: Atomic, Molecular and Optical Physics*, 54(1):015401, 2020. https://doi.org/10.1088/1361-6455/abc7ff [1]

F. D. Logue, J. D. Briscoe, D. Pizzey, S. A. Wrathmall, and I. G. Hughes, 'Exploiting non-orthogonal eigenmodes in a non-Hermitian optical system to realize sub-100 MHz magneto-optical filters', *arXiv Preprint*, 2303.00081, 2023. https://doi.org/10.48550/arXiv.2303.00081 [5]

In 4.1, we stated that general eigenmode and refractive index solutions had been derived on multiple occasions [372, 373, 374, 375, 376, 377, 357, 250, 249, 207, 156]. Despite this, only four oblique magneto-optical filters had ever been realised experimentally [148, 207, 208, 64]. We proposed that the difficulty interpreting the

birefringent and dichroic qualities of the vapour from these solutions alongside experimental challenges were a hindrance to further work. Chapter 4 served as a step towards overcoming these issues. However, upon exploring more exotic features of the oblique geometry, including propagation near a exceptional point of degeneracy in 5, we found disagreement between theory and experiment. Having seemingly also found a paradox in A.7 when calculating output electric fields at exceptional points, we might want to call the validity of these solutions into question.

In this appendix, we state the analytic solutions, derived by masters student Alex Webber, that have been used to calculate oblique theory curves throughout this thesis. We compare these solutions against the numerical method built into *ElecSus* and a previous set of analytic solutions from [249]. Most key, all three solutions show excellent agreement for the Oblique-Voigt filter profile realised in 4.4.1 suggesting our theoretical framework is reliable for the oblique field experiments conducted in this thesis. In addition, all three show avoided crossings and adiabatic swaps in the refractive index solutions. We show that Webber's solutions are competitive in terms of computation time and numerical stability. We commend Webber's solutions as the best candidates currently available to be used, extended or modified in continued oblique field studies.

B.1 Webber's Analytic Solutions

We define the permittivity tensor elements, ϵ_i, in terms of the susceptibilities due to $\sigma^{+/-}$ and π transitions, $\chi_{\sigma^{+/-}}$ and χ_π respectively [378],

$$\begin{aligned}\epsilon_x &= \frac{\epsilon_0}{2}(2+\chi_{\sigma^+}+\chi_{\sigma^-}),\\ \epsilon_{xy} &= \frac{\mathrm{i}\epsilon_0}{2}(\chi_{\sigma^-}-\chi_{\sigma^+}),\\ \epsilon_z &= \epsilon_0(1+\chi_\pi),\end{aligned} \tag{B.1}$$

with the permittivity of free space represented by ϵ_0. We want to solve this matrix equation posed in [207]:

$$\begin{bmatrix} (\frac{\epsilon_x}{\epsilon_0} - n^2)\cos\theta & \frac{\epsilon_{xy}}{\epsilon_0} & \frac{\epsilon_x}{\epsilon_0}\sin\theta \\ -\frac{\epsilon_{xy}}{\epsilon_0}\cos\theta & \frac{\epsilon_x}{\epsilon_0} - n^2 & -\frac{\epsilon_{xy}}{\epsilon_0}\sin\theta \\ (n^2 - \frac{\epsilon_z}{\epsilon_0})\sin\theta & 0 & \frac{\epsilon_z}{\epsilon_0}\cos\theta \end{bmatrix} \cdot \begin{bmatrix} E_x \\ E_y \\ 0 \end{bmatrix} = 0. \tag{B.2}$$

E_x and E_y are the components along x- and y- for some electric field vector. For more details, consult the original paper. Webber's solutions for the refractive indices, n_a and n_b are:

$$n_{a,b}^2 = \frac{A \pm \sqrt{B}}{C}, \tag{B.3}$$

$$\begin{aligned} A &= 2 \cdot \epsilon_x\epsilon_z + (\epsilon_x^2 - \epsilon_x\epsilon_z + e_{xy}^2)\sin^2\theta, \\ B &= (\epsilon_x^2 - \epsilon_x\epsilon_z + \epsilon_{xy}^2)^2 \sin^4\theta - 4 \cdot \epsilon_{xy}^2\epsilon_z^2\cos^2\theta, \\ C &= 2 \cdot (\epsilon_x \sin^2\theta + \epsilon_z\cos^2\theta). \end{aligned} \tag{B.4}$$

The eigenmodes associated with n_a and n_b, $\vec{a} = \begin{bmatrix} a_1 \\ a_2 \end{bmatrix}$ and $\vec{b} = \begin{bmatrix} b_1 \\ b_2 \end{bmatrix}$ respectively are:

$$a_1 = \frac{D}{(B - 2\cdot\epsilon_x\epsilon_z)\csc^2\theta - E}, \tag{B.5}$$

$$b_1 = \frac{-D}{(B + 2\cdot\epsilon_x\epsilon_z)\csc^2\theta + E}, \tag{B.6}$$

$$a_2 = \frac{F(G - 2\cdot e_z(e_x+e_z)\cot^2\theta - 2\cdot e_z^2\cot^4\theta - (B - 2\cdot e_x e_z)\csc^2\theta)\sin\theta}{(e_x^2+e_{xy}^2 - 3\cdot e_x e_z - 2\cdot e_z^2\cot^2\theta - (B - 2\cdot e_x e_z)\csc^2\theta)(H + 2\cdot e_x e_z\cot^2\theta + (B - 2\cdot e_x e_z)\csc^2\theta)}, \tag{B.7}$$

$$b_2 = \frac{F\sin^3\theta(B + 2\cdot e_x e_z + e_z(-e_x - 2\cdot e_z + e_x\cos 2\theta)\cot^2\theta + G\sin^2\theta)}{(B + 2\cdot e_x e_z - 2\cdot e_z^2\cos^2\theta + G\sin^2\theta)(-B - 2\cdot e_x e_z + 2\cdot e_x e_z\cos^2\theta + H\sin^2\theta)}, \tag{B.8}$$

$$
\begin{aligned}
D &= 2 \cdot \epsilon_z \cot\theta(\epsilon_x + \epsilon_z \cot^2\theta), \\
E &= \epsilon_x^2 - \epsilon_{xy}^2 + 3 \cdot \epsilon_x \epsilon_z + 2 \cdot \epsilon_z^2 \cot^2\theta, \\
F &= 2 \cdot e_{xy}(e_x + e_z \cot^2\theta), \\
G &= e_x^2 + e_{xy}^2 - 3 \cdot e_x e_z, \\
H &= e_x^2 - e_{xy}^2 + e_x e_z.
\end{aligned}
\tag{B.9}
$$

These solutions were obtained using *Mathematica's* `NullSpace` function [159].

B.2 Comparison with *ElecSus* numerical solutions

The python numerical solver imported by the extended version of *ElecSus* [156] can also calculate oblique eigenmodes and refractive indices. Using the `linsolve` function in SymPy [379], *ElecSus* finds refractive index solutions to eq. B.2 before calculating the eigenvectors using the `linalg.eig` function from NumPy [380].

The *ElecSus* solutions amongst other numerical solvers have offered advantages given that oblique calculations can be carried out without any prior knowledge of the solutions. However, it has its shortcomings. Firstly, the numerical solutions have long computation times. Tests on a Lenovo IdeaPad 5 with 2.4 GHz processor and 8 GB RAM determined that Webber's solutions [252] took on average 4.5 ± 0.1 seconds to compute 100 oblique spectra. On the other hand, the *ElecSus* numerical solver took 575 ± 5 seconds to do the same. Full computation test results are plotted in Fig. B.7.

Of more concern, the numerical solutions can predict obviously unphysical behaviour. We first realised this while studying 1 mm 99% isotopically pure ^{87}Rb cells in high magnetic fields (up to 1.5 T) [1]. These experiments were conducted in the Voigt geometry ($\theta = 90°$) but we were interested as to whether error in θ might cause significant change to the spectra. We consider some of these examples in Figs. B.1 and B.2. Fig. B.2 shows numerically calculated theory curves with transmission higher than 100% for detunings far from resonance. Alongside this,

the curves becomes noisy with the extent of the error and noise profile dependent on variables outside of the *ElecSus* package. The two panels in Fig. B.2 were computed on different machines with different specifications and python packages. Similarly, Fig. B.1 predicts smaller features, with some noise, that are not physical. In this case, some of the predicted features are less than 100% in transmission which made it difficult to gauge if these were glitches or genuine physics. As such, numerically generated results could not be used to explore tolerance on θ away from the Voigt geometry due to doubts over reliability. For the same reason, numerically generated results should not be used to explore the sharp spectral features associated with exceptional points.

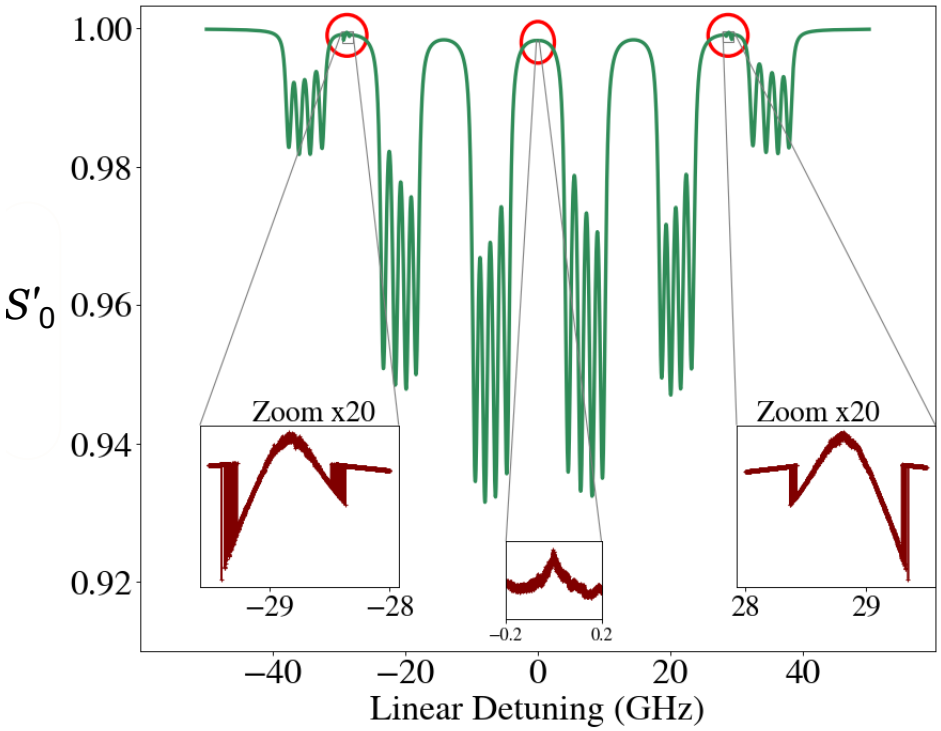

Geometry	$\boldsymbol{\theta}$ (°)	**D-line**	$\boldsymbol{T}$ (°C)	$\boldsymbol{B}$ (G)	**Inp. Pol.**
Oblique	87	D2	70	15000	Diagonal at 45° ↙↗

Figure B.1: A theory S'_0 spectrum calculated using the numerical method in *ElecSus* for light passing through a 1 mm 99% ^{87}Rb cell with 600 MHz broadening. Parameters are in table. The curve predicts small erroneous features at the points circled in red. Zoom-ins of the features are shown in the insets which exhibit numerical noise.

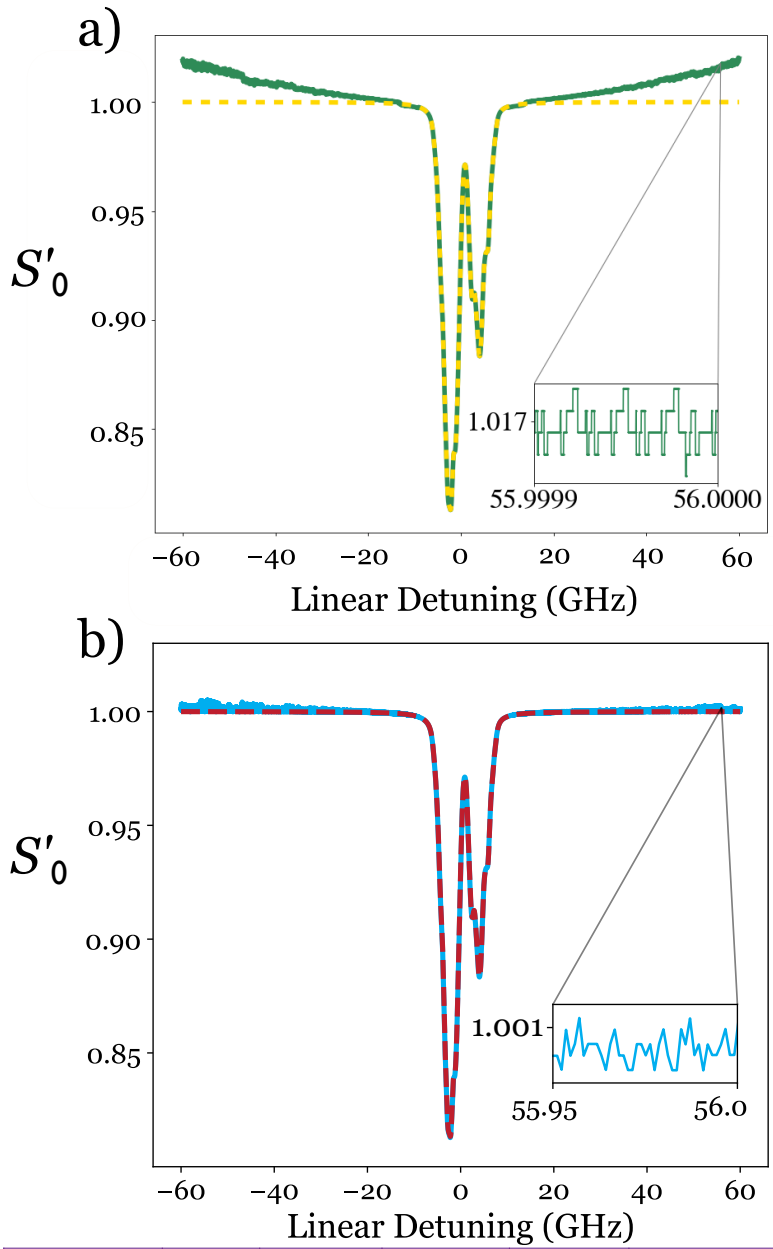

Geometry	θ (°)	D-line	T (°C)	B (G)	Inp. Pol.
Oblique	89.5	D2	70	800	Diagonal at 45° ↙↗

Figure B.2: Theory S'_0 curves calculated using the numerical method in *ElecSus* (green and blue) and Webber's analytic solutions (yellow and red) for light passing through a 1 mm 99% ^{87}Rb cell with 600 MHz broadening. Parameters are in table. a) and b) were calculated on two different computers with different python packages and versions installed. The numerical solutions incorrectly predict more than 100% light output. The error is more profound in a) showing the error is machine dependent. Both numerical curves show noise.

As discussed in A.7, exceptional points are highly sensitive to parameter changes

and hence our solutions need to be numerically stable [381, 382] i.e. small errors in input shouldn't propagate to large computational errors in output. One way of measuring the stability of matrix calculations is by condition number [383, 384] which is the maximum factor by which the relative error of the input to a calculation (i.e. input electric field) will be multiplied to the relative error of the output (i.e. output electric field) for a given calculation. It can be shown that the condition number, C, of a matrix A, involved in a matrix calculation $Ax = b$ is [385]:

$$C = \|A\| \cdot \|A^{-1}\| \tag{B.10}$$

where A^{-1} is the inverse matrix of A. The norm $\|A\|$ of the matrix in our studies is defined as the maximum *singular value* of the matrix A. As a rule of thumb a condition number of 10^k will result in a loss of k decimal digits of precision. Fig. B.3 plots the condition number for the propagation matrix $\mathcal{P}$ (see A.1), at each frequency numerically and using Webber's analytic solutions. Given that the condition number must be a minimum of one, both computations appear to be numerically stable by this metric with maximums of 1.18 and 1.07 computational error to be expected for the spectra in panels a) and b) respectively.

Where the numerical solutions are reliable, we can us them to audit the predictions of Webber's solutions. Fig. B.4 shows that the numerical solutions predict the same eigenvalues to 1 part in 10^{10} which also exhibit avoided crossings and adiabatic swaps. Fig. B.5 shows predictions for light output from the 1st cell in the Oblique-Voigt cascade realised in 4.4.1. While there are differences, the shapes are similar and there is excellent agreement for the filter profile itself in panel c).

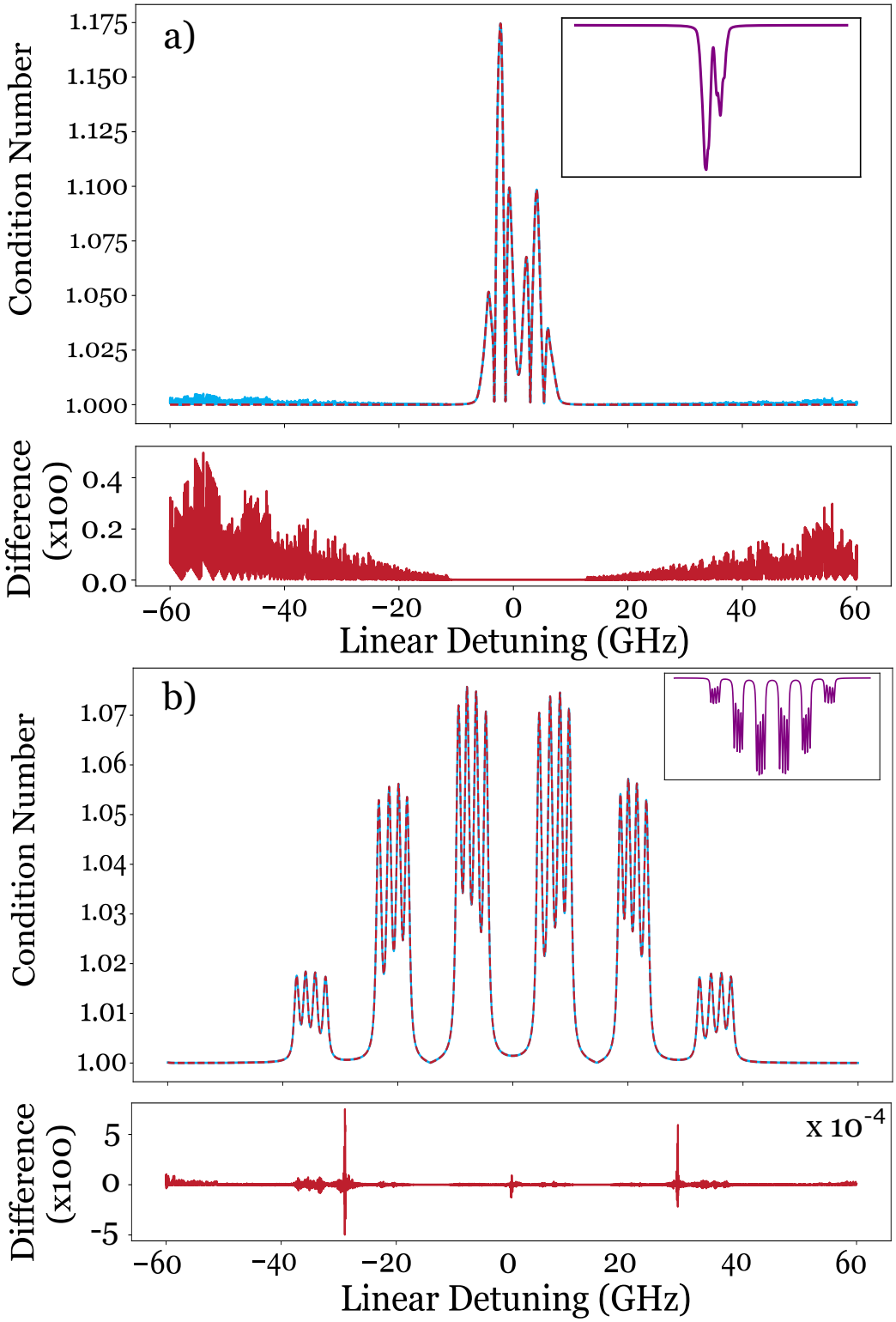

Figure B.3: Plots of the Condition Number for the Propagation matrices, $\mathcal{P}$, calculated using the numerical method (blue) and Webber's analytic solutions (red). a) corresponds to the propagation matrices resulting in the profile in Fig. B.2 and b) with the profile in Fig. B.1 which are shown as insets in purple. Parameters can be found in their respective figures. The difference in the condition numbers is plotted below.

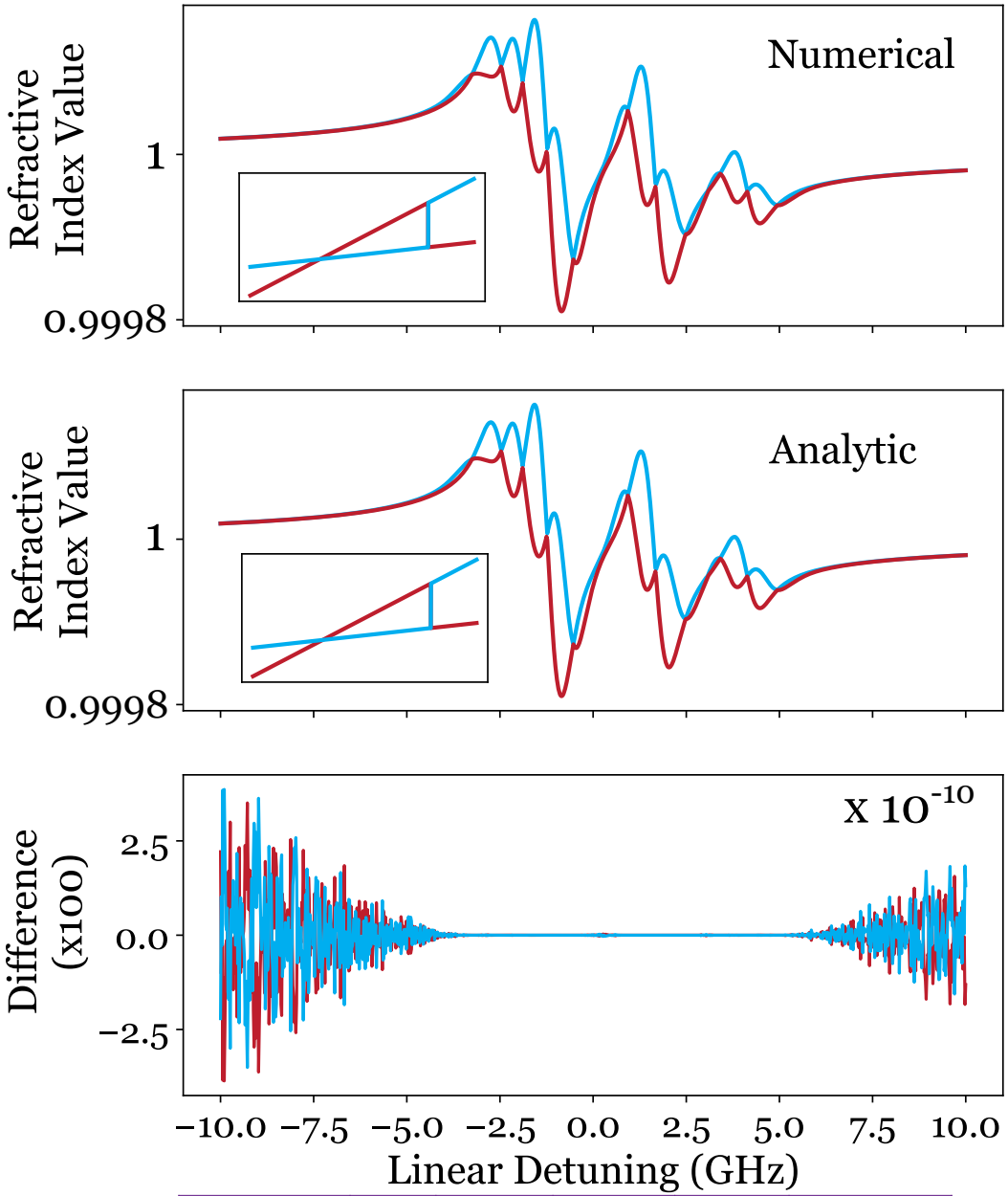

Geometry	θ(°)	D-line	T (°C)	B (G)	Inp. Pol.
Oblique	86	D2	97	227	Lin Hor.↔

Figure B.4: The refractive indices for the 75 mm natural abundance Rb Oblique cell in the Oblique-Voigt filter realised in 4.4.1 calculated numerically using *ElecSus* and analytically. Parameters in the table. The difference between the two calculations of n_a and n_b is shown below. Both diagrams show an inset of an adiabatic swap at approximately + 3 GHz. All refractive index solutions are practically identical exhibiting avoided crossings and adiabatic swaps.

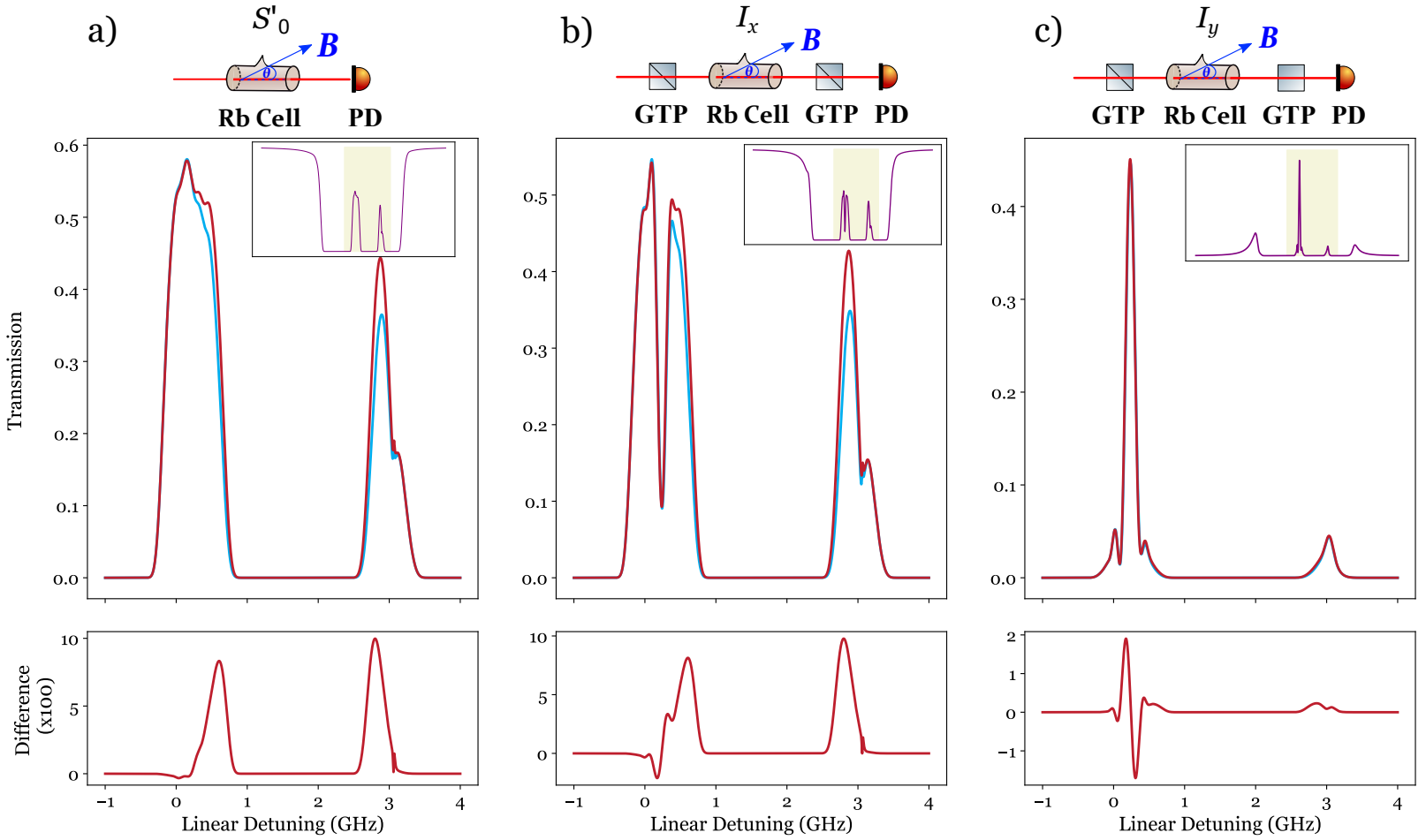

Figure B.5: Caption overleaf

Figure B.5: Theoretical curves computed using Webber's analytic solutions (red) and numerically using *ElecSus* (blue) for light entering the first 75 mm natural abundance Rb cell of the Oblique-Voigt filter realised in 4.4.1. Parameters are in Fig. B.4. a), b) and c) are plots of S_0', I_x and I_y respectively with diagrams showing how these values can be measured experimentally. c) is the filter profile of the Oblique-Voigt filter with the second cell removed. Insets of the whole spectra are shown in purple with beige shading indicating the regions considered in the main plots. The differences between the two solutions are shown below.

B.3 Comparison with Palik and Furdyna Analytic Solutions

We can find other complete sets of analytic solutions in the literature including those by Palik and Furdyna [249]. Their refractive index solutions are exactly the same as the Webber solutions. However, their eigenmode solutions are seemingly much simpler. Once again, they start with eq. B.2. Rather than calculating the null space explicitly, they read off the ratio relationships between the polarisation components along the x- and y-direction. Therefore the eigenmodes, $\vec{a} = \begin{bmatrix} a_1 \\ a_2 \end{bmatrix}$ and $\vec{b} = \begin{bmatrix} b_1 \\ b_2 \end{bmatrix}$ are represented by:

$$a_1 = 1, \tag{B.11}$$

$$a_2 = \frac{\epsilon_z(\epsilon_x - n_a^2)\cos\theta}{\epsilon_{xy}(\epsilon_z - n_a^2\sin^2\theta)}, \tag{B.12}$$

$$b_1 = 1, \tag{B.13}$$

$$b_2 = \frac{\epsilon_z(\epsilon_x - n_b^2)\cos\theta}{\epsilon_{xy}(\epsilon_z - n_b^2\sin^2\theta)}, \tag{B.14}$$

i.e. one polarisation component is set to be fixed while the other varies to generate the correct polarisation state. [1]

[1] We note that the authors incorrectly refer to these solutions as the waves 'whose polarisation does not change in the course of propagation'. These eigenmode solutions may not in general be invariant (see 4.2.3).

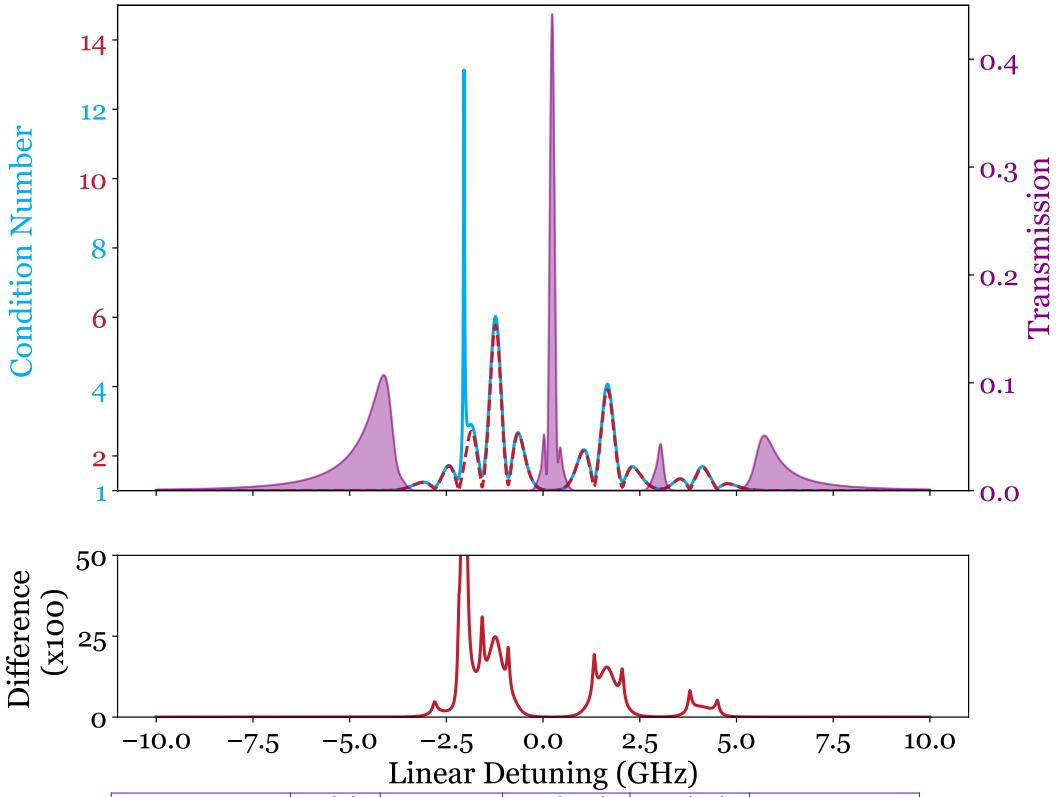

Geometry	θ(°)	D-line	T (°C)	B (G)	Inp. Pol.
Oblique	86	D2	97	227	Lin Hor.↔

Figure B.6: Plots of the Condition Number for propagation matrices computed using Palik and Furdyna's solutions (blue) and Webber's solutions (red) for light moving through the first 75 mm natural abundance Rb cell of the Oblique-Voigt filter. Parameters in table. Vertical scale shown on the left. The filter profile is shown in purple with its vertical scale on the right. Differences in the condition number plotted below. The values are similar for the two solutions and are near one when there is filter transmission. Palik and Furdyna's condition number spikes at ~ -2.5 GHz. This is due to the value of the eigenvector rapidly growing in magnitude in this frequency range.

While this leads to a simpler expression, this could have implications for numerical stability. Fig. B.6 plots the condition number for the propagation matrices $\mathcal{P}$ at each frequency for the light moving through the first cell of the Oblique-Voigt cascade as realised in 4.4.1. We note that both solutions have very similar condition numbers and most importantly low condition numbers in the transmission regions. However, the Palik and Furdyna solutions show a sharp spike in the condition number at ~ -2.5 GHz. Upon investigation, this was due to a large change in magnitude of the eigenmode in that small frequency range. It would appear that

while setting one polarisation component to be fixed may be simple, it requires the second component to rapidly change in response. While we have not investigated any situations where the spikes in condition number result in parasitic effects, this should be borne in mind with these solutions.

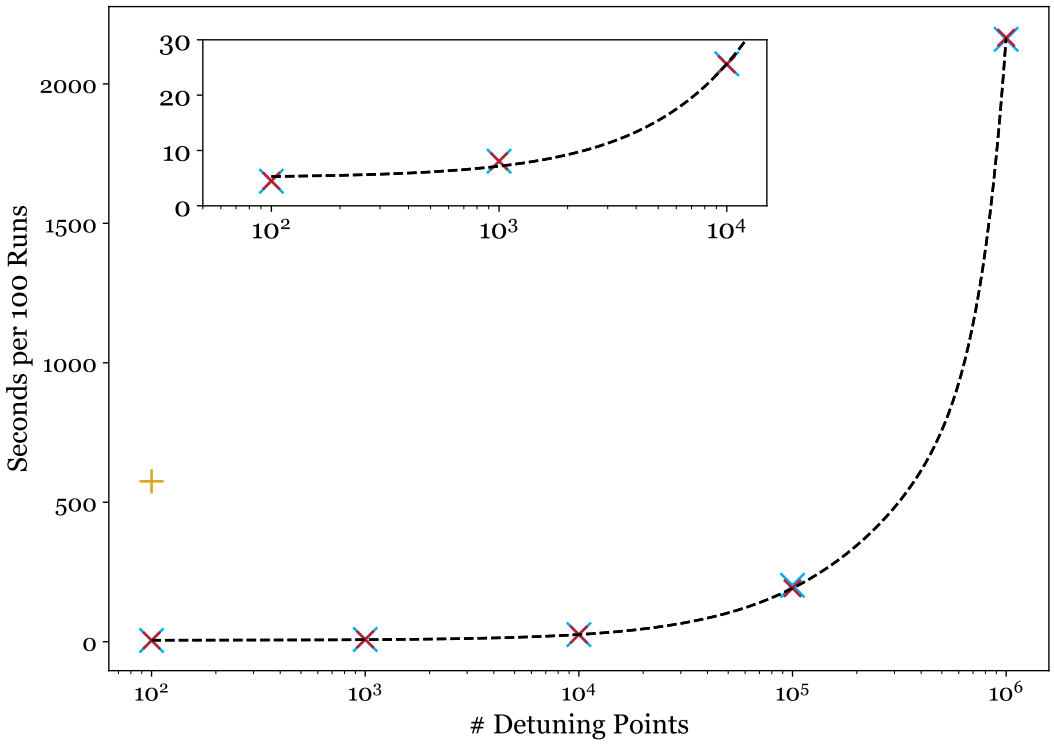

Figure B.7: A comparison of computation times for Webber analytic (red), Palik and Furdyna analytic (blue) and the *ElecSus* numerical (gold) solutions. The vertical axis measures time taken to perform 100 oblique field spectra. Mean values are plotted and error bars are too small to be visible. Note the log_{10} scale. The numerical solution performed so slowly for 100 detuning points, that we did not continue to measure its time scaling. The two analytic solutions show very similar time scaling. The two fits lie on top of each other and are largely linear with small quadratic and cubic contributions. The insets show a zoom in of the first three analytic points. Computations were carried out on a Lenovo IdeaPad 5 with i5 Gen Intel processor @ 2.4 GHz with 8 GB of RAM. Laptop was connected to mains power throughout.

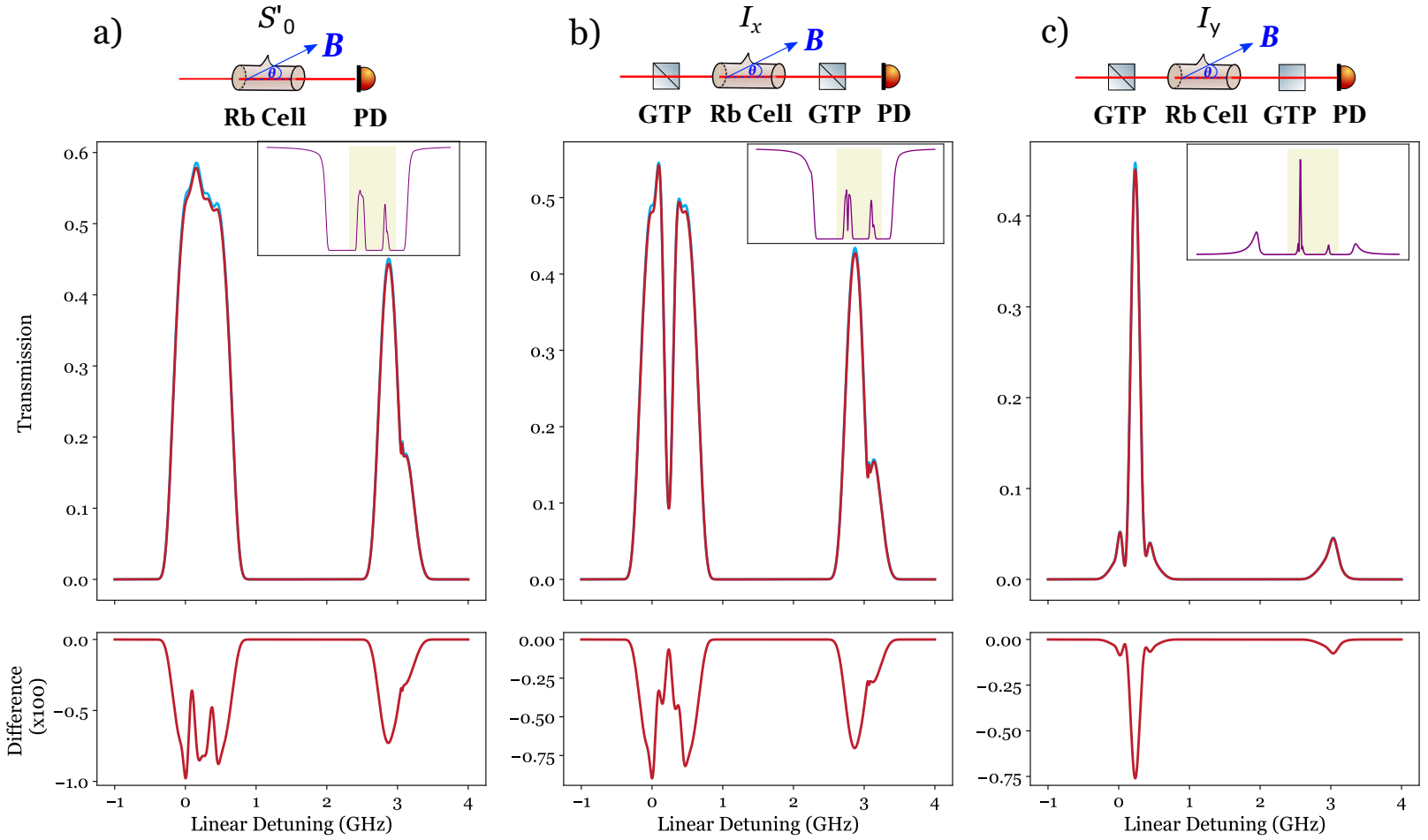

Figure B.8: Caption overleaf

Figure B.8: Theoretical curves computed using Webber's analytic solutions (red) and Palik and Furdyna's analytic solutions (blue) for light entering the 1st 75 mm natural abundance Rb cell of the Oblique-Voigt filter realised in 4.4.1. Parameters are in Fig. B.6. a), b) and c) are plots of S_0', I_x and I_y respectively with diagrams showing how these values can be measured experimentally. c) is the filter profile of the Oblique-Voigt filter with the second cell removed. Insets of the whole spectrum are shown in purple with beige shading indicating the region considered in the main plot. The differences between the two solutions are shown below.

Besides this, in terms of computational speed, the two analytic solutions are on par as shown in Fig. B.7. In addition, these solutions also confirm the oblique refractive index properties (since the refractive indices are exactly the same). Fig. B.8 shows plots of spectra computed using the two analytical methods for the first cell in the Oblique-Voigt cascade. The agreement once again for the realised filter profile is excellent.

B.4 Future Solutions

To summarise, we have good reason for using Webber's solutions throughout. Its key predictions are confirmed by two other sets of solutions. This includes concrete predictions that led to excellent agreement between data and theory for the two filters in Chapter 4, as well as the more speculative, with regards to exceptional points of degeneracy. Webber's solutions have competitive runtimes and have not yet shown issues with regards to numerical stability for any filter that has been experimentally realised. All this being said, there are still some points that need to be considered. Firstly, we have only studied the condition number of the matrix $\mathcal{P}$. As this matrix includes both the transformation in and out of the eigenmode basis, it would perhaps be more illuminating to also consider the condition numbers of the change of basis matrices.

Additionally for the highly cusp like peak filters studied in Chapter 5, we do see computational uncertainty resulting in large differences in prediction. Fig. B.9 shows evidence that standard computers may struggle to reliably predict filter

transmission at these highly coalescent features. The two spectra are both the supposed filter output of the Webber filter yet one has a peak and the other has a trough. Both are calculated using the same code but on different platforms. Nevertheless, the feature predicted in both cases has a FWHM on the order of 10 MHz. We have found computations across different platforms to be consistent in predicting the existence of coalescent features even if they predict different behaviour.

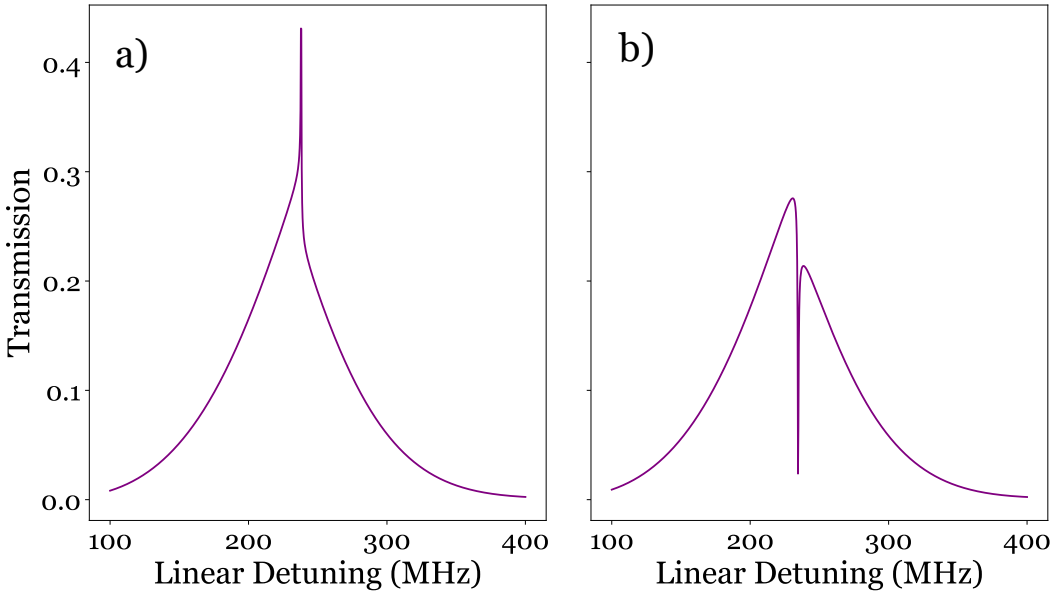

Figure B.9: Two spectra calculated using the Webber filter parameters. Both were computed using the same code but the code in a) was called as an import package and in b) was written directly in a jupyter notebook.

Fig. B.9 suggests there is some flaw in our computational process for coalescent features. Perhaps the paradox in A.7 would suggest that the very nature of our calculations may be flawed or needs amending in some way. Indeed, perhaps the collapse of the cusp feature in b) is indicative of the instability of the physics involved. This may encourage researchers to consider other formalisms such as perturbation theory [386] or master equations [387] to continue investigations. Nevertheless, we see Webber's solutions as the best candidates presently to be used, modified or extended in further research.

Appendix C

Transition Projection Operators

Author derived all proofs presented in this appendix starting from the general dipole matrix element expression [388]. All text written without the use of AI. Work is related to the article:

F. D. Logue, J. D. Briscoe, D. Pizzey, S. A. Wrathmall, and I. G. Hughes, 'Exploiting non-orthogonal eigenmodes in a non-Hermitian optical system to realize sub-100 MHz magneto-optical filters', *arXiv Preprint*, 2303.00081, 2023. https://doi.org/10.48550/arXiv.2303.00081 [5]

Throughout this thesis we have emphasised that the direction of the applied magnetic field relative to the k-vector, or the geometry, of the system determines the relationship between input polarisation and induced transitions. One such relationship is given by the propagation eigenmodes. From Appendix A, the eigenmodes form the change-of-basis matrix that transforms input polarisations to be acted on by the appropriate refractive indices. This relationship implicitly relates polarisation input with transitions given that the refractive indices are calculated from the individual transition susceptibilities (see B.1).

It is useful to have an implicit relationship since the electric dipole approximation [389, 390] assumes *three* polarisation sensitive transitions: σ^+ $(m_J = m'_J + 1)$, σ^- $(m_J = m'_J - 1)$ and π $(m_J = m'_J)$ [215] whereas the vapours we have been

considering are birefringent i.e. described by *two* eigenmodes. In this appendix, we derive the transition projection operators which give an explicit mapping between polarisation state and transition(s).

C.1 Angular Part of Dipole Matrix Element

A non-zero dipole matrix element between initial state i and final state f determines the transition stength when electromagnetic radiation is incident [391, 392, 393, 238, 394, 395]. The angular part of the dipole matrix element dictates the polarisation selection rules for each transition [388]. To begin, we exert a magnetic field parallel to the k-vector of the light. Defining z as the direction of the k-vector, the angular part of the dipole matrix element is,

$$\mathcal{M} = \sqrt{\frac{4\pi}{3}}\langle l' m_l' | \frac{\widehat{x} + \mathrm{i}\widehat{y}}{\sqrt{2}} Y_{1,1} + \frac{\widehat{x} - \mathrm{i}\widehat{y}}{\sqrt{2}} Y_{1,-1} + \widehat{z}\, Y_{1,0} | l m_l \rangle. \tag{C.1}$$

$Y_{l,m_l}(\theta, \phi)$ are spherical harmonic functions dependent on the orbital angular momentum l which is $+1$ for an electric dipole transition and the magnetic quantum number m_l [396, 397]. Given that electric dipole transitions do not alter spin ($m_s = m_s'$), the spherical harmonic functions equate to changes in $J = +1, m_J = 0, \pm 1$ or π and $\sigma^{+/-}$ transitions respectively. The prefactors composed of $\widehat{x}$, $\widehat{y}$ and $\widehat{z}$ cartesian operators are the polarisation projections that will induce each transition. Figures. C.1, C.2 and C.3 define the co-ordinate axes in terms of the cell orientation. Throughout these derivations, we will always rotate the cell (and the co-ordinate axes) to change the geometry and keep the magnetic field direction constant.

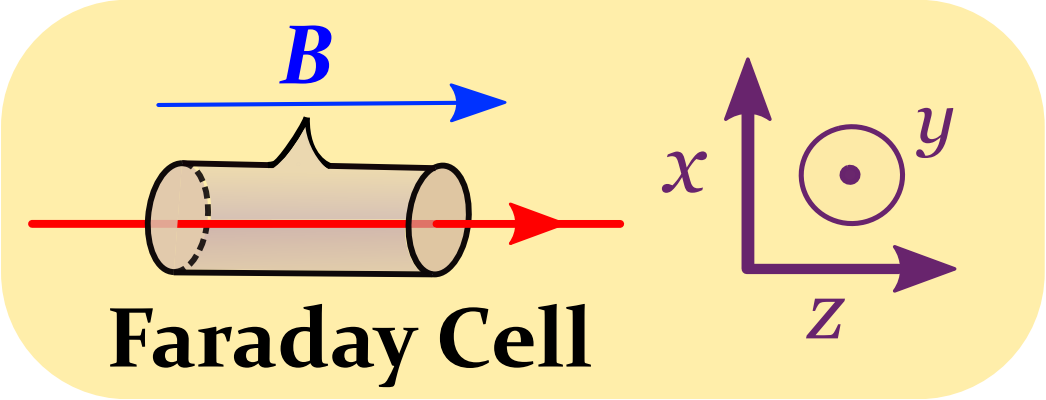

Figure C.1: A diagram defining the co-ordinate axes and relevant vectors for the Faraday geometry. The k-vector (red) and the magnetic field (blue) points in the z-direction. x points towards the top of the page while y points out of the page.

C.2 Faraday Projection Operators

Fig. C.1 defines the co-ordinate axes. We input plane waves in all our experiments. Since a plane wave is polarised transversely, the waves are not polarised along z and we can discard $\widehat{z}$ operators. Removing this term in C.1 gives the angular part of the dipole matrix element for the Faraday geometry:

$$\mathcal{M}_{\mathrm{F}} = \sqrt{\frac{4\pi}{3}}\langle l' m_l' | \frac{\overbrace{\widehat{x} + \mathrm{i}\widehat{y}}^{\circlearrowleft}}{\sqrt{2}} Y_{1,1} + \frac{\overbrace{\widehat{x} - \mathrm{i}\widehat{y}}^{\circlearrowright}}{\sqrt{2}} Y_{1,-1} | l m_l \rangle. \tag{C.2}$$

Using the conventions in Table A.1 and rewriting the operators as Jones vectors, $\sigma^{+/-}$ transitions are induced by left/right hand circular light whilst π transitions cannot be induced by a plane wave in the Faraday geometry. As highlighted in Table 4.6, the Faraday eigenmodes/invariant polarisations and the projection operators are the same polarisation states. Hence, each Faraday eigenmode when inputted to a thermal vapour induces one transition.

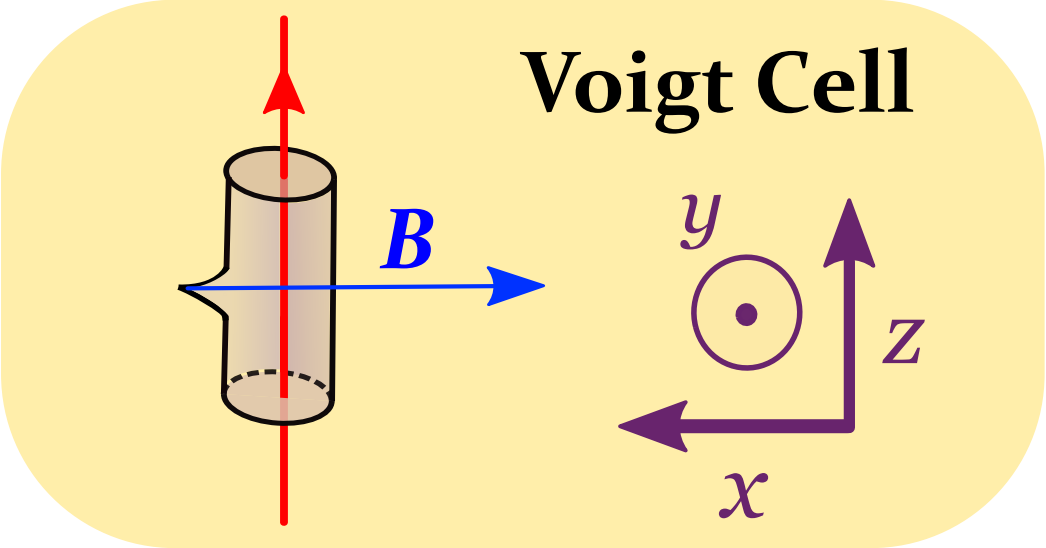

Figure C.2: A diagram defining the co-ordinate axes and relevant vectors for the Voigt geometry. The k-vector (red) points in the z-direction as it did for the Faraday cell in Fig. C.1. The magnetic field (blue) points in the $-x$ direction. y still points out of the page.

C.3 Voigt Projection Operators

To derive the Voigt projection operators, we rotate the k-vector by 90° while keeping the magnetic field direction constant[1]. We can choose to rotate in one of two planes and without loss of generality, we choose to rotate in the $x-z$ plane. The relevant co-ordinate transformations are:

$$\begin{aligned} \hat{z} &\rightarrow \hat{x}, \\ \hat{x} &\rightarrow -\hat{z}. \end{aligned} \tag{C.3}$$

Fig. C.2 defines the co-ordinate axes after these transformations. Applying the co-ordinate transformations to eq. C.1 and removing $\hat{z}$ operators we obtain the angular part of the dipole matrix element for the Voigt geometry:

$$\mathcal{M}_{\mathrm{V}} = \sqrt{\frac{4\pi}{3}}\langle l' m_l' | \overbrace{\hat{x}}^{\leftrightarrow} Y_{1,0} + \overbrace{\hat{y}}^{\updownarrow} (Y_{1,1} - Y_{1,-1}) | l m_l \rangle. \tag{C.4}$$

[1] In these derivations, we are not concerned with experimental practicalities of rotating the setup which in most cases would involve changing the magnetic field source to maintain homogeneity in the new geometry.

Using the conventions in Table A.1, normalising and rewriting the operators as Jones vectors, horizontally linear light induces π transitions and vertically linear light induces a linear combination of $\sigma^{+/-}$ transitions. Similarly as highlighted in Table 4.6, the Voigt eigenmodes/invariant polarisations and the projection operators are the same polarisation states. As such, the two Voigt eigenmodes induce π transitions and $\sigma^{+/-}$ transitions respectively.

For the reader's interest rotating in the y-z plane would result in vertically linear light inducing π transitions and horizontally linear light inducing a linear combination of $\sigma^{+/-}$ transitions.

C.4 Projection Operators at Arbitrary Field Angle

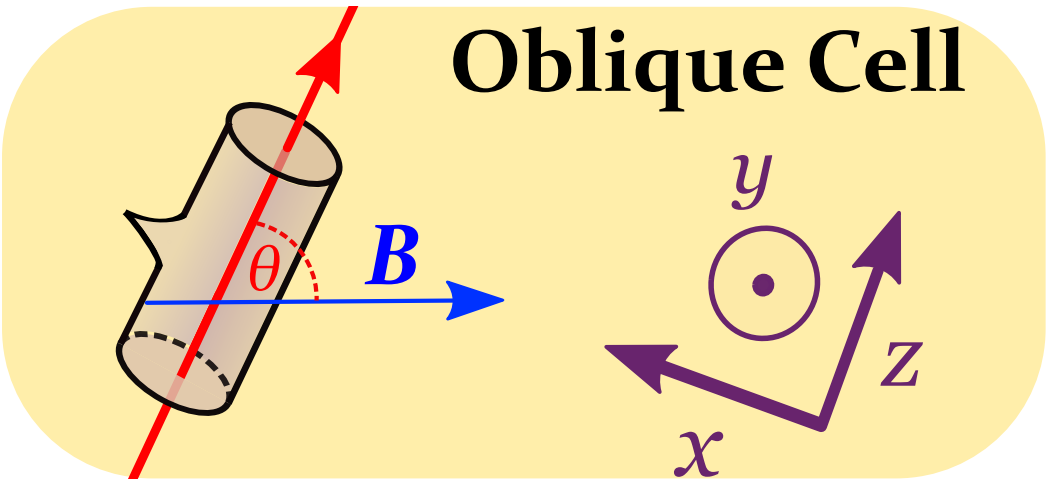

Figure C.3: A diagram defining the co-ordinate axes and relevant vectors for arbitrary angle θ between the k-vector and the magnetic field. The k-vector (red) once again points in the z-direction. The magnetic field (blue) points in the $-x\sin\theta$ direction. y still points out of the page.

For a general geometry, we rotate the cell by angle θ while keeping the magnetic field direction constant. Once again, without loss of generality we rotate in the $x-z$ plane and leave the reader to derive a similar expression for rotation in $y-z$. The co-ordinate transformations are:

$$\begin{aligned} \widehat{x} &\rightarrow \widehat{x}\cos\theta - \widehat{z}\sin\theta, \\ \widehat{z} &\rightarrow \widehat{z}\cos\theta + \widehat{x}\sin\theta. \end{aligned} \tag{C.5}$$

Fig. C.3 defines the co-ordinate axes after these transformations. Applying these transformations to C.1 and removing $\widehat{z}$ operators gives the arbitrary angular part of the dipole matrix element:

$$\begin{aligned} \mathcal{M}_{\mathrm{A}} = \sqrt{\frac{4\pi}{3}}\langle l' m_l' | \frac{\widehat{x}\cos\theta + \mathrm{i}\widehat{y}}{\sqrt{2}} Y_{1,1} + \frac{\widehat{x}\cos\theta - \mathrm{i}\widehat{y}}{\sqrt{2}} Y_{1,-1} \\ + \widehat{x}\sin\theta Y_{1,0} | l m_l \rangle. \end{aligned} \tag{C.6}$$

Applying normalisation, we gain the normalised arbitrary angular part of the dipole matrix element:

$$\begin{aligned} \mathcal{M}_{\mathrm{A}} = \sqrt{\frac{4\pi}{3}}\langle l' m_l' | \frac{\widehat{x}\cos\theta + \mathrm{i}\widehat{y}}{\sqrt{\cos^2\theta + 1}} Y_{1,1} + \frac{\widehat{x}\cos\theta - \mathrm{i}\widehat{y}}{\sqrt{\cos^2\theta + 1}} Y_{1,-1} \\ + \widehat{x} Y_{1,0} | l m_l \rangle. \end{aligned} \tag{C.7}$$

As this is a general expression, by substituting $\theta = 0$ or $90°$ we can obtain the same Faraday and Voigt results as above. Outside of these special cases, in the oblique geometry, left/right handed elliptical states induce $\sigma^{+/-}$ states and horizontally linear light induces π transitions. In this case, there are three non-zero projection operators. Consequently, a single polarisation state always induces at least two transitions provided the relevant transition linestrengths are all non-zero. As highlighted in Table 4.6, the relationship between eigenmodes and projection operators is more complicated than in the Faraday and Voigt cases.

C.5 Example Oblique Projection Operators at $\theta = 86°$

As an example, setting $\theta = 86°$ in eq. C.8 gives to two decimal places:

$$\mathcal{M}_{86°} = \sqrt{\frac{4\pi}{3}}\langle l' m_l' | \frac{0.07 \cdot \widehat{x} + \mathrm{i}\widehat{y}}{\sqrt{0.07^2 + 1}} Y_{1,1} + \frac{0.07 \cdot \widehat{x} - \mathrm{i}\widehat{y}}{\sqrt{0.07^2 + 1}} Y_{1,-1} + \widehat{x}\ Y_{1,0} | l m_l \rangle. \tag{C.8}$$

Depictions of the three normalised projection operator polarisations are shown in Fig. C.4.

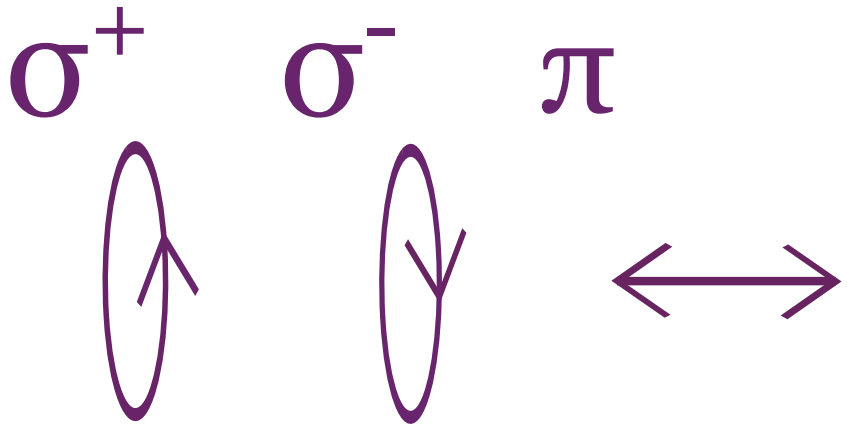

Figure C.4: The three projection operators for $\theta = 86°$. Written in normalised Jones vector form, the elliptical polarisations $\begin{pmatrix} 0.07 \\ \pm\mathrm{i} \end{pmatrix}$ induce $\sigma^{+/-}$ transitions and horizontally linear light $\begin{pmatrix} 1 \\ 0 \end{pmatrix}$ induces π transitions.

Appendix D

Data Processing

Author completed all theoretical computations, collected and processed all data and created all figures presented in this appendix. All text written without the use of AI. Work is related to the published article:

D. Pizzey, J. D. Briscoe, F. D. Logue, F. S. Ponciano-Ojeda, S. A. Wrathmall, and I. G. Hughes, 'Laser spectroscopy of hot atomic vapours: from 'scope to theoretical fit.', *New Journal of Physics*, **24**:125001, (2022). https://doi.org/10.1088/1367-2630/ac9cfe [3].

Data throughout this thesis was collected using an oscilloscope which displays voltage readings directly from a photodetector as time passes. While the main features of spectra can be seen by eye (see Fig. D.1), the data is in an inconvenient form to make more precise conclusions. The voltage readings include information about the photodetector responsivity [398] and laser power variation [399, 400] while the time readings are dependent on the laser frequency scanning waveform [401]. We are interested in how the atoms interact with light as a function of frequency which is independent of these variables. As such the data needs to be processed into a new form. Once processed, we can evaluate performance metrics like FOM, FWHM and ENBW. Additionally, we can compare the data and theory predictions by plotting them on the same graph. The is vital in making a case for the theory's validity (e.g. verifying optimised filters in Figs. 4.11) and for noting experimental

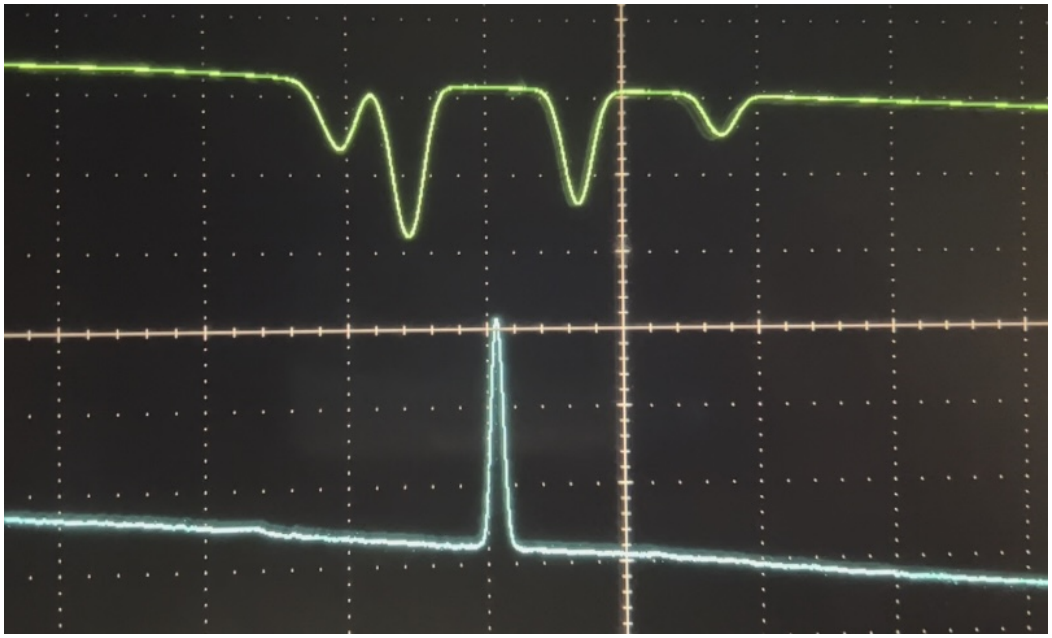

Figure D.1: Bandpass (blue) and notch (green) traces taken directly from an oscilloscope screen plotting voltage against time. Note the lines of 100 and 0% transmission are not horizontal and need to be normalised. More difficult to see, the spectra are non-linearly related to the frequency of the input light. If we were to compare these traces with theory, we would find some features appear more 'stretched' compared with others.

errors (e.g field inhomogeneity in Fig. 4.16). While one could compare the data on the oscilloscope screen the with that of the theory on the computer screen, as we have seen in Chapter 5, it is often the smallest of features that indicate theoretical paradigm shifts.

In this appendix, we will outline the three main procedures used to process our data: linearisation, absolute frequency calibration and normalisation which we consider for a Doppler broadened notch spectrum. Linearisation is the process by which the time axis is transformed into an axis in frequency units. Absolute frequency calibration finds the offset to convert the axis in frequency units to a linear detuning scale. Finally, normalisation converts the voltage readings to a percentage transmission between 0 (no transmission) and 1 (total transmission).

D.1 Experimental Setup

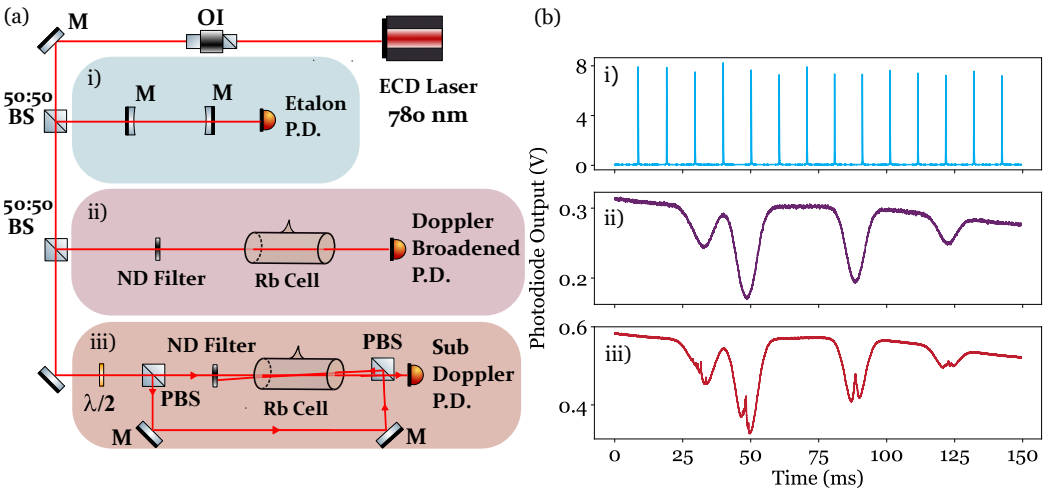

Figure D.2: a) The calibration setup for a notch spectrum alongside b) example signal outputs from the photodetectors of each arm. Light from a Toptica DL 100 external cavity (ECD) laser on the Rb-D2 line is directed towards three arms. ii) is the Doppler broadened notch spectrum we are interested in processing. A neutral density (ND) filter is placed before the cell to lower the power to ~ 300 nW with $1/e^2$ width of 100 µm as theory is readily available to model in the weak probe regime [169, 155]. i) is a Fabry-Pérot etalon setup composed of two confocal mirrors (M). The etalon signal will be used in linearisation. iii) is a sub-Doppler setup. The beam passes through a polarising beam splitter (PBS). The intensity of the light on each path is determined by the $\lambda/2$ waveplate and neutral density (ND) filter. The 'probe' beam is transmitted and is weaker in power than the reflected 'pump' beam. The 'probe' and 'pump' beams are optimised to have maximum overlap in the cell leading to spectra with sub-Doppler features. This signal will be used in absolute frequency calibration. Note that the setup in ii) should be interchanged for the setup requirements of the experiment. The setups in i) and iii) remain the same for all experiments. OI — Optical Isolator, P.D. — Photodetector.

In order to process a spectrum, we need to take additional data exclusively for the purposes of calibration. Fig. D.2 shows the setup and raw data needed to process a Doppler broadened notch spectrum (ii). The Fabry-Pérot etalon (i), or cavity lens [120, 121, 122], is built from two confocal curved mirrors with the radii of curvature of the two mirrors, r, equalling the distance, L, between their surfaces. The etalon transmits highly for frequencies that are multiples of the free spectral range, ν_{FSR} [402],

$$\nu_{\mathrm{FSR}} = \frac{c}{4L}. \tag{D.1}$$

Mirrors of high reflectivity, R_1 and R_2, should be chosen for the etalon to have high finesse, $\mathcal{F}$ [403],

$$\mathcal{F} = \frac{\pi \sqrt[4]{R_1 \cdot R_2}}{2(1 - \sqrt{R_1 \cdot R_2}}) = \frac{\nu_{\mathrm{FSR}}}{\mathrm{FWHM}}, \tag{D.2}$$

thus ensuring the FWHMs of the transmitted peaks are narrower minimising the uncertainty in the peak position. From eq. D.2, we also gather that increasing the free spectral range, or equivalently decreasing the mirrors' radii of curvature (curvier mirrors), also narrows the FWHM. The raw signal in i) shows these periodic narrow transmitted peaks.

Note that aligning an etalon can be fine work as the smallest mirror adjustments can have drastic changes on performance dependent on the *mirror geometry* [404, 405, 406]. Once completed the instrument should be mechanically and thermally stabilised [407, 408, 409].

The sub-Doppler setup (iii) involves a natural abundance Rb cell with optics sending two counter propagating beams through the cell aligned to have maximum spatial overlap with each other [410]. The beam transmitted through the first polarising beam splitter is known as the 'probe' and is detected. The reflected 'pump' beam is much stronger and is not detected. This scheme results in enhanced transmissions and absorptions as compared to the Doppler broadened notch spectrum (compare the raw signals in ii) and iii)). The exact profile of these sub-Doppler features can be varied by changing the power of both beams. For our purposes, the setup should be optimised so as to maximise the number of these features that can be discerned from noise.

Note that to calibrate other experiments, we replace the setup in ii) while maintaining i) and iii). The etalon signal is used for linearisation while the sub-Doppler

notch spectrum is used for absolute frequency calibration. All three of these signals should be taken simultaneously and cropped to the region of interest before processing.

D.2 Linearisation

The Toptica DL 100 [240] is an external cavity diode (ECD) laser in the Littrow configuration [411] which has a diffraction grating whose angle is micro-adjusted rapidly by a piezo [412, 413]. This small change in angle causes the varying frequency output of the laser. We want to continually scan in a small range around a central frequency. As such, it follows that the angular frequency will change as the grating comes to rest at its maximum and minimum angles and speeds up again to approach its minimum and maximum angles respectively. When we also consider piezo hysteresis and creep effects [414] amongst others [415], we have a non-linear relationship between the time recorded on our oscilloscope and the frequency of the laser light. The aim of linearisation is to transform the time data into data in frequency units given this non-linear relationship.

As discussed, in the previous section, the periodicity of the peaks in Fig. D.2 and D.3 is the free spectral range. In our particular case, $\nu_{\mathrm{FSR}} = 745$ MHz. With this information, we can find a linear fit between time passed and successive etalon peaks. The deviation from the linear fit is the difference between data and theory. By fitting the difference with a high order polynomial, we can subtract this fit from the time values as a correction. After scaling the data appropriately such that the distance between successive peaks is the free spectral range, we have transformed the axis to frequency units. Note that there is an arbitrary offset since the etalon peaks only give information about relative frequency differences and not absolute frequency differences. Fig. D.3 gives the details of this procedure visually.

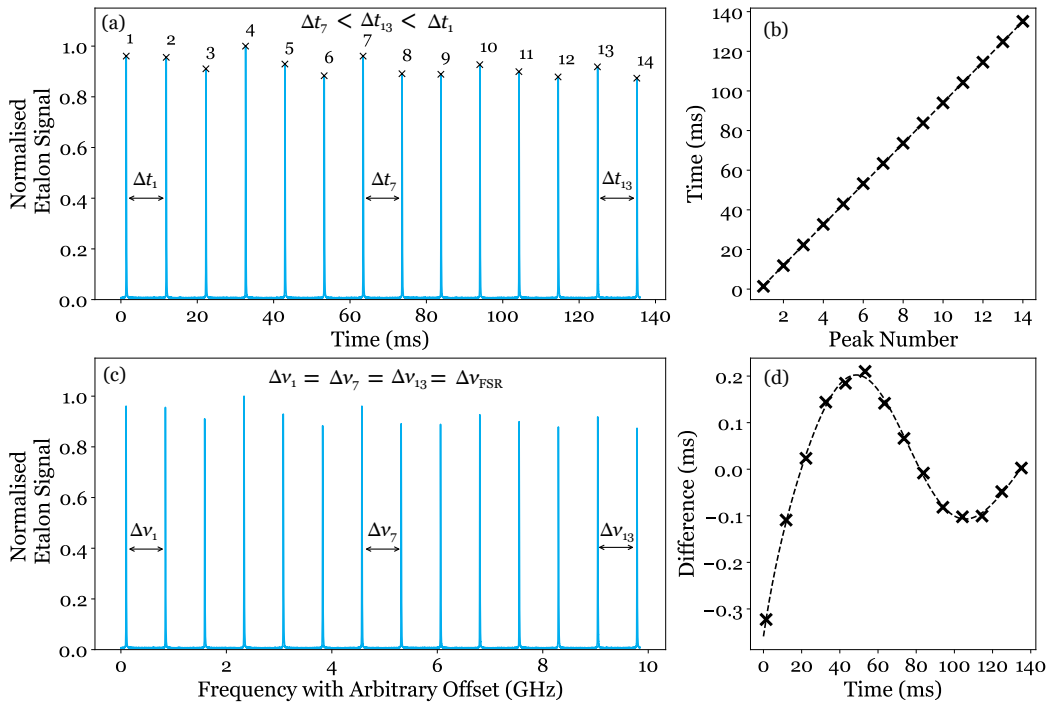

Figure D.3: Linearising the etalon signal. a) The etalon signal from i) in Fig. D.2 which has been normalised. The signal has different valued time intervals Δt_i between neighbouring peaks. This indicates that the frequency scanned by the laser varies with time. b) We plot the time each peak is recorded against its order in sequence. A straight line is fitted to it. d) The differences between the fit and data in b) are plotted against time. In this case, we fit a 7th order polynomial to the difference. c) shows the linearised etalon signal achieved by subtracting the fit in d) from the time-values and scaling the data appropriately. Note the x-axis is now in units of frequency and the frequency intervals, $\Delta\nu_i$, between neighbouring peaks are the same. The frequencies have an arbitrary offset which we find by completing absolute frequency calibration.

D.3 Absolute Frequency Calibration

While the free spectral range of the etalon gives us a reliable measure of frequency intervals, drift effects [64] make it unreliable for absolute frequency measurements. Our x-axis in frequency units, which we obtained from linearisation, is equivalent to an absolute frequency axis plus some offset. To find this offset, we need an atomic frequency reference which is provided by our sub-Doppler setup.

As discussed in Chapter 2, an atom moving at speed v_z in the opposite direction to the light's propagation observes the frequency of the probe beam ν_{atom} as [410],

$$\nu_{\text{atom}} = \nu_0(1 + \frac{v_z}{c}), \tag{D.3}$$

where c is the speed of light and ν_0 is the frequency observed in the lab frame. This Doppler shifting gives rise to Doppler widths [416] which prevent resolution of the individual hyperfine transitions. However, we can resolve these transitions with two counter-propagating beams as in our sub-Doppler setup. The same atom travelling at v_z observes the frequency of the pump beam ν'_{atom} as:

$$\nu'_{\text{atom}} = \nu_0(1 - \frac{v_z}{c}), \tag{D.4}$$

since the atom is moving towards it. The frequency observed at rest is still ν_0 as the two beams are at the same rest frequency. It is only possible to see spectral features due to atoms that have interacted with the detected probe beam. Hence, new features will arise for atoms excited by both the probe and pump beams. This is satisfied at hyperfine transition resonances when $v_z = 0$ (or within a natural linewidth) [417]. We also observe features halfway between two resonances where the atoms observe the pump and probe resonant with two separate resonances. These are known as crossover features [418].

These enhanced transmission and absorption features arise from two mechanisms which change the ground state atomic populations: saturation and hyperfine pumping.[1] Saturation leads to more atoms in the excited state to a maximum of half the ground population [169]. Hyperfine pumping refers to atoms being excited and decaying via a different pathway to another ground state [419].

As we can see in Fig. D.4, we have 6 hyperfine transitions each for ^{85}Rb and ^{87}Rb on the D2 line alongside 6 crossover features each. In total, we have 24 features. The transitions and crossover resonance frequencies for these 24 features are well known [212, 226, 221]. Therefore, we can use a sub-Doppler spectrum with

[1] This technique is often called *saturated* absorption spectroscopy. Given that hyperfine pumping plays an important role alongside saturation, we believe this term is misleading.

linearised x-axis in frequency units to calculate a linear fit between the positions of these features in frequency units with arbitrary offset and their known detuning values.

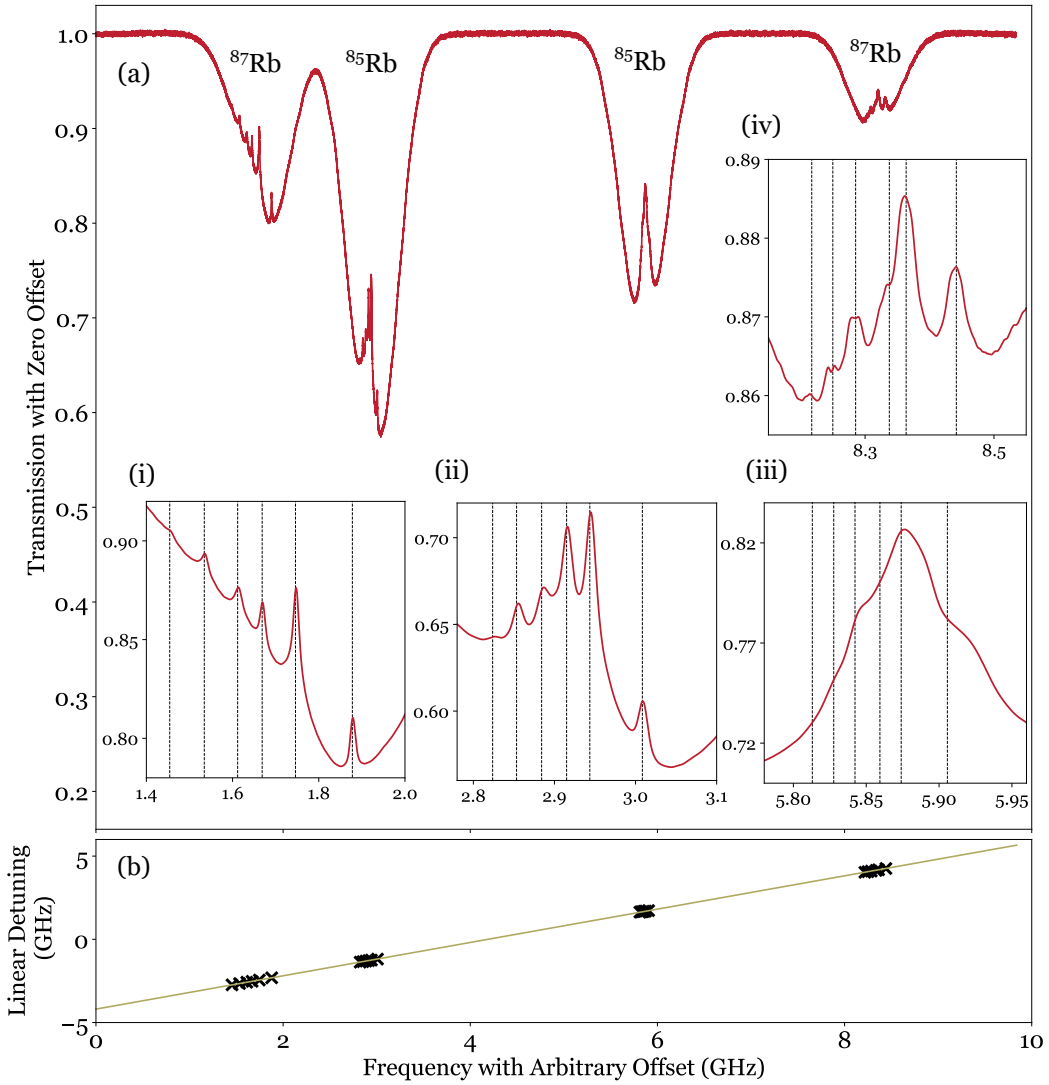

Figure D.4: Absolute frequency calibration using a sub-Doppler Spectrum generated from the setup (iii) in Fig. D.2. a) The main plot shows enhanced absorption and features located at the frequencies of the twelve $F \rightarrow F' = F, F \pm 1$ transitions alongside twelve crossover features whose detunings are well known [212, 226, 221]. Zero detuning is calculated as the weighted line centre of the Rb-D2 line. b) shows the i) ^{87}Rb, $F = 2 \rightarrow 1, 2, 3$, ii) ^{85}Rb, $F = 3 \rightarrow 2, 3, 4$ iii) ^{85}Rb, $F = 2 \rightarrow 1, 2, 3$ iv) ^{87}Rb, $F = 1 \rightarrow 0, 1, 2$ transitions along with their crossovers in more detail. Note some of the data for these insets were taken separately from the main plot and a triangular moving average has been applied to make features clearer. b) shows a plot of the identified features with their linearised frequency values on the x-axis alongside their known detuning values on the y-axis. The offset of the straight line fit gives the shift value needed to convert to absolute detuning. Note this spectrum has not been normalised. While 100% transmission has been set to 1 for ease of selecting features, it has not been scaled vertically.

The y-intercept of this fit gives the offset which when subtracted completes the transformation of the time axis to a frequency aixs. In the case of Fig. D.4, the offset is 4.2 GHz.

It can be difficult to resolve all 24 features in one spectrum. However, successful calibration can be completed with less than the total number of predicted features. Using our linearisation and absolute frequency calibration procedure, we find errors are less than 1%.

D.4 Normalisation

D.4.1 Doppler Broadened Notch Spectrum

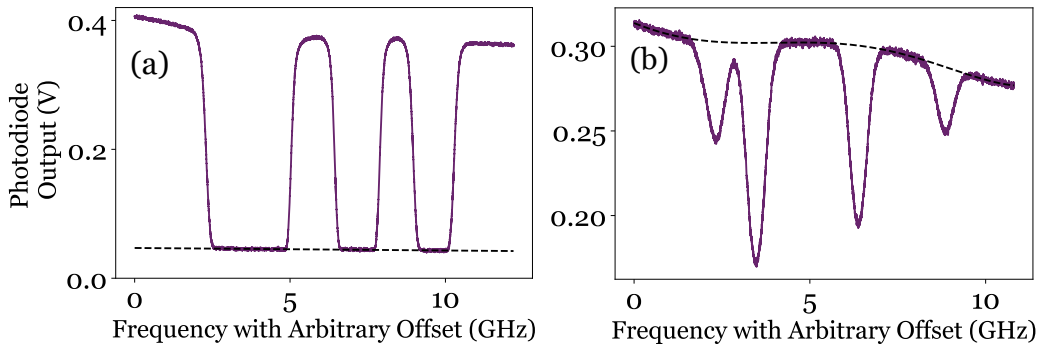

Figure D.5: Normalising a Doppler Broadened Notch Spectrum. a) A hot spectrum generated using the setup in ii) in Fig. D.2. The spectrum is heated such that the absorption reaches zero in three regions. We fit a straight line to these zero regions. We subtract this fit from all spectra so that zero signal corresponds with zero transmission. b) A Doppler broadened spectrum which we wish to normalise. Having subtracted the fit from a), we fit the four regions where the light is completely transmitted. The results of which are shown in the purple trace in Fig. D.6.

Unlike the process to calibrate the x-axis which remains the same for all data we want to process, the calibration of the y-axis depends on the spectral profile of the raw data in (ii) of Fig D.2. In this appendix we consider only the case of a Doppler broadened notch spectrum at room temperature and at zero field.

Normalisation is the process by which we convert the voltage y-axis to a percentage transmission axis with '1' indicating 100% transmission and '0' indicating 0%

transmission. Light is lost at many stages of the experiment and we could define 100%/0% transmission in many different ways. In this thesis, 100%/0% transmission is light that is transmitted/rejected entirely through all the vapours in the setup. This definition does not take into account losses through each of the optical components before or after the vapours including the vapour cell windows or laser power variations.

We begin by considering the '0' line. For many reasons, we do not observe zero voltage output when transmission is 0%. These include stray light incident on the photodetector, photodetector noise [420] and incoherent light from amplified stimulated emission of the laser [421, 422]. Therefore before beginning the experiment, the setup in (ii) should be heated such that a spectrum is obtained with regions of 0% transmission. These can then be fitted by some polynomial (see a in Fig. D.5) and the offset subtracted from voltage readings in any future data using the same photodetector and laser. Note however that conditions of the setup can change and one may want to calibrate the zero reading immediately before any experiment.

Having subtracted this zero offset, we want to define 100% transmission as '1'. In b) of Fig. D.5, we see a fit has been applied to the regions of 100% tranmission. By dividing the data by this fit, the voltage axis has now been transformed into a transmission axis and normalisation is complete. The data is now in a state ready to by fit with theory which can be seen in the purple trace in Fig. D.6.

As demonstrated in [22], one could incorporate intensity stabilisation optics such that maximum and minimum transmission values maintain a constant voltage reading. One would then simply remove the zero offset as before and scale the data appropriately to normalise.

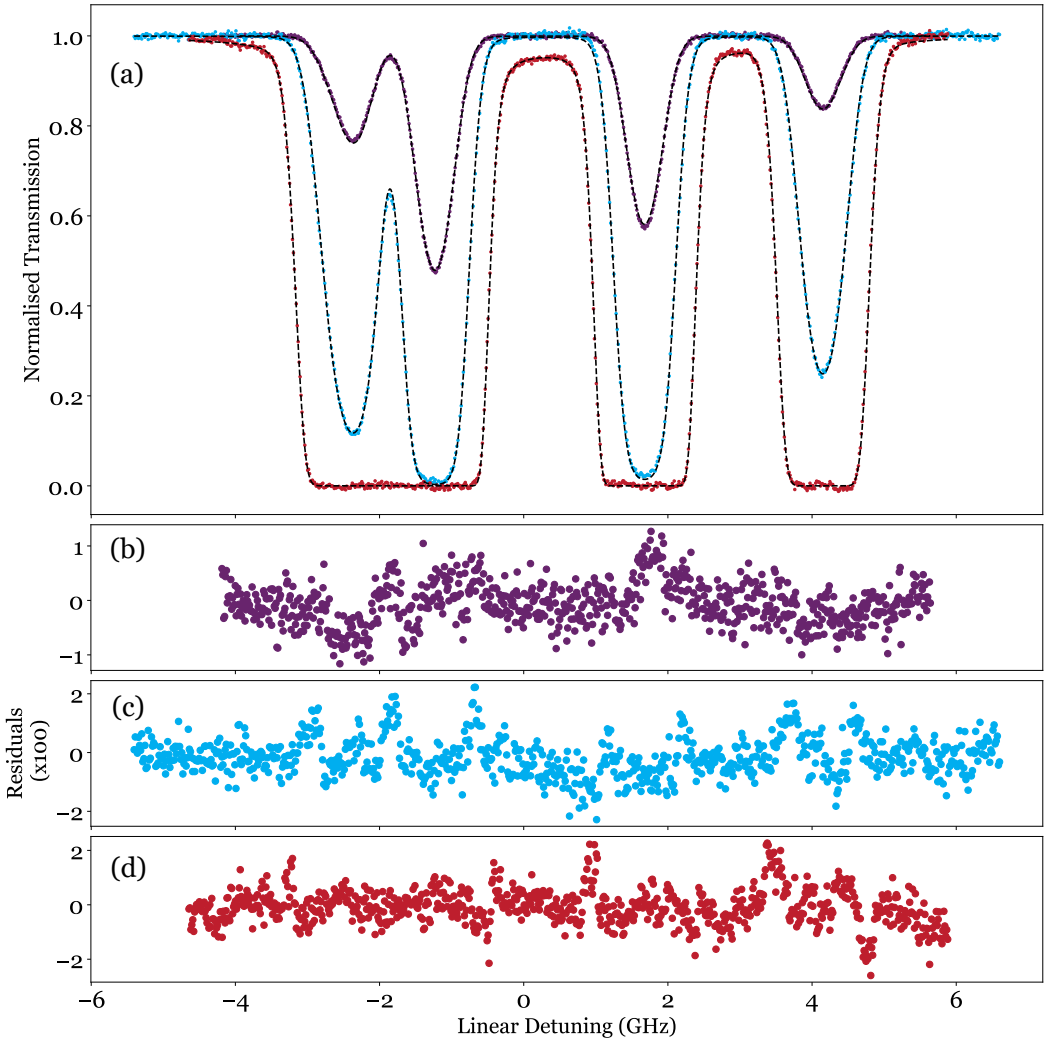

Figure D.6: Fits of three zero field notch spectra in natural abundance Rb. The temperature fits are $19.67 \pm 0.01°$ C (RMS = 0.40%), $40.12 \pm 0.01°$ C (RMS = 0.68%) and $72.77 \pm 0.02°$ C (RMS = 0.68%) for the purple, blue and red traces respectively. The residuals x 100 are shown for the purple, blue and red traces in b), c) and d) respectively. The data shows excellent agreement with theory [244].

D.5 Links to Additional Info

A jupyter notebook which follows the procedure described can be found at [423, 424]. Note it is not set up to process bandpass filter data but can be easily be modified to do so.

Analogous procedures to those discussed can be found in [425, 426, 427].

Etaloning can be present in spectral data which can be isolated and removed, see [3, 225] for more details.

Bibliography

[1] F. S. Ponciano-Ojeda, F. D. Logue, and I. G. Hughes. Absorption spectroscopy and Stokes polarimetry in a 87Rb vapour in the Voigt geometry with a 1.5 T external magnetic field. *Journal of Physics B: Atomic, Molecular and Optical Physics*, 54(1):015401, 2020.

[2] F. D Logue, J. D Briscoe, D. Pizzey, S. A. Wrathmall, and I. G. Hughes. Better magneto-optical filters with cascaded vapor cells. *Optics Letters*, 47(12):2975–2978, 2022.

[3] D. Pizzey, J. D. Briscoe, F. D Logue, F. S. Ponciano-Ojeda, S. A. Wrathmall, and I. G. Hughes. Laser spectroscopy of hot atomic vapours: from 'scope to theoretical fit. *New Journal of Physics*, 24:125001, 2022.

[4] J. D. Briscoe, F. D. Logue, D. Pizzey, S. A. Wrathmall, and I. G. Hughes. Voigt transmission windows in optically thick atomic vapours: a method to create single-peaked line centre filters. *Journal of Physics B: Atomic, Molecular and Optical Physics*, 56(10):105403, 2023.

[5] F. D. Logue, J. D. Briscoe, D. Pizzey, S. A. Wrathmall, and I. G. Hughes. Exploiting non-orthogonal eigenmodes in a non-Hermitian optical system to realize sub-100 MHz magneto-optical filters. *arXiv preprint*, 2303.00081, 2023.

[6] D. Budker, W. Gawlik, D. F. Kimball, S. M. Rochester, V. V. Yashchuk, and A. Weis. Resonant nonlinear magneto-optical effects in atoms. *Reviews of Modern Physics*, 74(4):1153, 2002.

[7] M. Faraday. I. Experimental researches in electricity.—Nineteenth series. *Philosophical Transactions of the Royal Society of London*, (136):1–20, 1846.

[8] J. Kerr. XL. A new relation between electricity and light: Dielectrified media birefringent. *The London, Edinburgh, and Dublin Philosophical Magazine and Journal of Science*, 50(332):337–348, 1875.

[9] J. Kerr. XLIII. On rotation of the plane of polarization by reflection from the pole of a magnet. *The London, Edinburgh, and Dublin Philosophical Magazine and Journal of Science*, 3(19):321–343, 1877.

[10] C. Christiansen. Untersuchungen über die optischen eigenschaften von fein vertheilten körpern. *Annalen der Physik*, 259(10):298–306, 1884.

[11] C. Christiansen. Untersuchungen über die optischen eigenschaften von fein vertheilten körpern. *Annalen der Physik*, 260(3):439–446, 1885.

[12] A. Cotton. Recherches sur l'absorption et la dispersion de la lumière par les milieux doués du pouvoir rotatoire. *Journal de Physique Théorique et Appliquée*, 5(1):237–244, 1896.

[13] P. Zeeman. The effect of magnetisation on the nature of light emitted by a substance. *Nature*, 55(1424):347, 1897.

[14] A. Righi. Sur l'absorption de la lumière pars un corps placé dans un champ magnétique. *Comptes Rendus de l'Académie des Sciences (Paris)*, 127, 1898.

[15] A. Righi. Note: Sur l'absorption de la lumière pars un corps placé dans un champ magnétique. *Comptes Rendus de l'Académie des Sciences (Paris)*, 128, 1899.

[16] D. Macaluso and O. M. Corbino. Sopra una nuova azione che la luce subisce attraversando alcuni vapori metallici in un campo magnetico. *Il Nuovo Cimento*, 8(1):257–258, 1898.

[17] W. Voigt. Doppelbrechung von im Magnetfelde befindlichem Natriumdampf in der Rischtung normal zu den Kraftlinien. *Nachrichten von der Gesellschaft der Wissenschaften zu Göttingen, Mathematisch-Physikalische Klasse*, pages 355–359, 1898.

[18] W. Voigt. Zur Theorie der magneto-optischen Erscheinungen. *Annalen der Physik*, 303(2):345–365, 1899.

[19] F. Pockels. Electro-Optisches Verhalten Piezoelektrisher Kristalle. *Goettingen Abhandlungen*, 39, 1894.

[20] A. Cotton and H. Mouton. Sur la biréfringence magnétique. Nouveaux liquides actifs. *Comptes Rendus de l'Académie des Sciences*, 141:349–351, 1905.

[21] I. Gerhardt. How anomalous is my Faraday filter? *Optics Letters*, 43(21):5295–5298, 2018.

[22] D. Uhland, H. Dillmann, Y. Wang, and I. Gerhardt. How to build an optical filter with an atomic vapor cell. *arXiv Preprint*, 2305.00570, 2023.

[23] W. Gerlach and O. Stern. Der experimentelle Nachweis der Richtungsquantelung im Magnetfeld. *Zeitschrift für Physik*, 9(1):349–352, 1922.

[24] M. Bauer. The Stern-Gerlach Experiment, Translation of: "Der experimentelle Nachweis der Richtungsquantelung im Magnetfeld". *arXiv preprint*, 2301.11343, 2023.

[25] E. V. Raevsky and V. L. Pavlovitch. Stabilizing the output of a Pockels cell Q-switched Nd: YAG laser. *Optical Engineering*, 38(11):1781–1784, 1999.

[26] H. Jelínková, J. Šulc, P. Koranda, M. Němec, M. Čech, M. Jelínek, and V. Škoda. LiNbO3 Pockels cell for Q-switch of Er: YAG laser. *Laser Physics Letters*, 1(2):59, 2004.

[27] M. Skorczakowski, J. Swiderski, W. Pichola, P. Nyga, A. Zajac, M. Maciejewska, L. Galecki, J. Kasprzak, S. Gross, A. Heinrich, et al. Mid-infrared

Q-switched Er: YAG laser for medical applications. *Laser Physics Letters*, 7(7):498, 2010.

[28] S. Mittal, K. Arvind, Laxmiprasad A. S., and Pruthvi S. S. Design and development of Pockels cell driver for Q switch LASER in space applications. *IETE Journal of Research*, 63(5):694–699, 2017.

[29] C. Zhao, Z. Bai, Y. Chen, Y. Qi, J. Ding, S. Li, X. Yan, Y. Wang, and Z. Lu. A pulse-width adjustable electro-optic Q-switched nanosecond laser oscillator. *Microwave and Optical Technology Letters*, 64(12):2239–2243, 2022.

[30] S. Kinoshita, H. Ozawa, Y. Kanematsu, I. Tanaka, N. Sugimoto, and S. Fujiwara. Efficient optical Kerr shutter for femtosecond time-resolved luminescence spectroscopy. *Review of Scientific Instruments*, 71(9):3317–3322, 2000.

[31] B. Schmidt, S. Laimgruber, W. Zinth, and P. Gilch. A broadband kerr shutter for femtosecond fluorescence spectroscopy. *Applied Physics B*, 76:809–814, 2003.

[32] F. Chen, J. Cheng, S. Dai, and Q. Nie. Z-scan and optical Kerr shutter studies of silver nanoparticles embedded bismuthate glasses. *Journal of Non-Crystalline Solids*, 377:151–154, 2013.

[33] H. Purwar, S. Idlahcen, C. Rozé, D. Sedarsky, and J. Blaisot. Collinear, two-color optical Kerr effect shutter for ultrafast time-resolved imaging. *Optics Express*, 22(13):15778–15790, 2014.

[34] K. Xie, J. Li, H. Jiang, and N. Goddard. A Christiansen filter realized with a cylindrical lens. *Journal of Optics*, 12(6):065403, 2010.

[35] K. Xie, D. Ma, J. Ma, L. Liang, D. Wei, X. Wang, M. Wang, Z. Hu, J. Zhang, and Q. Mao. Christiansen filters realized with cylindrical lenses of even symmetry. *JOSA A*, 39(3):431–439, 2022.

[36] O. Burdukova, V. Petukhov, and Y. Senatsky. Lasing in a medium with the properties of a Christiansen filter. *Optics Letters*, 45(12):3236–3239, 2020.

[37] J. Li, K. Xie, H. Jiang, and N. Goddard. Christiansen filters realized with spherical lenses. *Applied Optics*, 49(8):1201–1209, 2010.

[38] R. Ye, X. Wu, and M. Yin. Laser pulse reshaping with spectral scanning filtering based on optical Kerr effect. *Optik*, 157:382–387, 2018.

[39] K Balasubramanian, M. R. Jacobson, and H. A. MacLeod. New Christiansen filters. *Applied Optics*, 31(10):1574–1587, 1992.

[40] Y. Öhman. On some new auxilliary instruments in astrophysical research. *Stockholm Obs. Ann.*, 19(4):3–14, 1956.

[41] B. Lyot. Optical apparatus with wide field using interference of polarized light. *Comptes Rendus de l'Académie des Sciences (Paris)*, 197, 1933.

[42] B. Lyot. Le filtre monochromatique polarisant et ses applications en physique solaire. *Annales d'Astrophysique*, 7(1-2):31–79, 1944.

[43] Y. Öhman. A new monochromator. *Nature*, 141(3560):157–158, 1938.

[44] J. W. Evans. The birefringent filter. *JOSA*, 39(3):229–242, 1949.

[45] A. Gorman, D. W. Fletcher-Holmes, and A. R. Harvey. Generalization of the Lyot filter and its application to snapshot spectral imaging. *Optics Express*, 18(6):5602–5608, 2010.

[46] I. Šolc. A new kind of double refracting filter. *Czechoslovak Journal of Physics*, 4(1):65–66, 1954.

[47] I. Šolc. Chain bi-refringent filters. *Czechoslovak Journal of Physics*, 9(2):237–249, 1959.

[48] I. Šolc. Birefringent chain filters. *JOSA*, 55(6):621–625, 1965.

[49] J. W. Evans. Solc birefringent filter. *JOSA*, 48(3):142–145, 1958.

[50] J. Leroy. Solc elements in Lyot-Ohman filters. *Journal of Optics*, 11(5):293, 1980.

[51] D. C. Morton and J. D. Purcell. Observations of the extreme ultraviolet radiation in the night sky using an atomic hydrogen filter. *Planetary and Space Science*, 9(8):455–458, 1962.

[52] I. F. Silvera and J. T. M. Walraven. The Stabilization of Monoatomic Hydrogen-a New Bose Gas. *Europhysics News*, 11(5):9–10, 1980.

[53] Z. Yan, C. Mou, Z. Zhang, X. Wang, J. Li, K. Zhou, and L. Zhang. Single polarization, dual wavelength fiber laser based on a 3-stage all fiber lyot filter. *IEEE Photonics Technology Letters*, 26(11):1085–1088, 2014.

[54] J. Ge, H. Feng, G. Scott, and M. P. Fok. High-speed tunable microwave photonic notch filter based on phase modulator incorporated Lyot filter. *Optics Letters*, 40(1):48–51, 2015.

[55] R. V. Drobyshev, I. A. Lobach, and S. I. Kablukov. Narrow-linewidth self-sweeping fiber laser with scanning range control by a tunable lyot filter. *Laser Physics*, 29(10):105104, 2019.

[56] F. Yang and J. R. Sambles. Microwave liquid crystal wavelength selector. *Applied Physics Letters*, 79(22):3717–3719, 2001.

[57] T. D. Drysdale, I. S. Gregory, C. Baker, E. H. Linfield, W. R. Tribe, and D. R. S. Cumming. Transmittance of a tunable filter at terahertz frequencies. *Applied Physics Letters*, 85(22):5173–5175, 2004.

[58] H. Němec, P. Kužel, L. Duvillaret, A. Pashkin, M. Dressel, and M. T. Sebastian. Highly tunable photonic crystal filter for the terahertz range. *Optics Letters*, 30(5):549–551, 2005.

[59] C. Chen, C. Pan, C. Hsieh, Y. Lin, and . Pan. Liquid-crystal-based terahertz tunable Lyot filter. *Applied Physics Letters*, 88(10):101107, 2006.

[60] R. Mendis, A. Nag, F. Chen, and D. M. Mittleman. A tunable universal terahertz filter using artificial dielectrics based on parallel-plate waveguides. *Applied Physics Letters*, 97(13):131106, 2010.

[61] I. Abdulhalim. Liquid crystal devices tailored for specific imaging applications. *SPIE Newsroom*, 5th Sep. 2014.

[62] S. Li, H. Liu, Q. Sun, and N. Huang. A tunable terahertz photonic crystal narrow-band filter. *IEEE Photonics Technology Letters*, 27(7):752–754, 2015.

[63] S. Zarei. A design to tune the frequency in a terahertz filter based on dual-layered metallic slit arrays. *Photonics and Nanostructures-Fundamentals and Applications*, 34:5–10, 2019.

[64] C. R. Higgins, D. Pizzey, R. S. Mathew, and I. G. Hughes. Atomic line versus lens cavity filters: a comparison of their merits. *OSA Continuum*, 3(4):961–970, 2020.

[65] Y. Kong, Y. Wang, L. Zhang, and Y. Fang. A quartz birefringent filter insensitive to incident angle. *Optics & Laser Technology*, 44(5):1497–1500, 2012.

[66] A. K. Kaveev, G. I. Kropotov, D. I. Tsypishka, I. A. Tzibizov, I. A. Vinerov, and E. G. Kaveeva. Tunable wavelength terahertz polarization converter based on quartz waveplates. *Applied Optics*, 53(24):5410–5415, 2014.

[67] V. I. Skomorovsky, G. I. Kushtal, and L. S. Tokareva. Šolc filter in optically active anisotropic crystal slabs. *Optik*, 245:167655, 2021.

[68] K. Özgören and F. Ö. İlday. All-fiber all-normal dispersion laser with a fiber-based Lyot filter. *Optics Letters*, 35(8):1296–1298, 2010.

[69] Z. Xing, X. Guo, H. Qin, W. Zhang, Q. Sun, K. Zhou, Z. Yan, D. Liu, and L. Zhang. A simple all-fiber Solc filter based on 45°-tilted fiber gratings. *IEEE Photonics Technology Letters*, 31(20):1631–1634, 2019.

[70] R. H. Chu and J. J. Zou. Transverse strain sensing based on optical fibre solc filter. *Optical Fiber Technology*, 16(3):151–155, 2010.

[71] M. V. Balabas, A. O. Sushkov, and D. Budker. Rubidium 'whiskers' in a vapour cell. *Nature Physics*, 3(1):2–2, 2007.

[72] A. Sargsyan, A. Amiryan, A. Tonoyan, E. Klinger, and D. Sarkisyan. Circular dichroism in atomic vapors: magnetically induced transitions responsible for two distinct behaviors. *Physics Letters A*, 390:127114, 2021.

[73] P. Gádoros, A. Czitrovszky, A. Nagy, R. Holomb, L. Kocsányi, and M. Veres. Laser cleaning and Raman analysis of the contamination on the optical window of a rubidium vapor cell. *Scientific Reports*, 12(1):15530, 2022.

[74] D. Pan, X. Xue, H. Shang, B. Luo, J. Chen, and H. Guo. Hollow cathode lamp based Faraday anomalous dispersion optical filter. *Scientific Reports*, 6(1):1–6, 2016.

[75] L. Shen, R. Ma, L. Yin, B. Luo, D. Pan, S. Yu, J. Chen, and H. Guo. A Faraday anomalous dispersion optical filter based on rubidium hollow-cathode lamp. *Applied Sciences*, 10(20):7075, 2020.

[76] B. Luo, R. Ma, Q. Ji, L. Yin, J. Chen, and H. Guo. Thermal and temporal characteristics of Faraday anomalous dispersion optical filters based on a hollow cathode lamp. *Optics Letters*, 46(21):5372–5375, 2021.

[77] A. Cacciani and M. Fofi. The magneto-optical filter: II. Velocity field measurements. *Solar Physics*, 59:179–189, 1978.

[78] A. Cacciani, D. Ricci, P. Rosati, E. J. Rhodes, E. Smith, S. Tomczyk, and R. K. Ulrich. Solar magnetic fields measurements with a magneto-optical filter. *Il Nuovo Cimento C*, 13(1):125–130, 1990.

[79] A. Cacciani and M. Fofi. The magneto-optical filter. *Solar Physics*, 59(1):179–189, 1978.

[80] A. Cacciani, J. Varsik, and H. Zirin. Observations of vector magnetic fields with a magneto-optic filter. *Solar Physics*, 125(1):173–178, 1990.

[81] R. Erdélyi, M. B. Korsós, X. Huang, et al. The Solar Activity Monitor Network - SAMNet. *Journal of Space Weather and Space Climate*, 12:2, 2022.

[82] R. Speziali, A. Di Paola, M. Centrone, M. Oliviero, D. B. Calia, L. Dal Sasso, M. Faccini, V. Mauriello, and L. Terranegra. The first light of the Solar Activity MOF Monitor Telescope (SAMM). *Journal of Space Weather and Space Climate*, 11:22, 2021.

[83] R. Launay. Solar storms and their impacts on power grids recommendations for (re)insurers. *SCOR Papers*, 28, 2014.

[84] J. Brossel and F. Bitter. A New "Double Resonance" Method for Investigating Atomic Energy Levels. Application to Hg P 1 3. *Physical Review*, 86(3):308, 1952.

[85] F. Bitter, S. P. Davis, B. Richter, and J. E. R. Young. Optical studies of radioactive mercury. *Physical Review*, 96:1531–1539, Dec 1954.

[86] M. N. McDermott and W. L. Lichten. Hyperfine Structure of the 6^3P_2 State of Hg 199 80 and Hg 201 80. Properties of Metastable States of Mercury. *Physical Review*, 119(1):134, 1960.

[87] R. H. Garstang. Hyperfine structure and intercombination line intensities in the spectra of magnesium, zinc, cadmium, and mercury. *JOSA*, 52(8):845–851, 1962.

[88] W. R. C. Rowley. The definition of the metre: from polar quadrant to the speed of light. *Physics Bulletin*, 35(7):282, 1984.

[89] J. L. Hall. Learning from the time and length redefinitions, and the metre demotion. *Philosophical Transactions of the Royal Society A: Mathematical, Physical and Engineering Sciences*, 369(1953):4090–4108, 2011.

[90] C. V. Jackson. Wave-length standards in the first spectrum of krypton. *Philosophical Transactions of the Royal Society of London. Series A, Mathematical and Physical Sciences*, 236(758):1–24, 1936.

[91] T. A. Littlefield. Krypton vacuum wave-length measurements. *Proceedings of the Royal Society of London. Series A. Mathematical and Physical Sciences*, 187(1009):220–228, 1946.

[92] H. Barrell. Eleventh general conference of weights and measures, 1961.

[93] C. F. Bruce and R. M. Hill. Wavelengths of krypton 86, mercury 198, and cadmium 114. *Australian Journal of Physics*, 14(1):64–88, 1961.

[94] K. G. Kessler and W. G. Schweitzer. Zeeman-Split Absorption Lines as Very Narrow Pass Filters. *JOSA*, 49(2):199–199, 1959.

[95] W. G. Schweitzer. Hyperfine structure and isotope shifts in the 2537-A line of mercury. *JOSA*, 51(6):692_1–693, 1961.

[96] W. G. Schweitzer and K. G. Kessler. Wavelength of Hg 198 Zeeman Filter Relative to that of the 2537-Å Absorption Line of an Atomic Beam. *JOSA*, 53(12):1382–1388, 1963.

[97] K. G. Kessler and W. G. Schweitzer. Zeeman filter. *JOSA*, 55(3):284–288, 1965.

[98] E. B. Aleksandrov. Modulation and filtration of resonance radiation with the use of the Faraday effect. *Optics and Spectroscopy*, 19:455–457, 1965.

[99] B. M. Schmidt, J. M. Williams, and D. Williams. Magneto-Optic Modulation of a Light Beam in Sodium Vapor. *JOSA*, 54(4):454–459, 1964.

[100] R. L. Fork and L. C. Bradley. Dispersion in the vicinity of an optical resonance. *Applied Optics*, 3(1):137–142, 1964.

[101] W. Hanle. Die trägheitslosigkeit des diamagnetischen faradayeffekts. *Zeitschrift für Physik*, 85(5-6):304–309, 1933.

[102] T. H Maiman et al. Stimulated optical radiation in Ruby. *Nature*, 187(4736):493–494, 1960.

[103] P. P. Sorokin and M. J. Stevenson. Stimulated infrared emission from trivalent uranium. *Physical Review Letters*, 5(12):557, 1960.

[104] T. H. Maiman, R. H. Hoskins, I. J. D'Haenens, C. K. Asawa, and V. Evtuhov. Stimulated optical emission in fluorescent solids. II. Spectroscopy and stimulated emission in Ruby. *Physical Review*, 123(4):1151, 1961.

[105] A. Javan, W. R. Bennett, and D. R. Herriott. Population inversion and continuous optical maser oscillation in a gas discharge containing a He-Ne mixture. *Physical Review Letters*, 6(3):106, 1961.

[106] J. E. Geusic, H. M. Marcos, and L. Van Uitert. Laser oscillations in Nd-doped yttrium aluminum, yttrium gallium and gadolinium garnets. *Applied Physics Letters*, 4(10):182–184, 1964.

[107] P. P. Sorokin, J. R. Lankard, V. L. Moruzzi, and A. Lurio. Frequency-locking of organic dye lasers to atomic resonance lines. *Applied Physics Letters*, 15(6):179–181, 1969.

[108] T. Endo, T. Yabuzaki, M. Kitano, T. Sato, and T. Ogawa. Frequency-locking of a CW dye laser to the center of the sodium D lines by a Faraday filter. *IEEE Journal of Quantum Electronics*, 13(10):866–871, 1977.

[109] T. Endo, T. Yabuzaki, M. Kitano, T. Sato, and T. Ogawa. Frequency-locking of a CW dye laser to absorption lines of neon by a Faraday filter. *IEEE Journal of Quantum Electronics*, 14(12):977–982, 1978.

[110] K. Choi, J. Menders, P. Searcy, and E. Korevaar. Optical feedback locking of a diode laser using a cesium Faraday filter. *Optics Communications*, 96(4-6):240–244, 1993.

[111] H. Tang, H. Zhao, R. Wang, L. Li, Z. Yang, H. Wang, W. Yang, K. Han, and X. Xu. 18W ultra-narrow diode laser absolutely locked to the Rb D2 line. *Optics Express*, 29(23):38728–38736, 2021.

[112] X. Miao, L. Yin, W. Zhuang, B. Luo, A. Dang, J. Chen, and H. Guo. Note: Demonstration of an external-cavity diode laser system immune to current and temperature fluctuations. *Review of Scientific Instruments*, 82(8):086106, 2011.

[113] Z. Tao, Y. Hong, B. Luo, J. Chen, and H. Guo. Diode laser operating on an atomic transition limited by an isotope 87 Rb Faraday filter at 780 nm. *Optics Letters*, 40(18):4348–4351, 2015.

[114] Z. Jiang, Q. Zhou, Z. Tao, X. Zhang, S. Zhang, C. Zhu, P. Lin, and J. Chen. Diode laser using narrow bandwidth interference filter at 852 nm and its application in Faraday anomalous dispersion optical filter. *Chinese Physics B*, 25(8):083201, 2016.

[115] J. Keaveney, W. J. Hamlyn, C. S. Adams, and I. G. Hughes. A single-mode external cavity diode laser using an intra-cavity atomic Faraday filter with short-term linewidth < 400 kHz and long-term stability of < 1 MHz. *Review of Scientific Instruments*, 87(9):095111, 2016.

[116] P. Chang, H. Peng, S. Zhang, Z. Chen, B. Luo, J. Chen, and H. Guo. A Faraday laser lasing on Rb 1529 nm transition. *Scientific Reports*, 7(1):8995, 2017.

[117] P. Chang, Y. Chen, H. Shang, X. Guan, H. Guo, J. Chen, and B. Luo. A Faraday laser operating on Cs 852 nm transition. *Applied Physics B*, 125(12):230, 2019.

[118] T. Shi, X. Guan, P. Chang, J. Miao, D. Pan, B. Luo, H. Guo, and J. Chen. A dual-frequency Faraday laser. *IEEE Photonics Journal*, 12(4):1–11, 2020.

[119] H. Tang, H. Zhao, D. Zhang, L. Li, W. Yang, Z. Yang, H. Wang, X. Xu, et al. Polarization insensitive efficient ultra-narrow diode laser strictly locked by a Faraday filter. *Optics Express*, 30(16):29772–29780, 2022.

[120] D. J. Bradley, G. M. Gale, M. Moore, and P. D. Smith. Longitudinally pumped, narrow-band continuously tunable dye laser. *Physics Letters A*, 26(8):378–379, 1968.

[121] S. W. Corzine, R. S. Geels, J. W. Scott, R. Yan, and L. A. Coldren. Design of Fabry-Perot surface-emitting lasers with a periodic gain structure. *IEEE Journal of Quantum Electronics*, 25(6):1513–1524, 1989.

[122] J. Javaloyes and S. Balle. Mode-locking in semiconductor Fabry-Pérot lasers. *IEEE Journal of Quantum Electronics*, 46(7):1023–1030, 2010.

[123] L. D. Turner, V. Karaganov, P. J. O. Teubner, and R. E. Scholten. Sub-doppler bandwidth atomic optical filter. *Optics Letters*, 27(7):500–502, 2002.

[124] W. Zhuang, Y. Zhao, S. Wang, Z. Fang, F. Fang, and T. Li. Ultranarrow bandwidth Faraday atomic filter approaching natural linewidth based on cold atoms. *Chinese Optics Letters*, 19(3):030201, 2021.

[125] W. Zhuang and J. Chen. Active Faraday optical frequency standard. *Optics Letters*, 39(21):6339–6342, 2014.

[126] Z. Tao, X. Zhang, D. Pan, M. Chen, C. Zhu, and J. Chen. Faraday laser using 1.2 km fiber as an extended cavity. *Journal of Physics B: Atomic, Molecular and Optical Physics*, 49(13):13LT01, 2016.

[127] Z. Tao, X. Zhang, M. Chen, Z. Liu, C. Zhu, Z. Liu, and J. Chen. Cs 728 nm excited state faraday anomalous dispersion optical filter with indirect pump. *Physics Letters A*, 380(25-26):2150–2153, 2016.

[128] P. Chang, H. Shi, J. Miao, T. Shi, D. Pan, B. Luo, H. Guo, and J. Chen. Frequency-stabilized Faraday laser with 10^{-14} short-term instability for atomic clocks. *Applied Physics Letters*, 120(14):141102, 2022.

[129] Y. Yan, J. Yuan, L. Wang, L. Xiao, and S. Jia. A dual-wavelength bandpass Faraday anomalous dispersion optical filter operating on the D1 and D2 lines of rubidium. *Optics Communications*, 509:127855, 2022.

[130] Y. Yan, J. Yuan, L. Wang, L. Xiao, and S. Jia. Tailoring the pulse train of an optical frequency comb with a magnetized atomic medium. *Laser Physics Letters*, 19(10):105207, 2022.

[131] J. M. Beckers. Narrow band filters based on magnetooptical effects. *Applied Optics*, 9(3):595–599, 1970.

[132] A. Cacciani, D. Ricci, P. Rosati, E. J. Rhodes, E. Smith, S. Tomczyk, and R. K. Ulrich. Solar magnetic fields measurements with a magneto-optical filter. *Il Nuovo Cimento C*, 13:125–130, 1990.

[133] A. Cacciani, J. Varsik, and H. Zirin. Observations of vector magnetic fields with a magneto-optic filter. *Solar Physics*, 125:173–178, 1990.

[134] S. Tomczyk, K. Streander, G. Card, D. Elmore, H. Hull, and A. Cacciani. An instrument to observe low-degree solar oscillations. *Solar Physics*, 159:1–21, 1995.

[135] J. B. Marling, J. Nilsen, L. C. West, and L. L. Wood. An ultrahigh-Q isotropically sensitive optical filter employing atomic resonance transitions. *Journal of Applied Physics*, 50(2):610–614, 1979.

[136] J. A. Zielińska, F. A. Beduini, N. Godbout, and M. W. Mitchell. Ultranarrow Faraday rotation filter at the Rb D1 line. *Optics Letters*, 37(4):524–526, 2012.

[137] M. A. Zentile, D. J. Whiting, J. Keaveney, C. S. Adams, and I. G. Hughes. Atomic Faraday filter with equivalent noise bandwidth less than 1 GHz. *Optics Letters*, 40(9):2000–2003, 2015.

[138] P. Yeh. Dispersive birefringent filters. *Optics Communications*, 37(3):153–158, 1981.

[139] P. Yeh. Dispersive magnetooptic filters. *Applied Optics*, 21(11):2069–2075, 1982.

[140] P. Yeh. Zero crossing birefringent filters. *Optics Communications*, 35(1):15–19, 1980.

[141] P. Yeh. Christiansen-bragg filters. *Optics Communications*, 35(1):9–14, 1980.

[142] B. Yin and T. M. Shay. A potassium Faraday anomalous dispersion optical filter. *Optics Communications*, 94(1-3):30–32, 1992.

[143] L. Zhang and J. Tang. Experimental study on optimization of the working conditions of excited state Faraday filter. *Optics Communications*, 152(4-6):275–279, 1998.

[144] Y. Zhang, X. Jia, Z. Ma, and Q. Wang. Potassium Faraday optical filter in line-center operation. *Optics Communications*, 194(1-3):147–150, 2001.

[145] B. Yin and T. M. Shay. Theoretical model for a Faraday anomalous dispersion optical filter. *Optics Letters*, 16(20):1617–1619, 1991.

[146] J. Menders, K Benson, S. H. Bloom, C. S. Liu, and E. Korevaar. Ultranarrow line filtering using a Cs Faraday filter at 852 nm. *Optics Letters*, 16(11):846–848, 1991.

[147] B. Yin and T. M. Shay. Faraday anomalous dispersion optical filter for the Cs 455 nm transition. *IEEE photonics technology letters*, 4(5):488–490, 1992.

[148] J. Menders, P. Searcy, K. Roff, and E. Korevaar. Blue cesium Faraday and Voigt magneto-optic atomic line filters. *Optics Letters*, 17(19):1388–1390, 1992.

[149] Z. Yun-Dong, J. Xiao-Ling, B. Yong, M. Zu-Guang, and W. Qi. Filter performance of a cesium Faraday optical filter at 852 nm. *Chinese Physics Letters*, 19(6):807–809, 2002.

[150] H. Chen, C. She, P. Searcy, and E. Korevaar. Sodium-vapor dispersive Faraday filter. *Optics Letters*, 18(12):1019–1021, 1993.

[151] S. D. Harrell, C. Y. She, T. Yuan, D. A. Krueger, H. Chen, S. S. Chen, and Z. L. Hu. Sodium and potassium vapor Faraday filters revisited: theory and applications. *JOSA B*, 26(4):659–670, 2009.

[152] D. J. Dick and T. M. Shay. Ultrahigh-noise rejection optical filter. *Optics Letters*, 16(11):867–869, 1991.

[153] Z. Hu, X. Sun, X. Zeng, Y. Peng, J. Tang, L. Zhang, Q. Wang, and L. Zheng. Rb 780 nm Faraday anomalous dispersion optical filter in a strong magnetic field. *Optics Communications*, 101(3-4):175–178, 1993.

[154] B. Yin, L. S. Alvarez, and T. M. Shay. The Rb 780-nanometer Faraday anomalous dispersion optical filter: theory and experiment. *JPL, The Telecommunications and Data Acquisition Report*, 1994.

[155] M. A. Zentile, J. Keaveney, L. Weller, D. J. Whiting, C. S. Adams, and I. G. Hughes. ElecSus: A program to calculate the electric susceptibility of an atomic ensemble. *Computer Physics Communications*, 189:162–174, 2015.

[156] J. Keaveney, C. S. Adams, and I. G Hughes. ElecSus: Extension to arbitrary geometry magneto-optics. *Computer Physics Communications*, 224:311–324, 2018.

[157] S. Rochester. Linear Absorption Fitting (Atomic Density Matrix). https://www.rochesterscientific.com/ADM/AtomicDensityMatrix/tutorial/LinearAbsorptionFitting.html, 2020. accessed: 07-02-23.

[158] S. Rochester. Atomic Density Matrix. https://www.rochesterscientific.com/ADM/, 2020. accessed: 07-02-23.

[159] Wolfram Research, Inc. Mathematica, Version 13.2. Champaign, IL, 2022.

[160] G. Di Domenico and A. Weis. Spectra of the D-Lines of Alkali Vapors (Mathematica Package). https://demonstrations.wolfram.com/SpectraOfTheDLinesOfAlkaliVapors/, 2011. accessed: 07-02-23.

[161] G. Di Domenico and A. Weis. Vapor Pressure and Density of Alkali Metal (Mathematica Package). https://demonstrations.wolfram.com/VaporPressureAndDensityOfAlkaliMetals/, 2011. accessed: 07-02-23.

[162] R. I. Billmers, S. K. Gayen, M. F. Squicciarini, V. M. Contarino, W. J. Scharpf, and D. M. Allocca. Experimental demonstration of an excited-state Faraday filter operating at 532 nm. *Optics Letters*, 20(1):106–108, 1995.

[163] Y. Peng. Transmission characteristics of an excited-state Faraday optical filter at 532 nm. *Journal of Physics B: Atomic, Molecular and Optical Physics*, 30(22):5123–5129, 1997.

[164] L. Yin, B. Luo, J. Xiong, and H. Guo. Tunable rubidium excited state Voigt atomic optical filter. *Optics Express*, 24(6):6088–6093, 2016.

[165] Y. Wang, X. Zhang, D. Wang, Z. Tao, W. Zhuang, and J. Chen. Cs Faraday optical filter with a single transmission peak resonant with the atomic transition at 455 nm. *Optics Express*, 20(23):25817–25825, 2012.

[166] J. Xiong, L. Yin, B. Luo, and H. Guo. Analysis of excited-state Faraday anomalous dispersion optical filter at 1529 nm. *Optics Express*, 24(13):14925–14933, 2016.

[167] T. Jeong, I. Bae, and H. S. Moon. Noise filtering via electromagnetically induced transparency. *Optics Communications*, 383:31–35, 2017.

[168] G. Wang, Y. Wang, E. K. Huang, W. Hung, K. Chao, P. Wu, Y. Chen, and I. A. Yu. Ultranarrow-bandwidth filter based on a thermal EIT medium. *Scientific Reports*, 8(1):7959, 2018.

[169] B. E. Sherlock and I. G. Hughes. How weak is a weak probe in laser spectroscopy? *American Journal of Physics*, 77(2):111–115, 2009.

[170] B. Luo, L. Yin, J. Xiong, J. Chen, and H. Guo. Signal intensity influences on the atomic Faraday filter. *Optics Letters*, 43(11):2458–2461, 2018.

[171] V. Marshall. Experimental studies of the D2 line of 87 Rb vapour at 1.5 Tesla. Master's thesis, Durham University, 2017.

[172] R. Bala, J. Ghosh, and V. Venkataraman. A comprehensive model for doppler spectra in thermal atomic vapour. *Journal of Physics B: Atomic, Molecular and Optical Physics*, 55(16):165003, 2022.

[173] A. P. Yalin and R. B. Miles. Ultraviolet filtered Rayleigh scattering temperature measurements with a mercury filter. *Optics Letters*, 24(9):590–592, 1999.

[174] A. P. Yalin and R. B. Miles. Temperature measurements by ultraviolet filtered rayleigh scattering using a mercury filter. *Journal of Thermophysics and Heat Transfer*, 14(2):210–215, 2000.

[175] W. Rodgers, N. Murphy, and S. M. Jefferies. A calcium-based magneto-optical filter. In *AGU Spring Meeting Abstracts*, 2005.

[176] J. A. Zielińska, F. A. Beduini, V. G. Lucivero, and M. W. Mitchell. Atomic filtering for hybrid continuous-variable/discrete-variable quantum optics. *Optics Express*, 22(21):25307–25317, 2014.

[177] S. L. Portalupi, M. Widmann, C. Nawrath, M. Jetter, P. Michler, J. Wrachtrup, and I. Gerhardt. Simultaneous Faraday filtering of the Mollow triplet sidebands with the Cs-D1 clock transition. *Nature Communications*, 7(1):13632, 2016.

[178] W. Kiefer, M. Rezai, J. Wrachtrup, and I. Gerhardt. An atomic spectrum recorded with a single-molecule light source. *Applied Physics B*, 122:1–12, 2016.

[179] M. Widmann, S. L. Portalupi, P. Michler, J. Wrachtrup, and I. Gerhardt. Faraday filtering on the Cs-D1-line for quantum hybrid systems. *IEEE Photonics Technology Letters*, 30(24):2083–2086, 2018.

[180] L. Yin, D. Qian, Z. Geng, H. Zhan, and G. Wu. Using FADOF to eliminate the background light influence in ghost imaging. *Optics Express*, 30(20):36297–36306, 2022.

[181] L. Qian, S. Zaidi, and R. Miles. Narrow linewidth potassium imaging filter for near infrared detection of missile plumes. In *43rd AIAA Aerospace Sciences Meeting and Exhibit*, page 825, 2005.

[182] M. W. Kudenov, B. Pantalone, and R. Yang. Dual-beam potassium Voigt filter for atomic line imaging. *Applied Optics*, 59(17):5282–5289, 2020.

[183] K. Wu, Y. Feng, J. Li, G. Yu, L. Liu, Y. Xiong, and F. Li. Demonstration of a mid-infrared NO molecular Faraday optical filter. *Optics Express*, 25(25):30916–30930, 2017.

[184] K. Wu, Z. Luo, Y. Feng, G. Yu, L. Liu, Y. X., and F. Li. 2D visualization of hot gas based on a mid-infrared molecular Faraday imaging filter. *Optics Letters*, 43(15):3686–3689, 2018.

[185] K. Wu, Z. Luo, Y. Feng, Y. Xiong, G. Yu, W. Duan, and F. Li. Mid-IR Faraday optical filter with an ultra-narrow single transmission peak at 5.33 μm. *Applied Physics Express*, 12(9):092008, 2019.

[186] T. Junxiong, W. Qingji, L. Yimin, Z. Liang, G. Jianhua, D. Minghao, K. Jiankun, and Z. Lemin. Experimental study of a model digital space optical communication system with new quantum devices. *Applied Optics*, 34(15):2619–2622, 1995.

[187] L. Ling and G. Bi. Isotope 87 Rb Faraday anomalous dispersion optical filter at 420 nm. *Optics Letters*, 39(11):3324–3327, 2014.

[188] G. Bi, J. Kang, J. Fu, L. Ling, and J. Chen. Ultra-narrow linewidth optical filter based on Faraday effect at isotope 87Rb 420 nm transitions. *Physics Letters A*, 380(47):4022–4026, 2016.

[189] Z. Tao, M. Chen, Z. Zhou, B. Ye, J. Zeng, and H. Zheng. Isotope 87 Rb Faraday filter with a single transmission peak resonant with atomic transition at 780 nm. *Optics Express*, 27(9):13142–13149, 2019.

[190] J. Zhang, G. Gao, B. Wang, X. Guan, L. Yin, J. Chen, and B. Luo. Background noise resistant underwater wireless optical communication using Faraday atomic line laser and filter. *Journal of Lightwave Technology*, 40(1):63–73, 2021.

[191] X. Shan, X. Sun, J. Luo, Z. Tan, and M. Zhan. Free-space quantum key distribution with Rb vapor filters. *Applied Physics Letters*, 89(19):191121, 2006.

[192] X. Guan, W. Zhuang, T. Shi, J. Miao, J. Zhang, J. Chen, and B. Luo. Cold-atom optical filtering enhanced by optical pumping. *Frontiers in Physics*, 10:1090483, 2022.

[193] X. Guan, W. Zhuang, T. Shi, J. Miao, J. Zhang, J. Chen, and B. Luo. 420-nm Faraday Optical Filter With 2.7-MHz Ultranarrow Bandwidth Based on Laser Cooled ^{87}Rb Atoms. *IEEE Photonics Technology Letters*, 35(12):672–675, 2023.

[194] W. Lin, Z. Zhou, C. Li, and G. Guo. Proposed solid-state Faraday anomalous-dispersion optical filter. *Physical Review A*, 84(5):055803, 2011.

[195] C. Fricke-Begemann, M. Alpers, and J. Höffner. Daylight rejection with a new receiver for potassium resonance temperature lidars. *Optics Letters*, 27(21):1932–1934, 2002.

[196] J. Höffner and C. Fricke-Begemann. Accurate lidar temperatures with narrowband filters. *Optics Letters*, 30(8):890–892, 2005.

[197] S. D. Harrell, C. She, T. Yuan, D. A. Krueger, J. M. C. Plane, and T. Slanger. The Faraday filter-based spectrometer for observing sodium nightglow and studying atomic and molecular oxygen associated with the sodium chemistry in the mesopause region. *Journal of Atmospheric and Solar-terrestrial Physics*, 72(17):1260–1269, 2010.

[198] Y. Yong, C. Xuewu, L. Faquan, H. Xiong, L. Xin, and G. Shunsheng. A flat spectral Faraday filter for sodium lidar. *Optics Letters*, 36(7):1302–1304, 2011.

[199] T. Pan, T. Chen, D. Sun, Y. Han, X. Xue, R. Zhao, and J. Lan. Metastable helium faraday filter for helium lidar to measure the density of the thermosphere. *Optics Express*, 29(3):4431–4441, 2021.

[200] S. H. Bloom, P. A. Searcy, K. Choi, R. Kremer, and E. Korevaar. Helicopter plume detection by using an ultranarrow-band noncoherent laser Doppler velocimeter. *Optics Letters*, 18(3):244–246, 1993.

[201] H. Chen, M. A. White, D. A. Krueger, and C. Y. She. Daytime mesopause temperature measurements with a sodium-vapor dispersive Faraday filter in a lidar receiver. *Optics Letters*, 21(15):1093–1095, 1996.

[202] Z. Hu, X. Sun, Y. Liu, L. Fu, and X. Zeng. Temperature properties of Na dispersive Faraday optical filter at D1 and D2 line. *Optics Communications*, 156(4-6):289–293, 1998.

[203] F Vargas, A Liu, G Swenson, C Segura, P Vega, J Fuentes, D Pautet, M Taylor, Y Zhao, Y Morton, et al. Mesosphere and lower thermosphere changes associated with the July 2, 2019 total eclipse in South America over the Andes Lidar Observatory, Cerro Pachon, Chile. *Journal of Geophysical Research: Atmospheres*, 127(11):e2021JD035064, 2022.

[204] Y. Xia, X. Cheng, F. Li, Y. Yang, X. Lin, J. Jiao, L. Du, J. Wang, and G. Yang. Sodium lidar observation over full diurnal cycles in Beijing, China. *Applied Optics*, 59(6):1529–1536, 2020.

[205] A. Popescu and T. Walther. On the potential of Faraday anomalous dispersion optical filters as high-resolution edge filters. *Laser Physics*, 15(1):55–60, 2005.

[206] A. Popescu, D. Walldorf, K. Schorstein, and T. Walther. On an excited state Faraday anomalous dispersion optical filter at moderate pump powers for a Brillouin-lidar receiver system. *Optics Communications*, 264(2):475–481, 2006.

[207] M. D. Rotondaro, B. V. Zhdanov, and R. J. Knize. Generalized treatment of magneto-optical transmission filters. *JOSA B*, 32(12):2507–2513, 2015.

[208] J. Keaveney, S. A. Wrathmall, C. S. Adams, and I. G. Hughes. Optimized ultra-narrow atomic bandpass filters via magneto-optic rotation in an unconstrained geometry. *Optics Letters*, 43(17):4272–4275, 2018.

[209] H. M. Gibbs and G. C. Churchill. Laser Spectroscopic Measurement of the 87 Rb–85 Rb D 1-Line Isotope Shift. *JOSA*, 62(10):1130–1133, 1972.

[210] A. Corney. *Atomic and laser spectroscopy*. Clarendon Press Oxford, 1978.

[211] A. Banerjee, D. Das, and V. Natarajan. Absolute frequency measurements of the D1 lines in 39K, 85Rb, and 87Rb with 0.1 ppb uncertainty. *Europhysics Letters*, 65(2):172, 2004.

[212] P. Siddons, C. S. Adams, C. Ge, and I. G. Hughes. Absolute absorption on rubidium D lines: comparison between theory and experiment. *Journal of Physics B: Atomic, Molecular and Optical Physics*, 41(15):155004, 2008.

[213] M. Klein, I. Novikova, D. F. Phillips, and R. L. Walsworth. Slow light in paraffin-coated Rb vapour cells. *Journal of Modern Optics*, 53(16-17):2583–2591, 2006.

[214] J. A. Sedlacek, A. Schwettmann, H. Kübler, R. Löw, T. Pfau, and J. P. Shaffer. Microwave electrometry with Rydberg atoms in a vapour cell using bright atomic resonances. *Nature Physics*, 8(11):819–824, 2012.

[215] C. J. Foot. *Atomic Physics*. OUP Oxford, 2004.

[216] M. Auzinsh, D. Budker, and S. Rochester. *Optically polarized atoms: understanding light-atom interactions*. Oxford University Press, 2010.

[217] C. R. Higgins and I. G. Hughes. Electromagnetically induced transparency in a V-system with 87Rb vapour in the hyperfine Paschen-Back regime. *Journal of Physics B: Atomic, Molecular and Optical Physics*, 54(16):165403, 2021.

[218] M. A. Zentile, R. Andrews, L. Weller, S. Knappe, C. S. Adams, and I. G. Hughes. The hyperfine Paschen–Back Faraday effect. *J. Phys. B*, 47(7):075005, 2014.

[219] A. Sargsyan, G. Hakhumyan, C. Leroy, Y. Pashayan-Leroy, A. Papoyan, and D. Sarkisyan. Hyperfine Paschen–Back regime realized in Rb nanocell. *Optics Letters*, 37(8):1379–1381, 2012.

[220] J. Keaveney, F. S. Ponciano-Ojeda, S. M. Rieche, M. J. Raine, D. P. Hampshire, and I. G. Hughes. Quantitative optical spectroscopy of 87Rb vapour in the Voigt geometry in DC magnetic fields up to 0.4 T. *Journal of Physics B: Atomic, Molecular and Optical Physics*, 52(5):055003, 2019.

[221] D. A. Steck. Rubidium 87 D line data. https://steck.us/alkalidata/rubidium87numbers.1.6.pdf, 2001.

[222] M. A. Zentile. *Applications of the Faraday effect in hot atomic vapours*. PhD thesis, Durham University, 2015.

[223] M. D. Rotondaro and G. P. Perram. Collisional broadening and shift of the rubidium D1 and D2 lines ($5^2S_{1/2}$ $\rightarrow 5^2P1/2$, $5^2P3/2$) by rare gases, H2, D2, N2, CH4 and CF4. *Journal of Quantitative Spectroscopy and Radiative Transfer*, 57(4):497–507, 1997.

[224] I. G. Hughes. Velocity selection in a Doppler-broadened ensemble of atoms interacting with a monochromatic laser beam. *Journal of Modern Optics*, 65(5-6):640–647, 2018.

[225] F. S. Ponciano-Ojeda. *Stokes polarimetry and magnetometry using a thermal Rb vapour in the Voigt geometry with large magnetic field*. PhD thesis, Durham University, 2021.

[226] D. A. Steck. Rubidium 85 D line data. https://steck.us/alkalidata/rubidium85numbers.pdf, 2008.

[227] C. A. Ebbers. Optical polarizer material. Technical report, Lawrence Livermore National Lab, Livermore, CA (United States), 1999.

[228] W. Kiefer, R. Löw, J. Wrachtrup, and I. Gerhardt. Na-Faraday rotation filtering: the optimal point. *Scientific Reports*, 4(1):1–7, 2014.

[229] R. C. Jones. A new calculus for the treatment of optical systems I. description and discussion of the calculus. *JOSA*, 31(7):488–493, 1941.

[230] D. Uhland, T. Rendler, M. Widmann, S. Lee, J. Wrachtrup, and I. Gerhardt. Single molecule DNA detection with an atomic vapor notch filter. *EPJ Quantum Technology*, 2:1–12, 2015.

[231] M. A. Hafiz, G. Coget, E. De Clercq, and R. Boudot. Doppler-free spectroscopy on the Cs D 1 line with a dual-frequency laser. *Optics letters*, 41(13):2982–2985, 2016.

[232] M. Cimino, A. Cacciani, and N. Sopranzi. A sharp band resonance absorption filter. *Applied Optics*, 7(8):1654–1655, 1968.

[233] B. Schaefer, E. Collett, R. Smyth, D. Barrett, and B. Fraher. Measuring the Stokes polarization parameters. *American Journal of Physics*, 75(2):163–168, 2007.

[234] A. Z. Goldberg, P. De La Hoz, G. Björk, A. Klimov, M. Grassl, G. Leuchs, and L. L Sánchez-Soto. Quantum concepts in optical polarization. *Advances in Optics and Photonics*, 13(1):1–73, 2021.

[235] Z. Su and J. Wang. Measuring stokes parameters by means of unitary operations. *Applied Optics*, 60(31):9852–9857, 2021.

[236] M. Ortner and L. G. C. Bandeira. Magpylib: A free Python package for magnetic field computation. *SoftwareX*, 11:100466, 2020.

[237] N. P. Smart et al. *Cryptography: an introduction*, volume 3. McGraw-Hill New York, 2003.

[238] D. J. Whiting, J. Keaveney, C. S. Adams, and G. Hughes, I. Direct measurement of excited-state dipole matrix elements using electromagnetically induced transparency in the hyperfine Paschen-Back regime. *Physical Review A*, 93(4):043854, 2016.

[239] L. Weller, K. S. Kleinbach, M. A. Zentile, S. Knappe, C. S. Adams, and I. G. Hughes. Absolute absorption and dispersion of a rubidium vapour in the hyperfine Paschen–Back regime. *J. Phys. B*, 45(21):215005, 2012.

[240] Toptica. *Diode Laser Series: DL 100*. https://wiki.kip.uni-heidelberg.de/KIPwiki/images/1/18/Toptica_DL100_Werbung.pdf If link broken, copy of pdf can be found with data for this thesis at Durham Collections.

[241] Thorlabs. *PDA36A2 SI Switchable Gain Photodetectors*. https://www.thorlabs.com/_sd.cfm?fileName=TTN135069-D02.pdf&partNumber=PDA36A2 If link broken, copy of pdf can be found with data for this thesis at Durham Collections.

[242] D. J. McCarron, I. G. Hughes, P. Tierney, and S. L. Cornish. A heated vapor cell unit for dichroic atomic vapor laser lock in atomic rubidium. *Review of Scientific Instruments*, 78(9):093106, 2007.

[243] D. Brown, B. Ma, and Z. Chen. Developments in the processing and properties of NdFeB-type permanent magnets. *Journal of Magnetism and Magnetic Materials*, 248(3):432–440, 2002.

[244] I. G. Hughes and T. P. A. Hase. *Measurements and their Uncertainties: A Practical Guide to Modern Error Analysis*. OUP, Oxford, 2010.

[245] R. S. Mathew, R. O'Donnell, D. Pizzey, and I. G. Hughes. The Raspberry Pi auto-aligner: Machine learning for automated alignment of laser beams. *Review of Scientific Instruments*, 92(1):015117, 2021.

[246] M. Jiang, H. Wu, Y. An, T. Hou, Q. Chang, L. Huang, J. Li, R. Su, and P. Zhou. Fiber laser development enabled by machine learning: review and prospect. *PhotoniX*, 3(1):16, 2022.

[247] T. G. Tiecke. Properties of Potassium. https://www.tobiastiecke.nl/archive/PotassiumProperties.pdf, 2019.

[248] D. Pizzey. Tunable homogeneous kG magnetic field production using permanent magnets. *Review of Scientific Instruments*, 92(12):123002, 2021.

[249] E. D. Palik and J. K. Furdyna. Infrared and microwave magnetoplasma effects in semiconductors. *Reports on Progress in Physics*, 33(3):1193, 1970.

[250] C. H. Papas. *Theory of electromagnetic wave propagation*. Dover Publications Inc., New York, 1989.

[251] G. Nienhuis and F. Schuller. Magneto-optical effects of saturating light for arbitrary field direction. *Optics Communications*, 151(1-3):40–45, 1998.

[252] A. Webber. Optimisation of atomic filters. Master's thesis, Durham University, 2019. Internal document: May be available upon request.

[253] H. Cheng, H. Wang, S. Zhang, P. Xin, J. Luo, and H. Liu. Electromagnetically induced transparency of ^{87}Rb in a buffer gas cell with magnetic field. *Journal of Physics B: Atomic, Molecular and Optical Physics*, 50(9):095401, 2017.

[254] A. P. Petrović, B. H. M. Smit, K. L. Fong, B. Satywali, X. Y. Tee, and C. Panagopoulos. A perpendicular field electromagnet with a 250 mm access bore. *Review of Scientific Instruments*, 92(1):015102, 2021.

[255] A. Dantan, J. Cviklinski, E. Giacobino, and M. Pinard. Spin squeezing and light entanglement in coherent population trapping. *Physical Review Letters*, 97(2):023605, 2006.

[256] L. Weller, T. Dalton, P. Siddons, C. S. Adams, and I. G. Hughes. Measuring the Stokes parameters for light transmitted by a high-density rubidium

vapour in large magnetic fields. *Journal of Physics B: Atomic, Molecular and Optical Physics*, 45(5):055001, 2012.

[257] A. Chakravarty, M. Levy, A. A. Jalali, Z. Wu, and A. M. Merzlikin. Elliptical normal modes and stop band reconfiguration in multimode birefringent one-dimensional magnetophotonic crystals. *Physical Review B*, 84(9):094202, 2011.

[258] E. Baumann, J. Chiles, I. Coddington, et al. White paper: Frequency combs for aerospace applications. *Decadal Survey on Biological and Physical Sciences (BPS) Research in Space 2023-2032*.

[259] S. D. Leifer, S. A. Diddams, et al. White paper: Optical frequency combs for space applications. *Decadal Survey on Biological and Physical Sciences (BPS) Research in Space 2023-2032*.

[260] J. Gea-Banacloche. A new look at the Jaynes-Cummings model for large fields: Bloch sphere evolution and detuning effects. *Optics Communications*, 88(4-6):531–550, 1992.

[261] T. Lu, X. Miao, and H. Metcalf. Bloch theorem on the Bloch sphere. *Physical Review A*, 71(6):061405, 2005.

[262] A. A. Muller, P. Soto, D. Dascalu, D. Neculoiu, and V. E. Boria. A 3-D Smith chart based on the Riemann sphere for active and passive microwave circuits. *IEEE Microwave and Wireless Components Letters*, 21(6):286–288, 2011.

[263] J. W. Neuberger, C. Feiler, H. Maier, and W. P. Schleich. The Riemann hypothesis illuminated by the Newton flow of ζ. *Physica Scripta*, 90(10):108015, 2015.

[264] J. H. Hannay. The Majorana representation of polarization, and the Berry phase of light. *Journal of Modern Optics*, 45(5):1001–1008, 1998.

[265] S. Dogra, K. Dorai, and Arvind. Majorana representation, qutrit Hilbert space and NMR implementation of qutrit gates. *Journal of Physics B: Atomic, Molecular and Optical Physics*, 51(4):045505, 2018.

[266] J. Laatikainen, A. T. Friberg, O. Korotkova, and T. Setälä. Poincaré sphere of electromagnetic spatial coherence. *Optics Letters*, 46(9):2143–2146, 2021.

[267] J. Laatikainen, A. T. Friberg, O. Korotkova, and T. Setälä. Coherence Poincaré sphere of partially polarized optical beams. *Physical Review A*, 105(3):033506, 2022.

[268] H. Shang, B. Zhou, W. Quan, H. Chi, J. Fang, and S. Zou. Measurement of rubidium vapor number density based on Faraday modulator. *Journal of Physics D: Applied Physics*, 55(33):335106, 2022.

[269] OMEGA. *PLM Series Polyimide Flexible Heaters*. https://www.farnell.com/datasheets/3185354.pdf If link broken, copy of pdf can be found with data for this thesis at Durham Collections.

[270] J. Keaveney, D. A. Rimmer, and I. G. Hughes. Self-similarity of optical rotation trajectories around the Poincaré sphere with application to an ultra-narrow atomic bandpass filter. *arXiv preprint*, 1807.04652, 2018.

[271] Z. Zhu, H. Li, W. Sun, and S. Liu. Theoretical model of an atomic line filter based on the combination of a double selective pump. *Applied Optics*, 56(1):78–83, 2017.

[272] A. Ray, S. Ali, and A. Chakrabarti. Study of the effect of repump laser on atomic line filter. *JOSA B*, 30(9):2436–2442, 2013.

[273] B. Luo, L. Yin, J. Xiong, J. Chen, and H. Guo. Induced-dichroism-excited atomic line filter at 1529 nm. *IEEE Photonics Technology Letters*, 30(17):1551–1554, 2018.

[274] V. Shah, S. Knappe, P. D. D. Schwindt, and J. Kitching. Subpicotesla atomic magnetometry with a microfabricated vapour cell. *Nature Photonics*, 1(11):649–652, 2007.

[275] S. J. Ingleby, P. F. Griffin, A. S. Arnold, M. Chouliara, and E. Riis. High-precision control of static magnetic field magnitude, orientation, and gradient using optically pumped vapour cell magnetometry. *Review of Scientific Instruments*, 88(4):043109, 2017.

[276] J. U. Sutter, O. Lewis, C. Robinson, et al. Recording the heart beat of cattle using a gradiometer system of optically pumped magnetometers. *Computers and Electronics in Agriculture*, 177:105651, 2020.

[277] L. Bai, X. Wen, Y. Yang, L. Zhang, J. He, Y. Wang, and J. Wang. Quantum-enhanced rubidium atomic magnetometer based on Faraday rotation via 795 nm stokes operator squeezed light. *Journal of Optics*, 23(8):085202, 2021.

[278] H. S. Moon, E. B. Kim, S. E. Park, and C. Y. Park. Selection and amplification of modes of an optical frequency comb using a femtosecond laser injection-locking technique. *Applied Physics Letters*, 89(18):181110, 2006.

[279] H. Liu, M. Yin, D. Kong, Q. Xu, S. Zhang, and H. Chang. Selection and amplification of a single optical frequency comb mode for laser cooling of the strontium atoms in an optical clock. *Applied Physics Letters*, 107(15):151104, 2015.

[280] Y. Doumbia, D. Wolfersberger, K. Panajotov, and M. Sciamanna. Tailoring frequency combs through VCSEL polarization dynamics. *Optics Express*, 29(21):33976–33991, 2021.

[281] K. Balakier, H. Shams, M. J. Fice, L. Ponnampalam, C. S. Graham, C. C. Renaud, and A. J. Seeds. Optical phase lock loop as high-quality tuneable filter for optical frequency comb line selection. *Journal of Lightwave Technology*, 36(19):4646–4654, 2018.

[282] K. Balakier, L. Ponnampalam, M. J. Fice, C. C. Renaud, and A. J. Seeds. Integrated semiconductor laser optical phase lock loops. *IEEE Journal of Selected Topics in Quantum Electronics*, 24(1):1–12, 2017.

[283] B. Redding, J. D. McKinney, R. T. Schermer, and J. B. Murray. High-resolution wide-band optical frequency comb control using stimulated brillouin scattering. *Optics Express*, 30(12):22097–22106, 2022.

[284] M. Choi, I. C. Mayorga, S. Preußler, and T. Schneider. Investigation of gain dependent relative intensity noise in fiber brillouin amplification. *Journal of Lightwave Technology*, 34(16):3930–3936, 2016.

[285] E. Caldwell, I. Coddington, et al. White paper: Frequency comb based optical time transfer. *Decadal Survey on Biological and Physical Sciences (BPS) Research in Space 2023-2032*.

[286] C. M. Bender and S. Boettcher. Real spectra in non-Hermitian Hamiltonians having P T symmetry. *Physical Review Letters*, 80(24):5243, 1998.

[287] C. M. Bender. Making sense of non-Hermitian hamiltonians. *Reports on Progress in Physics*, 70(6):947, 2007.

[288] N. Moiseyev. *Non-Hermitian quantum mechanics*. Cambridge University Press, 2011.

[289] M. V. Berry. Physics of nonhermitian degeneracies. *Czechoslovak Journal of Physics*, 54(10):1039–1047, 2004.

[290] L. Feng, R. El-Ganainy, and L. Ge. Non-Hermitian photonics based on parity-time symmetry. *Nature Photonics*, 11(12):752–762, 2017.

[291] R. El-Ganainy, K. G. Makris, D. N. Christodoulides, and Z. H. Musslimani. Theory of coupled optical PT-symmetric structures. *Optics Letters*, 32(17):2632–2634, 2007.

[292] A. A. Zyablovsky, A. P. Vinogradov, A. A. Pukhov, A. V. Dorofeenko, and A. A. Lisyansky. PT-symmetry in optics. *Physics-Uspekhi*, 57(11):1063, 2014.

[293] P. Peng, W. Cao, C. Shen, W. Qu, J. Wen, L. Jiang, and Y. Xiao. Anti-parity-time symmetry with flying atoms. *Nature Physics*, 12(12):1139–1145, 2016.

[294] Y. Jiang, Y. Mei, Y. Zuo, Y. Zhai, J. Li, J. Wen, and S. Du. Anti-parity-time symmetric optical four-wave mixing in cold atoms. *Physical Review Letters*, 123(19):193604, 2019.

[295] F. Zhang, Y. Feng, X. Chen, L. Ge, and W. Wan. Synthetic anti-PT symmetry in a single microcavity. *Physical Review Letters*, 124(5):053901, 2020.

[296] Q. Wang, J. Wang, H. Z. Shen, S. C. Hou, and X. X. Yi. Exceptional points and dynamics of a non-Hermitian two-level system without PT symmetry. *Europhysics Letters*, 131(3):34001, 2020.

[297] T. Z. Luan, H. Z. Shen, and X. X. Yi. Shortcuts to adiabaticity with general two-level non-Hermitian systems. *Physical Review A*, 105(1):013714, 2022.

[298] A. E. Siegman. Excess spontaneous emission in non-Hermitian optical systems. I. Laser amplifiers. *Physical Review A*, 39(3):1253, 1989.

[299] M. V. Berry. Optical polarization evolution near a non-Hermitian degeneracy. *Journal of Optics*, 13(11):115701, 2011.

[300] R. El-Ganainy, M. Khajavikhan, D. N. Christodoulides, and Ş. K. Özdemir. The dawn of non-Hermitian optics. *Communications Physics*, 2(1):1–5, 2019.

[301] R. El-Ganainy, K. G. Makris, M. Khajavikhan, Z. H. Musslimani, S. Rotter, and D. N. Christodoulides. Non-Hermitian physics and PT symmetry. *Nature Physics*, 14(1):11–19, 2018.

[302] A. U. Hassan, G. L. Galmiche, G. Harari, P. LiKamWa, M. Khajavikhan, M. Segev, and D. N. Christodoulides. Chiral state conversion without encircling an exceptional point. *Physical Review A*, 96(5):052129, 2017.

[303] A. U. Hassan, B. Zhen, M. Soljačić, M. Khajavikhan, and D. N. Christodoulides. Dynamically Encircling Exceptional Points: Exact Evolution and Polarization State Conversion. *Physical Review Letters*, 118(9):093002, 2017.

[304] J. B. Khurgin, Y. Sebbag, E. Edrei, R. Zektzer, K. Shastri, U. Levy, and F. Monticone. Emulating exceptional-point encirclements using imperfect (leaky) photonic components: asymmetric mode-switching and omnipolarizer action. *Optica*, 8(4):563–569, 2021.

[305] M. C. Rechtsman. Optical sensing gets exceptional. *Nature*, 548(7666):161–162, 2017.

[306] W. Chen, K. Ş. Özdemir, G. Zhao, J. Wiersig, and L. Yang. Exceptional points enhance sensing in an optical microcavity. *Nature*, 548(7666):192–196, 2017.

[307] Jan Wiersig. Prospects and fundamental limits in exceptional point-based sensing. *Nature Communications*, 11:2454, May 2020.

[308] H. Hodaei, M. Miri, M. Heinrich, D. N. Christodoulides, and M. Khajavikhan. Parity-time-symmetric microring lasers. *Science*, 346(6212):975–978, 2014.

[309] P. Miao, Z. Zhang, J. Sun, W. Walasik, S. Longhi, N. M. Litchinitser, and L. Feng. Orbital angular momentum microlaser. *Science*, 353(6298):464–467, 2016.

[310] Z. Gao, S. T. M. Fryslie, B. J. Thompson, P. S. Carney, and K. D. Choquette. Parity-time symmetry in coherently coupled vertical cavity laser arrays. *Optica*, 4(3):323–329, 2017.

[311] Y. Ashida, Z. Gong, and M. Ueda. Non-hermitian physics. *Advances in Physics*, 69(3):249–435, 2020.

[312] R. Hamazaki, K. Kawabata, N. Kura, and M. Ueda. Universality classes of non-Hermitian random matrices. *Physical Review Research*, 2(2):023286, 2020.

[313] F. E. Öztürk, T. Lappe, G. Hellmann, J. Schmitt, J. Klaers, F. Vewinger, J. Kroha, and M. Weitz. Observation of a non-Hermitian phase transition in an optical quantum gas. *Science*, 372(6537):88–91, 2021.

[314] L. Jin and Z. Song. Symmetry-protected scattering in non-Hermitian linear systems. *Chinese Physics Letters*, 38(2):024202, 2021.

[315] W. Zhu, X. Fang, D. Li, Y. Sun, Y. Li, Y. Jing, and H. Chen. Simultaneous observation of a topological edge state and exceptional point in an open and non-Hermitian acoustic system. *Physical Review Letters*, 121(12):124501, 2018.

[316] D. R. Nelson and N. M. Shnerb. Non-hermitian localization and population biology. *Physical Review E*, 58(2):1383, 1998.

[317] A. Amir, N. Hatano, and D. R. Nelson. Non-Hermitian localization in biological networks. *Physical Review E*, 93(4):042310, 2016.

[318] W. D. Heiss. The physics of exceptional points. *Journal of Physics A: Mathematical and Theoretical*, 45(44):444016, 2012.

[319] D. Heiss. Circling exceptional points. *Nature Physics*, 12(9):823–824, 2016.

[320] Ş. K. Özdemir, S. Rotter, F. Nori, and L. Yang. Parity–time symmetry and exceptional points in photonics. *Nature Materials*, 18(8):783–798, 2019.

[321] M. Miri and A. Alù. Exceptional points in optics and photonics. *Science*, 363(6422):eaar7709, 2019.

[322] J. B. Khurgin. Exceptional points in polaritonic cavities and subthreshold Fabry–Perot lasers. *Optica*, 7(8):1015–1023, 2020.

[323] K. Takata, K. Nozaki, E. Kuramochi, S. Matsuo, K. Takeda, T. Fujii, S. Kita, A. Shinya, and M. Notomi. Observing exceptional point degeneracy of radiation with electrically pumped photonic crystal coupled-nanocavity lasers. *Optica*, 8(2):184–192, 2021.

[324] A. Roy, S. Jahani, Q. Guo, A. Dutt, S. Fan, M. Miri, and A. Marandi. Nondissipative non-hermitian dynamics and exceptional points in coupled optical parametric oscillators. *Optica*, 8(3):415–421, 2021.

[325] Y. Chen, F. Zhang, T. Qin, G. Zhao, J. Hou, X. Chen, L. Ge, and W. Wan. Exceptional points with memory in a microcavity Brillouin laser. *Optica*, 9(9):971–979, 2022.

[326] W. D. Heiss and W. Steeb. Avoided level crossings and Riemann sheet structure. *Journal of Mathematical Physics*, 32(11):3003–3007, 1991.

[327] J. Matsuda, K. Aoyagi, Y. Kondoh, M. Iizuka, and K Mukasa. A three-dimensional measuring method for magnetic stray fields. *IEEE Transactions on Magnetics*, 26(5):2061–2063, 1990.

[328] X. Xu, Z. Wang, R. Jiao, C. Yi, W. Sun, and S. Chen. Ultra-low noise magnetic field for quantum gases. *Review of Scientific Instruments*, 90(5), 2019.

[329] C. Liang, Y. Tang, A. Xu, and Y. Liu. Observation of exceptional points in thermal atomic ensembles. *Physical Review Letters*, 130(26):263601, 2023.

[330] W. Goldshlag, R. Su, S. Park, T. O. Reboli, and J. G. Eden. Interference between atomic Rb (5d 5/2–5p 3/2) and (5p 3/2–5s 1/2) coherences: observation of an exceptional point by quantum beating at 2.1 Thz. *Journal of Physics B: Atomic, Molecular and Optical Physics*, 54(16):165001, 2021.

[331] V. Gasparian, P. Guo, and E. Jódar. Anomalous Faraday effect in a PT-symmetric dielectric slab. *Physics Letters A*, 453:128473, 2022.

[332] S. A. Diddams, J. C. Bergquist, S. R. Jefferts, and C. W. Oates. Standards of time and frequency at the outset of the 21st century. *Science*, 306(5700):1318–1324, 2004.

[333] F. Riehle. Towards a redefinition of the second based on optical atomic clocks. *Comptes Rendus Physique*, 16(5):506–515, 2015.

[334] H. Katori. Optical lattice clocks and quantum metrology. *Nature Photonics*, 5(4):203–210, 2011.

[335] A. D. Ludlow, M. M. Boyd, J. Ye, E. Peik, and P. O. Schmidt. Optical atomic clocks. *Reviews of Modern Physics*, 87(2):637, 2015.

[336] J. Chen. Active optical clock. *Chinese Science Bulletin*, 54(3):348–352, 2009.

[337] J. Zhang, T. Shi, J. Miao, and J. Chen. The development of active optical clock. *AAPPS Bulletin*, 33(1):10, 2023.

[338] D. Yu and J. Chen. Optical clock with millihertz linewidth based on a phase-matching effect. *Physical Review Letters*, 98(5):050801, 2007.

[339] S. J. M. Kuppens, M. P. Van Exter, and J. P. Woerdman. Quantum-limited linewidth of a bad-cavity laser. *Physical Review Letters*, 72(24):3815, 1994.

[340] M. P. Van Exter, S. J. M. Kuppens, and J. P. Woerdman. Theory for the linewidth of a bad-cavity laser. *Physical Review A*, 51(1):809, 1995.

[341] E. D. Black. An introduction to Pound–Drever–Hall laser frequency stabilization. *American Journal of Physics*, 69(1):79–87, 2001.

[342] P. Gill. Optical frequency standards. *Metrologia*, 42(3):S125–S137, 2005.

[343] S. L. Kristensen, E. Bohr, J. Robinson-Tait, T. Zelevinsky, J. W. Thomsen, and J. H. Müller. Subnatural Linewidth Superradiant Lasing with Cold Sr 88 Atoms. *Physical Review Letters*, 130(22):223402, 2023.

[344] G. Trénec, W. Volondat, O. Cugat, and J. Vigué. Permanent magnets for Faraday rotators inspired by the design of the magic sphere. *Applied Optics*, 50(24):4788–4797, 2011.

[345] E. A. Mironov, I. Snetkov, A. V. Voitovich, and O. V. Palashov. Permanent-magnet Faraday isolator with the field intensity of 25 kOe. *Quantum Electronics*, 43(8):740, 2013.

[346] E. A. Mironov, A. V. Voitovich, and O. V. Palashov. Permanent-magnet Faraday isolator with the field intensity of more than 3 Tesla. *Laser Physics Letters*, 17(1):015001, 2019.

[347] R. C. Jones. A new calculus for the treatment of optical systems V. A more general formulation, and description of another calculus. *JOSA*, 37(2):107–110, 1947.

[348] N. G. Parke III. *Matrix Optics*. PhD thesis, Massachussetts Institute of Technology, 1948.

[349] R. C. O'Handley. Modified Jones calculus for the analysis of errors in polarization-modulation ellipsometry. *JOSA*, 63(5):523–528, 1973.

[350] S. N. Savenkov, O. I. Sydoruk, and R. S. Muttiah. Eigenanalysis of dichroic, birefringent, and degenerate polarization elements: a Jones-calculus study. *Applied Optics*, 46(27):6700–6709, 2007.

[351] S. N. Savenkov. Jones and Mueller matrices: structure, symmetry relations and information content. In *Light Scattering Reviews 4: Single Light Scattering and Radiative Transfer*, pages 71–119. Springer, 2009.

[352] C. Menzel, C. Rockstuhl, and F. Lederer. Advanced Jones calculus for the classification of periodic metamaterials. *Physical Review A*, 82(5):053811, 2010.

[353] M. Baier, F. M. Soares, T. Gärtner, M. Moehrle, and M. Schell. Fabrication tolerant integrated polarization rotator design using the Jones Calculus. *Journal of Lightwave Technology*, 37(13):3106–3112, 2019.

[354] A. Tufaile, M. Snyder, and A. P. B. Tufaile. Study of Light Polarization by Ferrofluid film using Jones Calculus. *Condensed Matter*, 7(1):28, 2022.

[355] F. Sanaâ, Y. Makhlouka, and M. Gharbia. Linear retardance and diattenuation dispersion measurements of anisotropic medium with Jones calculus based spectrometric technique. *Results in Physics*, 37:105522, 2022.

[356] C. S Adams and I. G. Hughes. *Optics f2f: from Fourier to Fresnel*. Oxford University Press, 2018.

[357] V. L. Ginzburg. The propagation of electromagnetic waves in plasmas. *International Series of Monographs in Electromagnetic Waves*, 1970.

[358] T. Curtright and L. Mezincescu. Biorthogonal quantum systems. *Journal of Mathematical Physics*, 48(9):092106, 2007.

[359] D. C. Brody. Biorthogonal quantum mechanics. *Journal of Physics A: Mathematical and Theoretical*, 47(3):035305, 2013.

[360] F. Bagarello, H. Inoue, and C. Trapani. Biorthogonal vectors, sesquilinear forms, and some physical operators. *Journal of Mathematical Physics*, 59(3):033506, 2018.

[361] G. Sun, J. Tang, and S. Kou. Biorthogonal quantum criticality in non-hermitian many-body systems. *Frontiers of Physics*, 17:1–9, 2022.

[362] J. H. Wilkinson. Error analysis of floating-point computation. *Numerische Mathematik*, 2:319–340, 1960.

[363] J. Muller, N. Brisebarre, F. De Dinechin, et al. *Handbook of floating-point arithmetic*. Springer, 2018.

[364] T. L. Heath et al. *The thirteen books of Euclid's Elements*. Courier Corporation, 1956.

[365] E. C. G. Sudarshan, P.M. Mathews, and J. Rau. Stochastic dynamics of quantum-mechanical systems. *Physical Review*, 121(3):920, 1961.

[366] W. H. Greub. *Linear algebra*. Springer Science & Business Media, 2012.

[367] J. H. Wilkinson, F. L. Bauer, and C. Reinsch. *Linear algebra*. Springer, 2013.

[368] G. Ballard, A. R. Benson, A. Druinsky, B. Lipshitz, and O. Schwartz. Improving the numerical stability of fast matrix multiplication. *SIAM Journal on Matrix Analysis and Applications*, 37(4):1382–1418, 2016.

[369] Z. Strakoš and J. Liesen. On numerical stability in large scale linear algebraic computations. *ZAMM-Journal of Applied Mathematics and Mechanics/Zeitschrift für Angewandte Mathematik und Mechanik: Applied Mathematics and Mechanics*, 85(5):307–325, 2005.

[370] Y. Chatelain, Kiar G. S. Young, N. Yong, and T. Glatard. PyTracer: Automatically profiling numerical instabilities in Python. *IEEE Transactions on Computers*, 72:1792–1803, 2022.

[371] P. Virtanen, R. Gommers, T. Oliphant, et al. SciPy 1.0: Fundamental Algorithms for Scientific Computing in Python. *Nature Methods*, 17:261–272, 2020.

[372] J. A. Ratcliffe. *The Magneto-ionic Theory and Its Application to the Ionosphere*. Cambridge University Press, 1959.

[373] P. C. Clenmow and J. P. Dougherty. *Electrodynamics of Particles and Plasmas*. Addison-Wesley, 1969.

[374] W. P. Allis, S. J. Buchsbaum, and A. Bers. *Waves in Anisotropic Plasmas*. M. I. T. Press, 1963.

[375] T. H. Stix. *The Theory of Plasma Waves*. McGraw-Hill, 1962.

[376] M. C. Steele and B. Vural. *Wave interactions in solid state plasmas*. McGraw-Hill, 1969.

[377] Kenneth George Budden. Radio waves in the ionosphere. *Radio Waves in the Ionosphere*, 2009.

[378] A. Yariv and P. Yeh. *Optical waves in crystals*. Wiley New York, 1984.

[379] A. Meurer, C. P. Smith, M. Paprocki, et al. Sympy: symbolic computing in python. *PeerJ Computer Science*, 3:e103, 2017.

[380] C. R. Harris, K. . Millman S. J. van der Walt, et al. Array programming with NumPy. *Nature*, 585(7825):357–362, 2020.

[381] G. Dahlquist. 33 years of numerical instability, part i. *BIT Numerical Mathematics*, 25:188–204, 1985.

[382] N. J. Higham. *Accuracy and stability of numerical algorithms*. SIAM, 2002.

[383] A. K. Cline, C. B. Moler, G. W. Stewart, and J. H. Wilkinson. An estimate for the condition number of a matrix. *SIAM Journal on Numerical Analysis*, 16(2):368–375, 1979.

[384] A. Edelman. Eigenvalues and condition numbers of random matrices. *SIAM journal on matrix analysis and applications*, 9(4):543–560, 1988.

[385] J. W. Demmel. The geometry of ill-conditioning. *Journal of Complexity*, 3(2):201–229, 1987.

[386] D. Manzano. A short introduction to the Lindblad master equation. *AIP Advances*, 10(2):025106, 2020.

[387] T. Kato. *A short introduction to perturbation theory for linear operators*. Springer Science & Business Media, 2012.

[388] J. T. M. Walraven. Lecture notes: Atomic physics, December 2018.

[389] H. J. Metcalf and P. Van der Straten. *Laser cooling and trapping*. Springer Science & Business Media, 1999.

[390] M. Inguscio and L. Fallani. *Atomic physics: precise measurements and ultracold matter*. OUP Oxford, 2013.

[391] U. Volz and H. Schmoranzer. Precision lifetime measurements on alkali atoms and on helium by beam–gas–laser spectroscopy. *Physica Scripta*, 1996(T65):48, 1996.

[392] M. S. Safronova, C. J. Williams, and C. W. Clark. Relativistic many-body calculations of electric-dipole matrix elements, lifetimes, and polarizabilities in rubidium. *Physical Review A*, 69(2):022509, 2004.

[393] B. K. Sahoo. Conforming the measured lifetimes of the $5d^2D_{3/2,5/2}$ states in Cs with theory. *Physical Review A*, 93(2):022503, 2016.

[394] X. Wang, J. Jiang, L. Xie, D. Zhang, and C. Dong. Polarizabilities and tune-out wavelengths of the hyperfine ground states of Rb 87, 85. *Physical Review A*, 94(5):052510, 2016.

[395] X. Wang, J. Jiang, Z. Wu, and C. Dong. Determination of oscillator strengths by using magic wavelengths of the $5_{s_{1/2}} \rightarrow 5_{p_{1/2,3/2}}$ transitions for Rb. *Journal of Quantitative Spectroscopy and Radiative Transfer*, 242:106783, 2020.

[396] C. Müller. *Spherical harmonics*. Springer, 2006.

[397] D. A. Varshalovich, A. N. Moskalev, and V. K. Khersonskii. *Quantum theory of angular momentum*. World Scientific, 1988.

[398] R. Hui and M. O'Sullivan. *Fiber-Optic Measurement Techniques*. Academic Press, 2022.

[399] O. K. Kwon, K. H. Kim, E. D. Sim, J. H. Kim, H. S. Kim, and K. R. Oh. Broadly wavelength-tunable external cavity lasers with extremely low power variation over tuning range. *IEEE Photonics Technology Letters*, 17(3):537–539, 2005.

[400] S. Dutta, D. S. Elliott, and Y. P. Chen. Mode-hop-free tuning over 135 GHz of external cavity diode lasers without antireflection coating. *Applied Physics B*, 106:629–633, 2012.

[401] B. Deng, C. Sima, Y. Xiao, X. Wang, Y. Ai, T. Li, P. Lu, and D. Liu. Modified laser scanning technique in wavelength modulation spectroscopy for advanced TDLAS gas sensing. *Optics and Lasers in Engineering*, 151:106906, 2022.

[402] N. Ismail, C. C. Kores, D. Geskus, and M. Pollnau. Fabry-Pérot resonator: spectral line shapes, generic and related Airy distributions, linewidths, finesses, and performance at low or frequency-dependent reflectivity. *Optics Express*, 24(15):16366–16389, 2016.

[403] R. P. Stanley, R. Houdre, U. Oesterle, M. Gailhanou, and M. Ilegems. Ultrahigh finesse microcavity with distributed bragg reflectors. *Applied Physics Letters*, 65(15):1883–1885, 1994.

[404] J. Y. Lee, J. W. Hahn, and H. Lee. Spatiospectral transmission of a plane-mirror Fabry–Perot interferometer with nonuniform finite-size diffraction beam illuminations. *JOSA A*, 19(5):973–984, 2002.

[405] R. Sauleau, P. Coquet, T. Matsui, and J. Daniel. A new concept of focusing antennas using plane-parallel Fabry-Perot cavities with nonuniform mirrors. *IEEE Transactions on Antennas and Propagation*, 51(11):3171–3175, 2003.

[406] H. Pfeifer, L. Ratschbacher, J Gallego, C. Saavedra, A. Faßbender, A. von Haaren, W. Alt, S. Hofferberth, M. Köhl, S. Linden, et al. Achievements and perspectives of optical fiber Fabry–Perot cavities. *Applied Physics B*, 128(2):29, 2022.

[407] Y. Aso, M. Ando, K. Kawabe, S. Otsuka, and K. Tsubono. Stabilization of a Fabry–Perot interferometer using a suspension-point interferometer. *Physics Letters A*, 327(1):1–8, 2004.

[408] L. Chen, J. L. Hall, J. Ye, T. Yang, E. Zang, and T. Li. Vibration-induced elastic deformation of Fabry-Perot cavities. *Physical Review A*, 74(5):053801, 2006.

[409] J. Alnis, A. Matveev, N. Kolachevsky, T. Udem, and T. W. Hänsch. Subhertz linewidth diode lasers by stabilization to vibrationally and thermally compensated ultralow-expansion glass Fabry-Pérot cavities. *Physical Review A*, 77(5):053809, 2008.

[410] D. W. Preston. Doppler-free saturated absorption: Laser spectroscopy. *American Journal of Physics*, 64(11):1432–1436, 1996.

[411] C. Ye. *Tunable external cavity diode lasers*. World Scientific, 2004.

[412] A. T. Schremer and C. L. Tang. External-cavity semiconductor laser with 1000 GHz continuous piezoelectric tuning range. *IEEE Photonics Technology Letters*, 2(1):3–5, 1990.

[413] S. C. Doret. Simple, low-noise piezo driver with feed-forward for broad tuning of external cavity diode lasers. *Review of Scientific Instruments*, 89(2):023102, 2018.

[414] H. Kaizuka and B. Siu. A simple way to reduce hysteresis and creep when using piezoelectric actuators. *Japanese Journal of Applied Physics*, 27(5A):L773, 1988.

[415] K. Tian, Z. Liu, T. Jing, and Y. Zhu. Rate-dependent input curve shaping of the piezoelectric actuator based optical resonator cavity displacement characteristics for an external cavity diode laser. *Review of Scientific Instruments*, 92(9):095008, 2021.

[416] C. Leahy, J. T. Hastings, and P. M. Wilt. Temperature dependence of Doppler-broadening in rubidium: An undergraduate experiment. *American Journal of Physics*, 65(5):367–371, 1997.

[417] M. L. Harris, S. L. Cornish, A. Tripathi, and I. G. Hughes. Optimization of sub-Doppler DAVLL on the rubidium D2 line. *Journal of Physics B: Atomic, Molecular and Optical Physics*, 41(8):085401, 2008.

[418] K. B. MacAdam, A Steinbach, and C. Wieman. A narrow-band tunable diode laser system with grating feedback, and a saturated absorption spectrometer for Cs and Rb. *American Journal of Physics*, 60(12):1098–1111, 1992.

[419] D. A. Smith and I. G. Hughes. The role of hyperfine pumping in multi-level systems exhibiting saturated absorption. *American Journal of Physics*, 72(5):631–637, 2004.

[420] M. B. Gray, D. A. Shaddock, C. C. Harb, and H. Bachor. Photodetector designs for low-noise, broadband, and high-power applications. *Review of Scientific Instruments*, 69(11):3755–3762, 1998.

[421] A. Daffurn, R. F. Offer, and A. S. Arnold. A simple, powerful diode laser system for atomic physics. *Applied Optics*, 60(20):5832–5836, 2021.

[422] N. Agnew, G. Machin, E. Riis, and A. S. Arnold. Practical Doppler broadening thermometry. *arXiv preprint*, 2307.06229, 2023.

[423] D. Pizzey, J. D. Briscoe, F. D. Logue, S. Wrathmall, and I. G. Hughes. Data Processing Jupyter Notebook (Collections). https://www.doi.org/10.15128/r2m326m176m.

[424] D. Pizzey, J. D. Briscoe, F. D. Logue, S. Wrathmall, and I. G. Hughes. Data Processing Jupyter Notebook (GitHub). https://github.com/durham-qlm/scope2elecsus.

[425] J. Keaveney. *Cooperative interactions in dense thermal Rb vapour confined in nm-scale cells.* PhD thesis, Durham University, 2013.

[426] L. Weller. *Absolute Absorption and Dispersion in a Thermal Rb Vapour at High Densities and High Magnetic Fields.* PhD thesis, Durham University, 2013.

[427] D. J. Whiting. *Nonlinear optics in a thermal Rb vapour at high magnetic fields.* PhD thesis, Durham University, 2017.

Colophon

This thesis is based on a template developed by Matthew Townson and Andrew Reeves. It was typeset with LaTeX $2_\varepsilon$and compiled using *Overleaf*. It was created using the *memoir* package, maintained by Lars Madsen, with the default chapter style. The font used for texts is Latin Modern, derived from fonts designed by Donald E. Kunith. For figures, the fonts Georgia, designed by Matthew Carter, and Constantia, designed by John Hudson, are used. Figures were generated using the *matplotlib* package in python 3 and *Inkscape*.